

**Universidade do Minho**
Escola de Engenharia

Francisca Rocha Melo Fonseca

# Design of osteogenic-stimulating implants by mechanotransduction modulation

Design of osteogenic-stimulating implants by mechanotransduction modulation

Francisca Rocha Melo Fonseca

UMinho | 2023

outubro de 2023

REPÚBLICA PORTUGUESA FCT Fundação para a Ciência e a Tecnologia NORTE2020 POCH PORTUGAL 2020

**Universidade do Minho**
Escola de Engenharia

Francisca Rocha Melo Fonseca

# Design of osteogenic-stimulating implants by mechanotransduction modulation

Tese de Doutoramento

Programa Doutoral em Líderes para Indústrias Tecnológicas

Trabalho realizado sob a orientação de

Professora Doutora Maria Georgina Macedo Miranda

Professor Doutor Filipe Samuel Correia Pereira da Silva

Professor Doutor Michael Gasik

outubro de 2023

## DIREITOS DE AUTOR E CONDIÇÕES DE UTILIZAÇÃO DO TRABALHO POR TERCEIROS

Este é um trabalho académico que pode ser utilizado por terceiros desde que respeitadas as regras e boas práticas internacionalmente aceites, no que concerne aos direitos de autor e direitos conexos.

Assim, o presente trabalho pode ser utilizado nos termos previstos na licença abaixo indicada.

Caso o utilizador necessite de permissão para poder fazer um uso do trabalho em condições não previstas no licenciamento indicado, deverá contactar o autor, através do RepositóriUM da Universidade do Minho.

**Licença concedida aos utilizadores deste trabalho**



**Atribuição-NãoComercial-SemDerivações**

**CC BY-NC-ND**

https://creativecommons.org/licenses/by-nc-nd/4.0/

Universidade do Minho, 17 /10 /2023

Assinatura: _____

# ACKNOWLEDGMENTS

Many were the people who gave their contribution during this PhD. To all who helped me get this far, thank you very much.

First, I would like to thank my supervisors who guided me and whose contributions were essential to this thesis' success. To Professor Georgina Miranda for her availability, dedication and support. To Professor Filipe Silva for his enthusiasm, expertise and for providing an optimal working environment. To Professor Michael Gasik for helping me see the bigger picture, for his knowledge and assistance.

My genuine appreciation to Doctor Inês Mendes Pinto for the care and support, and to Professor Óscar Carvalho for his motivation and optimism in seeking solutions. To the dearly missed Professor Pedro Souto for his encouragement to engage in business courses and competitions.

To all members of the Microfabrication and Integrated Systems Laboratory for the warm welcome, team-spirit and shared knowledge. Thank you for your friendship and being my family when I missed mine the most.

To the International Iberian Nanotechnology Laboratory, particularly to Professor Paulo Freitas and to the Nanodevices team for their welcome. To Doctor Sofia Domingues whose love of biology and science was contagious. To Doctor Andrea Cruz for her laboratory teachings and constant availability. To Doctor Diana Pinho for her motivation and support.

To the Glial Cell Biology research group from the Institute for Innovation and Research in Health, for the support and providing facilities to perform the last experiments of this thesis.

To all the people from other research facilities who contributed equipment and knowledge.

To my friends who, despite the distance, have maintained a close and meaningful friendship.

To the Fernandes family, my adoptive Guimarães family, for their hospitality and care.

To my family, especially to my mother and father, for their encouragement, affection and granting me all opportunities. To my sister Matilde for inspiring resilience and serenity. To my grandmother Lina for her cosy food and life lessons and my uncle Rui for his curiosity.

Finally, I would like to acknowledge Fundação para a Ciência e a Tecnologia for my PhD grant SFRH/BD/141056/2018 and COVID/BD/152996/2022.

## Statement of Integrity

I hereby declare having conducted this academic work with integrity. I confirm that I have not used plagiarism or any form of undue use of information or falsification of results along the process leading to its elaboration.

I further declare that I have fully acknowledged the Code of Ethical Conduct of the University of Minho.

University of Minho, 17 /10 /2023

_____

Francisca Rocha Melo Fonseca

# RESUMO


## Design de implantes estimulantes de osteogénese por modulação de mecanotransdução

À medida que a esperança de vida aumenta, aumenta também o número de doentes que necessitam de intervenções ortopédicas. Além disso, a idade média dos pacientes de cirurgia ortopédica tem vindo a diminuir devido à maior prevalência de um estilo de vida sedentário e obesidade. Uma das doenças esqueléticas mais comuns é a osteoartrite, que afeta principalmente as articulações da anca e do joelho. As soluções terapêuticas atuais incluem a substituição da articulação por um implante ortopédico, frequentemente composto por uma liga de Titânio 6-Alumínio 4-Vanádio (Ti6Al4V). No entanto, quando inserido na cavidade óssea, há uma diminuição da estimulação mecânica na interface osso-implante, quando comparada com o carregamento fisiológico do osso levando, portanto, à perda de fixação do implante e consequente dor.

Tendo identificado esta preocupação, esta tese de doutoramento visa melhorar a interface entre o osso e o implante através da ativação de processos de mecanotransdução responsáveis pela diferenciação das células estaminais mesenquimais humanas em células ósseas. Diferentes modificações superficiais de substratos de Ti6Al4V foram investigadas, com a produção de micro-pilares através de uma técnica subtrativa a laser, de modo a induzir um carregamento mecânico adequado ao nível celular, promovendo simultaneamente uma interligação na interface implante-osso. As propriedades potencialmente bioativas da camada de óxido e a topografia assistida por laser foram avaliadas em condições estáticas, e o modo dinâmico foi explorado para abordar o efeito da carga mecânica na osteogénese. Para tal, um dispositivo customizado para estimulação mecânica celular foi desenhado e fabricado por tecnologia laser, pioneiro na utilização de substratos metálicos para cultura celular e para estudos de mecanobiologia utilizando *live imaging*.

Este projeto interdisciplinar estabelece a base para o desenvolvimento de implantes ortopédicos capazes de induzir cargas mecânicas que promovam osteogénese na interface osso-implante. Ao assegurar uma atividade osteogénica adequada das células em torno dos implantes endósseos, espera-se a promoção da regeneração óssea saudável e a integração do implante, reduzindo potencialmente a necessidade de substituição do implante nos anos subsequentes.


**Palavras-chave:** Implantes ortopédicos; Mecanotransdução; Células estaminais mesenquimais; Ti6Al4V; Tratamento hidrotérmico; Texturização superficial a laser; Carregamento dinâmico; Modulação de tensão/deformação.

# ABSTRACT

**Design of osteogenic-stimulating implants by mechanotransduction modulation**

As life expectancy increases, so does the number of patients requiring orthopaedic interventions. Furthermore, the average age of orthopaedic surgery patients has declined due to the higher prevalence of a sedentary lifestyle and obesity. One of the most common skeletal diseases is osteoarthritis, primarily affecting the hip and knee joints. Current therapeutic solutions include joint replacement by an orthopaedic implant, often composed of Titanium 6 Aluminium 4 Vanadium (Ti6Al4V) alloy. However, when inserted into the bone cavity, there is a diminished mechanical stimulation at the bone-implant interface when compared to the physiological bone stimulation leading, therefore, to the loss of implant fixation and subsequent pain.

Having identified this concern, this PhD thesis aims to improve the interface between bone and implant by activating the mechanotransduction processes responsible for the differentiation of human mesenchymal stem cells into bone cells. Different surface modifications to Ti6Al4V substrates were investigated, with micro-pillars being produced on the surface via laser subtractive technique aiming to induce an adequate mechanical loading at the cellular level, while also promoting an interlocking at implant-bone interface. The potentially bioactive properties of the oxide layer and laser-assisted topography were assessed under static conditions, and the dynamic mode was explored to address the effect of mechanical loading on osteogenesis. For that purpose, a custom device for cell mechanical stimulation was designed and fabricated using laser technology, pioneering the use of metallic substrates for cell culture and for mechanobiology studies using live imaging.

This interdisciplinary project lays the foundation for the development of orthopaedic implants capable of inducing osteogenic-stimulating mechanical loading at the bone-implant interface. By assuring an adequate osteogenic activity of cells around endosseous implants, it is hoped to promote healthy bone regeneration and implant integration, potentially reducing the need for implant replacement in subsequent years.

**Keywords:** Orthopaedic implants; Mechanotransduction; Mesenchymal stem cells; Ti6Al4V; Hydrothermal treatment; Laser surface texturing; Dynamic loading; Stress/strain modulation.

# CONTENTS

Acknowledgments ..... iii
Resumo ..... v
Abstract ..... vi
Contents ..... vii
List of symbols, annotations and abbreviations ..... xiii
List of figures ..... xxii
List of tables ..... xxxv
Chapter 1 Introduction ..... 1
1.1. Motivation ..... 2
1.1.1. Leaders for Technical Industries doctoral program ..... 3
1.2. Objectives ..... 4
1.3. Structure of the thesis ..... 4
Chapter 2 Reengineering bone-implant interfaces for improved mechanotransduction and clinical outcomes ..... 7
Abstract ..... 8
2.1. Conventional therapeutic approaches for hip and knee replacements ..... 8
2.2. Fundamental aspects underlying bone formation and maintenance ..... 10
2.3. Extracellular and intracellular mechanical forces that regulate MSC differentiation and linked osteogenic activity ..... 13
2.4. Exploring biomaterials with the ability to provide optimal niches for MSC to robust bone repair ..... 17
2.5. The concept idea for new generation design of novel pro-active orthopaedic implants 26
2.6. Conclusion ..... 29
Acknowledgments ..... 29
References ..... 30
Chapter 3 Surface characterization of titanium-based substrates for orthopaedic applications ... 46
Abstract ..... 47
3.1. Introduction ..... 47
3.2. Materials and methods ..... 50
3.2.1. Mechanical and chemical pre-treatments of Ti-based substrates ..... 51
3.2.2. Anodic oxidation ..... 51
3.2.3. Hydrothermal process ..... 52
3.2.4. Anodizing and hydrothermal process ..... 52

3.2.5. Sterilization and storage ..... 53
3.2.6. Samples characterization ..... 53
3.2.6.1. Morphology ..... 53
3.2.6.2. Phase composition ..... 53
3.2.6.3. Roughness and $TiO_2$ thickness ..... 53
3.2.6.4. Wettability ..... 54
3.3. Results and discussion ..... 54
3.3.1. Morphology ..... 54
3.3.2. Phase composition ..... 57
3.3.3. Roughness and $TiO_2$ thickness ..... 60
3.3.4. Wettability analysis ..... 66
3.4. Conclusions ..... 71
Acknowledgments ..... 72
References ..... 72
Appendix A. Supplementary data ..... 81
Chapter 4 Augmenting the osteogenic capacity of human mesenchymal stem cells through the application of human fibronectin coating in xeno-free and serum-free culture environments ..... 84
Abstract ..... 85
4.1. Introduction ..... 85
4.2. Materials and Methods ..... 86
4.2.1. Cell culture ..... 86
4.2.2. Substrate preparation and osteogenic differentiation ..... 88
4.2.3. Evaluation of the osteogenic differentiation capacity ..... 88
4.2.3.1. Cell morphology and subcellular profiling ..... 88
4.2.3.2. Mineralization analysis ..... 89
4.2.3.3. Statistical analysis ..... 89
4.3. Results and discussion ..... 90
4.3.1. MSC morphological profile is similar in coated and uncoated substrates ..... 90
4.3.2. Fibronectin coating promotes the osteogenic differentiation of MSC ..... 91
4.4. Conclusions ..... 99
Acknowledgments ..... 99
References ..... 99
Chapter 5 Engineering a hybrid Ti6Al4V-based system for responsive and consistent osteogenesis ..... 104

Abstract ..... 105
5.1. Introduction ..... 105
5.2. Materials and methods ..... 107
5.2.1. Preparation of Ti6Al4V samples ..... 107
5.2.2. Cell culture and osteogenic differentiation of MSC ..... 108
5.2.3. Evaluation of the osteogenic capacity of MSC ..... 109
5.2.3.1. Measurement of calcium deposition ..... 109
5.2.3.2. Analysis of Quantitative Real-Time Polymerase Chain Reaction (qRT-PCR) 109
5.2.3.3. Statistical analysis ..... 110
5.3. Results and discussion ..... 111
5.3.1. Human fibronectin-based functionalization of Ti6Al4V substrates ..... 112
5.3.2. Hydrothermal treated Ti6Al4V interface promotes osteogenic programming .... 114
5.3.3. Summary of the results ..... 117
5.4. Conclusions ..... 119
Acknowledgments ..... 120
References ..... 120
Appendix A. Supplementary information ..... 127
Chapter 6 Experimental analysis and predictive modelling of Ti6Al4V laser surface texturing for biomedical applications ..... 128
Abstract ..... 129
6.1. Introduction ..... 129
6.2. Materials and methods ..... 131
6.2.1. Laser surface texturing ..... 131
6.2.2. Statistical analysis of the drawing and laser parameters ..... 136
6.2.3. Surface characterization ..... 137
6.2.3.1. Surface topography ..... 137
6.2.3.2. Surface wettability ..... 137
6.2.3.3. Surface roughness and shape factor ..... 138
6.3. Results and discussion ..... 139
6.3.1. Grooves design and texturing ..... 139
6.3.1.1. Discrete vs consecutive processing laser ..... 139
6.3.1.2. Pre-set vs continuous marking ..... 139
6.3.2. Pillars design and texturing ..... 140
6.3.3. Mathematical models ..... 142

a) Groove width model ..... 143
b) Pillar width model ..... 143
c) Pillar depth model ..... 144
6.3.3.1. Effect of the parameters on texture dimensions ..... 144
6.3.4. Characterization of textured samples ..... 148
6.3.4.1. Wettability ..... 148
6.3.4.2. Roughness, topography and morphology ..... 150
6.4. Conclusions ..... 153
Acknowledgments ..... 154
References ..... 154
Appendix A. Supplementary data ..... 160
Chapter 7 Hydrothermal treatment of laser micro-textured Ti6Al4V systems for osseointegration of orthopaedic implants ..... 173
Abstract ..... 174
7.1. Introduction ..... 174
7.2. Materials and methods ..... 176
7.2.1. Ti6Al4V systems production ..... 176
7.2.2. Ti6Al4V surface characterization ..... 178
7.2.2.1. Ti6Al4V surface topography ..... 178
7.2.2.2. Crystallographic analysis ..... 178
7.2.2.3. Surface wettability ..... 178
7.2.3. Processing Ti6Al4V systems for *in vitro* studies ..... 178
7.2.4. MSC culture and osteogenic programming within Ti6Al4V systems ..... 179
7.2.4.1. Intracellular and extracellular profile of RUNX2 within Ti6Al4V systems ..... 179
7.2.4.2. Mineralization assessment ..... 180
7.2.4.3. Statistical analysis ..... 181
7.3. Results and discussion ..... 181
7.3.1. Detailed characterization of the laser processed Ti6Al4V ..... 181
7.3.2. Textured Ti6Al4V samples promote differentiation of MSC ..... 183
7.4. Conclusions ..... 185
Acknowledgments ..... 185
References ..... 186
Appendix A. Supplementary data ..... 190

Chapter 8 Mechanical stimulation devices for mechanobiology studies: a market, literature, and patents review ..... 193
Abstract ..... 194
8.1. Contextualization ..... 194
8.2. The cellular microenvironment ..... 194
8.3. Moving from 2 to 3D models ..... 195
8.4. Emerging mechanical stimulation devices ..... 198
8.5. Commercially available cell-stimulation devices ..... 201
8.6. Custom-built cell-stimulation devices ..... 208
8.6.1. Tensile loading devices ..... 208
8.6.2. Compressive loading devices ..... 214
8.7. Review of patents ..... 216
8.8. Potential and future perspectives ..... 235
Acknowledgments ..... 235
References ..... 236
Chapter 9 Design of a device for cell mechanical stimulation and real-time monitoring ..... 250
Abstract ..... 251
9.1. Introduction ..... 251
9.2. Materials and methods ..... 254
9.2.1. Device requirements, design and fabrication ..... 254
9.2.2. Preliminary validation of the device ..... 257
9.2.3. Substrate preparation and topographical characterization ..... 259
9.2.4. Cell culture and stimulation conditions ..... 259
9.3. Results and discussion ..... 260
9.3.1. Description of the cell mechanical stimulation device ..... 260
9.3.2. Preliminary validation ..... 262
9.3.2.1 Numerical simulation ..... 262
9.3.2.2 Experimental analysis ..... 264
9.3.3. *In vitro* testing of the device ..... 264
9.4. Conclusions ..... 266
Acknowledgments ..... 267
References ..... 267
Appendix A ..... 269
Appendix B ..... 270

Chapter 10 Discussion and conclusions ..... 272
10.1. General discussion ..... 273
10.2. Main conclusions ..... 276
10.3. Suggestions for future works ..... 276
10.4. Further contributions to this thesis ..... 277
References ..... 278

# LIST OF SYMBOLS, ANNOTATIONS AND ABBREVIATIONS

## Chapter 1

| | |
|---|---|
| CAGR | Compound annual growth rate |
| Ti6Al4V | Titanium 6 Aluminum 4 Vanadium |

## Chapter 2

| | |
|---|---|
| 2-Propanol | Isopropyl alcohol |
| ALP | Alkaline phosphatase |
| BMP-2 | Bone morphogenetic protein 2 |
| Col | Collagen |
| CT | Computed tomography |
| DEX | Dexamethasone |
| DSQ20 | Disordered square arrays with 20 nm |
| DSQ50 | Disordered square arrays with 50 nm |
| ECM | Extracellular matrix |
| FA | Focal adhesions |
| FAK | Focal adhesion kinase |
| HEX | Hexagonal array |
| MRI | Magnetic resonance imaging |
| MSC | Mesenchymal stem cells |
| NA | Nascent adhesions |
| NSQ50 | Near square random displacement of 50 nm |
| OC | Osteocalcin |
| OECD | Organization for Economic Co-operation and Development |
| ON | Osteonectin |
| OP | Osteopontin |
| OSX | Osterix |
| PC | Polycarbonate |
| PCL | Polycaprolactone |
| PDMS | Poly(dimethylsiloxane) |
| PI | Polyimide |

| | |
|---|---|
| PLA | Poly-L-lactic acid |
| PMMA | Polymethylmethacrylate |
| PU | Polyurethane |
| RGD | Arginine-glycine-aspartic acid |
| SQ | Square array |
| TCP | Tricalcium phosphate |
| THA | Total hip arthroplasty |
| TKA | Total knee arthroplasty |

**Chapter 3**

| | |
|---|---|
| 5XPBS | 5 Times concentrated phosphate buffered saline |
| AC | Alcohol cleaning |
| AFM | Atomic force microscopy |
| AO | Anodic oxidation |
| AP | Acidic pre-treatment |
| ASTM | American Society for Testing and Materials International |
| Ca-P | Calcium phosphate |
| $Ca(OH)_2$ | Calcium hydroxide |
| ECM | Extracellular matrix |
| $H_2SO_4$ | Sulfuric acid |
| $H_3PO_4$ | Phosphoric acid |
| HCl | Hydrochloric acid |
| Hydro | Hydrothermal treatment |
| MSC | Mesenchymal stem cells |
| $Na_2S_2O_8$ | Sodium peroxydisulfate |
| NaOH | Sodium hydroxide |
| PTFE | Polytetrafluoroethylene |
| Ra | Arithmetic average roughness |
| $R_{exp}$ | Expected R-factor |
| ROI | Region of interest |
| Rq | Root-mean-square roughness |

| | |
|---|---|
| $R_{wp}$ | Weighted profile R-factor |
| Sa | Amplitude of the mean height deviation |
| SD | Standard deviation |
| SEM | Scanning electron microscopy |
| SiC | Silicon carbide |
| STPP | Sodium tripolyphosphate |
| Ti | Titanium |
| Ti6Al4V | Titanium 6 Aluminum 4 Vanadium |
| $TiO_2$ | Titanium dioxide |
| WCA | Water contact angles |
| XRD | X-rays diffraction |
| $\chi^2$ | Goodness-of-fit |
| θ | Contact angle |

**Chapter 4**

| | |
|---|---|
| 2D | Two-dimensional |
| ACF | Animal component-free |
| ARS | Alizarin red solution |
| BSA | Bovine serum albumin |
| CPC | Hexadecylpyridinium chloride monohydrate |
| cycRGD | Cyclic peptide ligands |
| DDW | Double-distilled water |
| DEX | Dexamethasone |
| DMSO | Dimethyl sulfoxide |
| ECM | Extracellular matrix |
| FBS | Foetal bovine serum |
| HSA | Human serum albumin |
| LINC | Linker of nucleoskeleton and cytoskeleton |
| linRGD | Linear peptide ligands |
| MSC | Mesenchymal stem cells |
| NM2B | Non-muscle myosin 2 B |

| | |
|---|---|
| PBS | Phosphate buffered saline |
| RGD | Arginine-glycine-aspartic acid |
| rh | Recombinant human |
| ROI | Region of interest |

**Chapter 5**

| | |
|---|---|
| 5XPBS | 5 Times concentrated phosphate buffered saline |
| A | Adenine |
| Ad | Adenovirus |
| ALP | Alkaline phosphatase |
| ARS | Alizarin red solution |
| BM | Bone marrow |
| BMP-2 | Bone morphogenetic protein 2 |
| BSP | Bone sialoprotein |
| C | Cytosine |
| CPC | Hexadecylpyridinium chloride monohydrate |
| Ct | Cycle threshold |
| DDW | Double-distilled water |
| DEX | Dexamethasone |
| ECM | Extracellular matrix |
| FGF-2 | Fibroblast growth factor 2 |
| G | Guanine |
| GAPDH | Glyceraldehyde-3-phosphate dehydrogenase |
| IQR | Interquartile range |
| mRNA | Messenger RNA |
| MSC | Mesenchymal stem cells |
| OA | Osteoarthritis |
| OC | Osteocalcin |
| OPN | Osteopontin |
| PBS | Phosphate buffered saline |
| PDGFs | Platelet-derived growth factors |

| | |
|---|---|
| PTFE | Polytetrafluoroethylene |
| Q1 | First quartile |
| Q3 | Third quartile |
| qRT-PCR | Quantitative real-time polymerase chain reaction |
| rh | Recombinant human |
| RNA | Ribonucleic acid |
| RUNX2 | Runt-related transcription factor 2 |
| T | Thymine |
| Ti | Titanium |
| Ti6Al4V | Titanium 6-Aluminum 4-Vanadium |

**Chapter 6**

| | |
|---|---|
| 2-Propanol | Isopropyl alcohol |
| Adj MS | Adjusted mean of squares |
| Adj SS | Adjusted sum of squares |
| AP | After processing |
| ASTM | American Society for Testing and Materials International |
| d | Line spacing |
| DF | Degrees of freedom |
| DOE | Design of experiments |
| E | Energy density |
| Goal | G |
| LIPSS | Laser-induced periodic surface structures |
| LST | Laser surface texturing |
| $M^2$ | Beam quality factor |
| ns | Nanosecond |
| N | Number of passages |
| P | Power |
| R | Output response |
| Ra | Arithmetic average roughness |
| Rq | Root-mean-square roughness |

| | |
|---|---|
| RSM | Response surface methodology |
| Sa | Amplitude of the mean height deviation |
| SEM | Scanning electron microscopy |
| Sku | Kurtosis |
| SLC | Sisma laser controller |
| Sq | Root Mean Square Height |
| Ti | Titanium |
| Ti6Al4V | Titanium 6 Aluminum 4 Vanadium |
| UV | Ultraviolet |
| v | Scanning speed |
| WCA | Water contact angles |
| wt. % | Weight percentage |

**Chapter 7**

| | |
|---|---|
| 5XPBS | 5 Times concentrated phosphate buffered saline |
| $Al_2O_3$ | Alumina |
| ARS | Alizarin red solution |
| ASTM | American Society for Testing and Materials International |
| bcc | Body-centred cubic |
| CPC | Hexadecylpyridinium chloride monohydrate |
| DDW | Double-distilled water |
| DEX | Dexamethasone |
| ELISA | Enzyme-Linked Immunosorbent Assay |
| EtOH | Ethanol |
| $H_20$ | Water |
| $H_2SO_4$ | Sulfuric acid |
| HCl | Hydrochloric acid |
| hcp | Hexagonal closed packed |
| LST | Laser surface texturing |
| MSC | Mesenchymal stem cells |
| PBS | Phosphate buffered saline |

| | |
|---|---|
| Ra | Arithmetic average roughness |
| RUNX2 | Runt-related transcription factor 2 |
| SLA | Sand-blasted, large-grit, acid-etched |
| Ti | Titanium |
| Ti6Al4V | Titanium 6-Aluminum 4-Vanadium |
| $TiO_2$ | Titanium dioxide |
| UV | Ultraviolet-C |
| XRD | X-rays diffraction |

**Chapter 8**

| | |
|---|---|
| 2D | Two-dimensional |
| 3D | Three-dimensional |
| ALP | Alkaline phosphatase |
| bm-hMSC | Bone-marrow-derived human mesenchymal stem cells |
| BMB | Demineralized bone matrix |
| CG | Collagen-glycosaminoglycan |
| Col | Collagen |
| DC | Direct current |
| ECM | Extracellular matrix |
| EPCs | Endothelial progenitor cells |
| HDMECs | Human dermal microvascular endothelial cells |
| hEBd | Human embryonic body-derived |
| hESCs | Human embryonic stem cells |
| hiPSC | Human-induced pluripotent stem cells-derived cardiomyocytes |
| hiPSC-CMs | Human-induced pluripotent stem-cell-derived cardiomyocytes |
| hiPSCs-VSCMCs | Vascular smooth muscle cells derived from human-induced pluripotent stem |
| hMSC | Human mesenchymal stem cells |
| MFC | Meniscal fibrochondrocytes |
| OPF | Oligo(poly(ethylene glycol) fumarate) |
| PCL | Polycaprolactone |
| PCL-TCP | Polycaprolactone-β tricalcium phosphate |

| | |
|---|---|
| PDMS | Poly(dimethylsiloxane) |
| PEG | Poly(ethylene glycol) |
| PEGDA | Poly(ethylene glycol) diacrylate |
| PEUUR | Poly(esterurethane urea) |
| PLGA | Poly(L-lactide-co-glycolide) |
| PU | Polyurethane |
| SC | Stromal cells |
| SD | Standard deviation |
| WIPO | World Intellectual Property Organization |
| YRGDS | Tyrosine-glycine-aspartate-serine |

**Chapter 9**

| | |
|---|---|
| AFM | Atomic force microscopy |
| e | Bridge output voltage |
| E | Electromotive force |
| $E_v$ | Excitation voltage |
| FP | Fluorescent proteins |
| I | Electric current |
| Ks | Gage factor |
| MPA | Micropipette aspiration |
| MSC | Human mesenchymal stem cells |
| N | North |
| P | Load |
| PDMS | Poly(dimethylsiloxane) |
| S | South |
| TFM | Traction force microscopy |
| Ti6Al4V | Titanium 6-Aluminum 4-Vanadium |
| UV | Ultraviolet |
| $\varepsilon$ | Strain |
| $\Phi$ | Magnetic flux |

**Chapter 10**

| | |
|---|---|
| JRC | Joint Research Centre |
| MSC | Human mesenchymal stem cells |
| SLA | Sand-blasted, large-grit, acid-etched |
| Ti | Titanium |
| Ti6Al4V | Titanium 6-Aluminum 4-Vanadium |

# LIST OF FIGURES

## Chapter 2

Figure 2.1 - Illustration of a total hip and knee arthroplasties on the left and right, respectively. Hip implants are composed by an acetabular, femoral head and femur components, whereas knee implants are comprised by femoral, tibial and patellar components (the latter not represented). During locomotion, the femur is subjected to tensile strains (represented in red) on the lateral and anterior sides and to compressive strains (represented in green) on the medial and posterior sides. ..... 10

Figure 2.2 - Illustration of the bone structure at a macroscale, and the osteogenic commitment of mesenchymal stem cells (MSC) at a microscale. MSC reside in the bone marrow niches and differentiate into bone cells in the bone site under regeneration. ..... 12

Figure 2.3 - Schematic representation of the main features governing the mechanotransduction system organization. Integrins are organized into larger structures named focal adhesions (FA), which formation is dependent on myosin-II mediated cell contractility. By clustering into FA, integrins recognized and bind to multiple extracellular matrix (ECM) ligands, therefore transmitting information from the ECM, to the cytoskeleton and to the nucleus, and vice versa. The mechanoresponse involves not only the rapid remodelling of the cytoskeleton but also the activation of specific genetic programs which involves different cell compartments, such as the ribosomes, Golgi apparatus and mitochondria. ..... 16

Figure 2.4 - Actin cytoskeleton rearrangement during MSC osteogenic differentiation. Bone marrow-derived MSC were seeded on glass coverslips coated with human fibronectin and cultured in a xeno-free osteogenic differentiation medium for 21 days, as described in [81, 82]. Human MSC (day 0) and fully differentiated bone cells (day 21) were fixed and stained with Alexa Fluor 488 Phalloidin. Scale bar: 100 μm. ..... 17

Figure 2.5 - Some typical topographical patterns include grooves/ridges, pillars and wells and the patterning parameters are: pillar diameter/ridge width (a), pillar interspacing/groove width (b), and pillar height/groove depth (c). ..... 20

Figure 2.6 - Example of a novel pro-active hip implant combining an auxetic material and engineered topography. The optimized and improved design is for the purpose of osteointegration

at the bone-implant interface, particularly at the lateral side of the proximal femur which, under physiological loading, experiences mostly tensile stress. ..... 28

**Chapter 3**

Figure 3.1 - Flowchart of the methodology followed in the present work. ..... 51

Figure 3.2 - The surface modification of Ti-based samples was achieved either by (a) anodizing using $H_3PO_4$ as electrolyte, (b) hydrothermal treatment with distilled water or by a combination of both techniques. ..... 52

Figure 3.3 - Photographs of anodized Ti grade 2 and Ti grade 5, previously subjected to alcohol cleaning (G4) and acidic pre-treatment (G5). ..... 55

Figure 3.4 - Morphology of the anodized Ti grade 5 samples previously subjected to alcohol cleaning (G4) and to acidic pre-treatment (G5). The oxide film was obtained by anodic oxidation at an applied voltage of 120 V, leading to the displayed correspondent anodizing curves. ..... 56

Figure 3.5 - Morphology of the anodized Ti grade 2 and Ti grade 5 samples subjected to acidic pre-treatment followed by hydrothermal treatment (G7) and both anodic oxidation and hydrothermal treatment (G9). ..... 57

Figure 3.6 - X-ray diffraction patterns of Ti grade 2 groups and identification of Bragg diffraction peaks characteristic of Ti ccp phase (# 01-089-4913), Ti hcp phase (# 00-001-1198), anatase phase (# 01-089-4921) and rutile phase (# 04-003-0648) ..... 58

Figure 3.7 - X-ray diffraction pattern of Ti grade 5 groups and identification of Bragg diffraction peaks characteristic of Ti ccp phase (# 01-089-4913), Ti hcp phase (# 00-001-1198), TiV phase (# 03-065-5971) anatase phase (# 01-075-1537) and rutile phase (# 04-003-0648). ..... 58

Figure 3.8 - Roughness of Ti grade 2 groups. Data are presented as mean ± standard deviation (SD) (n = 12). Statistically significant differences between groups are denoted by **** ($p<0.0001$), by ## ($p<0.01$) and #### ($p<0.0001$) compared to G2 and by ++++ ($p<0.0001$) compared to G3. ..... 61

Figure 3.9 - Roughness of Ti grade 5 groups. Data are presented as mean ± standard deviation (SD) (n = 12). Statistically significant differences between groups are denoted by * ($p<0.05$) and **** ($p<0.0001$), by #### ($p<0.0001$) compared to G2 and by ++++ ($p<0.0001$) compared to G3. ..... 62

Figure 3.10 - AFM images of the interface between non-treated (A) and treated (B) regions on as-anodized Ti grade 2 samples, previously subjected to alcohol cleaning (G4) or acidic pre-treatment (G5). The minimum and maximum height baselines were calculated in the ROI represented by the horizontal solid grey dash, and the oxide film thickness was calculated by calculating the difference between both height baselines, as represented graphically for one of ten measurements performed along the AFM image. ..... 64

Figure 3.11 - AFM images of the interface between non-treated (A) and treated (B) regions on Ti grade 2 samples subjected to both anodizing and hydrothermal treatment, previously subjected to alcohol cleaning (G8) or acidic pre-treatment (G9). The minimum and maximum height baselines were calculated in the ROI represented by the horizontal solid grey dash, and the oxide film thickness corresponds to the difference between both height baselines, as represented graphically for one of ten measurements performed along the AFM image. ..... 65

Figure 3.12 - Thickness of the oxide film formed upon anodic oxidation (G4 and G5) and anodic oxidation followed by hydrothermal treatment (G8 and G9) on Ti grade 2 and Ti grade 5. Data are presented as mean ± standard deviation (SD) (n=10) and statistically significant differences were only found for Ti grade 5 samples, which are denoted by **** (p<0.0001). ..... 65

Figure 3.13 - AFM images of (a) Ti grade 2 and (b) Ti grade 5 samples subjected to alcohol cleaning prior to hydrothermal treatment (G6). ..... 66

Figure 3.14 - Wettability of Ti grade 2 samples. Data are presented as mean ± SD (n = 5) and the hydrophilicity-hydrophobicity demarcation is represented by a dashed line at 90°. Statistically significant differences between 0 h and 24 hrs storage in 5XPBS are denoted by ** (p<0.01), *** (p<0.001) and **** (p<0.0001). ..... 67

Figure 3.15 - Differences between 0 h and 24 hrs storage in 5XPBS of Ti grade 5 samples. Data are presented as mean ± SD (n = 5) and the hydrophilicity-hydrophobicity demarcation is represented by a dashed line at 90°. Statistically significant differences between both timepoints are denoted by *** (p<0.005) and **** (p<0.0001). ..... 68

Figure 3.16 - Wettability differences among Ti grade 2 and Ti grade 5 groups (G1-G9), at 0 h and 24 hrs storage in 5XPBS. Statistically significant differences are denoted by * (p<0.05), ** (p<0.01) and **** (p<0.0001). The control group is not represented due to the fact that no statistically significant differences were found between the control group and G1 for both Ti-based materials. ..... 69

## Chapter 4

Figure 4.1 - Morphology of MSC cultured on uncoated (left) and fibronectin-coated (right) plastic wells during incubation for 21 days in osteogenic differentiation medium. All figures have a 20 μm scale bar. ..... 90

Figure 4.2 - Microscope images of MSC cultured on tissue culture plastic and stained with ARS to detect mineralization. All images include a 50 μm scale bar. ..... 92

Figure 4.3 - Quantification by spectrophotometric analysis of mineralization in osteogenic- induced MSC cells cultured on uncoated and fibronectin-coated plastic wells up to 21 days. Data are shown in mean ± standard error of mean and statistically significant differences are denoted by * ($p<0.05$), ** ($p<0.01$), *** ($p<0.001$) and **** ($p<0.0001$). ..... 93

Figure 4.4 - Flatbed scanner acquired images of osteogenic-induced MSC stained with ARS, during incubation period of 21 days in osteogenic differentiation medium. ..... 94

Figure 4.5 - For each timepoint, two 24 well-plate wells were cropped for both conditions and analysed by the "ColonyArea" ImageJ plugin. Colour bar represents the intensity scale displayed in the thresholded wells, where the zero intensity (white) corresponds to areas where no deposits were identified (background). ..... 95

Figure 4.6 - Intensity percent and area percent plot for both uncoated and fibronectin-coated wells, during the incubation time. Data are presented as mean ± standard error of the mean and statistically significant differences are denoted by * ($p<0.05$). ..... 95

Figure 4.7 - Immunofluorescent images of induced MSC osteogenic differentiation cultured on uncoated glass coverslips. Cells are stained for nuclei (blue), F-actin (green), NM2B (orange) and cell mask (red). Images include a 50 μm scale bar. ..... 96

Figure 4.8 - Immunofluorescence images of induced MSC osteogenic differentiation cultured on human fibronectin-coated glass coverslips. Cells are stained for nuclei (blue), F-actin (green), NM2B (orange) and cell mask (red). Scale bar: 50 μm. ..... 97

Figure 4.9 - Simultaneous staining of actin (green) and NM2B (orange) of MSC cultured on uncoated (top) and human fibronectin-coated (bottom) glass coverslips at 0 and at 21 days in osteogenic differentiation medium. Images have a scale bar of 50 μm. ..... 98

## Chapter 5

Figure 5.1 - Groups detailed description. ..... 108

Figure 5.2 - Conventional implants result in bone resorption compromising their success implantation outcomes. On the other hand, implants with modified surface present unique features capable of improving the surface properties of the implant, resulting in the activation of cellular response and long-term maintenance. The programming and responsiveness of bone cells is expected to increase the longevity of the implant, which would improve the patient's quality of life, and reduce healthcare cost burdens by minimizing the need for revision surgeries. ..... 111

Figure 5.3 - (a) Mineralization values (absorbance read at 550 nm) from 0 to 21 days are shown in a scatter plot, in which the mean of each group is displayed by a cross. (b) Mineralization is displayed for both Ti-O and Ti-OC (left) and both Ti-H and Ti-HC (right) as mean ± standard error of the mean, and kinetics are displayed on top of each line (A.U./day, $x10^3$). ..... 113

Figure 5.4 - (a) Biogenesis of osteoblasts. MSC are programmed to commit and differentiate into osteoblasts which express specific osteoblastic markers (highlighted in red), some of which are responsible for the extracellular matrix mineralization, consisting of collagen, calcium, and phosphorus. (b) Expression of osteogenic markers during osteogenic differentiation. Values are reported as mean ± standard error of the mean. ..... 115

Figure 5.5 - Fibronectin coating reduces variability in mineralization and when combined with hydrothermal treatment upregulates the expression of gene associated with osteogenic differentiation. (a) Variability (standard deviation) in mineralization at different timepoints of bone marrow-derived human mesenchymal stem cells (MSC) seeded on Ti6Al4V subjected to different treatments. (b) Relative gene expression levels of hallmarks of osteogenic differentiation in MSC seeded on Ti6Al4V subjected to different treatments. Gene expression data are presented as fold-change at day 21 relative to expression level on day 0. ..... 118

## Chapter 6

Figure 6.1 - The study of the micro-pillar surface laser texturing was divided into three main steps: (a) grooves design and texturing, followed by (b) pillars design and texturing and, finally, (c) a fine adjustment of the drawing and laser parameters to obtain a micro-scale pillars pattern with uniform size and dimensions in the selected range. ..... 133

Figure 6.2 - Schematic representation of the grooves texturing processing, in which n is the number of grooves engraved by scanning vertical lines, spaced in between by d, in discrete and consecutive processing strategies. In the former, the laser engraves each groove (represented by one colour) at a time, whereas in the latter strategy each line is engraved consecutively from left to right, N number of passages (each passage is represented by one colour). ..... 134

Figure 6.3 - The laser surface texturing begins at the point s (starting point) and finishes at f (finishing point), considering the laser scanning from left to right. In the set-marking approach the laser direction is from down to top repeatedly, whereas in the continuous marking parallel lines are connected so that the laser remains on as much as possible. ..... 135

Figure 6.4 - Representation of the pillar laser texture dimensions: groove width, pillar width and pillar depth. ..... 136

Figure 6.5 - Sku measures the sharpness of the roughness profile. ..... 138

Figure 6.6 - The shape factor of a (a) rectangular geometry is equal to one, whereas a (b) pyramid geometry presents a shape factor higher than 1 (D>d). ..... 139

Figure 6.7 – Top and cross-section scanning images of discrete laser processing (left) and consecutive laser processing (middle) strategies by pre-set marking and consecutive laser processing and continuous marking (right). One to ten lines (from left to right) were engraved with 3 W laser power, scanning speed of 100 mm/s and 80 laser passages. ..... 140

Figure 6.8 - CAD drawings of cross-hatched patterns with a groove width of (a) 50 μm, (b) 80 μm and (c) 110 μm and pillar width of (d) 30 μm, (e) 35 μm and (f) 40 μm, in this case exemplified for the design pattern with a groove width of 50 μm. ..... 141

Figure 6.9 - (a) 2D and (b) 3D optical profilometry images of a textured sample and the corresponding (c) extracted profiles, in which the black corresponds to the horizontal line and the grey to the diagonal one. Pillar peaks are in red and deeper holes in blue. The displayed images were acquired for Exp. No. 35 (A_CAD=50 μm, B_CAD=40 μm and N=70). ..... 142

Figure 6.10 - Main effects of each parameter on (a) groove width, (b) pillar width and (c) pillar depth. ..... 145

Figure 6.11 - Contour plots of groove width (A), pillar width (B) and pillar depth (C) in response of the combination of the input variables (A_CAD, B_CAD and N), by holding the third variable at the middle of its range. ..... 146

Figure 6.12 - Water contact angles of the experiment numbers which dimensions after processing are in the range of the target texture dimensions. The dark bar corresponds to the control group (non-textured), blue bars to textures with A_G = 60±5 μm, green bars to A_G = 90±5 μm and orange bars to A_G = 120±5 μm. The demarcation of hydrophilic and hydrophobic behaviour is represented by a dashed line at 90°. ..... 149

Figure 6.13 - The shape factor was calculated by randomly selecting lines in the 2D profile, as the acquired for Exp. No. 41 (A_CAD=50 μm, B_CAD=40 μm and N=75). ..... 151

Figure 6.14 - SEM images of the selected patterns (top view and with tilting of 30°). The micro-scale pattern with pillar width of 20±5 μm, depth of 50±5 μm and groove width of 60±5, 90±5 and 120±5 μm correspond to the Exp. No. 46, 71 and 65, respectively. ..... 153

Supplementary Figure 6.1 - Schematic representation of the Nd:YAG laser surface texturing performed on Ti6Al4V plates. ..... 160

Supplementary Figure 6.2 – (a) Normal distribution of residuals and (b) plot of residuals versus fitted values for groove width model data. ..... 168

Supplementary Figure 6.3 - (a) Normal distribution of residuals and (b) plot of residuals versus fitted values for pillar width model data. ..... 169

Supplementary Figure 6.4 - (a) Normal distribution of residuals and (b) plot of residuals versus fitted values for depth model data. ..... 169

**Chapter 7**

Figure 7.1 - 3D (left) and 2D (middle) optical profilometry images of the GW60, GW90 and GW120 micro-pillar textured samples and fluorescence images of MSC culture (right). Phalloidin staining was used to visualize the cytoskeleton of the cells (green fluorescence), the DAPI staining was used to demonstrate the nuclei of cells (blue fluorescence), the expression of RUNX2 was detected using brown fluorescence staining. All images include a 100 μm scale bar. ..... 181

Figure 7.2 - Fraction of anatase and rutile in textured samples after laser processing (LP) and after hydrothermal treatment (Hydro). ..... 182

Figure 7.3 - Water contact angles of SLA, GW60, GW90 and GW120 after laser processing (LP), after hydrothermal treatment in the case of textured samples and after UV irradiation for 2 hrs. ..... 183

Figure 7.4 - Alizarin Red staining on MSCs cultured both on textured and control samples at 0 and 21 days. ..... 184

Figure 7.5 - Quantitative analysis assessing the impact of contact angle, anatase and rutile levels on the fold change of mineralization over a 21-day culture period. ..... 185

Supplementary Figure 7.1 - CAD drawings of cross-hatched patterns with a drawing pillar width of 30 μm and groove width of (a) 50 μm, (b) 80 μm and (c) 110 μm of the textures GW60, GW90 and GW120, respectively. ..... 191

Supplementary Figure 7.2 - X-ray diffraction patterns of the sandblasted and acid etched (SLA), and textured samples (GW60, GW90 and GW120) after laser processing (LP) and further hydrothermal treatment (Hydro). Identification of Bragg diffraction peaks characteristic of Ti ccp phase (# 04-016-5468), Ti hcp phase (# 04-001-8963), TiVAl ccp phase (04-0018-5433), TIVAl hcp phase (04-002-8708), anatase phase (# 04-007-0701) and rutile phase (# 04-003-0648). ..... 191

Supplementary Figure 7.3 - Concentration of RUNX2 present in the culture medium at day 21 (mean ± standard deviation). ..... 192

**Chapter 8**

Figure 8.1 - Cell culture models may be in a static or dynamic mode. In 2D monolayer cultures, adherent cells are in contact with the culture vessel, neighbouring cells, and the culture medium. In non-adherent plates, 3D spheroids are grown in suspension, either without or with medium agitation (fed-batch bioreactor). In spinner-flask bioreactors, cell dispersion or cell-based constructs attached to a needle are in contact with a homogeneous medium due to agitation and medium perfusion. Rotating wall vessels enable cell culture mixing without an internal stirring mechanism by definition of a proper rotation speed. Perfusion bioreactors use continuous and fresh medium perfusion through cell-based constructs, provided by peristaltic pumps. Microfluidic systems are used for culturing and monitoring of both adherent and non-adherent cells. The fluid dynamics is represented by the red arrow. ..... 197

Figure 8.2 - Examples of mechanical stimulation devices used for mechanobiology studies. The commonly studied mechanical stresses are compressive and tensile stresses, either applied to cells incorporated inside 3D constructs (left) or cells seeded on a flexible substrate (right). The movement imposed on the biomaterials is represented by the red arrow..... 198

Figure 8.3 - The substrate on which cells (represented by green circles) are cultured may be subjected to different strain modes: uniaxial, biaxial, or equiaxial, as a consequence of substrate movement imposed by the load. ..... 199

Figure 8.4 - Graphical arrangement of the commercially available mechanical stimulation devices according to their maximum strain/displacement and frequency. ..... 203

Figure 8.5 - Cellular results of studies which made use of commercially available devices. Von Kossa staining of cell layers after 16 days in culture showed that compared to the unstrained condition (a), hMSCs that underwent mechanical strain imposed by Flexcell FX-2000 had greater matrix mineralization (b), as corroborated by measurement of matrix-deposited calcium (c) (reproduced from [59], Copyright 2003, with permission from Elsevier). d Sarcomere length analysis by actin (ACTN, red) and nuclei (DAPI, cyan) staining of samples: non-conditioned (NC), electrically conditioned (E), mechanically conditioned by an IonOptix C-stretch (M), and electromechanically conditioned (EM) (scale bar: 25 mm). Results for different conditioning procedures (1Hz 3d, 2Hz 3d, and 1Hz 7d) are shown in a boxplot (e) (reproduced from [64], Copyright 2017, with permission from Elsevier). Empty and non-loaded scaffolds were loaded by a TA Instruments BioDynamic device coupled with an Electroforce testing machine, then cut into cross sections and stained with Sirius red (for collagen) (f) and alizarin red (for calcium) (g). Absorbance of MTS (for cell-viability assessment), alizarin red, and Sirius red per loaded scaffold at day 20 was normalized to a paired non-loaded scaffold (mean±SD) (h), and showed an increase of matrix mineralization after loading (reproduced from [66], Copyright 2009, with permission from Elsevier). (i) Expression of gremlin-1 (Grem1) protein (green) in mouse primary chondrocytes increased 24 hrs after tensile stress loading (stress+) was applied with the Strex STB-140 system, compared to the unloading condition (stress−) (scale bar: 50 μm). (j) An acceleration of mouse osteoarthritis development after surgical induction was observed through safranin O staining and gremlin-1 immunofluorescence. Scale bars: 100 μm and 50 μm, respectively (reproduced from [69] authored by Chang et al. under the Creative Commons license CC BY 4.0). hMSCs: human mesenchymal stem cells. ..... 207

Figure 8.6 - Representation of four tensile working principles. In the four- point bending apparatus, the cell-based construct is supported by stationary supports and strain is distributed in the perpendicular plane to the applied load. However, the strain magnitude is not distributed uniformly between these horizontal planes because it increases from the central horizontal axis to the external

medial and lateral faces (which are subjected to maximum tensile and compressive strains, respectively) [73]. Constructs can also be placed in cages and fixed at two opposite ends: one rigidly and the other to the rake attachment. The linear sliding rake is then controlled at the desired frequency and amplitude. Cell-based samples can also be clamped and connected to a tensile device (one end of the rectangular membrane is fixed while the other is connected to a computer-controlled movable frame). Finally, polymeric substrates may be exposed to uniaxial tensile loading with a vacuum-actuated tensile device. The movement imposed by the tensile loading device is represented by the red arrow. ..... 208

Figure 8.7 - Graphical arrangement of the devices designed and produced by research groups according to the maximum tensile strain/displacement studied at a particular frequency. Observation: despite the fact that Subramanian et al. [57] applied 2% uniaxial tensile strain to cells encapsulated in collagen constructs, the device used in this study may operate at a loading strain up to 12% at cyclic frequencies of 0.01–1 Hz. ..... 209

Figure 8.8 - Results of studies performed with customized tensile loading devices. ALP staining at 24 hrs was higher for cells subjected to mechanical loading by a four-point bending device (a) compared to unstretched cells (b) and control cells (c) (reproduced from [43], Copyright 2008, with permission from Elsevier). (d) Scanning electron micrographs of 3D collagen constructs encapsulated with OB6, C2C12, or AC10 cells at day 3 either loaded by a linear sliding rake system or non-loaded (scale bar: 100 μm) indicated that the fibre orientation of loaded cells was parallel to the axis of load application (reproduced from [57], Copyright 2017, with permission from Wiley). (e) Staining of actin (green), sarcomeric z-lines (red), and nuclei (blue) of cardiomyocytes cultured on clamped samples connected to a tensile device revealed that after being subjected to 6 hrs of cyclic uniaxial tensile loading, the cells aligned in the direction of loading (white arrow) (reproduced from [3], Copyright 2018, with permission from ASME). (f) No significant differences in the average normalized total fluorescence of nuclei were found between non-stretched (control) and stretched groups, but F-actin fluorescence significantly increased with loading performed with a vacuum-actuated tensile device. The spatial distribution of per cent change between stretched and control average nuclei (g) and F-actin fluorescence (h) showed that expression of F-actin increased after tensile loading (reproduced from [52], Copyright 2018, with permission from Springer Science Business Media, LLC, part of Springer Nature) ..... 210

Figure 8.9 - Schematic representation of the cross section of cells (represented in green) cultured on flexible membranes (a) and the deformation of the latter as the pin moves upwards (b). The alignment of C2C12 and HDMECs in response to loading is illustrated by fluorescent images of HDMECs (c, d), C2C12 myoblast cells (e, f), and A549 alveolar epithelial cells (g, h) stained with Calcein AM before loading (left column) and after being subjected to cyclical tensile loading (5 Hz for 12 hrs) (right column) (reproduced from [72], Copyright 2008, with permission from Elsevier). HDMECs: human dermal microvascular endothelial cells. ..... 213

Figure 8.10 – Illustration of compression models: unconfined compression, confined compression, and semi-confined compression. The three-dimensional cell-based construct is compressed by the movement of a piston, in this case as a result of pressurized air (represented by the red arrow). ..... 214

Figure 8.11 - Finite-element simulations of three compression modes all involved application of 10% compressive strain on PEG hydrogel (adapted from [88], Copyright 2011, with permission from IOP Publishing Ltd). Strain field within the hydrogel was generated for unconfined (a), confined (b), and semi-confined (c) compression modes and the radial, circumferential, and axial strains (mean and standard deviation) were plotted for the total axial thickness of the hydrogel. ..... 216

Figure 8.12 – Actuation principles of various mechanical cell-stimulation devices, divided by frequency level: low to high for values up to 200 Hz and extremely high frequency for values up to 100 MHz. ..... 230

Figure 8.13 - The device of invention number US 2013/0059324 AI may be operated (a) by a mechanical drive mechanism, in which the rotation of a non-circular shaft (218) moves the movable support (216), thereby pushing the push members (214) in respect to the pins (118); or (b) by a pressurized mechanism (220), in which the change of fluid volume moves the support (216), imparting mechanical strain to the cells located in the wells (112). Illustrations from [96]. ..... 230

Figure 8.14 - Illustrations of invention number US 5,348,879 of Shapiro et al., with three different displacement applicators (represented in the drawing by 24). In (a), a cam deforms the membrane, in (b), the membrane is secured by plates and is deformed by the displacement applicator moving upward, and in (c), each well is mounted above the displacement applicator. Schematics from [118]. ..... 231

Figure 8.15 - The displacement applicator moves up and down, which may create friction between the flexible membrane and the loading post. ..... 232

Figure 8.16 - Illustrations of invention number US10,421,955B2, assigned to IonOptix LLC. (a) is a side view of the electromechanical stage (28a) composed by a fixed support (32) and a moving support (36) connected to a stepper motor (42). (b) is a perspective view illustrating six culture dishes and supporting parts of the electromechanical stage. Figures from [111]. ..... 233

Figure 8.17 - SchematicsofinventionnumberUS2012/0219981Al, assigned to Muthiah and Lane [115], in which each motor (denoted by 504 and 506) is connected to an opposite end of the cell culture device (502). The embodiment includes a water reservoir (512), an electric heating unit (508) and cooling fans (510), and computer interface connections (514). Figures from [115]. 234

**Chapter 9**

Figure 9.1 - Ti6Al4V plate at (a) neutral position and (b) under imposed force P. Cells (represented in green circles) cultured on the upper side of the substrate are subjected to tension and visualized through an inverted microscope. Note: image is not to scale. ..... 256

Figure 9.2 - Boundary restrictions imposed on the numerical simulation. ..... 258

Figure 9.3 - Drawings of the mechanical stimulation device. The device is composed of two main parts: the cell culture container represented by 1 (a, b and c), and the mechanical cell stimulation involves the connection of a wire (6) fixed on one extremity of the Ti6Al4V substrate (5) (d), which involves mounting the cell culture container in an external container represented by 12 (e and f). ..... 261

Figure 9.4 – First principal strain of the Ti6Al4V plate after applying a vertical load of 1.5 N at one extremity of the plate. The plate zone subjected to higher strain will be imaged through an inverted fluorescence microscope. Scale bar is in microstrain (strain x $10^6$, dimensionless). ..... 263

Figure 9.5 – Total displacement of the Ti6Al4V plate by applying a load of 1.5 N. Scale bar is in mm units. ..... 263

Figure 9.6 - Strain values of Ti6Al4V plate under tensile stress by setting a total rotation angle of 180°. ..... 264

Figure 9.7 - (a) 2D and (b) 3D optical profilometry images of the textured sample. Pillar peaks are represented in red whereas deeper holes are in blue. ..... 265

Figure 9.8 - Fluorescence microscopy was used to analyse MSC cultured in osteogenic differentiation medium for 4 days (a) before and (b) after mechanical loading. CellMask™ was used

to visualize the plasma membrane (green fluorescence). All images include a 100 μm scale bar. ..... 265

Figure 9.9 - Time-lapses live cell-imaging of MSC after performing the mechanical loading. Each image was taken every 30 sec, and all images include a 100 μm scale bar. ..... 266

Supplementary Figure 9.1 - A silicone membrane would be fixed and act as an impermeabilized material, in such a way that it would seal the region filled with liquid (sterile environment). The deformation of the silicone membrane while pulling down the plate would prevent contaminations. .....270

Supplementary Figure 9.2 - The magnetic principle would include the attachment of two magnets aside the titanium plate which, when desired, would deflect by the action of an induction coil. 270

# LIST OF TABLES

## Chapter 2

Table 2.1 - Osteogenic results from mechanical loading on MSC. ..... 18

Table 2.2 – Substrate topography effect on human MSC. ..... 22

Table 2.3 - Combined data on physiological conditions for bone performance. ..... 26

## Chapter 3

Table 3.1 - Chemical composition of Ti grade 2 and Ti grade 5 provided by the manufacturer .. 50

Table 3.2 - Comparison of tensile strength, yield strength and elastic modulus of both titanium grades ..... 50

Table 3.3 - Samples group number and description. ..... 53

Table 3.4 - Phase composition of Ti grade 2 and Ti grade 5 treated samples. ..... 60

Table 3.5 - Wettability of Ti grade 2 and Ti grade 5 subjected to different surface treatments is directly influenced by the phase composition of the oxide film. The averaged percentage of anatase and rutile was ranked from + to ++++, whereas wettability was ranked from **+** to **+++** (the latest referring to moderate hydrophilicity). ..... 69

Supplementary Table 3.1 - Rietveld indices obtained after the refining process for all Ti grade 2 groups. ..... 81

Supplementary Table 3.2 - Rietveld indices obtained after the refining process for all Ti grade 5 groups. ..... 82

Supplementary Table 3.3 - Roughness parameters measured on all Ti grade 2 groups (mean ± standard deviation (SD)) ..... 82

Supplementary Table 3.4 - Roughness parameters measured on all Ti grade 5 groups (mean ± standard deviation (SD)) ..... 83

## Chapter 4

Table 4.1 - Origin of human derived and recombinant proteins included in the cell culture media. ..... 87

**Chapter 5**

Table 5.1 - RT-PCR primers used for osteogenic gene expression. ..... 110

Supplementary Table 5.1 - Osteogenic markers and their impact on osteogenesis.....127

**Chapter 6**

Table 6.1 - Chemical composition of Ti6Al4V, according to manufacturer. ..... 132

Table 6.2 - Laser Nd:YAG technical specifications. ..... 132

Table 6.3 - Multilevel factorial design of the experiment, including the input parameters and corresponding levels. ..... 136

Table 6.4 - Texture dimension denomination along the study. ..... 137

Table 6.5 - Significant effect of combined parameters in the final response for the obtained mathematical models. ..... 147

Table 6.6 - Combinations of drawing and laser parameters for the targeted dimensions (groove width (A_G) of 60±5, 90±5 and 120±5 μm, pillar width (B_G) of 20±5 μm and pillar depth (C_G) of 50±5 μm). ..... 148

Table 6.7 - Groove and surface roughness values and shape factor of the experiment numbers which dimensions after processing met the target texture dimensions. ..... 151

Supplementary Table 6.1 - Design of experiments for samples texturing. ..... 161

Supplementary Table 6.2 - Discrete laser processing and pre-set marking of one to ten lines for different laser parameters. for a laser energy of 120 or 240 J/mm$^2$. ..... 163

Supplementary Table 6.3 - Consecutive laser processing and pre-set marking vs continuous marking of one to ten lines for different laser parameters. for a laser energy of 120 or 240 J/mm$^2$. ..... 165

Supplementary Table 6.4 - Analysis of variance of groove width model. ..... 169

Supplementary Table 6.5 - Analysis of variance of pillar width model. ..... 170

Supplementary Table 6.6 - Analysis of variance of pillar depth model. ..... 171

Supplementary Table 6.7 - Surface roughness values of the experiment numbers which dimensions after processing met the target texture dimensions, according to ISO 25178. ..... 171

**Chapter 7**

Table 7.1 - Set of laser parameters. ..... 177

Table 7.2 - Texture dimensions of samples with micro-pillars produced by LST (mean ± standard deviation). ..... 182

Supplementary Table 7.1 - Technical specifications of the Nd:YAG laser.....190

**Chapter 8**

Table 8.1 - List of operational features of mechanical stimulation devices ..... 200

Table 8.2 - Summary of commercially available devices which apply tensile and/or compressive stresses. ..... 202

Table 8.3 – Loading features of the uniaxial tensile loading applied by the custom-built devices to the cell-based constructs, grouped by the device working principle..... 211

Table 8.4 - Overview of inventions related to mechanical stimulation of cells. ..... 217

**Chapter 9**

Table 9.1 - Features of the customized cell mechanical stimulation device and the correspondent aim and advantages..... 254

Table 9.2 - Specifications of the Micro Servo MG90S with metallic gear. ..... 257

Table 9.3 - Properties of the Ti6Al4V selection used in the numerical simulation. ..... 258

Table 9.4 - Strain gauge characteristics. ..... 259

# CHAPTER 1

## INTRODUCTION

The following chapter aims to highlight the purpose of this PhD project, by presenting a motivation subchapter, the global and detailed objectives of this PhD and finally an outline on the structure of the thesis.

## 1.1. Motivation

After concluding the integrated master's degree in Biomedical Engineering at the University of Coimbra, I began my journey at the Center for MicroElectroMechanical Systems (C-MEMS) at the University of Minho. As a research fellow on the project "ADAPTPROSTHESIS - Development of smart designed adaptive prosthesis for orthopaedic applications" I was enlightened by the high prevalence of orthopaedic diseases and injuries and how serious challenges remain unsolved. This was a force of motivation to focus on titanium-based materials and their interaction with bone cells to develop novel solutions for orthopaedic applications.

A progressive increase of the average life expectancy comes with the increasing risk of skeletal diseases. Furthermore, a sedentary lifestyle and obesity contribute to the demand for orthopaedic interventions which, associated with technological advancements, results in the continuous growth of the orthopaedic sector. According to the Grand View Research Inc. report published in 2023, the orthopaedic devices global market size was valued at USD 33.5 billion in 2022 and is expected to expand at a compound annual growth rate (CAGR) of 6.3% from 2023 to 2030. One of the most prevalent skeletal diseases is osteoarthritis, characterized by cartilage degeneration in a given joint, such as the hip or knee. To reduce the pain and restore the mobility of people suffering from an arthritic hip or knee, current therapeutic solutions include its replacement – a procedure entitled total hip or knee arthroplasty, respectively. The joint is replaced by an orthopaedic implant, often composed of Titanium 6 Aluminium 4 Vanadium (Ti6Al4V) alloy, which is inserted inside a bone cavity. Despite the fact these total replacements are considered the most effective interventions for the treatment of osteoarthritis, over time bone starts to reabsorb contributing to the loss of implant fixation causing pain.

When inserted into the bone cavity, there is a diminished mechanical stimulation at the bone-implant interface when compared to the normal physiological bone stimulation leading, therefore, to implant loosening. In a healthy condition, bone cells are subjected to cyclic mechanical loading, namely by tensile, compressive and shear forces. However, when the implant is inserted, bone cells are less effectively mechanically stimulated and the bone in the vicinity starts to reabsorb. As a consequence, the implant starts to detach from the bone and a second intervention, so called revision surgery, is considered to replace the older implant for a new one. The elevated rate of these surgical procedures significantly impacts both the patient's well-being and the healthcare-related expenditures.

Mechanical signals are key regulators from early times of human development, such as organ and tissue development, to everyday organ and tissue events including remodelling, regeneration and, in some cases, the emergence of diseases. The term mechanobiology was first introduced by Dennis Carter in 1998, who presented a computational study on how local tissue mechanical loading guides the differentiation of mesenchymal tissue into bone, cartilage, or fibrous tissue during the initial phase of regeneration of bone tissue. Later, in 2002, van der Meulen and Huiskes reviewed and discussed the progress of skeletal tissue mechanobiology based on experimental and computational approaches and foresaw the promising potential of mechanobiology. Mechanobiology has, therefore, emerged as a novel interdisciplinary field of science that combines biology, mechanics and engineering.

Organ- or tissue-specific loading conditions are present, for example, in musculoskeletal, cardiac and respiratory systems. The mechanisms of mechanobiology encompass a multiscale approach since mechanical loads are tunnelled from organ to tissue and further down to the cellular and subcellular levels. Understanding how cells respond to mechanical loading will contribute to the development of technologies for regenerative medicine and tissue engineering.

This project aims to improve the interface between bone and implant by activating the mechanotransduction processes responsible for the differentiation of human MSC into bone cells. This will contribute to the design of novel implants capable of transducing external mechanical loading into an adequate physiological osteogenic activity of cells around endosseous implants. It is hoped that this strategy will promote healthy bone regeneration and implant integration.

It is my belief that mechanobiology is the key to shaping the new generation of orthopaedic implants, poised to generate substantial value and make a significant and meaningful impact, in accordance with the third goal of the United Nations, by *ensuring healthy lives and promoting well-being for all at all ages*.

### 1.1.1. Leaders for Technical Industries doctoral program

In highly competitive markets, such as the orthopaedic device market, new engineering solutions require an in-depth scientific knowledge. This is one of the premisses of the Leaders for Technical Industries (LTI) doctoral program (MIT Portugal Program) withing the Engineering Design and Advanced Manufacturing area. The vision of this doctoral program comprises an integrated learning education philosophy by combining science and advanced technology to propose social/economic solutions. Despite the evolution in medical biomaterials research, serious

challenges remain unsolved. This is evidenced by the high percentage of revision surgeries with severe health consequences to the patient and significant economic costs. In fact, besides the direct healthcare costs, disease burden results in indirect costs, such as the work loss and premature retirement. The continuous search for better products and technologies to propose new solutions with profound and positive impact on society is a mutual characteristic of both the orthopaedic devices industry and LTI doctoral program. In 2021, North America had the largest revenue share of this market with more than 46%, followed by Europe and Asia Pacific. Some of the major players are Medtronic PLC, Stryker Corporation, and Zimmer-Biomet Holdings, Inc., all based in the United States of America. As a result of the close relationship between academia and the highly competitive industrial environment, the focus on the problem underlying the high demand for revision surgery will foster the creation of novel orthopaedic implants with extended longevity and thus improve patients' quality of life and reduce economic expenses.

## 1.2. Objectives

This PhD project aims to improve orthopaedic implant's surface to promote a healthy bone formation at the interface between bone and implant. Mechanobiology plays an important role in bone regeneration, and the study of surface features and the impact of mechanical loading on human cells crucial to designing orthopaedic implants that can induce osteogenic-stimulating mechanical loading at the bone-implant interface. To achieve this purpose, the following specific objectives were defined:

- Identify the limitations of current therapeutic strategies to treat osteoarthritis;
- Investigate different surface modification techniques to improve the bone-implant interface;
- Explore the dynamic mode to study the effect of mechanical loading on osteogenesis using metallic substrates.

## 1.3. Structure of the thesis

This PhD thesis is organized in ten chapters, the majority following the typical organization of review and research articles. The majority (4) are currently published, but some (2) are submitted to international ISI journals, as mentioned at the beginning of each chapter. Seven chapters are mainly focused on static conditions, transitioning to dynamic mode in the last two chapters. A brief description of each chapter is detailed below.

Chapter 1 corresponds to the Introduction, detailing the motivation, main objectives of the research work and the structure of the thesis.

Chapter 2 entitled "Reengineering bone-implant interfaces for improved mechanotransduction and clinical outcomes" is a review article aiming to contextualize the state of the art of relevant concepts related to the developed work. The prevalence of total hip and knee arthroplasties, the design of current implants and main failures were addressed in order to propose a novel concept for orthopaedic implants. This paper was published in Stem Cell Reviews and Reports 16:1121–1138 (2020), a Springer journal with an impact factor of 5.7 (2020) (quartile 2).

Chapter 3 corresponds to the research article "Surface characterization of titanium-based substrates for orthopaedic applications", in which the effects of different surface modification techniques on the surface of titanium grade 2 and Ti6Al4V substrates were investigated. A potentially bioactive and hydrophilic layer was obtained by hydrothermal treatment, and this strategy was proposed as being able to enhance the bioactivity of the orthopaedic implants surface. This paper was published in Materials Characterization, 177: 111161 (2021), an Elsevier journal with an impact factor of 4.5 (2021) (quartile 1).

Chapter 4, entitled "Augmenting the osteogenic capacity of human mesenchymal stem cells through the application of human fibronectin coating in xeno-free and serum-free culture environments" addresses the culture of human mesenchymal stem cells on conventional substrates. By using xeno-free and serum-free reagents, the osteogenic differentiation capacity of was evaluated and surface functionalization with human fibronectin was proposed for further studies.

Chapter 5 corresponds to a research article entitled "Engineering a hybrid Ti6Al4V-based system for responsive and consistent osteogenesis", in which the osteogenic differentiation of mesenchymal stem cells was evaluated on treated Ti6Al4V substrates. Surface modifications induced by hydrothermal treatment followed by functionalization with human fibronectin improved the surface bioactivity as cellular performance was enhanced. This manuscript was submitted to an ISI index journal.

Chapter 6 corresponds to the research article "Experimental analysis and predictive modelling of Ti6Al4V laser surface texturing for biomedical applications" aiming the use of a nanosecond laser to texture micro-scale pillars on Ti6Al4V parts to improve the interaction between

bone and implant. A combination of drawing and laser parameters was selected considering the targeted dimensions and surface properties. This paper was published in Surfaces and Interfaces, 35: 102466 (2022), an Elsevier journal with an impact factor of 6.2 (2022) (quartile 1).

Chapter 7, entitled "Hydrothermal treatment of laser micro-textured Ti6Al4V surfaces for improved stability of orthopaedic implants" investigates the combination of laser surface texturing with hydrothermal treatment and further functionalization with human fibronectin to increase adhesiveness and consequent osteogenesis of human mesenchymal stem cells. This research article was submitted to an ISI index journal.

Chapter 8 is a review article entitled "Mechanical stimulation devices for mechanobiology studies: a market, literature, and patents review", that covers the working principles of mechanical stimulation devices used for mechanobiology studies and highlights the main features still open to improvement. This literature review was published in Bio-Design and Manufacturing, 6:340–371 (2023), a Springer journal with an impact factor of 7.9 (2022) (quartile 1).

Chapter 9, entitled "Design of a device for cell mechanical stimulation and real-time monitoring", describes the requirements and the design of a custom-made mechanical stimulation device for mechanobiological studies. The device aims to subject a substrate, either polymeric or metallic, to a bending loading that promotes tensile stress on its upper surface and allows to simultaneously perform cell culture, mechanical stimulation, and live imaging. The working principle of device was validated, and a preliminary cellular study were performed. A provisional patent proposal was submitted.

Chapter 10, the last chapter of this thesis, presents a general discussion and conclusions of the developed work described in the previous chapters and the integration of all results and comparison with the literature. In addition, some suggestions for future works are proposed and further achieved contributions as a result of this thesis are referenced.

# CHAPTER 2

## REENGINEERING BONE-IMPLANT INTERFACES FOR IMPROVED MECHANOTRANSDUCTION AND CLINICAL OUTCOMES

Published in Stem Cell Reviews and Reports, 2020, 16, 1121–1138

https://doi.org/10.1007/s12015-020-10022-9

F. Melo-Fonseca[a,*], G. Miranda[a], Helena S. Domingues[b,c,d], Inês Mendes Pinto[b], Michael Gasik[e,f], F. S. Silva[a]

[a]Center for MicroElectroMechanical Systems (CMEMS-UMinho), University of Minho, Campus de Azurém, 4800-058 Guimarães – Portugal

[b]International Iberian Nanotechnology Laboratory (INL), Braga, Portugal

[c]Life and Health Sciences Research Institute (ICVS), School of Medicine, University of Minho, Campus de Gualtar, 4710-057 Braga, Portugal

[d]ICVS/3B's Associate Laboratory, PT Government Associated Laboratory, Braga/Guimarães, Portugal

[e]School of Chemical Engineering, Aalto University Foundation, Espoo, Finland

[f]Seqvera Ltd., Helsinki, Finland

*Corresponding author

Michael Gasik and F. S. Silva share co-last authorship.

**Abstract**

The number of patients undergoing joint replacement surgery has progressively increased worldwide due to world population ageing. In the Unites States, for example, the prevalence of hip and knee replacements has increased more than 6 and 10 times, respectively, since 1980. Despite advances in orthopaedic implant research, including the development of novel implantable biomaterials, failures are still observed due to inadequate biomechanical compliance at the bone-implant interface. This comprises static and dynamic mechanical mismatch between the bone and the implant surface. The importance and robustness of biomechanical cues for controlling osteogenic differentiation of mesenchymal stem cells (MSC) have been highlighted in recent studies. However, in the context of bone regenerative medicine, it remains elusive how mechanobiological signals controlling MSC osteogenic differentiation dynamics are modulated in their interaction with the bone and with implants. In this review, we highlight recent technological advances aiming to improve host bone-implant interactions based on the osteogenic and mechanoresponsive potential of MSC, in the context of joint replacement surgery. First, we discuss the extracellular and intracellular mechanical forces underlying proper receptivity and stimulation of physiological MSC differentiation and linked osteogenic activity. Second, we provide a critical overview on how this knowledge can be integrated towards the development of biomaterials for improved bone-implant interfaces. Third, we discuss cross-disciplinarily which contributes to the next generation design of novel pro-active orthopaedic implants and their implantation success.

**Keywords:** Orthopaedic implants failures; Biomaterials surface design; Mechanobiology; Mesenchymal stem cells; Osteogenic differentiation

## 2.1. Conventional therapeutic approaches for hip and knee replacements

Joint replacement surgery (hip and knee replacements) is considered the most effective intervention for treating severe osteoarthritis, reducing pain and disability and considerably recovery of patient's motor activity [1]. In 2014, and according to the estimates provided by the Organization for Economic Co-operation and Development (OECD) countries, an average of 189 hip and 130 knee joints were replaced by prostheses per 100.000 habitants [1]. In the United States, according to a projection from 2010 to 2030, the demand for primary Total Hip Arthroplasty (THA) and Total Knee Arthroplasty (TKA) is estimated to grow by 60% to 4 million and by 58% to 7.4 million procedures, respectively, by simply considering the population ageing [2]. Despite advances in bone implant research, prosthetic failure is often observed with time, leading to high-

risk and high-cost revision surgeries and implant replacement [3–5]. Development of novel biomaterials and surgical techniques has improved the clinical outcomes, leading to enormous progress in patient care. Nevertheless, a number of unresolved problems still exist. For example, foreign body-associated infections are one of the most frequent reasons for implant failure [6]. It has been proposed that prompt and firm bacterial attachment combined with a poor host cell attachment can lead to implant-related infections (the "race for the space") [7]. However, "aseptic loosening" was also suggested as one of the most predominant causes for limited longevity of orthopaedic implants after 10–15 years [4, 5, 8, 9]. Over 25–75% of "aseptic loosening" cases were, in fact, due to non-diagnosed or negative tests of bacterial contamination [10–12]: there is often no sensitive testing of the implants for biofilms allowing quantitative and qualitative determination of the pathogens on the implant surface. It was reported that certain infections might never become clinically evident or may only result in a presumably aseptic loosening sooner or later [13, 14]. Therefore, data analysis from joint registries can lead to distorted results with limited reliability and the lack of information about true aseptic loosening. Nevertheless, even in this context, the share of really "aseptic" failures (where implant loses its contact with the surrounding bone) is still high.

In the orthopaedic clinics, two implant fixation techniques are currently used in both hip and knee implants: cemented and cementless. Despite the similar outcomes for both fixation methods in THA, most surgeons prefer cementless and, therefore, press-fit implants, in which a slightly oversized stem is placed into the femoral cavity [15, 16]. Cementless knee implants were not adopted as readily as hip implants but are now gaining acceptance. In fact, cementless TKA allow a better long-term biologic fixation than cemented implants [17–19]. In addition, the press-fitting strategy facilitates the implant insertion and reduces surgical time [17]. Hip and knee implants require remarkably different designs due to the distinctive spatial and biophysical constraints [20–22], as illustrated in Fig. 2.1. During locomotion, the femur's highest tensile strains were reported to be along the lateral and anterior side of the femur, whereas the highest compressive strains were along the medial and posterior surface [23–25]. As a consequence, tensile, compressive and shear stresses are present in different regions of an hip implant during locomotion, while a knee implant is mainly subjected to compressive stresses [20–22]. THA and TKA prostheses transfer different loads along the surrounding bone, leading to different bone formation/resorption percentages along the bone/implant length. In fact, significant bone resorption on hip implants is found in the lateral side of the proximal femur [26, 27], whereas on knee implants bone resorption

is more significant underneath the tray on the tibial side [28]. As a result, the strain compliance becomes non-uniform along the bone-implant interface leading to weaker areas which mechanically would fail easier. Therefore, implants design should consider dynamics and temporal progress of the stress and strain distributions to avoid uncontrolled bone resorption. While changes in the geometry of the implant can address this non-uniform load distribution, previous studies regarding THA have shown that mismatched stiffness of these orthopaedic implants is one of the key parameters that influences the stability of strain compliance [29].

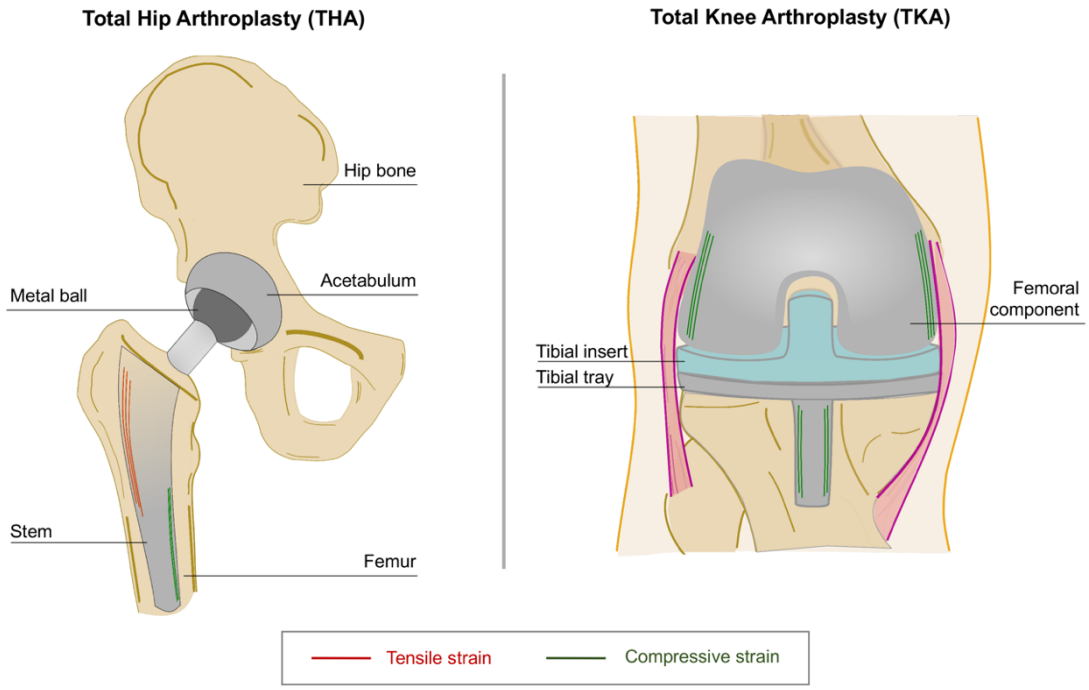



Figure 2.1 - Illustration of a total hip and knee arthroplasties on the left and right, respectively. Hip implants are composed by an acetabular, femoral head and femur components, whereas knee implants are comprised by femoral, tibial and patellar components (the latter not represented). During locomotion, the femur is subjected to tensile strains (represented in red) on the lateral and anterior sides and to compressive strains (represented in green) on the medial and posterior sides.

Here, we focus on combination of key mechanotransduction processes required for bone remodelling, proper biomechanical conditions, and, therefore, on critical aspects that should be considered to delay or even avoid the aseptic loosening events-related to revision surgeries.

## 2.2. Fundamental aspects underlying bone formation and maintenance

Bone is a highly vascularized tissue with an intrinsic property of self-repair [30] and its regeneration in vivo is stimulated by mechanical loading related to gravity [31]. As a result of the mechanical usage, i.e., physical loads and motions imposed on the skeleton by normal physical activities, bone biological mechanisms are regulated by modulating the bone basic multicellular units [32, 33]. These units comprise osteoblasts (bone-forming cells), osteoclasts (bone-resorbing

cells), bone lining cells (couple resorption to bone formation) and osteocytes (responsible for bone tissue maintenance) [32, 34, 35]. Various stem cell populations are present in the bone marrow, including very-small embryonic-like stem cells (proposed as the most primitive population), hematopoietic stem cells, endothelial progenitor cells and mesenchymal stem cells [36–38]. Pluripotent stem cells are able to differentiate not only into germline layers but also into three germ layers (meso-, ecto- and endoderm), whereas multipotent cells may only differentiate into two germ layers [36–38]. Mesenchymal stem cells (MSC) are present, for example, in bone marrow, periosteum and adipose tissue. Besides the ability of self-renewal, MSC are pluripotent cells with the capacity to differentiate into three tissue types: adipose, bone and cartilage and, consequently, currently used in bone regenerative therapies [39–41]. To avoid any confusions, according to the International Society of Cell and Gene Therapy, the term MSC is not equivalent to mesenchymal stromal cells, the latter corresponding to a heterogeneous population that supports hematopoietic development and presents notable secretory, immunomodulatory and homing properties. Bone marrow derived MSC play an important role in bone tissue regeneration, as represented in Fig. 2.2.

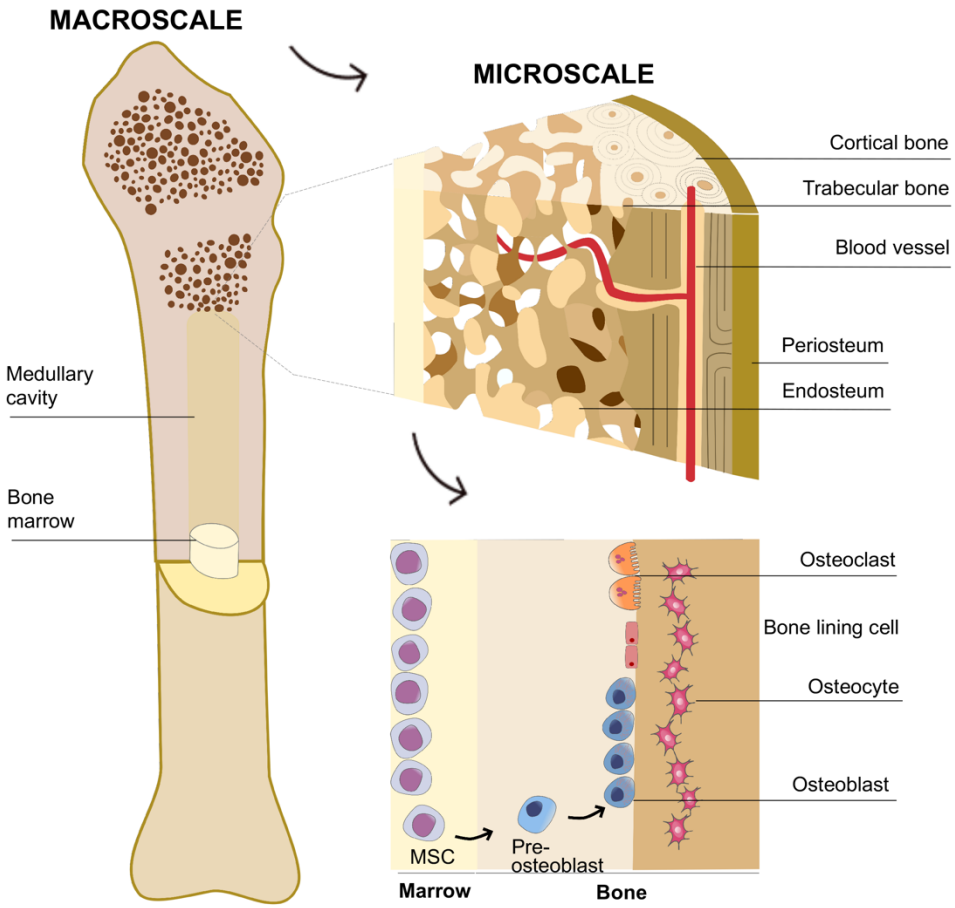



Figure 2.2 - Illustration of the bone structure at a macroscale, and the osteogenic commitment of mesenchymal stem cells (MSC) at a microscale. MSC reside in the bone marrow niches and differentiate into bone cells in the bone site under regeneration.

Gravitational forces and muscle contractions result in small bone deformations which generate matrix strain and interstitial fluid flow within bone porosity [42]. While strain is applied directly through the bone cell attachments, fluid flow is sensed through the cell membrane and both cause cell deformation [42]. The balance between bone formation and resorption is tightly controlled, among others, by osteocytes, which sense mechanical strain and load generated factors (e.g., fluid flow and pressure) through a canalicular network [43, 44]. As a consequence, signal factors are released, regulating osteoclast and osteoblast activity [42]. Bone remodelling processes are modulated by mechanics, as the bone-marrow derived mesenchymal stem cells undergo osteoblastic differentiation in response to mechanical loading. Furthermore, the bone adaptation occurs only when dynamically loaded and thus, in response to cyclic, not static, loading [45, 46]. One extreme example that lack of proper mechanical loads results in bone loss is that astronauts, who live in a microgravity environment, experience a hip bone density loss up to 2% each month [47].

Biomechanical stimuli play a very important role in organisms' development, homeodynamics and homeostasis, and on the level of a cell, mechanical signalling is one of the three fundamental pathways (electrical, (bio)chemical and mechanical) for cell to communicate with its environment [48]. Here we may describe mechanobiology, biomechanics and biomechanology as three areas comprising studying of these phenomena. The first one describes combined synergetic effects of acting mechanical forces on the subcellular and the cell levels as they modulate morphological and structural features of the tissues especially like bone, cartilage, ligament and tendon [49, 50] but it also can have a critical influence on cell behaviour, even in tissues and organs that do not serve an apparent biomechanical role in the body [48, 51]. Biomechanics addresses mainly macroscopic aspects of performance of tissues and biomaterials under proper structural, functional and locomotory actions, and it usually involves simplified models of both materials and tissues [49, 52, 53]. Biomechanology is a recently introduced term [48] postulated as a discipline combining practically feasible, controllable and measurable biomechanical stimuli and parameters on the level of tissues and organs, which has closer clinical and physiological relevancy. In other words, biomechanology aims on design, characterization, analysis, quantification of biomaterials and tissues in a way to cover the most of physiological relevance, address unmet practical clinical needs and to be fitted with regulatory approval procedures: what are correct properties of a biomaterial or tissue, how they needed to be measured and how these data have to be used in a clinical practice?

## 2.3. Extracellular and intracellular mechanical forces that regulate MSC differentiation and linked osteogenic activity

Bone regeneration in situ comprises the MSC lineage commitment towards osteogenesis and recent studies have highlighted the role of external mechanical cues in controlling MSC differentiation [54–57]. Although it remains elusive the biochemical and mechanical principles regulating MSC differentiation in the bone vicinity during locomotion, MSC may be subject to indirect regulation through paracrine signalling from mature cells [58] or may sense the applied mechanical stimulus directly and only then start the differentiation process [59]. MSC, which reside in bone marrow niches near the bone surface, are exposed to multiple biophysical signals, including fluid flow induced shear stress, hydrostatic pressure, substrate strain, stiffness and topography [60]. The mechanical stimuli are not limited to externally-imposed forces but also include the intrinsic tensions generated by active cell contraction that occur in the absence of external forces [61]. In response to their microenvironment, MSC modulate their niche by generating intrinsic

tensions by active cell contraction, or physical forces on the surrounding extracellular matrix (ECM) or neighbouring cells [61, 62].

MSC are highly mechanosensitive and able to adjust to the continuously changing dynamic mechanical environment. The process by which cells sense the mechanical properties of the ECM, including stress/strain, substrate rigidity, topology and adhesiveness is denominated cell mechanosensing [63]. The surrounding mechanical cues are sensed by cells via surface cell receptors (mechanoreceptor). Afterwards, the mechanical signal wave propagates inside the cytoplasm and when it arrives to the nucleus it is transduced into changes in the intracellular biochemistry and gene expression [42]. The adaptation of cells to different mechanical stimuli is governed by a four events chain [64]:

1. Mechanocoupling which corresponds to the conversion of the applied forces into a signal which acts directly on cells;
2. Mechanotransduction, that is the conversion of the mechanical cues into electrical, chemical or biochemical responses;
3. Transduction of the intracellular signals into final signals;
4. Cellular response.

The mechanoresponse involves the rapid and dynamic remodelling of the cytoskeleton in response to the local mechanical cues, such as variations of ECM stiffness or changes in cell shape [65, 66]. Cellular contractility and cytoskeletal tension modulate the fate of MSC [66–69] and an optimal contractility threshold triggers their osteogenic differentiation. Besides the important role of the cytoskeleton in mechanotransduction, given that forces act directly on the cell membrane and that the applied force is transmitted to the cytoskeleton [64], mechanical-based signal propagation through the cytoskeleton is much faster than chemical diffusion- or translocation-based signal propagation [70, 71]. The force propagation from the ECM toward the cell interior and finally to the nucleus occurs in a form of a stress wave and depends on the stiffness differences along the cytoskeleton [71–73]. The rate of mechanotransduction (via stresses and strains) is yet overlooked method affecting cells and tissues. It was shown that the chemical transport able to trigger cellular response is substantially slower than a mechanical stress wave, giving about a million times faster response due to the cytoplasmic viscoelasticity [71].

Transmembrane integrins not only conduct information from the ECM to the cytoskeleton [74, 75] but are also responsible for transmitting cell-intrinsic forces to matrix proteins [61]. Integrins are organized into small adhesive structures in membrane protrusions, named nascent adhesions (NA), which either disassemble after a short lifespan or mature into larger and longer-lived structures, termed focal adhesions (FA). The formation of FA is dependent on myosin-II mediated cell contractility [75]. By clustering into FA, integrins recognize multiple ligands. For example, integrin receptors bind to ECM ligands such as RGD, which activates focal adhesion kinase (FAK), an important regulator of cell adhesion [61]. Integrins are able to communicate either with the ECM and with the cytoskeleton, contributing to outside-in and inside-out signalling, respectively [61, 74], as illustrated in Fig. 2.3. Stem cells are able to maintain their physiological functions when experiencing intracellular and extracellular stresses by inducing autophagy [41]. As a result, a number of organelles are recycled, such as mitochondria, important controllers of cellular quality. Moreover, mechanical homeostasis in stem cells is maintained by modifying FA ligand affinity, by regulating FA assembly/disassembly and by regulating the underlying cytoskeleton and actomyosin contractility [76]. In fact, integrins play an important role in the osteogenic differentiation of MSC, given that the activation of particular integrins enhanced the expression of osteogenic markers [77, 78]. As integrins are closely related to the cytoskeleton, although it is widely accepted that the cytoskeleton is one of the main structural components responsible for inducing a particular cellular behaviour [75, 79], its structural organization during MSC osteogenic differentiation in response to physical cues remains poorly characterized.

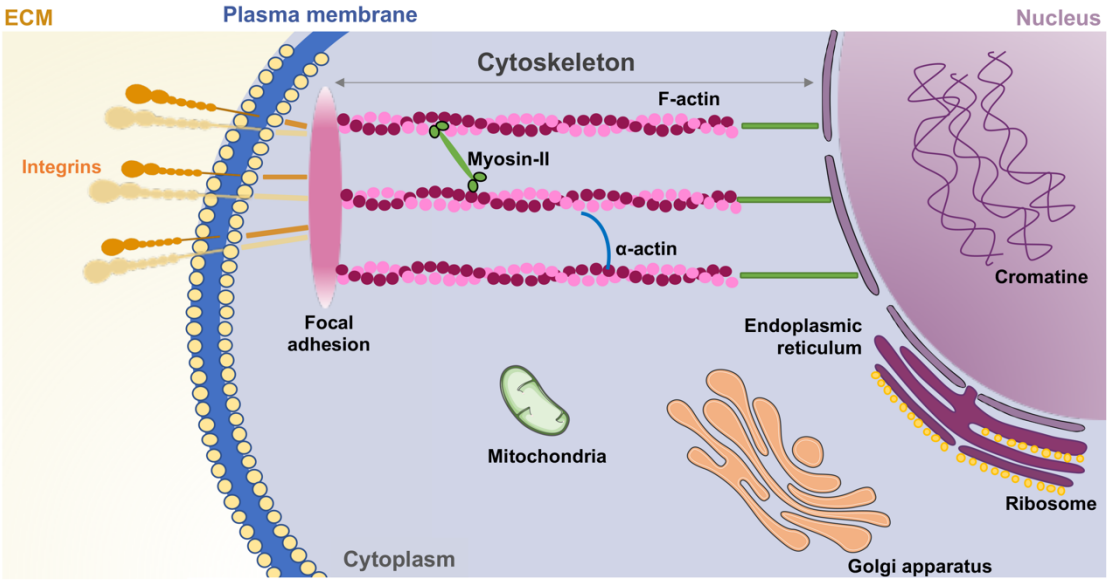



Figure 2.3 - Schematic representation of the main features governing the mechanotransduction system organization. Integrins are organized into larger structures named focal adhesions (FA), which formation is dependent on myosin-II mediated cell contractility. By clustering into FA, integrins recognized and bind to multiple extracellular matrix (ECM) ligands, therefore transmitting information from the ECM to the cytoskeleton and to the nucleus, and vice versa. The mechanoresponse involves not only the rapid remodelling of the cytoskeleton but also the activation of specific genetic programs which involves different cell compartments, such as the ribosomes, Golgi apparatus and mitochondria.

During chemically-induced MSC osteogenic differentiation, a decrease in cellular stiffness, size, and circularity were observed [80], given the changing of F-actin staining parameters (mean intensity, total intensity, and the number of F-actin branches). One group characterized quantitatively the actin cytoskeleton remodelling during osteogenic commitment and concluded that its structure and dynamics appear to regulate several mechanical parameters of MSC [54]. As shown in Fig. 2.4, undifferentiated MSC present a fibroblast-like shape whereas fully differentiated bone cells present a near spherical shape. Within 21 days of osteogenic induction, thick actin fibers in MSC were progressively replaced with a thinner actin meshwork. Furthermore, and in agreement to the literature [54, 83, 84], MSC display long and parallel stress fibers while, during osteogenesis, these fibers acquire a crisscross pattern. The actin organization is a key mechanism for decreasing cell stiffness during osteogenic differentiation [54]. Moreover, the membrane-cytoskeleton interaction in MSC is mostly through focal complexes, often associated with the formation of thick stress fibers, whereas in mature osteoblasts the membrane–cytoskeleton crosslinking is also mediated by actin-binding proteins (e.g., ezrin, radixin and moesin) [54]. Altogether, these structural and mechanical changes lead to significant differences in cellular mechanics between MSC and osteoblasts. As suggested by Titushkin et al., 2007 [54], MSC are extremely sensitive to

the environment and highly responsive to multiple mechanical cues due to a stiff cytoskeleton owing to the rapid propagation of the stress waves in prestressed inhomogeneous materials [71, 72]. On the other hand, osteoblasts are morphologically stable despite being constantly subjected to different stresses and strains.

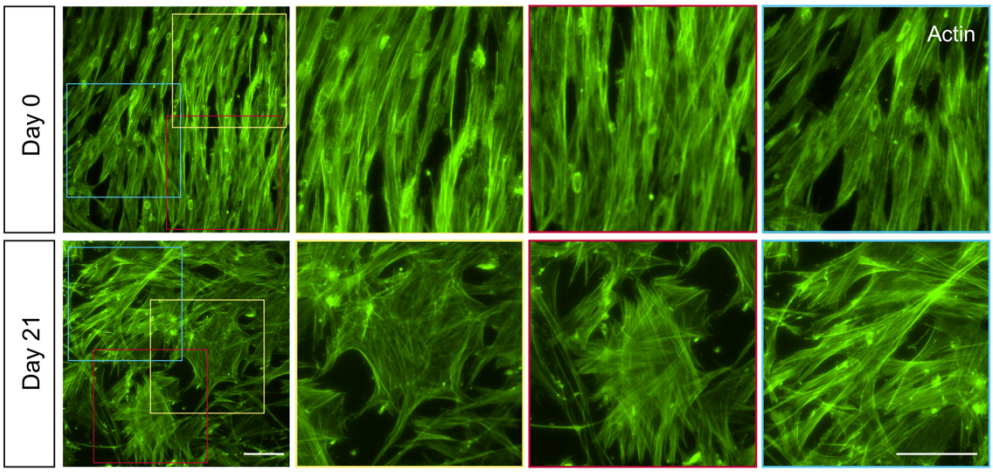



Figure 2.4 - Actin cytoskeleton rearrangement during MSC osteogenic differentiation. Bone marrow-derived MSC were seeded on glass coverslips coated with human fibronectin and cultured in a xeno-free osteogenic differentiation medium for 21 days, as described in [81, 82]. Human MSC (day 0) and fully differentiated bone cells (day 21) were fixed and stained with Alexa Fluor 488 Phalloidin. Scale bar: 100 μm.

## 2.4. Exploring biomaterials with the ability to provide optimal niches for MSC to robust bone repair

Among the diverse biophysical stimuli present in MSC niche, in vitro mechanobiological studies have contributed to ascertain which are the preferable signals for promoting physiological osteogenic differentiation and, therefore, regulating bone turnover [54–57]. Synthetic matrices are being used to create engineered systems that can generate different stress and strain conditions and thus manipulate the extracellular microenvironment of MSC [61, 85], as summarized in Table 2.1.

Table 2.1 - Osteogenic results from mechanical loading on MSC.

| Mechanical loading | Strain | Conditions | Material | Osteogenic results | Ref |
|---|---|---|---|---|---|
| Cyclic stretching | 2%, 8% | 2h, three times per day, for 3 days | Silicone either with or without DEX | Only the 2% elongation increased ALP and OC levels and upregulated Col I, III | [86] |
| | 0%, 10%, 12% | 1 Hz for 4 h/day for 7 or 14 days | Linear 3D Col I matrices | Osteogenic differentiation was significantly promoted at 12% strain in 14 days | [87] |
| | 3% | 0.25 Hz (continuously), for 16 days | Silicon rubber, pre-coated with Col I | Proliferation was inhibited whereas the matrix mineralization increased | [88] |
| Cyclic compression | 0.22% (physiological), 0.88%, 1.1% (supra-physiological) | 1 Hz, for 4 weeks | PCL-TCP | Higher levels of ALP activity, mineralization, and expression of ON, Col I and OC were obtained for 0.22% strain. | [89] |
| | 5% | 2 hours every 5 days, for 10 days | 3D PU scaffolds either with or without DEX | Expression of Col I mRNA and calcium deposition doubled comparing to the non-loaded constructs | [90] |
| Fluid shear stress | Unknown | 1.2 Pa for 30 and 90 mins | Sandwich of a silicone gasket between the glass slide and an acrylic plate | Significant increase in ALP gene expression and a marked decrease in Col I | [91] |
| | Unknown | Maximum peak shear force at 0.051 Pa, starting from day 4 of culture, 1 h per day, 5 days per week, for 21 days | Gelatine-coated plastic | Upregulation of ALP, Col and calcium production | [92] |
| | Unknown | 90 Pa for 24 h, 3 days after being in culture | PC and glass slide | ALP activity in osteogenic medium was significantly increased and at days 4 and 8 of culture the mRNA expression of BMP-2 and OP was significantly higher | [93] |
| | Unknown | Maximum mean surface stress of 0.013 Pa for 4 and 8 days | Porous foams and nonwoven fibrous meshes of PLA | Dynamic culturing using flow perfusions enhanced growth and differentiation within the first 8 days | [94] |

Polymers: polycarbonate (PC), polycaprolactone-β (PCL), poly-L-lactic acid (PLA), polyurethane (PU). Bioactive material: tricalcium phosphate (TCP). Chemotherapeutic agent: dexamethasone (DEX). Osteogenesis markers: alkaline phosphatase (ALP), bone morphogenetic protein 2 (BMP-2), collagen (Col), osteocalcin (OC), osteonectin (ON), osteopontin (OP)

Due to the variety of factors selected in mechanobiological experiments, including the dimensionality of the model system (in vitro vs in vivo), mechanical stimuli (tensile, compression and shear), loading conditions (strain magnitude, frequency and duration), substrate materials and culture medium composition, the optimum conditions for controlling osteogenic lineage of MSC differentiation remain unspecified. Nevertheless, it can be concluded that tensile strain and fluid flow induced stress promote osteogenesis, but compressive loading can also be beneficial for bone formation. For low cellular contractility levels, stem cells retain their multipotency, whereas upon exposure to physiological fluid flow forces, for example, the intracellular tension in MSC was found to increase, inducing osteogenic differentiation [95]. One, however, must be careful drawing conclusions on biomechanical effects of fluid flow alone, often reported in literature [96]. First, fluid flow causing shear stress does not always lead to cell mechanostimulation, as pure shear stress does not lead to volumetric changes of the object, so fluid flow pressure is not at all equivalent to direct mechanical stimulation [48, 97]. Second, the shear stress cannot be measured so many assumptions are needed, which are not always reasonably justified. Third, changing the fluid flow not only changes the shear stress (many biological fluids are not Newtonian), but also changes amount of nutrients brought to the cells per time and unit area, and amount of their metabolic products to be removed [98, 99]. Forth, as there are many ways of expression of strain and stresses tensors, failure to describe rationale why that particular form has been selected and how it relates to physiological relevance does not allow further translation of these studies into practice.

The majority of the in vitro studies found in literature focused on linear elastic 2D polymeric substrates, which strain range is much different from those achieved by metallic orthopaedic implants (physiological strains ranging from 0.02– 0.35%) and don't directly correlate with the microscale loading promoted on bone cells niche [61]. Although cyclic stress at lower/equal physiological frequencies resulted in osteogenic differentiation [87], the physiological frequencies during locomotion are around 1–3 Hz [89]. Despite many loading systems aim to only study the effect of a particular mechanical stimulus, depending on the scaffold material and architecture, secondary effects are expected in 3D cell-seeded tissue engineered constructs in vitro [100, 101].

Mechanically rigid matrices that mimic collagenous bone [66], 3D-dimensional microcarrier cell cultures [102], or specific texture patterns [103] were found to increase cytoskeletal tension and actomyosin contraction which induced the osteogenic differentiation of MSC without the need for exogenous stimuli. Both cell-cell and cell-substrate adhesions are important in stem cell maintenance, proliferation and differentiation [104]. Substrate topography (with micro- or nano-

features) has direct effects on cell orientation and morphology and on cytoskeleton arrangements [105]. Some topographical surface features including the pattern shape and dimensional parameters as diameter, spacing, height and depth and spatial arrangement, schematized in Fig. 2.5, influence the cell response and behaviour [103]. The main cellular responses of human MSC cultured on different patterns are summarized in Table 2.2.

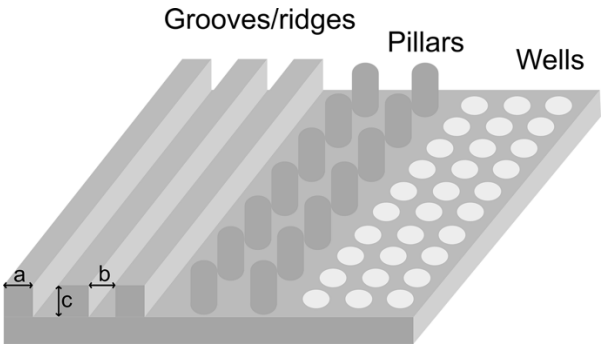



Figure 2.5 - Some typical topographical patterns include grooves/ridges, pillars and wells and the patterning parameters are: pillar diameter/ridge width (a), pillar interspacing/groove width (b), and pillar height/groove depth (c).

Engineered topographies should promote an optimal arrangement, number and size of FA, so that the osteogenic signalling mechanotransduction processes enhance osteoinduction, osteoconduction and finally, osteointegration [103]. As presented in Table 2.2, architectural signals, including cell shape and geometry, defined by the surface pattern, have a profound impact on cell behaviour [120, 121]. The osteogenic differentiation of human MSC is highly sensitive to the topographical feature diameter/ridge width when cultured on nanopits on ridges, respectively. When cultured on nanopillars and nanotubes, MSC osteogenic commitment is regulated by the feature height, shape and spatial arrangement. Surface nanoporosity was shown to have a direct impact on cell adhesion [113, 122]. Consequently, a strong interaction between the cytoskeleton and substrate contributes preferentially to osteogenic differentiation. In addition, nano-displaced topography significantly increases osteospecific differentiation, given that a degree of disorder facilitates FA formation, intracellular tension and subsequent cellular spreading [116, 123]. Despite the promising results found in literature, it is difficult to systematically compare the effects of different patterns and corresponding dimensional parameter. Moreover, in vivo results may be different from those reported in the in vitro studies. Therefore, till date, no optimal surface patterns have been specified for inducing osteogenic differentiation of MSC. MSC self-renewal, proliferation and differentiation depend not only on the substrate topography, but also on its stiffness. Experimental studies found that MSC differentiate towards different cell lineages in direct response to tissue mechanics [66, 124] due to variations in extracellular mechanical force exerted on the

cultured cells [62]. Osteogenesis is favoured upon a more rigid [125], and highly adhesive substrates [126], as one study concluded that MSC cultured on elastically- tuneable polyacrylamide gels with bone-like (25–40 kPa), muscle-like (8–17 kPa) and brain-like (0.1–1 kPa) stiffness, resulted in osteogenic, myogenic and neuronal differentiation, respectively [66]. However, using the 'stiffness' value alone, without proper detail, is a great oversimplification for estimation of tissue formation. All tissue models have a great number of assumptions – even for tissues known to be highly non-linear and viscoelastic, often 'Young modulus' is addressed in the calculations to simplify interactions of implant surface geometry with the environment or tissue-implant interface development [127]. For example, the guidelines of National Physical Laboratory (UK) list nine methods of measurement and calculation of elastic modulus [128], all giving different outcomes, and it is not at all straightforward for an implant designer which method would be the most suitable. Actual mechanical stimuli for bone formation are implant-, surface- and geometry specific, so getting the primary stability does not yet guarantee subsequent failure due to differences in the pattern of bone formation. This has important implications to the design of bone fracture repair devices and engineered skeletal tissues [129].

Table 2.2 – Substrate topography effect on human MSC.

| Material | Pattern shape | Pattering dimensions | | | | Parameter on study | Osteogenic results | Ref |
|---|---|---|---|---|---|---|---|---|
| | | Aspect ratio | a (µm) | b (µm) | c (µm) | | | |
| PDMS stamps with pattern adhesive islands of octadecanethiolate | Rectangle | 1:1; 3:2; 4:1 | | | | Aspect ratio | Yield of osteogenesis increased with aspect ratio | [68] |
| | Flower | | | | | Types of curvature (convex or concave edges) | The star shape was preferred for an osteogenic fate | |
| | Star | | | | | | | |
| | Pentagonal | | | | | | | |
| | Circular shape | | | | | Local curvature and aspect ratio | The "holly leaf" was the only that promoted osteogenic fate | |
| | "Holly leaf" | 2:1 | | | | | | |
| PI | Grooves and ridges | | 2-15 | 2-15 | | Ridges dimensions | Osteogenesis was enhanced on thinner ridges (2 µm) comparing to wider ridges. Gradual reduction of osteogenic differentiation with increasing ridge width, whereas groove width was less relevant | [106] |
| | | | 5 | 2/15 | | | Osteogenic differentiation was enhanced on 2 µm ridges | |
| $SiO_2$ | Nanopillars | | 0.01/0.03 | 0.05-0.12 | 0.02-0.035 | Pillar dimensions | Osteogenic differentiation was clearly favoured on high nanopillars (0.05 µm) of moderate distance (0.01 µm) | [107] |

| | | | | | | | |
|---|---|---|---|---|---|---|---|
| $TiO_2$ | Nanopillars | 0.02<br>0.03<br>0.04 | 0.04<br>0.07<br>0.105 | 0.015<br>0.055<br>0.09 | Pillar heights | 0.015 μm nanopillars demonstrated enrichment of RUNX2 and OC | [108] |
| $TiO_2$ | Nanopillars | 0.03<br>0.04<br>0.055 | 0.04<br>0.075<br>0.115 | 0.015<br>0.055<br>0.1 | Pillar heights | OP and OC nodules decreased as height increased. | [109] |
| $TiO_2$ | Nanopillars | | | 0.008<br>0.015 | Pillar heights | Both heights showed more OC relative to planar control, but enhanced size of OC deposits was reported on the highest pillars | [110] |
| $TiO_2$ | Nanotubes | 0.03<br>0.05<br>0.07<br>0.1 | 20 | | Tubes diameter | 0.1 μm diameter tubes displayed the highest up regulation of ALP, OC and OP | [111] |
| Ti | Hemisphere-like topographic nanostructures | 0..88<br>0.130<br>0.238 | 462 | 0.05<br>0.1<br>0.2 | Nanoparticle size | Higher RUNX2 expression was found on flat and 0.2 μm compared with 0.05 μm surfaces; ALP activity significantly increased as the size increased, and calcium | [112] |

| | | | | | | | |
|---|---|---|---|---|---|---|---|
| | | | | | | phosphate deposition was superior on 0.1 μm and 0.2 μm surfaces. | |
| Ti | Nanopits | 0.03<br>0.15<br>0.3 | | | Nanopits diameter | OC was upregulated on nanopits with 30 and 0.15 μm diameter by greatest mineralization was found on 0.3μnm diameter nanostructures | [113] |
| PDMS | Silicon hexagonanally micropost arrays | 1.83 | 4 | 0.97<br>6.1<br>12.9 | Rigidity | Osteogenic differentiation was promoted on rigid micropost arrays (K=1556 $nN\mu m^{-1}$), which corresponds to the lowest height | [114] |
| PMMA | Islands | 2.2<br>1.7<br>0.144 | 4.3<br>2.9<br>0.184 | 0.045<br>0.033<br>0.01 | Height | All nanotopographies stimulated the osteoprogenitor cell differentiation towards an osteoblastic phenotype. However, it was more evident for the 0.033 μm height islands which presented bone nodules | [115] |
| PMMA | Nanopits | 0.120 | 0.3 | 0.1 | Square array (SQ), hexagonal array (HEX), disordered square arrays with 20 nm (DSQ20) and 50 nm (DSQ50) displacement from their square position, and randomly positioned (RAND) | On the DSQ50 surfaces, MSC displayed areas of positive OC and OP staining and nodule formation | [116] |

| | | | | | | | |
|---|---|---|---|---|---|---|---|
| PC | Nanopits | 0.120 | 0.3 | 0.1 | Square (SQ) vs near square random displacement of 50 nm (NSQ50) | RUNX2 was expressed significantly higher on NSQ50 compared to planar controls and SQ surfaces | [117] |
| PCL | Nanopits | 0.120 | 0.3 | 0.1 | Near square random displacements of up to ±50 nm (NSQ50) | NSQ50 induced higher levels of BMP2 mRNA expression and increased OPN and mineralization, compared to flat surface | [118] |
| PCL | Nanopits | 0.120 | 0.3 | 0.1 | Near square random displacements of up to ±50 nm (NSQ50) | RUNX2, OSX, ALP, OC and OP were up regulated in NSQ50 compared to planar control. | [119] |
| PDMS | Lines | 2 | 1 | 0.08 | Distinct topographies and dimensions | The first 'gratings' dimensions and wells exhibited the maximum difference in the cell spreading area. Between these, cells spread widely and generated higher contractility in the 'well' topography. | [95] |
| | | 1 | 2 | 0.12 | | | |
| | | 0.25 | 0.25 | 0.25 | | | |
| | | 0.25 | 0.25 | 0.11 | | | |
| | | 0.46 | 0.07 | 0.040 | | | |
| | Pillars | 2 | 12 | 2 | | | |
| | | 0.5 | 10 | 0.5 | | | |
| | Wells | 1 | 6.5 | 1 | | | |

Polymers: polydimethylsiloxane (PDMS), polyimide (PI), polymethylmethacrylate (PMMA). Osteogenesis markers: alkaline phosphatase (ALP), osteocalcin (OC), osteopontin (OP), osterix (OSX)

## 2.5. The concept idea for new generation design of novel pro-active orthopaedic implants

Despite advances in bone implant research, including the development of novel implantable biomaterials, the available orthopaedic implants do not elicit a proper mechanical stimulation at the bone-implant interface. In fact, the innovation rate in the orthopaedic industry has been declining, showing the importance of a clinical need-based strategy [130]. In this sense, the clear evidence that orthopaedic implants still fail, often due to aseptic loosening, creates new challenges and the development of new solutions. Here we have analysed the most relevant conditions for the orthopaedic implants which are in a way optimal for neo-bone formation, stability and endurance limits (as presented in literature [131–135], validated by in silico and in vivo studies), as represented in Table 2.3. These values might be considered as a guideline for implants, biomaterials and conditions of their design for proper orthopaedic applications. Note that these values are also depending on the number of loading cycles and history, as well as must be supported by other necessary conditions. For example, proper fluid supply, generated by the relative micromotions of the implant and bone - as related to mechano-regulative index [136, 137] is needed for cells proliferation and growth.

Table 2.3 - Combined data on physiological conditions for bone performance.

| **Conditions** | **Frequency (Hz)** | **Strain* (millistrain)** | **Strain rate (1/s)** | **Comments** |
|---|---|---|---|---|
| Free walking | 0.5 – 1.0 | 0.3 - 0.5 | ~0.001 | |
| Brisk walking, jogging | 1.2 - 1.8 | 0.6 - 1.0 | ~0.01 | |
| Slow running | 2 - 3 | 1.0 ~ 1.5 | ~0.03 | |
| Bone yield limit | - | 3.0 ~ 6.7 | - | Depends on bone and loading conditions |
| Fracture | - | 25 ~ 30 (static), ~10 (dynamic) | ~1 | |
| Trauma | - | >30 | >1 | |

* here strain (1 millistrain = 0.001 x strain) means octahedral resolved strain, i.e. deviatoric value of principal true (logarithmic) strain values [136].

As mentioned, hip and knee implants failures are often related to aseptic loosening events. During locomotion, surrounding bone experiences different loads along the bone/implant length, leading to different bone resorption percentages. The awareness about non-uniform strain

miscompliance along an implant is pushing forward the (re)design of new implants. Recently, auxetic cellular structures have gained substantial interest due to their unique properties given the negative Poisson's ratio, which corresponds to the ability of expand laterally when stretched [138]. Auxetic meta-biomaterials offer a feasible route to design different parts of an implant with different strains as response to a given loading [139], privileging the most suited strains for a given area of hip and knee implants. Focusing, for example, on the hip implant, its femoral part is repeatedly loaded, predominantly, under axial compression [23, 140], creating tensile loading on the lateral side and compression on the medial side [141]. The side that experiences tension will retract from bone, causing a diminished mechanical stimulation at the bone-implant interface and an increased chance of wear particles entering the interface space, becoming more susceptible to failure. Although no animal models or clinical trials were conducted up to now, in theory, if the femoral part is able to create compression on both sides, the bone-implant contact is enhanced [139]. In this regard, if under physiological loading the implant is able to expand on the areas more prone to suffer bone resorption, the surrounding bone will be mechanically stimulated. This pro-active characteristic will promote an adequate stress/strain conditions at the bone-implant interface to assure a healthy bone formation. Furthermore, bone-implant interfaces may be improved by controlling some properties of the implant surface, including surface energy and topography. As some groups concluded, micro- and nano-topography may promote osteogenic differentiation of human MSC. Different surface patterns, including ridges, pillars, pits and wells, forced stem cells to change their shape, strongly influencing the stem cell fate. Combined effects of topography and mechanical stimulation were found to augment the osteogenic commitment of MSC. One group studied the effect of fluid shear stress on human MSC seeded on 1 μm wells and on 2 μm gratings [95]. Cells generated higher contractility onto the well topography, on contrary to the grating topography where MSC poorly spread and presented lower contractility. After an exposure of 48 h of continuous 1 Pa fluid flow induced shear stress, MSC exhibited increased contractility only on the well topography and increased number of FA, leading to their osteogenic differentiation. In this sense, in addition to the externally applied mechanical loading, physical cues may be employed to increase the cytoskeleton tension of MSC, promoting osteogenesis. Based on this, Fig. 2.6 illustrates a novel concept for discussion of a pro-active hip implant. The proposed design represents a one-for-all solution which should succeed in the majority of joint replacement cases, given the following features:

- Adaptive surface to generate a proper mechano-regulative index;

- Use of an auxetic material to achieve a pro-active lateral expansion under physiological loading to stimulate the surrounding bone and promote healthy bone formation;
- Engineered topography to elicit proper cell adhesion, biomechanics and fluidics and therefore promote MSC osteogenic differentiation but also able to enhance the implant expansion effect;
- Feasible production and commercialization on a large scale

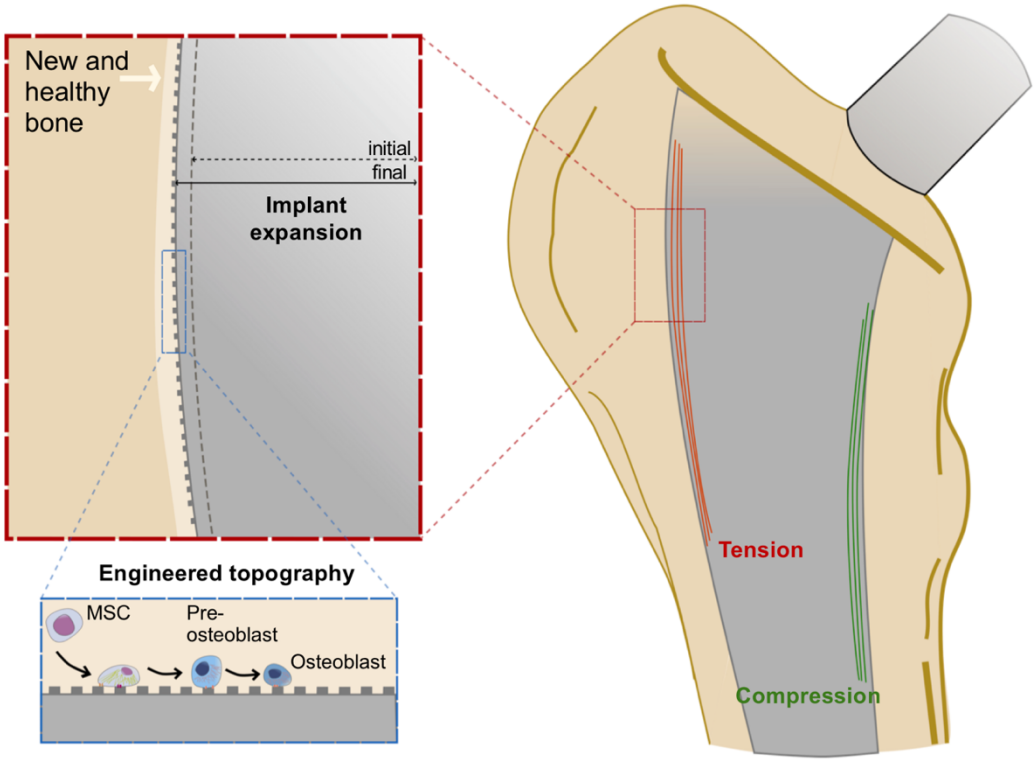



Figure 2.6 - Example of a novel pro-active hip implant combining an auxetic material and engineered topography. The optimized and improved design is for the purpose of osteointegration at the bone-implant interface, particularly at the lateral side of the proximal femur which, under physiological loading, experiences mostly tensile stress.

Altogether, it presents advantages, on average, superior to the existing ones and thus, could substitute the current orthopaedic solutions available in the market as it would extend the longevity of the orthopaedic implant and improve the patient's quality of life.

Given that the short- and long-term maintenance of the implant is assured if the host bone is mechanically stimulated to recruit MSC from the bone marrow and consequently induce their osteogenic differentiation, the study of MSC response to physical and mechanical cues will improve stem cell therapeutics in a biomaterial-based regenerative medicine [55]. Focusing on orthopaedic applications, future studies should be performed using metallic substrates and reproducing the conditions of a real implantation scenario. The know-how underlying the proposed design combined

with the suggested studies will lead, in the future, to the development of a "patient-specific" solution. Customized orthopaedic prostheses would present an "adaptive" design, in which the proper implant expansion and surface pattern would be positioned and designed based on image acquisition techniques, e.g., computed tomography (CT) and magnetic resonance imaging (MRI) [142]. Customizing would consider, among other requirements, the patient-specific bone anatomy, mechanical properties and load pattern and, finally the biochemical complex [143]. Although in the current scenario it is only feasible to propose a one-for-all solution that could be large-scale produced, it is expected that in the future, the focus will be on the development of personalized medicine in orthopedy.

## 2.6. Conclusion

The study of external loading conditions and/or ECM physical cues has shown that MSC osteogenic commitment may be enhanced. Tensile strain and fluid flow are more prone to induce osteogenesis however, the majority of the mechanobiology studies use polymeric substrates which strain range is much different from those achieved by metallic implants. In this sense, real stress/strain conditions in hip and knee implants should be reproduced in vitro in order to mimic the dynamic environment of MSC when in contact with these orthopaedic implants' interfaces. Moreover, micro- and nano-topographies have direct effects on cell morphology and cytoskeleton arrangements and thus, in regulating the stem cell fate.

Based on the osteogenic and mechanoresponsive potential of MSC, host bone-implant interactions may be improved in joint replacement surgery. Although this review focused on hip and knee implants, the conclusions presented here can be translated into any orthopaedic application, as this knowledge can be integrated towards the development of better biomaterials and bone-implant interfaces. Furthermore, the mechanical regulation of MSC by the identification of the most appropriate loading parameters combined with proper substrate topography will contribute to the next generation design of novel pro-active orthopaedic implants, to their implantation success and, in the future, to the development of personalized medicine in orthopedy.

**Acknowledgments**

This work was supported by FCT (Fundação para a Ciência e Tecnologia) through the grant SFRH/BD/141056/2018 and the projects FCT/PTDC/EMSTEC/5422/20 and POCI-01-0145-FEDER- 030498. Additionally, this work was supported by FEDER fund through the project reference NORTE-01-0247-FEDER-034074, by European Cooperation in Science and Technology

through the project reference COST Action MP1301 and also Marie Sklodowska-Curie COFUND Programme 'NanoTRAINforGrowth', from the European Union's Seventh Framework Programme for research, technological development and demonstration.

## References

[1] OECD/EU. (2016). Health at a glance: Europe 2016 - state of health in the EU cycle. Paris: OECD Publishing. https://doi.org/ 10.1787/9789264265592-en.

[2] Kremers, H. M., Larson, D. R., Crowson, C. S., Kremers, W. K., Washington, R. E., Steiner, C. A., ... Berry, D. J. (2014). Prevalence of total hip and knee replacement in the United States. Journal of Bone and Joint Surgery - American, 97(17), 1386–1397. https://doi.org/10.2106/JBJS.N.01141.

[3] American Joint Replacement Registry. (2016). Third AJRR annual report on hip and knee Arthroplasty data. 2016 Annual Report.

[4] Sundfeldt, M., Carlsson, L. V., Johansson, C. B., Thomsen, P., & Gretzer, C. (2006). Aseptic loosening, not only a question of wear: A review of different theories. Acta Orthopaedica, 77(2), 177–197. https://doi.org/10.1080/17453670610045902.

[5] Apostu, D., Lucaciu, O., Berce, C., Lucaciu, D., & Cosma, D. (2018). Current methods of preventing aseptic loosening and improving osseointegration of titanium implants in cementless total hip arthroplasty: A review. Journal of International Medical Research, 46(6), 2104–2119. https://doi.org/10.1177/0300060517732697.

[6] Trebše, R. (Ed.). (2012). Infected total joint arthroplasty: The algorithmic approach. Springer Science & Business Media.

[7] Gristina, A. G., Naylor, P., & Myrvik, Q. (1998). Infections from biomaterials and implants: A race for the surface. Medical Progress through Technology, 14(3–4), 205–224.

[8] Schmolders, J., Amvrazis, G., Pennekamp, P. H., Strauss, A. C., Friedrich, M. J., Wimmer, M. D., Rommelspacher, Y., Wirtz, D. C., & Wallny, T. (2017). Thirteen year follow-up of a cementless femoral stem and a threaded acetabular cup in patients younger than fifty years of age. International Orthopaedics, 41(1), 39–45. https://doi.org/10.1007/s00264-016-3226-z.

[9] Tan, X. P., Tan, Y. J., Chow, C. S. L., Tor, S. B., & Yeong, W. Y. (2017). Metallic powder-bed based 3D printing of cellular scaffolds for orthopaedic implants: A state-of-the-art review on

manufacturing, topological design, mechanical properties and biocompatibility. Materials Science and Engineering: C, 76, 1328– 1343. https://doi.org/10.1016/J.MSEC.2017.02.094.

[10] Perdreau-Remington, F., Stefanik, D., Peters, G., Ludwig, C., Rütt, J., Wenzel, R., & Pulverer, G. (1996). A four-year prospective study on microbial ecology of explanted prosthetic hips in 52 patients with "aseptic" prosthetic joint loosening. European Journal of Clinical Microbiology and Infectious Diseases, 15(2), 160–165. https://doi.org/10.1007/BF01591491.

[11] Bereza, P. L., Ekiel, A., Auguściak -Duma, A., Aptekorz, M., Wilk, I., Kusz, D. J., ... Martirosian, G. (2013). Identification of silent prosthetic joint infection: Preliminary report of a prospective controlled study. International Orthopaedics, 37(10), 2037–2043. https://doi.org/10.1007/s00264-013-1955-9.

[12] Donlan, R. M. (2005). New approaches for the characterization of prosthetic joint biofilms. Clinical Orthopaedics and Related Research, 437, 12–19. https://doi.org/10.1097/01.blo. 0000175120.66051.29.

[13] Boot, W., Moojen, D. J. F., Visser, E., Lehr, A. M., De Windt, T. S., Van Hellemondt, G., ... Vogely, H. C. (2015). Missed low-grade infection in suspected aseptic loosening has no consequences for the survival of total hip arthroplasty. Acta Orthopaedica, 86(6), 678–683. https://doi.org/10.3109/ 17453674.2015.1086942.

[14] Ince, A., Rupp, J., Frommelt, L., Katzer, A., Gille, J., & Löhr, J. F. (2004). Is "aseptic" loosening of the prosthetic cup after Total hip replacement due to Nonculturable bacterial pathogens in patients with low-grade infection? Clinical Infectious Diseases, 39(11), 1599–1603. https://doi.org/10.1086/425303.

[15] American Joint Replacement Registry. (2018). Annual Report 2018. AAOS - American Academy of Orthopaedic Surgeons, 0–19.

[16] Vanrusselt, J., Vansevenant, M., Vanderschueren, G., & Vanhoenacker, F. (2015). Postoperative radiograph of the hip arthroplasty: What the radiologist should know. Insights Into Imaging, 6(6), 591–600. https://doi.org/10.1007/s13244-015- 0438-5.

[17] Jauregui, J. J., Elmallah, R. K., Cherian, J. J., Mont, M. A., & Harwin, S. F. (2015). Outcomes of a newer-generation Cementless Total knee Arthroplasty design. Orthopedics, 38(10), 620–624. https://doi.org/10.3928/01477447-20151002-

[18] Prudhon, J. L., & Verdier, R. (2017). Cemented or cementless total knee arthroplasty?: comparative results of 200 cases at a minimum follow-up of 11 years Sicot-J, 3, 70. https://doi.org/10.1051sicotj/2017046.

[19] clinicaltrials.gov/NCT02155712. (n.d.).

[20] Gervais, B., Vadean, A., Brochu, M., & Raison, M. (2018). Influence of the load modelling during gait on the stress distribution in a femoral implant. Multibody System Dynamics, 44(1), 93–105. https://doi.org/10.1007/s11044-018-9621-z.

[21] Moewis, P., Checa, S., Kutzner, I., Hommel, H., & Duda, G. N. (2018). Physiological joint line total knee arthroplasty designs are especially sensitive to rotational placement - A finite element analysis. PLoS One, 13(2), e0192225. https://doi.org/10.1371/journal. pone.0192225.

[22] Jetté, B., Brailovski, V., Simoneau, C., Dumas, M., & Terriault, P. (2017). Development and in vitro validation of a simplified numerical model for the design of a biomimetic femoral stem. Journal of the Mechanical Behavior of Biomedical Materials. https://doi.org/10.1016/j.jmbbm.2017.10.019.

[23] Taylor, M., Tanner, I., Freemant, M., & Yettram, A. (1996). Stress and strain distribution within the intact femur: Compression or bending? Med. Eng. Hys, 18(4), 122–131.

[24] Edwards, W. B., Miller, R. H., & Derrick, T. R. (2016). Femoral strain during walking predicted with muscle forces from forward dynamics simulation versus inverse-dynamics-based static optimization. Journal of Orthopaedic Research, 34, 1206–1213. https:// doi.org/10.1002/jor.23247.

[25] Anderson, D. E., & Madigan, M. L. (2013). Effects of age-related differences in femoral loading and bone mineral density on strains in the proximal femur during controlled walking. Journal of Applied Biomechanics, 29(5), 505–516. https://doi.org/10.1038/ mp.2011.182.doi.

[26] Arabnejad, S., Johnston, B., Tanzer, M., & Pasini, D. (2017). Fully porous 3D printed titanium femoral stem to reduce stress-shielding following total hip arthroplasty. Journal of Orthopaedic Research, 35(8), 1774–1783. https://doi.org/10.1002/jor.23445.

[27] Ebrahimi, H., Rabinovich, M., Vuleta, V., Zalcman, D., Shah, S., Dubov, A., Roy, K., Siddiqui, F. S., H. Schemitsch, E., Bougherara, H., & Zdero, R. (2012). Biomechanical properties of an intact, injured, repaired, and healed femur: An experimental and computational study. Journal of

the Mechanical Behavior of Biomedical Materials, 16, 121–135. https://doi.org/10.1016/j.jmbbm.2012.09.005.

[28] Rahimizadeh, A., Nourmohammadi, Z., Arabnejad, S., Tanzer, M., & Pasini, D. (2018). Porous architected biomaterial for a tibial-knee implant with minimum bone resorption and bone- implant interface micromotion. Journal of the Mechanical Behavior of Biomedical Materials, 78 (February 2017), 465–479. https://doi.org/10.1016/j.jmbbm.2017.11.041.

[29] Cilla, M., Checa, S., & Duda, G. N. (2017). Strain shielding inspired re-design of proximal femoral stems for total hip arthroplasty. Journal of Orthopaedic Research, 35(11), 2534– 2544. https://doi.org/10.1002/jor.23540.

[30] Sedel, L., Viateau, V., Petite, H., Meunier, A., Oudina, K., de Pollak, C., ... Bensaïd, W. (2000). Tissue-engineered bone regeneration. Nature Biotechnology, 18(9), 959–963. https://doi.org/10.1038/79449.

[31] Blaber, E. A., Dvorochkin, N., Torres, M. L., Yousuf, R., Burns, B. P., Globus, R. K., & Almeida, E. A. C. (2014). Mechanical unloading of bone in microgravity reduces mesenchymal and hematopoietic stem cell-mediated tissue regeneration. Stem Cell Research, 13(2), 181–201. https://doi.org/10.1016/J.SCR.2014. 05.005.

[32] Roseti, L., Parisi, V., Petretta, M., Cavallo, C., Desando, G., Bartolotti, I., & Grigolo, B. (2017). Scaffolds for bone tissue engineering: State of the art and new perspectives. Materials Science & Engineering C, 78, 1246–1262. https://doi.org/10. 1016/j.msec.2017.05.017.

[33] Zhang, W., Zhu, Y., Li, J., Guo, Q., Peng, J., Liu, S., Yang, J., & Wang, Y. (2016). Cell-derived extracellular matrix: Basic characteristics and current applications in orthopedic tissue engineering. Tissue Engineering Part B: Reviews, 22(3), 193–207. https://doi.org/10.1089/ten.teb.2015.0290.

[34] Arvidson, K., Abdallah, B. M., Applegate, L. A., Baldini, N., Cenni, E., Gomez-Barrena, E., Granchi, D., Kassem, M., Konttinen, Y. T., Mustafa, K., Pioletti, D. P., Sillat, T., & Finne- Wistrand, A. (2011). Bone regeneration and stem cells. Journal of Cellular and Molecular Medicine, 15(4), 718–746. https://doi.org/ 10.1111/j.1582-4934.2010.01224.x.

[35] Florencio-Silva, R., Sasso, G. R. D. S., Sasso-Cerri, E., Simões, M. J., & Cerri, P. S. (2015). Biology of Bone Tissue: Structure, Function, and Factors That Influence Bone Cells. BioMed Research International, 2015. https://doi.org/10.1155/2015/ 421746.

[36] Ratajczak, M. Z., Marycz, K., Poniewierska-Baran, A., Fiedorowicz, K., Zbucka-Kretowska, M., & Moniuszko, M. (2014). Very small embryonic-like stem cells as a novel developmental concept and the hierarchy of the stem cell compartment. Advances in Medical Sciences, 59(2), 273–280. https://doi.org/ 10.1016/j.advms.2014.08.001.

[37] Marędziak, M., Śmieszek, A., Chrząstek, K., Basinska, K., & Marycz, K. (2015). Physical activity increases the Total number of bone-marrow-derived Mesenchymal stem cells, enhances their Osteogenic potential, and inhibits their Adipogenic properties. Stem Cells International, 2015. https://doi.org/10.1155/2015/ 379093.

[38] Marycz, K., Mierzejewska, K., Śmieszek, A., Suszynska, E., Malicka, I., Kucia, M., & Ratajczak, M. Z. (2016). Endurance exercise mobilizes developmentally early stem cells into peripheral blood and increases their number in bone marrow: Implications for tissue regeneration. Stem Cells International, 2016. https://doi.org/10.1155/2016/5756901.

[39] Garg, P., Mazur, M. M., Buck, A. C., Wandtke, M. E., Liu, J., & Ebraheim, N. A. (2017). Prospective review of Mesenchymal stem cells differentiation into osteoblasts. Orthopaedic Surgery, 9(1), 13–19. https://doi.org/10.1111/os.12304.

[40] Uccelli, A., Moretta, L., & Pistoia, V. (2008). Mesenchymal stem cells in health and disease. Nature Reviews Immunology, 8(9), 726–736. https://doi.org/10.1038/nri2395.

[41] Marycz, K., Kornicka, K., Grzesiak, J., Śmieszek, A., & Szłapka, J. (2016). Macroautophagy and selective Mitophagy ameliorate Chondrogenic differentiation potential in adipose stem cells of equine metabolic syndrome: New findings in the field of progenitor cells differentiation. Oxidative Medicine and Cellular Longevity, 2016, 1–18. https://doi.org/10.1155/2016/3718468.

[42] Wittkowske, C., Reilly, G. C., Lacroix, D., & Perrault, C. M. (2016). In vitro bone cell models: Impact of fluid shear stress on bone formation. Frontiers in Bioengineering and Biotechnology, 4, 1–22. https://doi.org/10.3389/fbioe.2016. 00087.

[43] Gu, Q., Yang, H., & Shi, Q. (2017). Macrophages and bone inflammation. Journal of Orthopaedic Translation, 10, 86–93. https://doi.org/10.1016/j.jot.2017.05.002.

[44] Lewiecki, E. M. (2014). Role of sclerostin in bone and cartilage and its potential as a therapeutic target in bone diseases. Therapeutic Advances in Musculoskeletal Disease, 6(2), 48–57. https://doi.org/10.1177/1759720X13510479.

[45] Prendergast, P. J., & Huiskes, R. (1996). Finite element analysis of fibrous tissue morphogenics - a study of the osteogenic index with a biphasic approach. Mechanics of Composite Materials, 32(2), 144–150.

[46] Prendergast, P.J, Huiskes, R., Soballe, K. (1997). Biophysical stimuli on cells during tissue differentiation at implant interfaces. Journal of Biomechanics, 30(6), 539–548. Retrieved from http:// www.sciencedirect.com/science/article/pii/S0021929096001406.

[47] Lang, T., LeBlanc, A., Evans, H., Lu, Y., Genant, H., & Yu, A. (2004). Cortical and trabecular bone mineral loss from the spine and hip in long-duration spaceflight. Journal of Bone and Mineral Research, 19(6), 1006–1012. https://doi.org/10.1359/JBMR. 040307.

[48] Vrana, N., Knopf-Marques, H., & Barthes, J. (2020). Biomaterials for organ and tissue regeneration: new technologies and future prospects. Woodhead Publishing Limited.

[49] Van der Meulen, M. C. H., & Huiskes, R. (2002). Why mechanobiology? A survey article. Journal of Biomechanics, 35(4), 401–414. https://doi.org/10.1016/S0021-9290(01)00184-1.

[50] Huang, C., & Ogawa, R. (2010). Mechanotransduction in bone repair and regeneration. FASEB Journal, 24(10), 3625–3632. https://doi.org/10.1096/fj.10-157370.

[51] Scheiner, S., Pivonka, P., & Hellmich, C. (2013). Coupling systems biology with multiscale mechanics, for computer simulations of bone remodeling. Computer Methods in Applied Mechanics and Engineering, 254, 181–196. https://doi.org/10.1016/j.cma. 2012.10.015.

[52] Huiskes, R., Rulmerman, R., Van Lenthe, G. H., & Janssen, J. D. (2000). Effects of mechanical forces on maintenance and adaptation of form in trabecular bone. Nature, 405(6787), 704–706. https://doi.org/10.1038/35015116.

[53] Simmons, C. A., Meguid, S. A., & Pilliar, R. M. (2001). Mechanical regulation of localized and appositional bone formation around bone-interfacing implants. Journal of Biomedical Materials Research. https://doi.org/10.1002/1097- 4636(200104)55:1<63::AID-JBM90>3.0.CO;2-V

[54] Titushkin, I., & Cho, M. (2007). Modulation of cellular mechanics during osteogenic differentiation of human Mesenchymal stem cells. Biophysical Journal, 93, 3693–3702. https://doi.org/10. 1016/j.jbiomech.2011.07.024.

[55] Shin, J. W., & Mooney, D. J. (2016). Improving stem cell therapeutics with Mechanobiology. Cell Stem Cell, 18(1), 16–19. https://doi.org/10.1016/j.stem.2015.12.007.

[56] Chaudhuri, O., Gu, L., Klumpers, D., Darnell, M., Bencherif, S. A., Weaver, J. C., Huebsch, N., Lee, H. P., Lippens, E., Duda, G. N., & Mooney, D. J. (2016). Hydrogels with tunable stress relax- ation regulate stem cell fate and activity. Nature Materials, 15(3), 326–334. https://doi.org/10.1038/nmat4489.

[57] Khetan, S., Guvendiren, M., Legant, W. R., Cohen, D. M., Chen, C. S., & Burdick, J. A. (2013). Degradation-mediated cellular traction directs stem cell fate in covalently crosslinked three-dimensional hydrogels. Nature Materials, 12(5), 458–465. https://doi.org/10.1038/nmat3586.

[58] Brady, R. T., O'Brien, F. J., & Hoey, D. A. (2015). Mechanically stimulated bone cells secrete paracrine factors that regulate osteoprogenitor recruitment, proliferation, and differentiation. Biochemical and Biophysical Research Communications, 459(1), 118–123. https://doi.org/10.1016/j.bbrc.2015.02.080.

[59] Stavenschi, E., Labour, M.-N., & Hoey, D. A. (2017). Oscillatory fluid flow induces the osteogenic lineage commitment of mesenchymal stem cells: The effect of shear stress magnitude, frequency, and duration. Journal of Biomechanics, 55, 99–106. https:// doi.org/10.1016/j.jbiomech.2017.02.002.

[60] Gurkan, U. A., & Akkus, O. (2008). The mechanical environment of bone marrow: A review. Annals of Biomedical Engineering, 36(12), 1978–1991. https://doi.org/10.1007/s10439-008-9577-x.

[61] Vining, K. H., & Mooney, D. J. (2017). Mechanical forces direct stem cell behaviour in development and regeneration. Nature Reviews Molecular Cell Biology, 18(12), 728–742. https://doi. org/10.1038/nrm.2017.108.

[62] Barui, A., Chowdhury, F., Pandit, A., & Datta, P. (2018). Rerouting mesenchymal stem cell trajectory towards epithelial lineage by engineering cellular niche. Biomaterials, 156, 28–44. https://doi.org/10.1016/j.biomaterials.2017.11.036.

[63] Chen, Y., Ju, L., Rushdi, M., Ge, C., & Zhu, C. (2017). Receptor-mediated cell mechanosensing. Molecular Biology of the Cell, 28(23), 3134–3155. https://doi.org/10.1091/mbc.e17-04-0228.

[64] Stoltz, J.-F., Magdalou, J., George, D., Chen, Y., Li, Y., De Isla, N., ... Remond, Y. (2018). Influence of mechanical forces on bone: Introduction to mechanobiology and mechanical

adaptation concept. Journal of Cellular Immunotherapy, (1880). https://doi.org/10.1016/j.jocit.2018.09.003.

[65] Dupont, S., Morsut, L., Aragona, M., Enzo, E., Giulitti, S., Cordenonsi, M., Zanconato, F., le Digabel, J., Forcato, M., Bicciato, S., Elvassore, N., & Piccolo, S. (2011). Role of YAP/ TAZ in mechanotransduction. Nature, 474(7350), 179–184. https://doi.org/10.1038/nature10137.

[66] Engler, A. J., Sen, S., Sweeney, H. L., & Discher, D. E. (2006). Matrix elasticity directs stem cell lineage specification. Cell, 126(4), 677–689. https://doi.org/10.1016/j.cell.2006.06.044.

[67] Chen, C. S., Alonso, J. L., Ostuni, E., Whitesides, G. M., & Ingber, D. E. (2003). Cell shape provides global control of focal adhesion assembly. Biochemical and Biophysical Research Communications, 307(2), 355–361. https://doi.org/10.1016/ S0006-291X(03)01165-3.

[68] Kilian, K. A., Bugarija, B., Lahn, B. T., & Mrksich, M. (2010). Geometric cues for directing the differentiation of mesenchymal stem cells. Proceedings of the National Academy of Sciences, 107(11), 4872–4877. https://doi.org/10.1073/pnas.0903269107.

[69] McBeath, R., Pirone, D. M., Nelson, C. M., Bhadriraju, K., & Chen, C. S. (2004). Cell shape, cytoskeletal tension, and RhoA regulate stem cell lineage commitment. Developmental Cell, 6(4), 483–495. https://doi.org/10.1016/S1534-5807(04)00075-9.

[70] Jaalouk, D. E., & Lammerding, J. (2009). Mechanotransduction gone awry. Nature Reviews Molecular Cell Biology, 10(1), 63–73. https://doi.org/10.1038/nrm2597.

[71] Wang, N., Tytell, J. D., & Ingber, D. E. (2009). Mechanotransduction at a distance: Mechanically coupling the extracellular matrix with the nucleus. Nature Reviews Molecular Cell Biology, 10(January), 75–82. https://doi.org/10. 1038/nrm2594.

[72] Wang, N., & Suo, Z. (2005). Long-distance propagation of forces in a cell. Biochemical and Biophysical Research Communications, 328(4), 1133–1138. https://doi.org/10.1016/j.bbrc.2005.01.070.

[73] Ingber, D. E. (2006). Cellular mechanotransduction: Putting all the pieces together again. The FASEB Journal, 20(7), 811–827. https://doi.org/10.1096/fj.05-5424rev.

[74] Jansen, K. A., Donato, D. M., Balcioglu, H. E., Schmidt, T., Danen, E. H. J., & Koenderink, G. H. (2015). A guide to mechanobiology: Where biology and physics meet. Biochimica et Biophysica

Acta - Molecular Cell Research, 1853(11), 3043– 3052. https://doi.org/10.1016/j.bbamcr.2015.05.007.

[75] Wasik, A. A., & Schiller, H. B. (2017). Functional proteomics of cellular mechanosensing mechanisms. Seminars in Cell and Developmental Biology, 71, 118–128. https://doi.org/10.1016/j. semcdb.2017.06.019.

[76] Weng, S., Shao, Y., Chen, W., & Fu, J. (2016). Mechanosensitive subcellular rheostasis drives emergent single-cell mechanical homeostasis. Nature Materials, 15(9), 961–967. https://doi.org/10. 1038/nmat4654.

[77] Marycz, K., Sobierajska, P., Roecken, M., Kornicka-Garbowska, K., K pska, M., Idczak, R., ... Wiglusz, R. J. (2020). Iron oxides nanoparticles (IOs) exposed to magnetic field promote expression of osteogenic markers in osteoblasts through integrin alpha-3 (INTa-3) activation, inhibits osteoclasts activity and exerts anti-inflammatory action. Journal of Nanobiotechnology, 18(1), 1–24. https://doi.org/10.1186/s12951-020-00590-w.

[78] Marycz, K., Alicka, M., Kornicka-Garbowska, K., Polnar, J., Lis-Bartos, A., Wiglusz, R. J., Roecken, M., & Nedelec, J. M. (2020). Promotion through external magnetic field of osteogenic differentiation potential in adipose-derived mesenchymal stem cells: Design of polyurethane/poly(lactic) acid sponges doped with iron oxide nanoparticles. Journal of Biomedical Materials Research - Part B Applied Biomaterials, 108(4), 1398–1411. https://doi.org/ 10.1002/jbm.b.34488.

[79] Schiller, H. B., & Fässler, R. (2013). Mechanosensitivity and compositional dynamics of cell-matrix adhesions. EMBO Reports, 14(6), 509–519. https://doi.org/10.1038/embor.2013.49.

[80] Bongiorno, T., Kazlow, J., Mezencev, R., Griffiths, S., Olivares- Navarrete, R., McDonald, J. F., Schwartz, Z., Boyan, B. D., McDevitt, T. C., & Sulchek, T. (2014). Mechanical stiffness as an improved single-cell indicator of osteoblastic human mesenchymal stem cell differentiation. Journal of Biomechanics, 47(9), 2197–2204. https://doi.org/10.1016/j.jbiomech.2013.11.017.

[81] Ledwon, J. K., Galat, Y., Topczewska, J. M., & Gosain, A. K. (2018). Osteogenic differentiation of MSCs A model study of the postnatal progressive Crouzon syndrome. Plastic and Reconstructive Surgery - Global Open, 6(4S), 116.

[82] Moloudi, R., Oh, S., Yang, C., Teo, K. L., Lam, A. T. L., Warkiani, M. E., & Naing, M. W. (2018). Inertial-based filtration method for removal of microcarriers from Mesenchymal stem cell suspensions. Scientific Reports, 8(1), 1–10. https://doi.org/10. 1038/s41598-018-31019-y.

[83] Yourek, G., Hussain, M. A., & Mao, J. J. (2007). Cytoskeletal changes of mesenchymal stem cells during differentiation. ASAIO Journal, 53(2), 219–228. https://doi.org/10.1097/MAT. 0b013e31802deb2d.

[84] Titushkin, I. A., & Cho, M. R. (2009). Controlling cellular biomechanics of human mesenchymal stem cells. Proceedings of the 31st Annual International Conference of the IEEE Engineering in Medicine and Biology Society: Engineering the Future of Biomedicine, EMBC 2009, 60607, 2090–2093. https://doi.org/ 10.1109/IEMBS.2009.5333949.

[85] Uto, K., Tsui, J. H., Deforest, C. A., & Kim, D. H. (2017). Dynamically tunable cell culture platforms for tissue engineering and Mechanobiology. Progress in Polymer Science, 65, 53–82. https://doi.org/10.1016/j.progpolymsci.2016.09.004.

[86] Jagodzinski, M., Drescher, M., Zeichen, J., Hankemeier, S., Krettek, C., Bosch, U., ... Evans, C. (2004). Effects of cyclic longitudinal mechanical strain and dexamethasone on osteogenic differentiation of human bone marrow stromal cells. European Cells and Materials, 7, 35–41. https://doi.org/10.22203/eCM. v007a04.

[87] Sumanasinghe, R. D., Bernacki, S. H., & Loboa, E. G. (2006). Osteogenic differentiation of human Mesenchymal stem cells in collagen matrices: Effect of uniaxial cyclic tensile strain on bone morphogenetic protein (BMP-2) mRNA expression. Tissue Engineering, 12(12), 3459–3465. https://doi.org/10.1089/ten. 2006.12.3459.

[88] Simmons, C. A., Matlis, S., Thornton, A. J., Chen, S., Wang, Y., & Mooney, D. J. (2003). Cyclic strain enhances matrix mineralization by adult human mesenchymal stem cells via the extracellular signal-regulated kinase (ERK1/2) signaling pathway. Journal of Biomechanics, 36, 1087–1096. https://doi.org/10. 1016/S0021-9290(03)00110-6.

[89] Ravichandran, A., Lim, J., Chong, M. S. K., Wen, F., Liu, Y., Pillay, Y. T., Chan, J. K. Y., & Teoh, S. H. (2016). In vitro cyclic compressive loads potentiate early osteogenic events in engineered bone tissue. Journal of Biomedical Materials Research - Part B Applied Biomaterials, 105(8), 2366–2375. https://doi.org/10.1002/jbm.b.33772.

[90] Sitticholechaiwut, A., Edwards, J. H., Scutt, A. M., & Reilly, G. C. (2010). Short bouts of mechanical loading are as effective as dexamethasone at inducing matrix production by human bone marrow mesenchymal stem cells. European Cells and Materials, 20, 45– 57. https://doi.org/10.1111/j.1749-6632.1954.tb45891.x.

[91] Grellier, M., Bareille, R., & Bourget, C. (2009). Responsiveness of human bone marrow stromal cells to shear stress. Journal of Tissue Engineering and Regenerative Medicine, 3(March), 302– 309. https://doi.org/10.1002/term.

[92] Delaine-Smith, R. M., MacNeil, S., & Reilly, G. C. (2012). Matrix production and collagen structure are enhanced in two types of osteogenic progenitor cells by a simple fluid shear stress stimulus. European Cells and Materials, 24(0), 162–174.

[93] Yourek, G., McCormick, S. M., Mao, J. J., & Reilly, G. C. (2010). Shear stress induces osteogenic differentiation of human mesenchymal stem cells. Regenerative Medicine, 5(5), 713–724.

[94] Vangordon, S. B., Voronov, R. S., Blue, T. B., Shambaugh, R. L., Papavassiliou, D. V., & Sikavitsas, V. I. (2011). Effects of scaffold architecture on preosteoblastic cultures under continuous fluid shear. Industrial and Engineering Chemistry Research, 50(2), 620–629. https://doi.org/10.1021/ie902041v.

[95] Sonam, S., Sathe, S. R., Yim, E. K. F., Sheetz, M. P., & Lim, C. T. (2016). Cell contractility arising from topography and shear flow determines human mesenchymal stem cell fate. Scientific Reports, 6, 1–12. https://doi.org/10.1038/srep20415.

[96] Wittkowske, C., Reilly, G. C., Lacroix, D., & Perrault, C. M. (2016). In vitro bone cell models: impact of fluid shear stress on bone formation. Frontiers in Bioengineering and Biotechnology, 4, 1–22. https://doi.org/10.3389/fbioe.2016.00087.

[97] Huiskes, R., & Ito, K. (2008). A mechano-regulatory bone-healing model incorporating cell-phenotype specific activity. Journal of Theoretical Biology, 252(2), 230–246. https://doi.org/10.1016/j. jtbi.2008.01.030.

[98] Gasik, M. (2017). Understanding biomaterial-tissue interface quality: combined in vitro evaluation. Science and Technology of Advanced Materials, 18(1), 550–562. https://doi.org/10.1080/ 14686996.2017.1348872.

[99] Van C., M., & Huiskes, R. (Eds.). (2005). Basic orthopaedic biomechanics & mechano-biology. Lippincott Williams & Wilkins.

[100] Sikavitsas, V. I., Bancroft, G. N., Holtorf, H. L., Jansen, J. A., & Mikos, A. G. (2003). Mineralized matrix deposition by marrow stromal osteoblasts in 3D perfusion culture increases with increas- ing fluid shear forces. Proceedings of the National Academy of Sciences, 100(25), 14683–14688.

[101] Bancroft, G. N., Sikavitsas, V. I., Van Den Dolder, J., Sheffield, T. L., Ambrose, C. G., Jansen, J. A., & Mikos, A. G. (2002). Fluid flow increases mineralized matrix deposition in 3D perfusion culture of marrow stromal osteoblasts in a dose-dependent manner. Proceedings of the National Academy of Sciences, 99(20), 12600– 12605.

[102] Tseng, P. C., Young, T. H., Wang, T. M., Peng, H. W., Hou, S. M., & Yen, M. L. (2012). Spontaneous osteogenesis of MSCs cultured on 3D microcarriers through alteration of cytoskeletal tension. Biomaterials, 33(2), 556–564. https://doi.org/10.1016/j. biomaterials.2011.09.090.

[103] Sjöström, T., Brydone, A. S., Meek, R. D., Dalby, M. J., Su, B., & Mcnamara, L. E. (2013). Titanium nanofeaturing for enhanced bioactivity of implanted orthopedic and dental devices. Nanomedicine, 8(1), 89–104. https://doi.org/10.2217/nnm.12. 177.

[104] Turner, L. A., Dalby, J., & M. (2014). Nanotopography-potential relevance in the stem cell niche. Biomaterials Science, 2(11), 1574–1594. https://doi.org/10.1039/c4bm00155a.

[105] Martínez, E., Engel, E., Planell, J. A., & Samitier, J. (2009). Effects of artificial micro- and nano-structured surfaces on cell behaviour. Annals of Anatomy, 191(1), 126–135. https://doi.org/10.1016/j.aanat.2008.05.006.

[106] Abagnale, G., Steger, M., Nguyen, V. H., Hersch, N., Sechi, A., Joussen, S., Denecke, B., Merkel, R., Hoffmann, B., Dreser, A., Schnakenberg, U., Gillner, A., & Wagner, W. (2015). Surface topography enhances differentiation of mesenchymal stem cells towards osteogenic and adipogenic lineages. Biomaterials, 61, 316–326. https://doi.org/10.1016/j.biomaterials.2015.05.030.

[107] Fiedler, J., Özdemir, B., Bartholomä, J., Plettl, A., Brenner, R. E., & Ziemann, P. (2013). The effect of substrate surface nanotopography on the behavior of multipotent mesenchymal stromal cells and osteoblasts. Biomaterials, 34(35), 8851–8859. https://doi.org/10.1016/j.biomaterials.2013.08.010.

[108] McNamara, L. E., Sjöström, T., Burgess, K. E. V., Kim, J. J. W., Liu, E., Gordonov, S., Moghe, P. V., Meek, R. M. D., Oreffo, R. O. C., Su, B., & Dalby, M. J. (2011). Skeletal stem cell physiology on functionally distinct titania nanotopographies. Biomaterials, 32(30), 7403–7410. https://doi.org/10.1016/j.biomaterials.2011. 06.063.

[109] Sjöström, T., Dalby, M. J., Hart, A., Tare, R., Oreffo, R. O. C., & Su, B. (2009). Fabrication of pillar-like titania nanostructures on titanium and their interactions with human skeletal stem cells. Acta Biomaterialia, 5(5), 1433–1441. https://doi.org/10.1016/j.actbio. 2009.01.007.

[110] Sjöström, T., Mcnamara, L. E., Meek, R. M. D., Dalby, M. J., & Su, B. (2013). 2D and 3D nanopatterning of titanium for enhancing osteoinduction of stem cells at implant surfaces. Advanced Healthcare Materials, 2(9), 1285–1293. https://doi.org/10.1002/ adhm.201200353.

[111] Oh, S., Brammer, K. S., Li, Y. S. J., Teng, D., Engler, A. J., Chien, S., & Jin, S. (2009). Stem cell fate dictated solely by altered nano-tube dimension. Proceedings of the National Academy of Sciences of the United States of America, 106(7), 2130–2135. https://doi. org/10.1073/pnas.0903663106.

[112] de Peppo, G. M., Agheli, H., Karlsson, C., Ekström, K., Brisby, H., Lennerås, M., ... Petronis, S. (2014). Osteogenic response of human mesenchymal stem cells to well-defined nanoscale topography in vitro. International Journal of Nanomedicine, 9(1), 2499–2515. https://doi.org/10.2147/IJN.S58805.

[113] Lavenus, S., Berreur, M., Trichet, V., Pilet, P., Louarn, G., & Layrolle, P. (2011). Adhesion and osteogenic differentiation of human mesenchymal stem cells on titanium nanopores. European Cells and Materials, 22, 84–96. https://doi.org/10. 22203/eCM.v022a07.

[114] Fu, J., Wang, Y. K., Yang, M. T., Desai, R. A., Yu, X., Liu, Z., & Chen, C. S. (2010). Mechanical regulation of cell function with geometrically modulated elastomeric substrates. Nature Methods, 7(9), 733–736. https://doi.org/10.1038/nmeth.1487.

[115] Dalby, M. J., McCloy, D., Robertson, M., Agheli, H., Sutherland, D., Affrossman, S., & Oreffo, R. O. C. (2006). Osteoprogenitor response to semi-ordered and random nanotopographies. Biomaterials, 27(15), 2980–2987. https://doi.org/10.1016/j. biomaterials.2006.01.010.

[116] Dalby, M. J., Gadegaard, N., Tare, R., Andar, A., Riehle, M. O., Herzyk, P., Wilkinson, C. D. W., & Oreffo, R. O. C. (2007). The control of human mesenchymal cell differentiation using nano-

scale symmetry and disorder. Nature Materials, 6(12), 997– 1003. https://doi.org/10.1038/nmat2013.

[117] Tsimbouri, P. M., Murawski, K., Hamilton, G., Herzyk, P., Oreffo, R. O. C., Gadegaard, N., & Dalby, M. J. (2013). A genomics approach in determining nanotopographical effects on MSC phenotype. Biomaterials, 34(9), 2177–2184. https://doi.org/10. 1016/j.biomaterials.2012.12.019.

[118] Wang, J. R., Ahmed, S. F., Gadegaard, N., Meek, R. M. D., Dalby, M. J., & Yarwood, S. J. (2014). Nanotopology potentiates growth hormone signalling and osteogenesis of mesenchymal stem cells. Growth Hormone and IGF Research, 24(6), 245–250. https://doi.org/10.1016/j.ghir.2014.10.003.

[119] Yang, J., McNamara, L. E., Gadegaard, N., Alakpa, E. V., Burgess, K. V., Meek, R. M. D., & Dalby, M. J. (2014). Nanotopographical induction of osteogenesis through adhesion, bone morphogenic protein cosignaling, and regulation of microRNAs. ACS Nano, 8, 9941–9953. https://doi.org/10.1021/ nn504767g.

[120] Aragona, M., Panciera, T., Manfrin, A., Giulitti, S., Michielin, F., & Elvassore, N. (2013). A mechanical checkpoint controls multi-cellular growth through YAP / TAZ regulation by actin-processing factors. Cell, 154(5), 1047–1059. https://doi.org/10. 1016/j.cell.2013.07.042.

[121] Halder, G., Dupont, S., & Piccolo, S. (2012). Transduction of mechanical and cytoskeletal cues by TAP and TAZ. Nature review molecular cell biology, 13, 591–600. https://doi.org/10.1038/ nrm3416.

[122] De Boer, J., & van Blitterswijk, C. A. (2013). Materiomics: High-throughput screening of biomaterial properties. Cambridge: Cambridge University Press.

[123] Biggs, M. J. P., Richards, R. G., & Dalby, M. J. (2010). Nanotopographical modification: A regulator of cellular function through focal adhesions. Nanomedicine: Nanotechnology, Biology, and Medicine, 6(5), 619–633. https://doi.org/10.1016/j. nano.2010.01.009.

[124] Guo, W. H., Frey, M. T., Burnham, N. A., & Wang, Y. L. (2006). Substrate rigidity regulates the formation and maintenance of tissues. Biophysical Journal, 90(6), 2213–2220. https://doi.org/10. 1529/biophysj.105.070144.

[125] Park, J. S., Chu, J. S., Tsou, A. D., Diop, R., Tang, Z., Wang, A., & Li, S. (2011). The effect of matrix stiffness on the differentiation of mesenchymal stem cells in response to TGF-b. Biomaterials, 32(16), 3921–3930. https://doi.org/10.1016/j.biomaterials.2011. 02.019.

[126] Lv, H., Li, L., Su, M., Zhang, Y., Chen, L., Rong, Y., & Li, Y. (2015). Mechanism of regulation of stem cell differentiation by matrix stiffness. Stem Cell Research and Therapy, 6(103), 1–11. https://doi.org/10.1186/s13287-015-0083-4.

[127] Verbruggen, S. W., Vaughan, T. J., & McNamara, L. M. (2014). Fluid flow in the osteocyte mechanical environment: A fluid-structure interaction approach. Biomechanics and Modeling in Mechanobiology, 13(1), 85–97. https://doi.org/10.1007/s10237- 013-0487-y.

[128] Lord, J. D., & Morrel, R. (2006). Elastic modulus measurement. In Measurement Good Practice Guide No. 98 (p. 100). UK: NPL Teddington.

[129] Pedersen, D. R., Brown, T. D., & Brand, R. A. (1991). Interstitial bone stress distributions accompanying ingrowth of a screen-like prosthesis anchorage layer. Journal of Biomechanics, 24(12), 1131–1142. https://doi.org/10.1016/0021-9290(91)90005-8.

[130] Bayon, Y., Bohner, M., Eglin, D., Procter, P., Richards, R. G., Weber, J., & Zeugolis, D. I. (2016). Innovating in the medical device industry – Challenges & opportunities ESB 2015 translational research symposium. Journal of Materials Science: Materials in Medicine, 27(9). https://doi.org/10.1007/s10856-016-5759-5.

[131] Maurel, W., Thalmann, D., Wu, Y., & Thalmann, N. M. (1998). Biomechanical models for soft tissue simulation. Berlin: Springer.

[132] Frost, H. M. (2004). A 2003 update of bone physiology and Wolff s law for clinicians. Angle Orthodontist, 74(1), 3–15. https://doi.org/10.1043/0003-3219(2004)074<0003:AUOBPA>2.0.CO;2.

[133] Gasik, M., & Bilotsky, Y. (2019). In vitro method for measurement and model-free evaluation of time-invariant biomaterials functions. US.

[134] Nordin, M., & Frankel, V. H. (Eds.). (2012). Basic biomechanics of the musculoskeletal system. Philadelphia: Lippincott Williams & Wilkins.

[135] Huiskes, R., Weinans, H., & van Rietbergen, B. (1992). The relationship between stress shielding and bone resorption around total hip stems and the effects of flexible materials. Clinical Orthopaedics and Related Research, 274, 124–134.

[136] Gasik, M. (2017). In vitro test method for implant materials. US.

[137] An, Y. H., & Draughn, R. A. (Eds.). (1999). Mechanical testing of bone and the bone–implant Interface. Boca Raton: CRC press.

[138] Beer, F. P., Johnston, J. E. R., Dewolf, J. T., & Mazurek, D. F. (2012). Mechanics of materials (6th ed.). New York: McGraw-Hill.

[139] Kolken, H. M. A., Janbaz, S., Leeflang, S. M. A., Lietaert, K., Weinans, H. H., & Zadpoor, A. A. (2018). Rationally designed meta-implants: A combination of auxetic and conventional meta-biomaterials. Materials Horizons, 5(1), 28–35. https://doi.org/10. 1039/c7mh00699c.

[140] Silva, M., Shepherd, E. F., Jackson, W. O., Dorey, F. J., & Schmalzried, T. P. (2002). Average patient walking activity approaches 2 million cycles per year: Pedometers under-record walking activity. Journal of Arthroplasty, 17(6), 693–697. https://doi.org/10.1054/arth.2002.32699.

[141] Verdonschot, N., & Huiskes, R. (1996). Mechanical effects of stem cement interface characteristics in total hip replacement. Clinical Orthopaedics and Related Research, 329, 326–336.https://doi.org/10.1097/00003086-199608000-00040.

[142] Haleem, A., & Javaid, M. (2018). Role of CT and MRI in the design and development of orthopaedic model using additive manufacturing. Journal of Clinical Orthopaedics and Trauma, 9(3), 213–217. https://doi.org/10.1016/j.jcot.2018.07.002.

[143] Stojkovic, M., Trajanovic, M., & Vitkovic, N. (2019). Personalized orthopedic surgery design challenge: Human bone redesign method. Procedia CIRP., 84, 701–706. https://doi.org/10.1016/j.procir.2019.04.170.

# CHAPTER 3

## SURFACE CHARACTERIZATION OF TITANIUM-BASED SUBSTRATES FOR ORTHOPAEDIC APPLICATIONS

Published in Materials Characterization, 2021, 17, 111161

https://doi.org/10.1016/j.matchar.2021.111161

F. Melo-Fonseca[a, *], M. Gasik[b, c], S. Madeira[a], F. S. Silva[a], G. Miranda[d]

[a]Center for MicroElectroMechanical Systems (CMEMS-UMinho), University of Minho, Campus de Azurém, 4800-058 Guimarães – Portugal

[b]School of Chemical Engineering, Aalto University Foundation, Espoo, Finland

[c]Seqvera Ltd., Helsinki, Finland

F. S. Silva and G. Miranda share co-last authorship.

**Abstract**

Orthopaedic implants for load-bearing applications are usually composed of titanium-based materials. Aiming to propose a strategy able to improve the bone-implant interface on these implants, commercially pure titanium and Ti6Al4V alloy were subjected to anodic oxidation, hydrothermal treatment and to anodic oxidation followed by hydrothermal treatment and the produced oxide film was investigated. In addition, different mechanical (as-received vs mechanical polished) and chemical pre-treatments (alcohol cleaning vs acidic pre-treatment) were studied. No significant differences were found between the chemical pre-treatments, whereas upon different surface treatments the $TiO_2$ layer presented different characteristics, namely regarding its crystallinity, roughness, thickness and wettability. The hydrothermal treatment followed by immersion for 24 hrs in 5XPBS was effective in creating a potentially bioactive oxide film, given the presence of anatase and rutile phases, and a hydrophilic layer for both Ti materials. Ti grade 2 subjected to alcohol cleaning and hydrothermal treatment resulted in a surface roughness of 226.7 ± 3.1 nm and water contact angle of 67.2 ± 8.7°, whereas for the Ti grade 5 subjected to the same surface treatment, Ra was equal to 20.4 ± 1.7 nm and the water contact angle to 83.5 ± 4.7°. In this context, the hydrothermal treatment is proposed as a simple treatment capable of improving the characteristics of the implant surface, thereby promoting osteoconductivity.

**Keywords:** Commercially pure titanium; Ti6Al4V; Pre-treatments; Surface modification; Anodic oxidation; Hydrothermal treatment

## 3.1. Introduction

Titanium (Ti) and its alloys are widely used in the orthopaedic field due to their biocompatibility, high strength and corrosion resistance, the latter arising from the spontaneous formation of a passive oxide layer upon exposure to ambient atmosphere [1,2]. Compared to other metallic implant materials, titanium and its alloys have become the preferential choice and some orthopaedic applications include fracture fixation, total hip and total knee arthroplasties [3,4]. However, insufficient bioactivity of metallic materials impairs the bonding with bone, compromising osseointegration at an early stage. The implant-bone interface may be improved by regulating some surface properties of the biomaterials, including surface chemical composition, surface energy, roughness and topography, which have been shown to influence the behaviour of bone cells [5,6]. As a consequence, different surface treatment strategies have been investigated to improve cell-surface interactions and enhance initial bone bonding [7,8].

When implanted in the host site, numerous proteins of the surrounding extracellular matrix (ECM) are adsorbed on the orthopaedic implant surface, which tends to develop a "conditioning film" responsible for regulating cellular response [9]. This initial interaction depends on the biomaterial surface chemistry and wettability which play a critical role on protein adsorption and on the attachment of mesenchymal stem cells (MSC) [10–12]. A high surface energy increases its wettability and hydrophilic surfaces are able to adsorb proteins in a more flexible conformation, improving the adhesion and spreading of cells [12–15]. The interlocking between bone and implant may be enhanced by increasing the implant contact surface area and thus by controlling the topography. Surface topography is dependent on the surface orientation and roughness [16] and is characterized by a succession of peaks and valleys [6]. Some in vivo and clinical studies suggest that bone integration is enhanced using implants with a moderate surface roughness (amplitude of the mean height deviation (Sa)) of 1–2 μm and so, micro-topography appears to promote a stronger osseointegration [16,17]. The aforementioned observations demonstrate that surface factors of Ti-based implants need to be carefully considered, including surface energy, wettability and topography.

The formation of a titanium dioxide ($TiO_2$) layer is essential for improving osseointegration however, in its native form, it presents poor tribological behaviour, as shown by a low sliding wear resistance [2,18–20], exposing the nascent surface to corrosive attack. In this sense, numerous techniques have been applied to control this layer formation and characteristics. The naturally formed oxidized layer has a thickness of 3–7 nm and is amorphous [21]. A thicker $TiO_2$, up to a thickness of 150 nm, was reported to enhance wettability, micro-roughness and crystallinity, promoting bone cells response [2,21] and consequently, influencing bone cellular interaction due to bioactivity improvement. In addition, a thicker oxide titanium layer improves the mechanical properties of Ti implants, as it protects the nascent surface and prevents possible release of metallic wear particles. Surface treatments also alter the titanium oxide crystallinity, particularly, in the form of anatase (tetragonal), rutile (tetragonal) and brookite (orthorhombic) crystal phases [22]. Anatase film may interact with calcium and phosphate ions from the physiological environment, whereas rutile film is associated with basic and acidic hydroxyl groups and also with surface energy [21]. These crystal phases were reported to improve the osteogenic activity of titanium [21–23]. In addition to bioactivity, new studies have been conducted to confer antibacterial properties to titanium surfaces and thus prevent prosthetic infections [24]. Some strategies aiming to produce controllable nanostructured surfaces (e.g., nanoporous or nanotubular) with antibacterial

properties include the growth of an oxide layer ($TiO_2$) and its doping with antibacterial agents [25] or the deposition of a coating, either $TiO_2$ or hydroxyapatite coating, doped by antibacterial agents [26,27].

Some of the surface modification techniques found in literature include sandblasting [28], acid-etching [28], plasma-spraying [29–31] and anodization [32–34]. Prior to the surface treatment, Ti-based samples may be subjected to pre-treatments, such as mechanical polishing, simply rinsing with water and drying or ultrasonic treatments with acidic solutions followed by ultrasonic rinsing with acetone. Titanium is very sensitive to surface preparation methods as they form a thin oxide layer with a potential in the active-passive region [35–37]. One group evaluated several cleaning methods of titanium surfaces using sodium peroxydisulfate ($Na_2S2O_8$), sulfuric acid ($H_2SO_4$) and hydrochloric acid (HCl), and concluded that the ultrasonic treatment with HCl followed by ultrasonic rinsing with acetone could effectively remove surface contaminants [38]. Anodic oxidation is an economic and versatile technique able to create interesting nanotopography features and also to form a crystalline titanium dioxide layer, particularly anatase [33]. This oxide film presents variable thickness, colour and morphology at different voltages [32,33,35,39,40] and can incorporate chemical elements from the electrolyte [41]. However, in addition to the numerous different conditions found in literature including the choice of pre-treatment, electrolyte chemical composition and concentration, applied voltage and anodizing time, this method is not easily replicated as many variables have to be carefully controllable. On the contrary, hydrothermal processes exhibit a simpler but yet effective process to create a bioactive surface on Ti implants [42]. Some aqueous solutions used for this treatment include sodium tripolyphosphate (STPP) and calcium hydroxide ($Ca(OH)_2$) [43,44], NaOH [45], calcium phosphate (Ca–P) solution [46], or simply distilled water [42,47,48].

Given the diversity of methodologies discussed in the literature, this study aims to compare specific surface treatments and investigate whether a simpler treatment might be feasible as it leads to similar results to more complex treatments, which will indeed result in numerous competitive advantages. In this sense, Ti-based materials were subjected to different surface modification techniques and the osseointegration potential of the formed $TiO_2$ layer was assessed by surface characterization techniques.

## 3.2. Materials and methods

Commercially pure titanium (Ti grade 2) and Ti6Al4V alloy (Ti grade 5) plates (ASTM B265) with a thickness of 0.5 mm were purchased from Titanium Products (United Kingdom) and cut into plates with dimensions of 10 × 11.25 mm. The chemical composition and mechanical properties of both Ti-based materials are summarized in Table 3.1 and Table 3.2, respectively.

Table 3.1 - Chemical composition of Ti grade 2 and Ti grade 5 provided by the manufacturer.

| **Material** | **Chemical composition (%, max)** | | | | | | | | |
|---|---|---|---|---|---|---|---|---|---|
| | **N** | **C** | **H** | **Fe** | **O** | **Al** | **V** | **Ti** | **Others** |
| Ti grade 2 | 0.03 | 0.1 | 0.015 | 0.3 | 0.25 | - | - | Matrix | 0.5 |
| Ti grade 5 | 0.05 | 0.1 | 0.015 | 0.4 | 0.2 | 5.5-6.75 | 3.5-4.5 | Matrix | 0.5 |

Table 3.2 - Comparison of tensile strength, yield strength and elastic modulus of both titanium grades.

| **Material** | **Ultimate tensile strength (MPa)** | **Yield strength (MPa)** | **Elongation (%)** | **Elastic modulus (GPa)** |
|---|---|---|---|---|
| Ti grade 2 | 345[a] | 275-450[a,+] | 20[a,+] | 103-115[b,·] |
| Ti grade 5 | 895[a,+] | 275-450[a,+] | 10[a,+] | 114-120[b,·] |

[a] according to the manufacturer; ·

[b] according to [4,49]

The Ti grade 2 and grade 5 plates were used to evaluate surface properties after being exposed to: anodization, hydrothermal treatment and the combination of both surface modification techniques (anodization followed by hydrothermal treatment). Previous polishing an alcohol cleaning was also performed, as seen in the flowchart of Fig. 3.1, that describes the procedure followed to prepare the different types of specimens tested in this work.

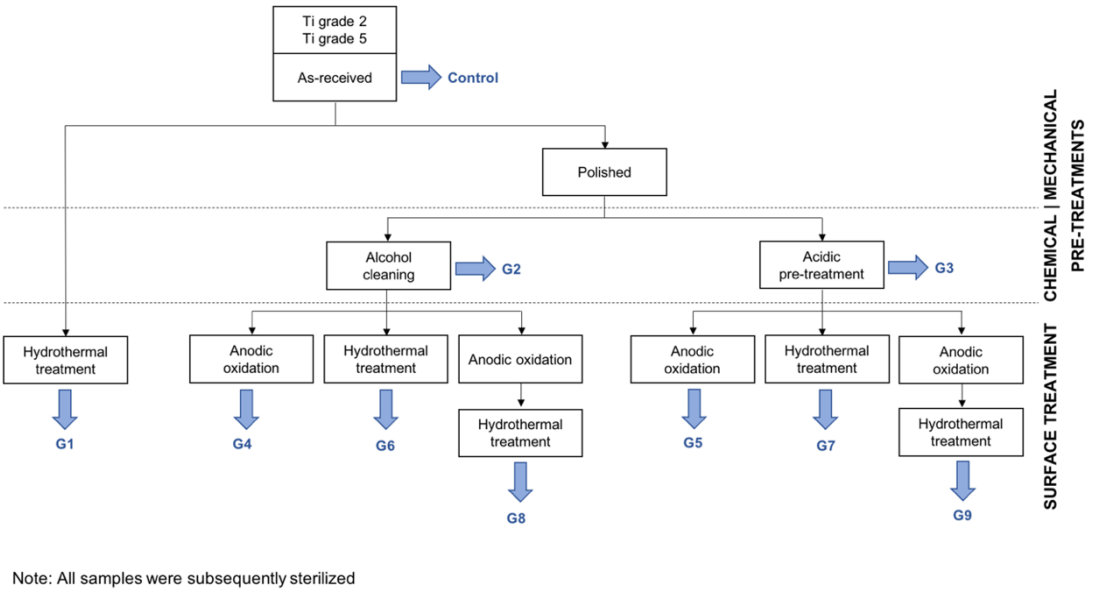



Figure 3.1 - Flowchart of the methodology followed in the present work.

### 3.2.1. Mechanical and chemical pre-treatments of Ti-based substrates

Samples with no surface modification were used as control, preserving the received surfaces, and those with no mechanical and chemical pre-treatments as G1. The specimens for the remaining groups were mechanically polished with SiC sandpapers (P320 to P4000) and finally with a cloth with diamond-suspension to achieve a mirror finishing. Then, they were cleaned either with isopropyl alcohol (2-Propanol, Labsolve, Portugal) and dried in air (alcohol cleaning) (G2) or with a pre-treatment of 10 M HCl (Hydrochloric acid, ThermoFisher Scientific, USA) for 30 min followed by ultrasonic rinsing with acetone (BCHEM, LaborSpirit, Portugal) for 30 min and dried in air (acidic treatment) (G3). After these pre-treatments, the following surface treatments were performed.

### 3.2.2. Anodic oxidation

After pre-treatments, Ti substrates were used for anodizing process. An in-house developed apparatus was used to fix the Ti sample (working electrode) and the graphite rod (counter electrode), assuring a distance between both electrodes of 58 mm. This two-electrodes system was connected to a DC power supply (Agilent Technologies N5751A), applying a constant voltage of 120 V for 1 min. Both electrodes were immersed in 0.4 M $H_3PO_4$ (Phosphoric acid, HoneyWell Fluka, USA), continuously stirred with a magnetic bar at room temperature. The anodic oxidation parameters were selected based on the results discussed in the literature [35,40,50,51]. At the end, the surfaces were gently rinsed with distilled water and dried in air. Anodized samples

previously subjected to alcohol cleaning and to acidic pre-treatments correspond to G4 and G5, respectively.

### 3.2.3. Hydrothermal process

The hydrothermal process was applied either on Ti samples with no pre-treatment (G1) and on mechanically polished samples followed by alcohol cleaning (G6) and acidic pre-treatment (G7). By this procedure, samples were immersed in a polytetrafluoroethylene (PTFE, Teflon) beaker with 80 mL of distilled water and placed inside a hydrothermal vessel. This metallic vessel was then placed inside a furnace (Termolab, Portugal) and the treatment occurred at a temperature of 180 °C for 180 min, as reported previously in the literature [42,47,48]. Afterwards, the beaker was removed from the furnace unit and cooled at room temperature.

### 3.2.4. Anodizing and hydrothermal process

The anodized Ti samples were afterwards hydrothermally treated in 80 mL of distilled water at 180 °C for 180 min using a furnace (Termolab, Portugal), either previously subjected to alcohol cleaning pre-treatment (G8) and to acidic pre-treatment (G9), as previously described in Sections 3.2.2 and 3.2.3.

Both surface modification techniques are represented in Fig. 3.2 and Table 3.3 summarizes the classification of samples group, including its description.

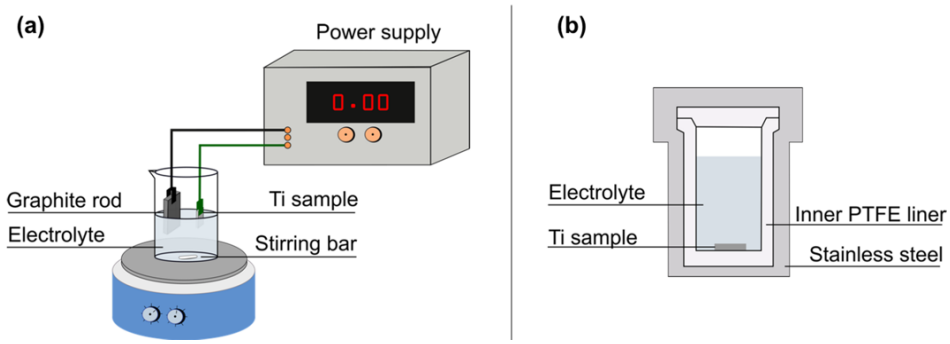



Figure 3.2 - The surface modification of Ti-based samples was achieved either by (a) anodizing using $H_3PO_4$ as electrolyte, (b) hydrothermal treatment with distilled water or by a combination of both techniques.

Table 3.3 - Samples group number and description.

| **Group #** | **Control** | **G1** | **G2** | **G3** | **G4** | **G5** | **G6** | **G7** | **G8** | **G9** |
|---|---|---|---|---|---|---|---|---|---|---|
| Pre-treatment | N | N | AC | AP | AC | AP | AC | AP | AC | AP |
| Surface treatment | N | Hydro | N | N | AO | AO | Hydro | Hydro | AO + Hydro | AO + Hydro |

N, None; AC, alcohol cleaning; AP, acidic pre-treatment; AO, Anodic oxidation; Hydro, Hydrothermal treatment

3.2.5. Sterilization and storage

All the tested samples were sterilized at 125 °C for 15 min using an automatic autoclave HYDRA 100 (Medical Trading S.R.L., Italy). Subsequently, samples were stored in 5 times concentrated phosphate buffered saline (5XPBS) for 24 hrs. The PBS solution was prepared from PBS tablets (A9201, PanReac AppliChem ITW Reagents, USA), which composition is 2.7 mM KCl, 140 mM NaCl and 10 mM phosphate, at a pH of 7.4 (25 °C).

3.2.6. Samples characterization

3.2.6.1. Morphology

The morphology of the produced samples was analysed by Scanning Electron Microscopy (SEM) using JSM-6010 LV (JEOL, Japan), including of the oxidized film.

3.2.6.2. Phase composition

X-rays diffraction (XRD) analyses were performed using a Bruker AXS D8 Discover equipment, with a CuKα radiation at a grazing angle of 1° and 2Θ between 20 and 80°. Crystalline phases were identified using the X'Pert HighScore program and afterwards, raw data was treated with Profex software (Nicola Döbelin, Switzerland). The Rietveld refinement was performed with the program BGMN using, among the favourite phases, anatase and rutile. The average percentage of anatase and rutile phases for treated samples was calculated using the Origin software.

3.2.6.3. Roughness and $TiO_2$ thickness

The roughness of each sample was obtained by Atomic Force Microscopy (AFM) using Bruker equipment at a scan rate of 0.7 Hz at room temperature in tapping in air mode. The cantilever (NCHV-A, Bruker) specifications are the following: thickness of 4 μm, length of 125 μm, width of 40 μm, resonant frequency of 320 kHz and spring constant of 42 N/m.

The thickness of the oxide films was also measured by AFM, in the same conditions. In order to measure the oxide film, all samples were first carefully polished to obtain a mirror finishing and then half of the surface was covered by DUPONTTM KAPTON® Polyimide films (DuPontTM), given its acid resistance and stability at high temperatures. The roughness and oxide film thickness differences between groups were obtained by performing one-way ANOVA with post hoc Bonferroni's multiple comparison test, using GraphPad Prism v8.2.0 from GraphPad Software (California, USA) for a statistical significance of $p < 0.05$. All images were treated using the NanoScope Analysis software by Veeco Instruments Inc. and Gwyddion software, whereas the Origin software was used to calculate of the oxide film thickness using the "Statistics Gadget" (addtool_curve_stats X-Function) tool.

#### 3.2.6.4. Wettability

The contact angle system OCA 15 plus (Dataphysics) was used to measure the angle formed by 5 μL droplet of distilled water at a dosing rate of 1 μL/s on samples after sterilization and after 24 hrs immersed in 5XPBS. Five droplets were measured for each group, at room temperature under ambient conditions, and the average was taken from these results. Wettability differences between two measures (0 h, 24 hrs) for each sample were assessed by performing a two-way ANOVA with post hoc Bonferroni's multiple comparison test. Moreover, in order to investigate wettability differences between groups, one-way ANOVA with post hoc Bonferroni's multiple comparison test was performed. Once again, statistical significance was defined for $p < 0.05$ and GraphPad Prism v8.2.0 from GraphPad Software (California, USA) was used for performing statistical analysis.

## 3.3. Results and discussion

### 3.3.1. Morphology

Ti grade 2 and Ti grade 5 samples were either non-polished (control and G1) or polished until obtaining a mirror finishing. Different groups were formed, using polished samples as a start: G2 and G3 – chemical pre-treatments & no surface treatment; G4 and G5 – chemical pre-treatments & anodic oxidation; G6 and G7 – chemical pre-treatments & hydrothermal treatment; G8 and G9 – chemical pre-treatments & anodic oxidation followed by hydrothermal treatment. The as-anodized samples are displayed in Fig. 3.3, showing that, after anodization each titanium material exhibited a different colour (grey mirrored surface corresponds to non-treated as-polished). The titanium oxide layer formed on as-anodized Ti grade 2 was pink, whereas on Ti grade 5 it was

blue or closer to green, when prior subjected to alcohol cleaning and acidic pre-treatments, respectively. The oxide layer formed during the hydrothermal treatment displayed a light-yellow colour, corresponding to a faint change compared to the dull metallic finish, whereas samples exposed both to anodic oxidation and hydrothermal treatment displayed similar colours to those obtained for as-anodized samples.

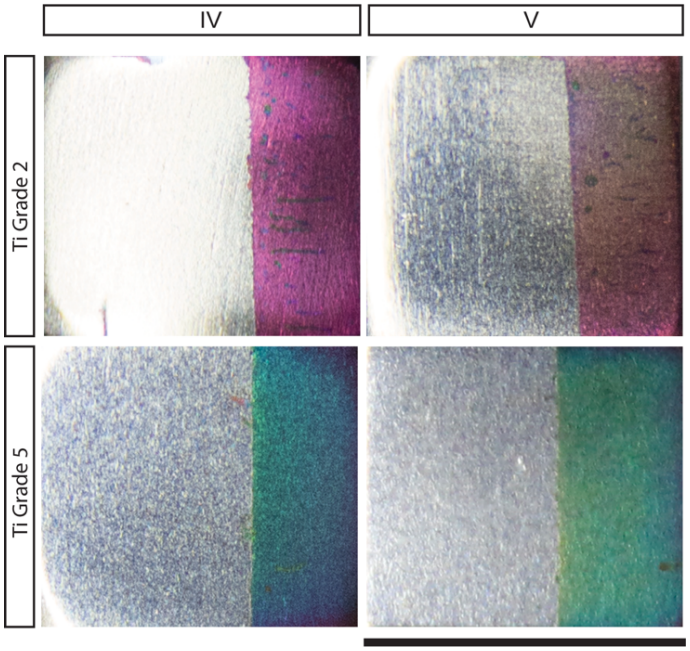



Figure 3.3 - Photographs of anodized Ti grade 2 and Ti grade 5, previously subjected to alcohol cleaning (G4) and acidic pre-treatment (G5).

During the first milliseconds of the anodizing process, a rapid change on the colouring of Ti-based sample was observed until reaching an unchanging colour at the maximum current value. The oxide film colouration, either obtained after anodizing process or hydrothermal treatment, arises from the phenomenon of light interference [52]. The oxide film colour corresponds to the one reinforced by the multiple-beam interferences which includes the ones reflected from the oxide surface and those that arise from the beam that penetrates the oxide and is then reflected from the interface between the oxide and titanium substrate. In this sense, the resultant colour is highly dependent on the oxide film thickness [40,51–53] and thus may be influenced by non-uniformity of the oxide film [54]. With this regard, Ti-based samples subjected to anodizing process are expected to have a thick oxide film, whereas faint yellowish film formed by hydrothermal treatment is expected to be angstrom to nanometre sized [53]. The colouring of the titanium oxide may also be ascribed to stoichiometric defects in the composition of the film and to the different crystalline

structures present in the film, as a consequence of the oxide growth rate and composition of the electrolyte, in the case of the anodizing process [40,54].

The morphology of all Ti-based samples was assessed by SEM. The transition between the anodized film, correspondent to the darker side, and the non-anodized region of Ti grade 5 samples is displayed in Fig. 3.4. In addition to the transition, the correspondent anodizing curve (current variation as a function of the anodizing time) is also present.

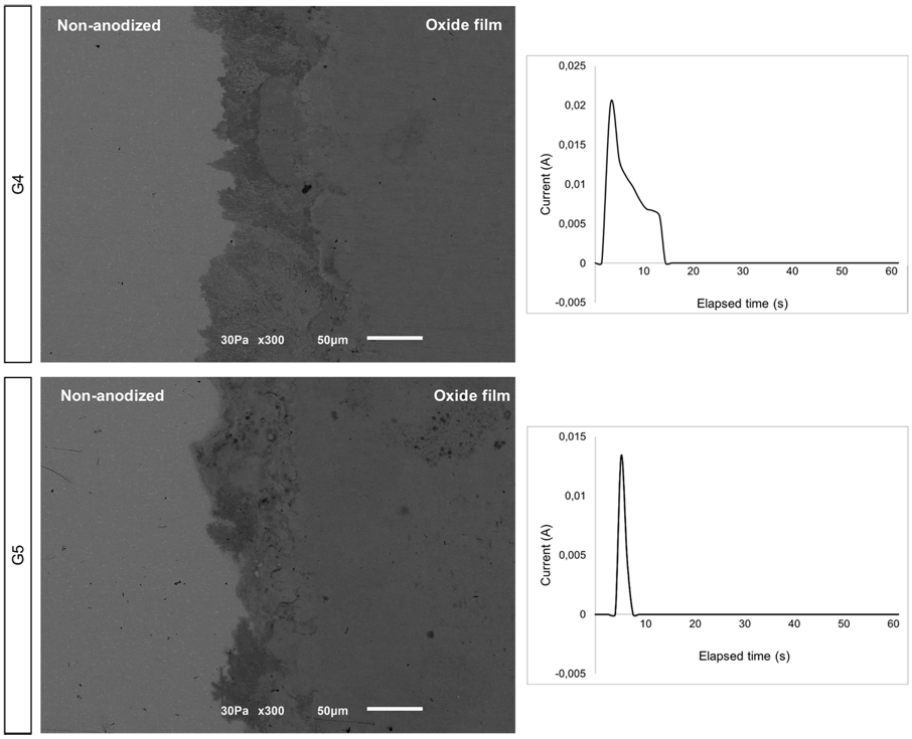



Figure 3.4 - Morphology of the anodized Ti grade 5 samples previously subjected to alcohol cleaning (G4) and to acidic pre-treatment (G5). The oxide film was obtained by anodic oxidation at an applied voltage of 120 V, leading to the displayed correspondent anodizing curves.

By applying a voltage of 120 V for 1 min, the produced film presented few defects, such as impurities and pores. During the anodizing process, the oxide film becomes thicker up to a point when a dielectric breakdown is observed between the most internal and exterior interface of the oxide film, resulting in the formation of pores [15,55]. For both Ti materials, no differences on the morphology were found between as-anodized samples previously subjected to alcohol cleaning or acidic pre-treatment. In this sense, both chemical pre-treatments were effective in samples cleaning and did not alter the surface morphology.

Fig. 3.5 shows Ti grade 2 and Ti grade 5 samples subjected to acidic pre-treatment followed by hydrothermal treatment (G7) and both anodic oxidation and hydrothermal treatment (G9).

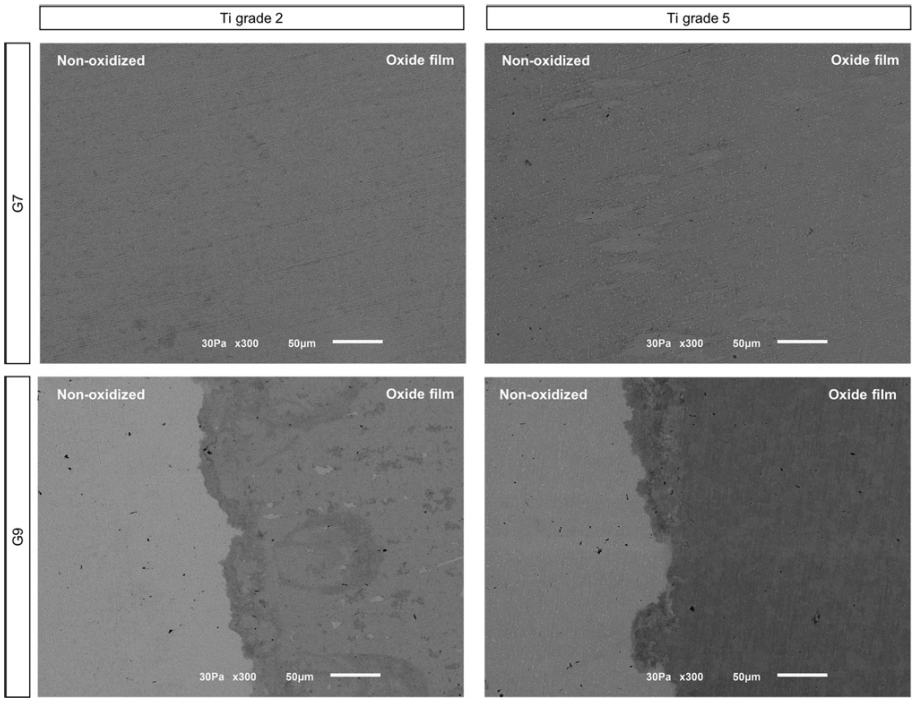



Figure 3.5 - Morphology of the anodized Ti grade 2 and Ti grade 5 samples subjected to acidic pre-treatment followed by hydrothermal treatment (G7) and both anodic oxidation and hydrothermal treatment (G9).

Once again, samples subjected to the same surface modification technique but previously cleaned with alcohol (G6 and G8) presented similar morphologies to those presented in Fig. 3.5. The surface morphology of the oxide film produced on both Ti materials after performing hydrothermal treatment did not present differences compared to the respective non-treated side. Additionally, the oxide film produced by hydrothermal treatment did not present a sufficient thickness able to ascertain a clear transition.

### 3.3.2. Phase composition

The Rietveld refinement is a method used for refining structures by fitting a calculated diffraction profile to the observed one. The calculated diffraction patterns of all Ti grade 2 and Ti grade 5 groups are displayed in Figs. 3.6 and 3.7, respectively. In order to assess the refinement quality, discrepancy values such as the goodness-of-fit, $\chi^2$, and R-factors are also present. One discrepancy index is the weighted profile R-factor, $R_{wp}$, and the "best possible $R_{wp}$" corresponds to the expected R-factor, $R_{exp}$. From these two indices, $\chi^2$ is calculated as follows, $\chi^2 = (R_{wp}/R_{exp})^2$ and is often used to measure the goodness of fit [56]. The obtained indices from both X-ray diffraction patterns are displayed in Supplementary Tables 3.1 and 3.2. Besides the visual inspection of the observed and calculated patterns, these indices help to determine not only if the structural model fits the diffraction intensities but also if the background, diffraction positions and the peak shapes

have also been fit [56]. In this sense, all the Rietveld refinements were successfully obtained, and the crystallographic phases identified.

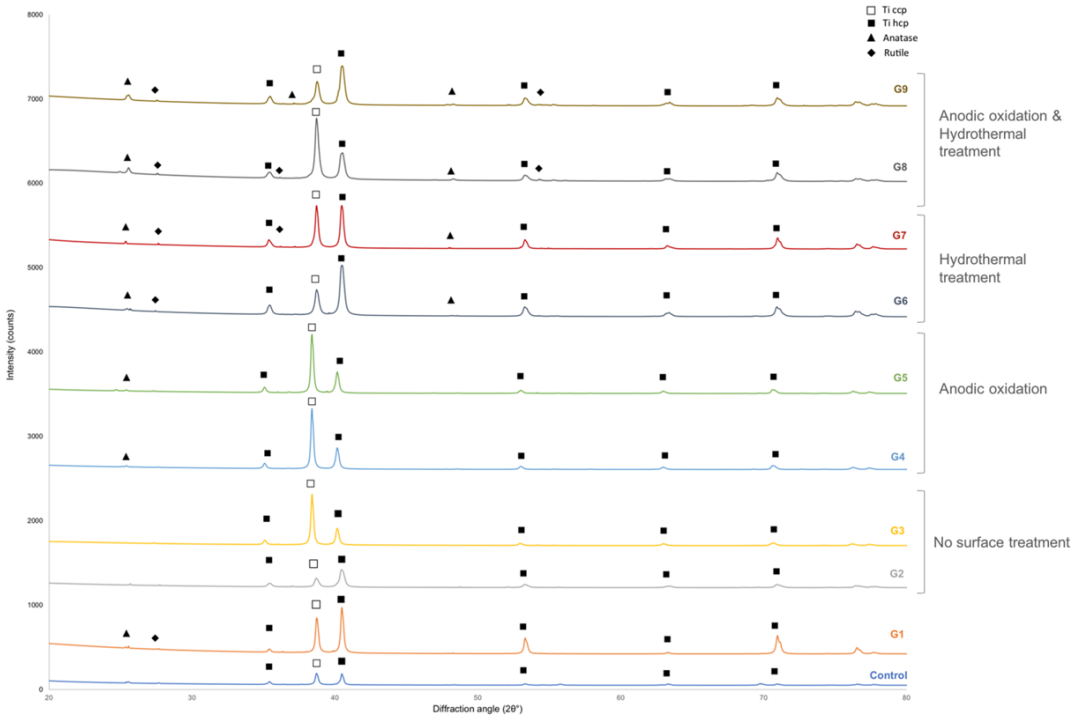



Figure 3.6 - X-ray diffraction patterns of Ti grade 2 groups and identification of Bragg diffraction peaks characteristic of Ti ccp phase (# 01-089-4913), Ti hcp phase (# 00-001-1198), anatase phase (# 01-089-4921) and rutile phase (# 04-003-0648).

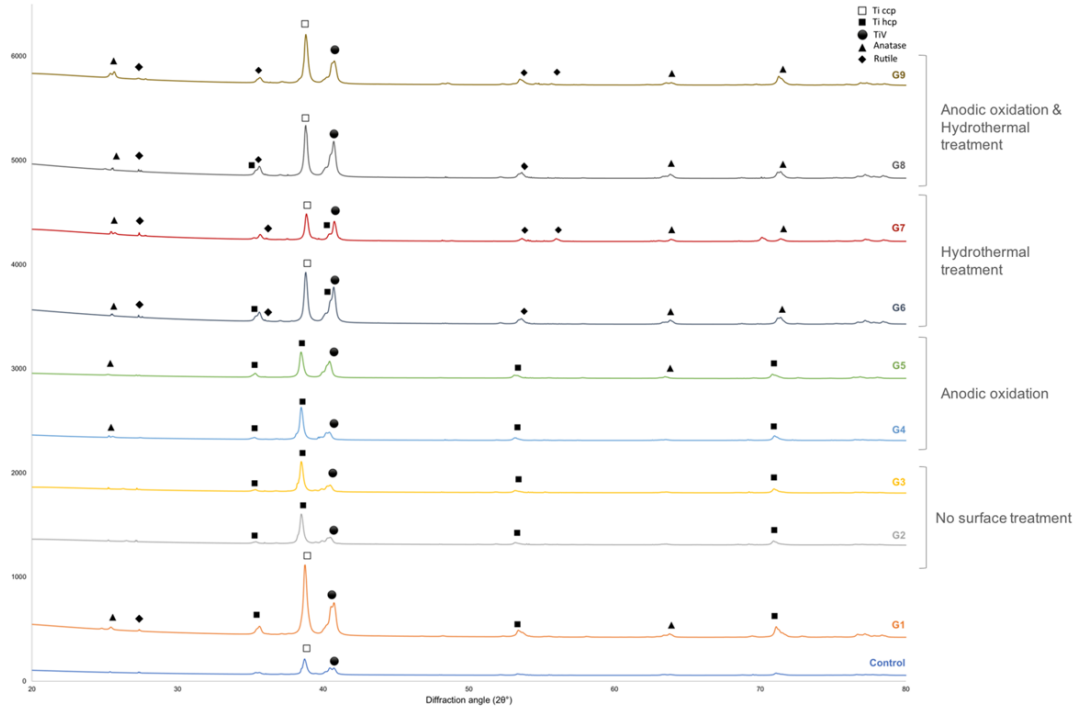



Figure 3.7 - X-ray diffraction pattern of Ti grade 5 groups and identification of Bragg diffraction peaks characteristic of Ti ccp phase (# 01-089-4913), Ti hcp phase (# 00-001-1198), TiV phase (# 03-065-5971) anatase phase (# 01-075-1537) and rutile phase (# 04-003-0648).

As expected, the control and non-treated Ti grade 2 samples (G2 and G3) only presented titanium peaks. On the other hand, crystalline structures of the titanium oxide layer were found on treated groups. For the hydrothermally treated samples, either non-polished (G1) or polished (G6 and G7), anatase and rutile phases were observed, whereas samples subjected to anodic oxidation (G4 and G5) presented only anatase. Finally, the anodic oxidation followed by hydrothermal treatment (G8 and G9) resulted in more peaks of anatase, especially the one previously subjected to acidic pre-treatment (G9), and also in the presence of rutile phase. Altogether, the oxide film formed on commercially pure titanium presented anatase in all three surface modification techniques, whereas rutile was only present for samples subjected to hydrothermal treatment.

Regarding Ti grade 5 samples, the control and non-treated polished samples (G2 and G3) only presented Ti and TiV peaks. Contrarily, hydrothermally treated samples, either non-polished (G1) or previously polished and subjected to alcohol cleaning (G6) or acidic pre-treatment (G7) presented anatase. The same crystalline structure was found on the titanium oxide formed on samples subjected to anodic oxidation (G4, G5, G8 and G9) whereas rutile was only obtained after applying hydrothermal treatment (G1, G6, G7, G8 and G9). Altogether, anatase was again obtained for all treated samples, whereas rutile was only obtained after performing the hydrothermal treatment.

In order to ascertain the contribution of each surface treatment on the presence of anatase and rutile phases, the average percentage of both phases for treated samples is present in Table 3.4.

Table 3.4 - Phase composition of Ti grade 2 and Ti grade 5 treated samples.

| **Surface treatment** | **Group #** | **Ti grade 2** | **Ti grade 5** |
|---|---|---|---|
| Hydro | G1 | 4% anatase / 2% rutile | 6% anatase / 2% rutile |
| AO | G4 | 3% anatase | 6% anatase |
| | G5 | 3% anatase | 4% anatase |
| Hydro | G6 | 4% anatase / 3% rutile | 4% anatase / 3% rutile |
| | G7 | 2% anatase / 6% rutile | 4% anatase / 4% rutile |
| AO + Hydro | G8 | 6% anatase / 2% rutile | 5% anatase / 4 % rutile |
| | G9 | 9% anatase / 2% rutile | 8% anatase / 3% rutile |

AO, Anodic Oxidation; Hydro, Hydrothermal treatment

During the growth of the oxide layer, either obtained by anodic oxidation or hydrothermal treatment, changes in the structure of the oxide film from amorphous to crystalline are often observed [15,57]. The bioactivity of oxide film obtained for all surface modification techniques was confirmed by the anatase crystalline phase. On another hand, rutile phase was only present for all treated Ti grade 2 and grade 5 subjected to hydrothermal treatment (G1, G6-G9). Despite the fact that anatase crystalline structure is often obtained by anodic oxidation while rutile is observed for hydrothermal treatment, both phases were reported to induce apatite formation when in contact with physiological related fluids [58,59]. However, higher predominance of anatase in comparison to rutile has been reported to result in greater cellular damage contributing to cytotoxic and genotoxic effects [60,61]. This suggests that the presence of both crystalline phases is preferable than an amorphous or plain anatase structure, given that rutile may decrease toxicity, not compromising the more stable and homogeneous film often associated with anatase structure [62–64].

### 3.3.3. Roughness and $TiO_2$ thickness

Nano and micro topographical features of Ti-based surfaces affect cell adhesion, orientation, morphology and therefore have a critical role on osseointegration [65]. The roughness of Ti grade 2 groups was obtained by AFM images, and the obtained arithmetic average roughness (Ra) and the root-mean-square roughness of the departures of the profile from the mean line (Rq) are summarized in Supplementary Table 3.3. For the as-polished samples with no surface treatments (G2 and G3), the mean was obtained using four random measurements of each non-treated surface

of the as-polished groups subjected to the same chemical pre-treatment, in order to obtain a total of 12 measurements. The roughness (Ra) values and the statistically significant differences between groups are represented in Fig. 3.8.

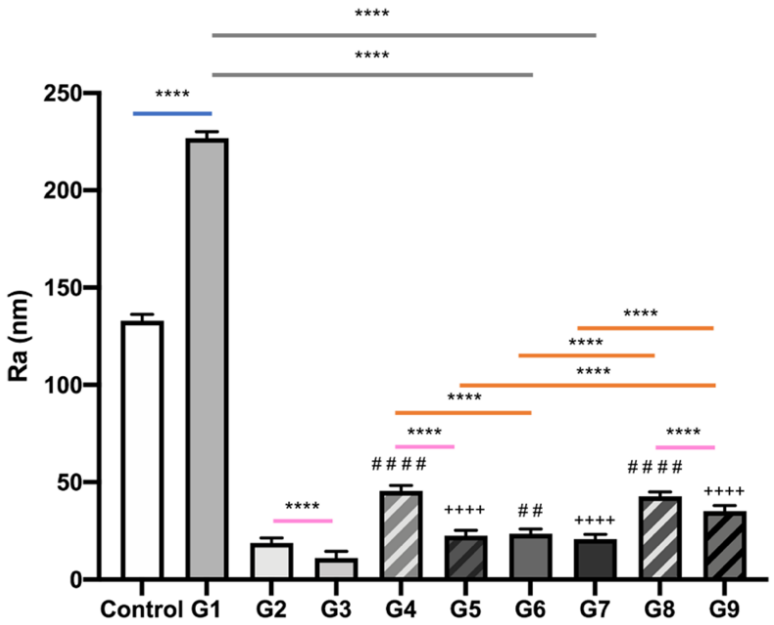



Figure 3.8 - Roughness of Ti grade 2 groups. Data are presented as mean ± standard deviation (SD) (n = 12). Statistically significant differences between groups are denoted by **** ($p<0.0001$), by ## ($p<0.01$) and #### ($p<0.0001$) compared to G2 and by ++++ ($p<0.0001$) compared to G3.

Using the AFM images of Ti grade 5 groups, the obtained Ra and Rq values are summarized in Supplementary Table 3.4 and plotted in Fig. 3.9, where statistically significant differences between groups are also present.

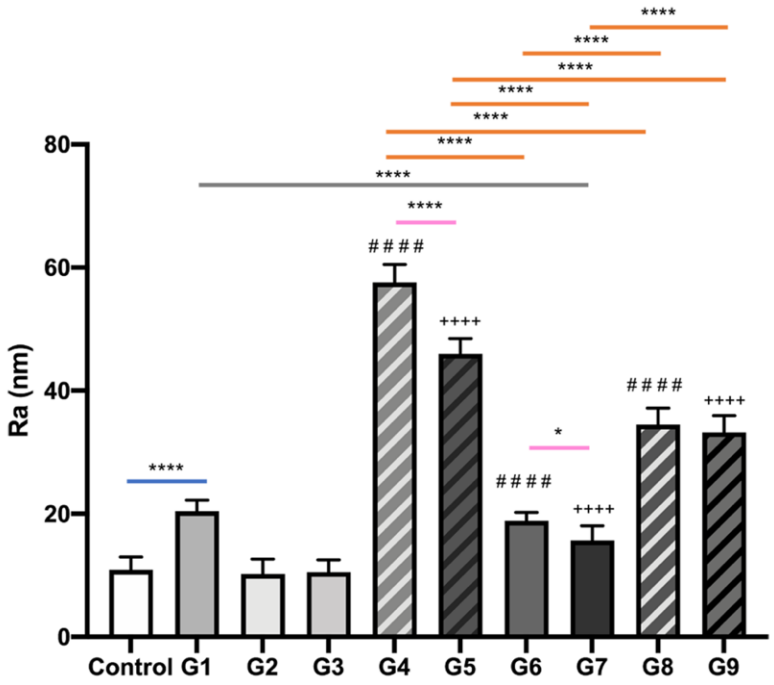



Figure 3.9 - Roughness of Ti grade 5 groups. Data are presented as mean ± standard deviation (SD) (n = 12). Statistically significant differences between groups are denoted by * ($p<0.05$) and **** ($p<0.0001$), by #### ($p<0.0001$) compared to G2 and by ++++ ($p<0.0001$) compared to G3.

All samples presented a smooth surface, given that Ra values are lower than 0.5 μm. As-received commercially pure samples (Ti grade 2) exhibited higher surface roughness values compared to as-received Ti grade 5 samples. For both titanium materials, a statistically significant increase was observed for the non-polished and hydrothermally treated sample (G1) compared to the control. After performing mechanical polishing (G2 and G3), a significant decrease was found for both materials compared to the control. As expected, samples subjected to hydrothermal treatment and previously polished (G6 and G7) presented a roughness decrease compared to the as-received sample also subjected to hydrothermal treatment (G1). For both Ti materials and compared to the as-polished samples (G2 and G3), anodic oxidation resulted in a statistically significant increase of the surface roughness for both pre-treatments. The formation of the oxide layer upon anodization was not uniform and the presence of defects lead to a roughness increase [32,66–68]. Considering samples subjected to hydrothermal treatment, a statistically significant increase was found for both Ti materials compared to the as-polished samples, for both chemical pre-treatments (G6 and G7), as reported in literature [44,57]. However, the obtained oxide layer by hydrothermal treatment was less rough than the oxide film formed by anodic oxidation, given that statistically significant differences were found for both Ti materials previously subjected to alcohol cleaning (G4 vs G6) and for Ti grade 5 samples previously subjected to acidic pre-treatment

(G5 vs G7). When subjected to both surface treatments (G8 and G9), Ra significantly increased compared to as-polished samples (G2 and G3). In this sense, all surface modification techniques increased Ra compared to the as-polished samples. Compared to the as-hydrothermally treated samples (G6 and G7), samples subjected to both surface treatments (anodic oxidation followed by hydrothermal treatment) showed an increased Ra for both chemical pre-treatments. For samples subjected to the same surface treatment but different pre- treatments (G4 vs G5; G6 vs G7 and G8 vs G9), a statistically significant decrease of Ra was found for samples subjected to the acidic pre-treatment compared to those subjected to alcohol cleaning. This decrease was associated with the destruction of the topographic peaks by the acidic pre-treatment. Despite the fact that all samples presented Ra < 1 μm, among all samples the roughest surfaces belong to the control and to the non-polished and hydrothermally treated group (G1) of Ti grade 2. Microrough surfaces are more prone for bone anchorage than smooth surfaces [16] which implies, therefore, that non-polished surfaces would be preferable for improved osseointegration. Following the implantation of the biomaterial, its surface becomes in contact with the surrounding fluid, and that interaction affects the adsorption of molecules and proteins which mediate cell adhesion. In this sense, micro-scale roughness enhances the surface area available for cell adhesion, in particular MSC, which may undergo osteoblast differentiation in order to form bone matrix and, ultimately, a successful osseointegration and therefore, improved clinical outcomes [69]. In addition, osteoblasts appear to act as paracrine regulators of the osteogenic commitment in MSC populations present nearby the implant site. With this regard, MSC seeded on micro-structured Ti grade 2 surfaces (Ra ≈ 3 μm) exhibited increased osteogenic-related markers compared to smooth surface [70,71]. Moreover, mature osteoblasts cultured on the same micro-rough surfaces induced osteoblast commitment of co-cultured MSC [70].

The thickness of the oxide layer formed after each surface treatment was also determined using AFM images. Figs. 3.10 and 3.11 represent the transition between the non-treated region (A) and the oxide film (B) and the calculation of one measurement of the oxide thickness is exemplified graphically for the as-anodized (G4 and G5) and as-anodized and further hydrothermally treated Ti grade 2 samples (G8 and G9), respectively. The height baselines correspondent to the non-treated and treated regions of each sample were determined by the "addtool_curve_stats X- Function" present in the Origin software. This function was used to obtain the height mean covered by the two defined Regions of Interest (ROI) – of the non-treated and treated regions – whereas the oxide layer thickness was further obtained by calculating the

difference between the two heights. Fig. 3.12 comprises the averaged thickness for a total of 10 measurements of Ti grade 2 and Ti grade 5 samples subjected to anodic oxidation (G4 and G5) and to both anodic oxidation and hydrothermal treatment (G8 and G9).

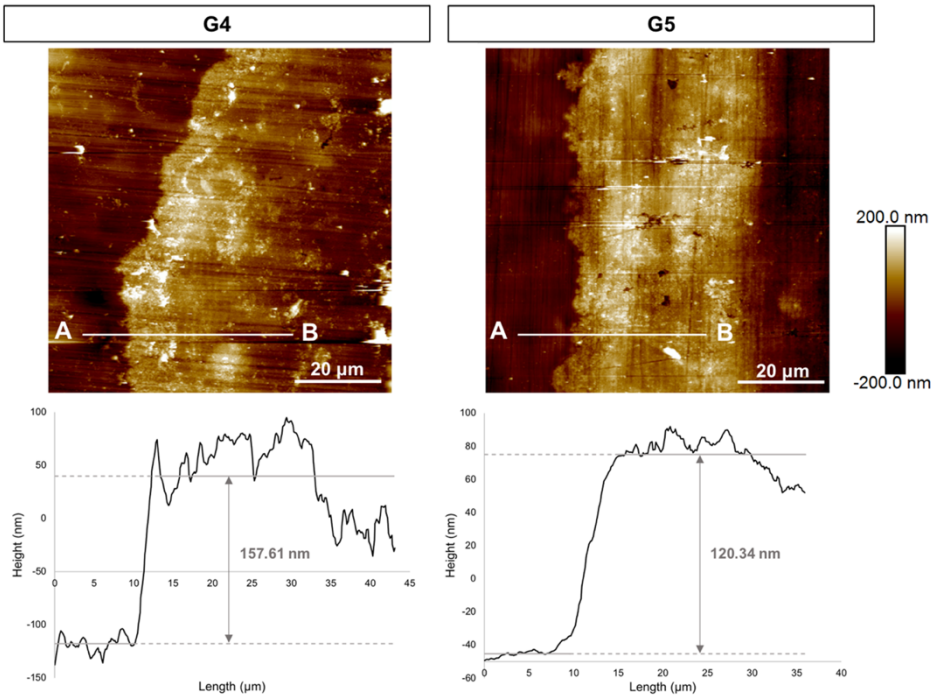



Figure 3.10 - AFM images of the interface between non-treated (A) and treated (B) regions on as-anodized Ti grade 2 samples, previously subjected to alcohol cleaning (G4) or acidic pre-treatment (G5). The minimum and maximum height baselines were calculated in the ROI represented by the horizontal solid grey dash, and the oxide film thickness was calculated by calculating the difference between both height baselines, as represented graphically for one of ten measurements performed along the AFM image.

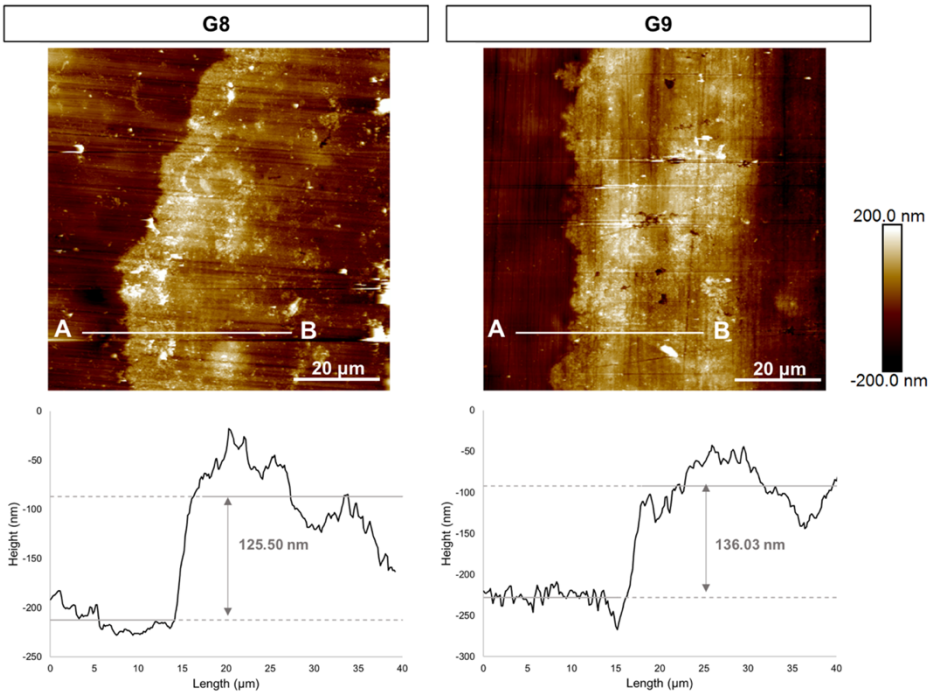



Figure 3.11 - AFM images of the interface between non-treated (A) and treated (B) regions on Ti grade 2 samples subjected to both anodizing and hydrothermal treatment, previously subjected to alcohol cleaning (G8) or acidic pre-treatment (G9). The minimum and maximum height baselines were calculated in the ROI represented by the horizontal solid grey dash, and the oxide film thickness corresponds to the difference between both height baselines, as represented graphically for one of ten measurements performed along the AFM image.

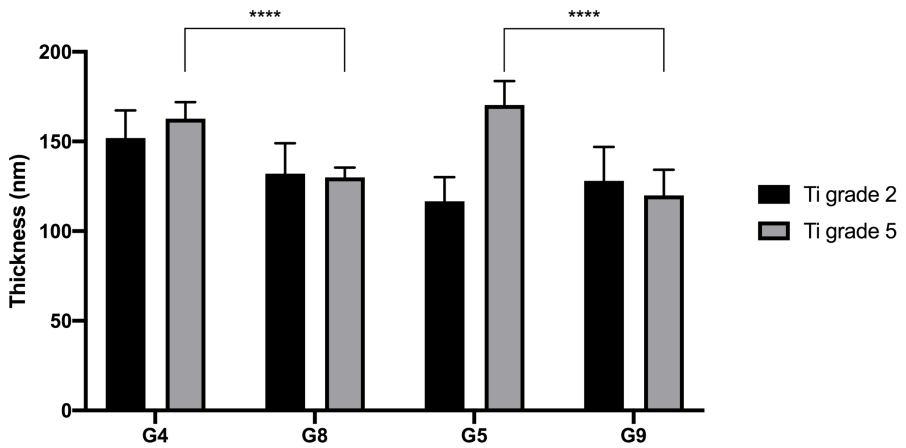



Figure 3.12 - Thickness of the oxide film formed upon anodic oxidation (G4 and G5) and anodic oxidation followed by hydrothermal treatment (G8 and G9) on Ti grade 2 and Ti grade 5. Data are presented as mean ± standard deviation (SD) (n=10) and statistically significant differences were only found for Ti grade 5 samples, which are denoted by **** ($p<0.0001$).

In order to assure durability and stability of the oxide film, thicknesses above that of the spontaneously formed film are often preferable [18]. In addition, compared to the spontaneously formed $TiO_2$ layer, a 100 nm thickness Ti oxide coating resulted in a significantly increase of the proliferation rate of osteoblasts [72], corrosion resistance [73] and also osteogenic activity [21].

The calculated thickness and correspondent standard deviation suggest, once again, that the thickening of the oxide layer is not uniform and varies along the transition between non-treated and oxide film regions. Moreover, the hydrothermal treatment does not enhance the creation of the oxide film. In fact, AFM images of samples only subjected to hydrothermal treatment presented a very subtle and almost imperceptible transition between the non-oxidized and the oxidized region, as presented in Fig. 3.13. For that reason, it was not possible to graphically calculate the thickness of the oxide film formed by hydrothermal treatment for both Ti materials, which is in accordance with the suggested nanometre sized thickness of the yellowish colour film [53].

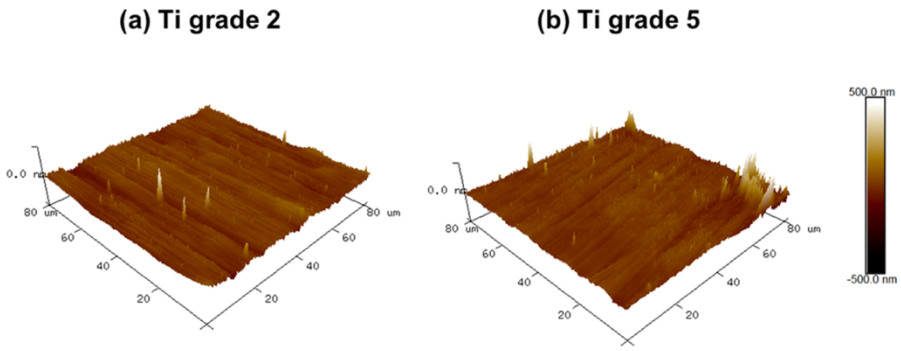



Figure 3.13 - AFM images of (a) Ti grade 2 and (b) Ti grade 5 samples subjected to alcohol cleaning prior to hydrothermal treatment (G6).

From all three surface treatments, the anodic oxidation and anodic oxidation followed by hydrothermal treatment are able to produce an oxide film with a thickness above 100 nm. Despite the fact that a thick oxide film protects the titanium substrate by increasing the wear resistance, high thicknesses are not ideal because they may cause oxide de-bonding and above 1000 nm no improvements of bone responses were found [74]. Additionally, oxide films with thicknesses below 100 nm were reported to significantly decrease the bacterial adhesion compared to higher thicknesses [53]. By altering one or more variables of a particular surface treatment, many oxide film properties are changed besides its thickness. In this sense, improved osteogenic response reported in literature may be due to these changes alone or together, making it difficult to ascertain an accurate correlation between oxide thickness and bone cell response [21].

### 3.3.4. Wettability analysis

Wettability was assessed in order to investigate the surface change as a result of the performed surface treatment. The contact angles were measured at the moment the water drop touched the surface. Surfaces with $\theta < 90°$ are defined as hydrophilic, whereas those with $\theta > 90°$

are defined as hydrophobic and with $\theta > 145^{\circ}$ as superhydrophobic [75]. The water contact angles (WCA) of Ti grade 2 and Ti grade 5 samples and statistically significant differences of WCA for each group immediately after sterilization and after immersion for 24 hrs in 5XPBS are represented graphically in Figs. 3.14 and 3.15, respectively, for a total of 5 measurements.

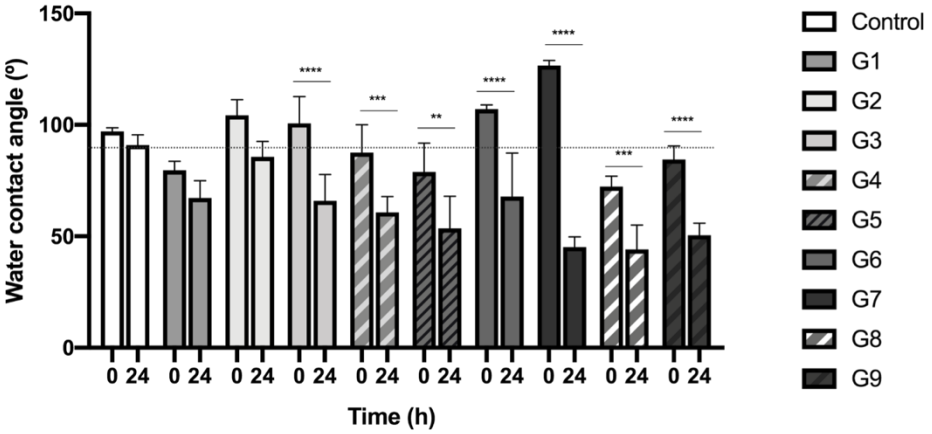



Figure 3.14 - Wettability of Ti grade 2 samples. Data are presented as mean ± SD (n = 5) and the hydrophilicity-hydrophobicity demarcation is represented by a dashed line at 90°. Statistically significant differences between 0 h and 24 hrs storage in 5XPBS are denoted by ** ($p<0.01$), *** ($p<0.001$) and **** ($p<0.0001$).

After sterilization (0 h), hydrophobic Ti grade 2 samples corresponded to the control (97 ± 1.8°), to the as-polished (G2 and G3) and to those subjected to hydrothermal treatment (G6 and G7), whereas the remaining were hydrophilic. By storing in PBS, $Na^{+}$ and $Cl^{-}$ are adsorbed on Ti surface, influencing its hydrophilicity [42,47,76]. In fact, after immersion for 24 hrs in 5XPBS, the wettability of all samples increased, by lowering the WCA, with statistically significant differences except for the control, for the non-polished and hydrothermally treated sample (G1) and for the as-polished and alcohol cleaned sample (G2). However, the control remained hydrophobic (90.9 ± 5.3°). The as-polished samples with no surface treatment (G2 and G3) presented a close WCA but, after 24 hrs, a significant decrease was found for that subjected to acidic pre-treatment (G3). The same trend was found on the as-anodized samples, in which the acidic-treated sample (G5) had a more pronounced statistically significant decrease ($p < 0.01$) compared to those subjected to alcohol cleaning (G4) ($p < 0.001$), after 24 hrs in 5XPBS. After sterilization and considering the hydrothermal treatment, sample subjected to alcohol cleaning (G6) showed a lower WCA than the acidic-treated sample (G7). However, after 24 hrs the wettability behaviour inverted, given that the lowest WCA was found on G7 against G6. Finally, the as-anodized Ti grade 2 samples which were also subjected to hydrothermal treatment presented a lower WCA when subjected to alcohol cleaning (G8) compared to those subjected to acidic pre-treatment (G9). Among all groups, the

most hydrophilic corresponded to that subjected to acidic pre-treatment followed by anodization and hydrothermal treatment (G8) (44.1 ± 12.1°) but the hydrothermally treated group with the same pre-treatment (G7) presented a very close WCA value (45.2 ± 5°).

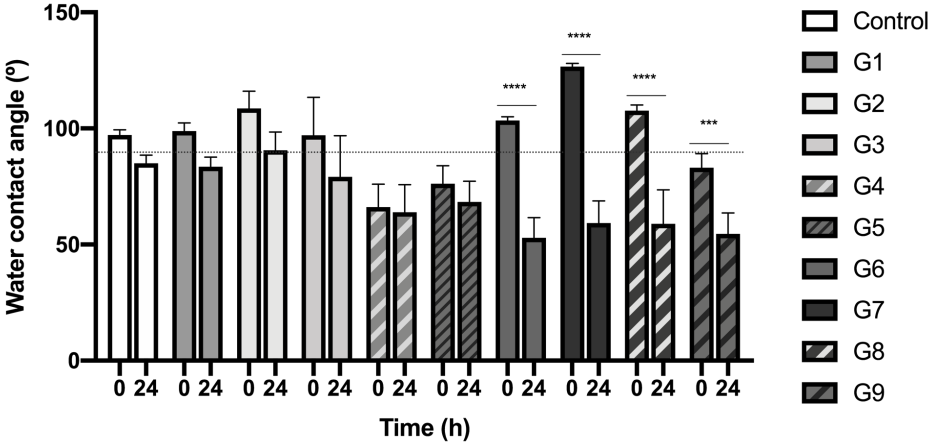



Figure 3.15 - Differences between 0 h and 24 hrs storage in 5XPBS of Ti grade 5 samples. Data are presented as mean ± SD (n = 5) and the hydrophilicity-hydrophobicity demarcation is represented by a dashed line at 90°. Statistically significant differences between both timepoints are denoted by *** ($p<0.005$) and **** ($p<0.0001$).

Immediately after performing the surface treatments, all Ti grade 5 samples were hydrophobic except for the as-anodized (G4 and G5) and the acidic pre-treated sample subjected to anodic oxidation followed by hydrothermal treatment (G9). However, after immersion for 24 hrs in 5XPBS, all samples became hydrophilic, excluding G2 (90.6 ± 8.9°), although very close to the hydrophilicity threshold. Despite that decrease, statistically significant differences were only found for four groups (G6, G7, G8 and G9). Following the same trend as the as-polished Ti grade 2 samples, acidic pre-treated sample (G3) presented a lower WCA, at 0 h and 24 hrs, compared to the alcohol cleaned one (G2). As- anodized samples displayed a lower WCA when subjected to alcohol treatment (G4) for both timepoints compared to that previously subjected to acidic pre-treatment (G5). The same trend was found for the as-hydrothermally treated samples, in which the alcohol cleaning (G6) resulted in a lower WCA compared to the acidic pre-treated sample (G7), after 24 hrs. When both surface treatments (anodic oxidation and hydrothermal treatment) were applied on Ti grade 5 samples, the acidic group (G9) presented lower WCA compared to that subjected to alcohol treatment (G8). Of all groups, those subjected to alcohol cleaning and hydrothermal treatment (G6) corresponded to the most hydrophilic one.

For each Ti grade, wettability differences between groups were assessed at both timepoints (0 h and after immersed in 5XPBS for 24 hrs), as illustrated in Fig. 3.16. Table 3.5 summarizes the wettability for each surface treatment and its relation to the presence of anatase and rutile.

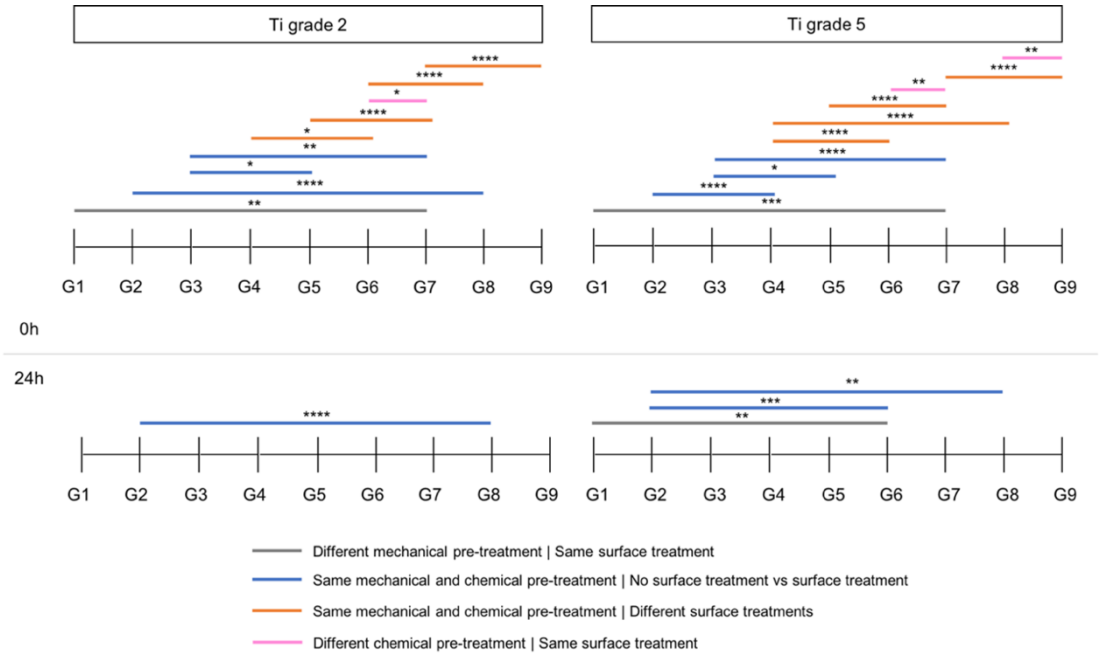



Figure 3.16 - Wettability differences among Ti grade 2 and Ti grade 5 groups (G1-G9), at 0 h and 24 hrs storage in 5XPBS. Statistically significant differences are denoted by * ($p<0.05$), ** ($p<0.01$) and **** ($p<0.0001$). The control group is not represented due to the fact that no statistically significant differences were found between the control group and G1 for both Ti-based materials.

Table 3.5 - Wettability of Ti grade 2 and Ti grade 5 subjected to different surface treatments is directly influenced by the phase composition of the oxide film. The averaged percentage of anatase and rutile was ranked from + to ++++, whereas wettability was ranked from **+** to **+++** (the latest referring to moderate hydrophilicity).

| | | **No pre-treatment** | **Mechanical polishing and chemical pre-treatment** | | | |
|---|---|---|---|---|---|---|
| | | Hydro (G1) | No surface treatment (G2 and G3) | AO (G4 and G5) | Hydro (G6 and G7) | AO + Hydro (G8 and G9) |
| Ti Gr 2 | Anatase phase | + | | + | + | ++++ |
| | Rutile phase | + | | | +++ | ++ |
| | Wettability (0 h) | **++** | **+** | **++** | **+** | **++** |
| | Wettability (24 hrs) | **++** | **+** | **++** | **++** | **+++** |
| Ti Gr 5 | Anatase phase | +++ | | ++ | + | ++++ |
| | Rutile phase | + | | | ++ | ++ |
| | Wettability (0 h) | **+** | **+** | **++** | **+** | **+** |
| | Wettability (24 hrs) | **++** | **++** | **++** | **+++** | **+++** |

Surface wettability has been suggested to be correlated with topography [58,77,78] and both influence the early biological response upon implantation. Besides topography, the crystalline structure of the oxide film may also be related to its wettability [47,57]. In fact, anatase was reported to be hydrophilic whereas rutile is hydrophobic [79]. Immediately after sterilization (0 h), a statistically significant higher WCA was observed for the as-polished and hydrothermally treated sample previously subjected to acidic pre-treatment (G7), compared to the non-polished and hydrothermally treated sample (G1), for both Ti materials, which may be due to the presence of rutile phase. Compared to the as-polished samples (G2 and G3) the wettability of as-anodized samples (G4 and G5) significantly increased for Ti grade 5 samples, whereas for Ti grade 2 a significant difference was only observed for samples previously subjected to the acidic pre-treatment (G4). The oxide film obtained upon anodic oxidation presented anatase which increases the surface wettability (Figs. 6 and 7 can explain these findings). For both Ti-based materials, a significantly higher WCA was found for as-hydrothermally treated (G7) samples in comparison to that only subjected to the acidic pre-treatment (G3), once again, possibly due to the transformation of amorphous $TiO_2$ into rutile phase. Considering the same pre-treatment, samples subjected to hydrothermal treatment (G6 and G7) presented higher percentage of rutile and higher WCA compared to the as-anodized samples (G4 and G5), for both Ti materials. On another hand, samples subjected to both surface modification techniques (G8 and G9), with higher percentages of anatase, had lower WCA compared to the as-anodized samples (G6 and G7) for Ti grade 2 samples, whereas for Ti grade 5 samples a significant decrease was only found for samples previously subjected to the acidic pre-treatment (G9 and G7, respectively). By comparing both pre-treatments, a higher WCA was found for both Ti samples previously subjected to acidic pre-treatment and subsequently to hydrothermal treatment (G6 vs G7), which is associated with higher percentages of rutile.

After immersion in 5XPBS for 24 hrs, the number of statistically significant differences was profoundly narrowed for both Ti grades. A statistically significant decrease was found for both Ti-based samples subjected to the same pre-treatment (alcohol cleaning) and anodic oxidation followed by hydrothermal treatment (G8) compared to the non-treated sample (G2), again due to the presence of crystalline phases.

A pre-treatment of HCl has been proposed to be an efficient cleaning method of titanium surfaces [38]. Although a decrease in hydrocarbon contamination increases surface energy and, in general, the wettability [47], no statistically significant differences were found between both pre-

treatments, after immersion for 24 hrs in 5XPBS. In this sense, it is believed there is no need to perform the acidic pre-treatment. Considering the wettability results obtained for both Ti grades subjected to the three surface treatments, the most hydrophilic surfaces were found on samples subjected to hydrothermal treatment and further immersed in 5XPBS for 24 hrs. Hydrophilic surfaces are usually preferable for biocompatibility given that more proteins are adsorbed resulting in an increase of cell adhesion [45,48,79]. However, high energy surfaces are more prone to adsorb organic hydrocarbon contaminants which will then decrease wettability [47]. Although the optimal wettability degree for improved clinical outcomes remains elusive, moderate hydrophilicity is often preferable than a super hydrophilicity because super-hydrophilicity has been reported to decrease cell adhesion [80,81]. Besides the important role of wettability on the formation of the conditioning film and consequent adhesion of cells, it also affects bacterial adhesion and thus, altogether, the in vivo osseointegration rate [81]. In this sense, we can conclude that the hydrothermal treatment followed by immersion in 5XPBS is an effective surface modification technique for producing hydrophilic surfaces which will potentially enhance the osteoconductivity of Ti-based implants.

## 3.4. Conclusions

In the present study commercially pure titanium and Ti6Al4V alloy were used to investigate the effect of three surface treatments, after performing two different chemical pre-treatments, on the characteristics of the obtained oxide films. Ti-based samples were subjected to anodic oxidation, hydrothermal treatment and to anodic oxidation followed by hydrothermal treatment. Regarding the pre-treatment choice, no major differences were observed between performing alcohol cleaning or acidic pre-treatment, considering the surface crystallinity, roughness and wettability. As a consequence, there is no need to perform the acidic pre-treatment, which simplifies the overall methodology. On another hand, among the three surface treatments, the $TiO_2$ layer presented different characteristics regarding its crystallinity, roughness, thickness and wettability. The presence of both anatase and rutile phases were only observed for samples subjected to hydrothermal treatment. Besides creating a potentially bioactive layer, the hydrothermal treatment was effective in obtaining a moderate hydrophilic surface after immersion in 5XPBS. For the as-received Ti grade 2 subjected to alcohol cleaning and hydrothermal treatment, a roughness of 226.7 ± 3.1 nm and water contact angle of 67.2 ± 8.7° were obtained, whereas for the Ti grade 5 subjected to the same surface treatment, Ra was equal to 20.4 ± 1.7 nm and the water contact angle to 83.5 ± 4.7°. It is a simple methodology that can be applied regardless the implant shape

and on multiple implants, simultaneously. In this context, alcohol cleaning followed by hydrothermal treatment is the strategy here suggested as capable of enhancing bone-implant interface and thus improve osseointegration.

## Acknowledgments

This work was supported by FCT (Fundação para a Ciência e a Tecnologia) through the grant SFRH/BD/141056/2018, and the projects POCI-01-0145-FEDER-030498 and UID/EEA/04436/2019.The authors would like to thank Professor Sandra Carvalho for allowing us to use the equipment for the anodising process.

## References

[1] M. Abdel-Hady Gepreel, M. Niinomi, Biocompatibility of Ti-alloys for long-term implantation, J. Mech. Behav. Biomed. Mater. 20 (2013) 407–415, https://doi.org/10.1016/j.jmbbm.2012.11.014.

[2] Y.J. Lee, D.Z. Cui, H.R. Jeon, H.J. Chung, Y.J. Park, O.S. Kim, Y.J. Kim, Surface characteristics of thermally treated titanium surfaces, J. Periodontal Implant Sci. 42 (2012) 81–87, https://doi.org/10.5051/jpis.2012.42.3.81.

[3] M. Kaur, K. Singh, Review on titanium and titanium based alloys as biomaterials for orthopaedic applications, Mater. Sci. Eng. C 102 (2019) 844–862, https://doi.org/10.1016/j.msec.2019.04.064.

[4] Q. Chen, G.A. Thouas, Metallic implant biomaterials, Mater. Sci. Eng. R. Rep. 87 (2015) 1–57, https://doi.org/10.1016/j.mser.2014.10.001.

[5] V. Goriainov, R. Cook, J. M. Latham, D. G. Dunlop, R. O. C. Oreffo, Bone and metal: an orthopaedic perspective on osseointegration of metals, Acta Biomater. 10 (2014) 4043–4057, https://doi.org/10.1016/j.actbio.2014.06.004.

[6] D.M. Dohan Ehrenfest, P.G. Coelho, B.S. Kang, Y.T. Sul, T. Albrektsson, Classification of osseointegrated implant surfaces: materials, chemistry and topography, Trends Biotechnol. 28 (2010) 198–206, https://doi.org/10.1016/j. tibtech.2009.12.003.

[7] S. Lavenus, V. Trichet, S. Le Chevalier, A. Hoornaert, G. Louarn, P. Layrolle, Cell differentiation and osseointegration influenced by nanoscale anodized titanium surfaces, Nanomedicine. 7 (2012) 967–980, https://doi.org/10.2217/nnm.11.181.

[8] Y. Kirmanidou, M.Sidira, M. E. Drosou, V. Bennani, A. Bakopoulou, A. Tsouknidas, N. Michailidis, K. Michalakis, New Ti-alloys and surface modifications to improve the mechanical properties and the biological response to orthopedic and dental implants: a review, Biomed. Res. Int. 2016 (2016), https://doi.org/10.1155/2016/ 2908570.

[9] M. Gasik, Understanding biomaterial-tissue interface quality: combined in vitro evaluation, Sci. Technol. Adv. Mater. 18 (2017) 550–562, https://doi.org/ 10.1080/14686996.2017.1348872.

[10] L.A. Hidalgo-Bastida, S.H. Cartmell, Mesenchymal stem cells, osteoblasts and extracellular matrix proteins: enhancing cell adhesion and differentiation for bone tissue engineering, Tissue Eng. Part B Rev. 16 (2010) 405–412, https://doi.org/ 10.1089/ten.teb.2009.0714.

[11] D. Kohavi, L. Badihi Hauslich, G. Rosen, D. Steinberg, M. N. Sela, Wettability versus electrostatic forces in fibronectin and albumin adsorption to titanium surfaces, Clin. Oral Implants Res. 24 (2013) 1002–1008, https://doi.org/10.1111/j.1600-0501.2012.02508.x.

[12] L. Hao, X. Fu, T. Li, N. Zhao, X. Shi, F. Cui, C. Du, Y. Wang, Surface chemistry from wettability and charge for the control of mesenchymal stem cell fate through self- assembled monolayers, Colloids Surf. B: Biointerfaces 148 (2016) 549–556, https://doi.org/10.1016/j.colsurfb.2016.09.027.

[13] L. Parisi, B. Ghezzi, M. G. Bianchi, A. Toffoli, F. Rossi, O. Bussolati, G. M. Macaluso, Titanium dental implants hydrophilicity promotes preferential serum fibronectin over albumin competitive adsorption modulating early cell response, Mater. Sci. Eng. C 117 (2020), https://doi.org/10.1016/j.msec.2020.111307.

[14] B. Li, Y. Li, J. Li, X. Fu, C. Li, H. Wang, S. Liu, L. Guo, S. Xin, C. Liang, H. Li, Improvement of biological properties of titanium by anodic oxidation and ultraviolet irradiation, Appl. Surf. Sci. 307 (2014) 202–208, https://doi.org/ 10.1016/j.apsusc.2014.04.015.

[15] H. A. Acciari, D. P. S. Palma, E. N. Codaro, Q. Zhou, J. Wang, Y. Ling, J. Zhang, Z. Zhang, Surface modifications by both anodic oxidation and ion beam implantation on electropolished titanium substrates, Appl. Surf. Sci. 487 (2019) 1111–1120, https://doi.org/10.1016/j.apsusc.2019.05.216.

[16] A. Wennerberg, T. Albrektsson, Effects of titanium surface topography on bone integration: a systematic review, Clin. Oral Implants Res. 20 (2009) 172–184, https://doi.org/10.1111/j.1600-0501.2009.01775.x.

[17] A. L. Raines, R. Olivares-Navarrete, M. Wieland, D. L. Cochran, Z. Schwartz, B. D. Boyan, Regulation of angiogenesis during osseointegration by titanium surface microstructure and energy, Biomaterials. 31 (2010) 4909–4917, https://doi.org/ 10.1016/j.biomaterials.2010.02.071.

[18] K. Aniołek, M. Kupka, A. Barylski, Sliding wear resistance of oxide layers formed on a titanium surface during thermal oxidation, Wear. 356–357 (2016) 23–29, https://doi.org/10.1016/j.wear.2016.03.007.

[19] Y. Luo, S. Ge, H. Liu, Z. Jin, Microstructure analysis and wear behavior of titanium cermet femoral head with hard TiC layer, J. Biomech. 42 (2009) 2708–2711, https://doi.org/10.1016/j.jbiomech.2009.08.003.

[20] A. Maytorena-Sánchez, J. Hernández-Torres, F. López-Huerta, M. A. Hernández- Campos, L. Zamora-Peredo, M. Pacio-Castillo, L. E. Serrano-De la Rosa, L. García-González, Analysis of the hardness and tribological properties of grade 2 titanium using the thermal oxidation process at different temperatures, Mater. Lett. 282 (2021) 2020–2022, https://doi.org/10.1016/j.matlet.2020.128679.

[21] G. Wang, J. Li, K. Lv, W. Zhang, X. Ding, G. Yang, X. Liu, X. Jiang, Surface thermal oxidation on titanium implants to enhance osteogenic activity and in vivo osseointegration, Sci. Rep. 6 (2016) 1–13, https://doi.org/10.1038/srep31769.

[22] M. F. Dias-Netipanyj, K. Cowden, L. Sopchenski, S. C. Cogo, S. Elifio-Esposito, K. C. Popat, P. Soares, Effect of crystalline phases of titania nanotube arrays on adipose derived stem cell adhesion and proliferation, Mater. Sci. Eng. C 103 (2019), https://doi.org/10.1016/j.msec.2019.109850.

[23] L. Lv, K. Li, Y. Xie, Y. Cao, X. Zheng, Enhanced osteogenic activity of anatase $TiO_2$ film: surface hydroxyl groups induce conformational changes in fibronectin, Mater. Sci. Eng. C 78 (2017) 96–104, https://doi.org/10.1016/j.msec.2017.04.056.

[24] S. Ferraris, S. Spriano, Antibacterial titanium surfaces for medical implants, Mater. Sci. Eng. C 61 (2016) 965–978, https://doi.org/10.1016/j.msec.2015.12.062.

[25] P. Piszczek, A. Radtke, M. Ehlert, T. Jędrzejewski, A. Sznarkowska, B. Sadowska, M. Bartmański, Y. K. Erdoğan, B. Ercan, W. Jedrzejczyk, Comprehensive evaluation of the biological properties of surface-modified titanium alloy implants, J. Clin. Med. 9 (2020) 342, https://doi.org/10.3390/jcm9020342.

[26] M. Bartmański, Ł. Pawłowski, A. Zieliński, A.G. Mielewczyk-Gryń, B.Cieślik Strugała, Electrophoretic deposition and characterization of chitosan-nanosilver composite coatings on a nanotubular $TiO_2$ layer, Coatings 10 (2020), 245, https://doi.org/10.3390/coatings10030245.

[27] M. Bartmanski, A. Zielinski, M. Jazdzewska, J. Głodowska, P. Kalka, Effects of electrophoretic deposition times and nanotubular oxide surfaces on properties of the nanohydroxyapatite/nanocopper coating on the Ti13Zr13Nb alloy, Ceram. Int. 45 (2019) 20002–20010, https://doi.org/10.1016/j.ceramint.2019.06.258.

[28] S. Li, J. Ni, X. Liu, X. Zhang, S. Yin, M. Rong, Z. Guo, L. Zhou, Surface characteristics and biocompatibility of sandblasted and acid-etched titanium surface modified by ultraviolet irradiation: an in vitro study, J. Biomed. Mater. Res. - Part B Appl. Biomater. 100 (B) (2012) 1587–1598, https://doi.org/10.1002/jbm. b.32727.

[29] A. Henningsen, R. Smeets, P. Hartjen, O. Heinrich, R. Heuberger, M. Heiland, C. Precht, C. Cacaci, Photofunctionalization and non-thermal plasma activation of titanium surfaces, Clin. Oral Investig. 22 (2018) 1045–1054, https://doi.org/ 10.1007/s00784-017-2186-z.

[30] K. Duske, L. Jablonowski, I. Koban, R. Matthes, B. Holtfreter, A. Sckell, J. Barbara Nebe, T. von Woedtke, K.D. Weltmann, T. Kocher, Cold atmospheric plasma in combination with mechanical treatment improves osteoblast growth on biofilm covered titanium discs, Biomaterials. 52 (2015) 327–334, https://doi.org/ 10.1016/j.biomaterials.2015.02.035.

[31] S.H. Choi, W.S. Jeong, J.Y. Cha, J.H. Lee, H.S. Yu, E.H. Choi, K.M. Kim, C. J. Hwang, Time dependent effects of ultraviolet and nonthermal atmospheric pressure plasma on the biological activity of titanium, Sci. Rep. 6 (2016) 1–12, https://doi.org/10.1038/srep33421.

[32] T. Wang, L. Wang, Q. Lu, Z. Fan, Changes in the esthetic, physical, and biological properties of a titanium alloy abutment treated by anodic oxidation, J. Prosthet. Dent. 121 (2019) 156–165, https://doi.org/10.1016/j.prosdent.2018.03.024.

[33] Z.J. Liu, X. Zhong, J. Walton, G.E. Thompson, Anodic film growth of titanium oxide using the 3-electrode electrochemical technique: effects of oxygen evolution and morphological characterizations, J. Electrochem. Soc. 163 (2016) E75–E82, https://doi.org/10.1149/2.0181603jes.

[34] F. Rupp, L. Liang, J. Geis-Gerstorfer, L. Scheideler, F. Hüttig, Surface characteristics of dental implants: a review, Dent. Mater. 34 (2018) 40–57, https://doi.org/ 10.1016/j.dental.2017.09.007.

[35] W. Asumpinwong, K. Saengkiettiyut, V. Srimaneepong, Different constant voltages of anodization on the corrosion behavior of Ti-6Al-4V alloy, Chiang Mai J. Sci. 42 (2015) 239–248.

[36] R. Narayanan, S.K. Seshadri, Phosphoric acid anodization of Ti-6Al-4V – Structural and corrosion aspects, Corros. Sci. 49 (2007) 542–558, https://doi.org/10.1016/j. corsci.2006.06.021.

[37] A. Karambakhsh, A. Afshar, S. Ghahramani, P. Malekinejad, Pure commercial titanium color anodizing and corrosion resistance, J. Mater. Eng. Perform. 20 (2011) 1690–1696, https://doi.org/10.1007/s11665-011-9860-0.

[38] M. Takeuchi, Y. Abe, Y. Yoshida, Y. Nakayama, M. Okazaki, Y. Akagawa, Acid pretreatment of titanium implants, Biomaterials. 24 (2003) 1821–1827, https:// doi.org/10.1016/S0142-9612(02)00576-8.

[39] B. Wu, S. Xiong, Y. Guo, Y. Chen, P. Huang, B. Yang, Tooth-colored bioactive titanium alloy prepared with anodic oxidation method for dental implant application, Mater. Lett. 248 (2019) 134–137, https://doi.org/10.1016/j. matlet.2019.04.015.

[40] A. Karambakhsh, A. Afshar, P. Malekinejad, Corrosion resistance and color properties of anodized Ti-6Al-4V, J. Mater. Eng. Perform. 21 (2012) 121–127, https://doi.org/10.1007/s11665-010-9791-1.

[41] I. S. Park, T. G. Woo, W. Y. Jeon, H. H. Park, M. H. Lee, T. S. Bae, K. W. Seol, Surface characteristics of titanium anodized in the four different types of electrolyte, Electrochim. Acta 53 (2007) 863–870, https://doi.org/10.1016/j. electacta.2007.07.067.

[42] M. Zuldesmi, A. Waki, K. Kuroda, M. Okido, High Osteoconductive surface of pure titanium by hydrothermal treatment, J. Biomater. Nanobiotechnol. 04 (2013) 284–290, https://doi.org/10.4236/jbnb.2013.43036.

[43] P.K. Srivas, K. Kapat, B. Das, P. Pal, P.G. Ray, S. Dhara, Hierarchical surface morphology on Ti6Al4V via patterning and hydrothermal treatment towards improving cellular response, Appl. Surf. Sci. 478 (2019) 806–817, https://doi.org/ 10.1016/j.apsusc.2019.02.039.

[44] K. Kapat, P.P. Maity, A.P. Rameshbabu, P.K. Srivas, P. Majumdar, S. Dhara, Simultaneous hydrothermal bioactivation with nano-topographic modulation of porous titanium alloys towards enhanced osteogenic and antimicrobial responses, J. Mater. Chem. B 6 (2018) 2877–2893, https://doi.org/10.1039/c8tb00382c.

[45] J. Vishnu, V.K. Manivasagam, V. Gopal, C. Bartomeu Garcia, P. Hameed, G. Manivasagam, T.J. Webster, Hydrothermal treatment of etched titanium: a potential surface nano-modification technique for enhanced biocompatibility, Nanomedicine 20 (2019), https://doi.org/10.1016/j.nano.2019.102016.

[46] S. Yang, S. Lee, I. Bajpai, S. Kim, Hydrothermal treatment of Ti surface to enhance the formation of low crystalline hydroxyl carbonate apatite, Biomater. Res. 19 (2015) 1–6, https://doi.org/10.1186/s40824-014-0022-y.

[47] M. Zuldesmi, A. Waki, K. Kuroda, M. Okido, Hydrothermal treatment of titanium alloys for the enhancement of osteoconductivity, Mater. Sci. Eng. C 49 (2015) 430–435, https://doi.org/10.1016/j.msec.2015.01.031.

[48] K. Kuroda, M. Okido, Osteoconductivity of protein adsorbed titanium implants using hydrothermal treatment, Mater. Sci. Forum 879 (2017) 1049–1052, https:// doi.org/10.4028/www.scientific.net/MSF.879.1049.

[49] C.N. Elias, J.H.C. Lima, R. Valiev, M.A. Meyers, Biomedical applications of titanium and its alloys, Jom. 60 (2008) 46–49, https://doi.org/10.1007/s11837-008-0031-1.

[50] N.K. Kuromoto, R.A. Simão, G.A. Soares, Titanium oxide films produced on commercially pure titanium by anodic oxidation with different voltages, Mater. Charact. 58 (2007) 114–121, https://doi.org/10.1016/j.matchar.2006.03.020.

[51] C. G. Moura, O. Carvalho, V. H. Magalhães, R. S. F. Pereira, M. F. Cerqueira, L. M. V. Gonçalves, R. M. Nascimento, F. S. Silva, Laser printing of micro-electronic communication systems for smart implants applications, Opt. Laser Technol. 128 (2020) 106211, https://doi.org/10.1016/j.optlastec.2020.106211.

[52] M. Wen, C. Wen, P. Hodgson, Y. Li, Thermal oxidation behaviour of bulk titanium with nanocrystalline surface layer, Corros. Sci. 59 (2012) 352–359, https://doi. org/10.1016/j.corsci.2012.03.005.

[53] J. Gopal, S. Chun, M. Doble, Attenuated total reflection Fourier transform infrared spectroscopy towards disclosing mechanism of bacterial adhesion on thermally stabilized titanium nano-interfaces, J. Mater. Sci. Mater. Med. 27 (2016) 1–12, https://doi.org/10.1007/s10856-016-5739-9.

[54] A. Gomez Sanchez, W. Schreiner, G. Duffó, S. Ceré, Surface modification of titanium by anodic oxidation in phosphoric acid at low potentials. Part 1. Structure, electronic properties and thickness of the anodic films, Surf. Interface Anal. 45 (2013) 1037–1046, https://doi.org/10.1002/sia.5210.

[55] R.S. Williamson, J. Disegi, A.V. Janorkar, J.A. Griggs, M.D. Roach, Effect of duty cycle on the crystallinity, pore size, surface roughness and corrosion resistance of the anodized surface on titanium, Surf. Coat. Technol. 277 (2015) 278–288, https://doi.org/10.1016/j.surfcoat.2015.07.020.

[56] B.H. Toby, R factors in Rietveld analysis: how good is good enough? Powder Diffract. 21 (2006) 67–70, https://doi.org/10.1154/1.2179804.

[57] M. Wang, Y. Wu, S. Lu, T. Chen, Y. Zhao, H. Chen, Z. Tang, Fabrication and characterization of selective laser melting printed Ti–6Al–4V alloys subjected to heat treatment for customized implants design, Prog. Nat. Sci. Mater. Int. 26 (2016) 671–677, https://doi.org/10.1016/j.pnsc.2016.12.006.

[58] C.M. Cotrut, I.C. Ionescu, E. Ungureanu, A. Berbecaru, R.I. Zamfir, A. Vladescu, D. M. Vranceanu, Evaluation of surface modification techniques on the ability of apatite formation and corrosion behavior in synthetic body fluid: an in vitro study, Surf. Interfaces. 22 (2021) 100866, https://doi.org/10.1016/j. surfin.2020.100866.

[59] X. Liu, T. Yoshioka, S. Hayakawa, Comparative study of in vitro apatite-forming abilities of highly ordered rutile nanorod arrays fabricated on cpTi and Ti6Al4V alloys, J. Asian Ceram. Soc. 8 (2020) 29–38, https://doi.org/10.1080/ 21870764.2019.1699230.

[60] C. Internalization, M.S. Cells, I.L. De Lima, E. Campos-fern, N.O. Dantas, A. Christine, A. Silva, M. Botelho, P. Soares, R. Ribeiro, C. Machado, A. Cardoso, L. Souza, D. Arag, C. Rocha, Characterization of crystalline phase of $TiO_2$ nanocrystals, cytotoxicity and cell internalization analysis on human adipose tissue-derived mesenchymal stem cells, Materials (Basel) 13 (2020) 4071, https:// doi.org/10.3390/ma13184071.

[61] É.M. de Reis, A.A.A. de Rezende, P.F. de Oliveira, H.D. Nicolella, D.C. Tavares, A.C. A. Silva, N.O. Dantas, M.A. Spanó, Evaluation of titanium dioxide nanocrystal-induced genotoxicity by the cytokinesis-block micronucleus assay and the Drosophila wing spot test, Food Chem. Toxicol. 96 (2016) 309–319, https://doi. org/10.1016/j.fct.2016.08.023.

[62] Y. Bai, I.S. Park, H.H. Park, M.H. Lee, T.S. Bae, W. Duncan, M. Swain, The effect of annealing temperatures on surface properties, hydroxyapatite growth and cell behaviors of $TiO_2$ nanotubes, Surf. Interface Anal. 43 (2011) 998–1005, https:// doi.org/10.1002/sia.3683.

[63] S. Popescu, I. Demetrescu, C. Sarantopoulos, A.N. Gleizes, D. Iordachescu, The biocompatibility of titanium in a buffer solution: compared effects of a thin film of $TiO_2$ deposited by MOCVD and of collagen deposited from a gel, J. Mater. Sci. Mater. Med. 18 (2007) 2075–2083, https://doi.org/10.1007/s10856-007-3133-3.

[64] B. Cervantes, F. López-Huerta, R. Vega, J. Hernández-Torres, L. García-González, E. Salceda, A.L. Herrera-May, E. Soto, Cytotoxicity evaluation of anatase and rutile $TiO_2$ thin films on CHO-K1 cells in vitro, Materials (Basel). 9 (2016) 1–11, https:// doi.org/10.3390/ma9080619.

[65] F. Melo-Fonseca, G. Miranda, H.S. Domingues, I.M. Pinto, M. Gasik, F.S. Silva, Reengineering bone-implant interfaces for improved mechanotransduction and clinical outcomes, Stem Cell Rev. Rep. (2020), https://doi.org/10.1007/s12015-020-10022-9.

[66] C.N. Elias, Titanium dental implant surfaces, 65th ABM Int. Congr. 18th IFHTSE Congr. 1st TMS/ABM Int. Mater. Congr. 2010 6 (2010) 5067–5072, https://doi. org/10.1590/s1517-70762010000200008.

[67] L. H. Li, Y. M. Kong, H. W. Kim, Y. W. Kim, H. E. Kim, S. J. Heo, J. Y. Koak, Improved biological performance of Ti implants due to surface modification by micro-arc oxidation, Biomaterials. 25 (2004) 2867–2875, https://doi.org/10.1016/j. biomaterials.2003.09.048.

[68] K.H. Park, S.J. Heo, J.Y. Koak, S.K. Kim, J.B. Lee, S.H. Kim, Y.J. Lim, Osseointegration of anodized titanium implants under different current voltages: a rabbit study, J. Oral Rehabil. 34 (2007) 517–527, https://doi.org/10.1111/j.1365-2842.2006.01688.x.

[69] D. Wang, G. Wu, X. Lin, Y. Liu, Coatings for osseointegration of metallic biomaterials, Surf. Coat. Modif. Met. Biomater. (2015) 345–358, https://doi.org/ 10.1016/B978-1-78242-303-4.00011-9.

[70] R. Olivares-Navarrete, S.L. Hyzy, D.L. Hutton, C.P. Erdman, M. Wieland, B. D. Boyan, Z. Schwartz, Direct and indirect effects of microstructured titanium substrates on the induction of mesenchymal stem cell differentiation towards the osteoblast lineage, Biomaterials. 31 (2010) 2728–2735, https://doi.org/10.1016/j. biomaterials.2009.12.029.

[71] R. A. Gittens, R. Olivares-Navarrete, A. Cheng, D. M. Anderson, T. McLachlan, I. Stephan, J. Geis-Gerstorfer, K. H. Sandhage, A. G. Fedorov, F. Rupp, B. D. Boyan, R. Tannenbaum, Z. Schwartz, The roles of titanium surface micro nanotopography and wettability on the differential response of human osteoblast lineage cells, Acta Biomater. 9 (2013) 6268–6277, https://doi.org/10.1016/j.actbio.2012.12.002.

[72] A. Ochsenbein, F. Chai, S. Winter, M. Traisnel, J. Breme, H.F. Hildebrand, Osteoblast responses to different oxide coatings produced by the sol-gel process on titanium substrates, Acta Biomater. 4 (2008) 1506–1517, https://doi.org/ 10.1016/j.actbio.2008.03.012.

[73] D. Velten, V. Biehl, F. Aubertin, B. Valeske, W. Possart, J. Breme, Preparation of $TiO_2$ layers on cp-Ti and Ti6Al4V by thermal and anodic oxidation and by sol-gel coating techniques and their characterization, J. Biomed. Mater. Res. 59 (2002) 18–28, https://doi.org/10.1002/jbm.1212.

[74] Y.T. Sul, C. Johansson, E. Byon, T. Albrektsson, The bone response of oxidized bioactive and non-bioactive titanium implants, Biomaterials. 26 (2005) 6720–6730, https://doi.org/10.1016/j.biomaterials.2005.04.058.

[75] K.-Y. Law, H. Zhao, Surface Wetting: Characterization, Contact Angle, and Fundamentals, Springer International Publishing, Basel, Switzerland, 2016, https://doi.org/10.1007/978-3-319-25214-8.

[76] D. Yamamoto, K. Arii, K. Kuroda, R. Ichino, M. Okido, A. Seki, Osteoconductivity of superhydrophilic anodized $TiO_2$ coatings on Ti treated with hydrothermal processes, J. Biomater. Nanobiotechnol. 04 (2013) 45–52, https://doi.org/ 10.4236/jbnb.2013.41007.

[77] J. W. Park, Y. J. Kim, C. H. Park, D. H. Lee, Y. G. Ko, J. H. Jang, C. S. Lee, Enhanced osteoblast response to an equal channel angular pressing-processed pure titanium substrate with microrough surface topography, Acta Biomater. 5 (2009) 3272–3280, https://doi.org/10.1016/j.actbio.2009.04.038.

[78] M. Gasik, L. Van Mellaert, D. Pierron, A. Braem, D. Hofmans, E. De Waelheyns, J. Ann´, M.F. Harmand, J. Vleugels, Reduction of biofilm infection risks and promotion of osteointegration for

optimized surfaces of titanium implants, Adv. Healthc. Mater. 1 (2012) 117–127, https://doi.org/10.1002/adhm.201100006.

[79] M. Manjaiah, R.F. Laubscher, A review of the surface modifications of titanium alloys for biomedical applications, Mater. Technol. 51 (2017) 181–193, https:// doi.org/10.17222/mit.2015.348.

[80] J.I. Rosales-Leal, M.A. Rodríguez-Valverde, G. Mazzaglia, P.J. Ramón-Torregrosa, L. Díaz-Rodríguez, O. García-Martínez, M. Vallecillo-Capilla, C. Ruiz, M.A. Cabrerizo-Vílchez, Effect of roughness, wettability and morphology of engineered titanium surfaces on osteoblast-like cell adhesion, Colloids Surfaces A Physicochem. Eng. Asp. 365 (2010) 222–229, https://doi.org/10.1016/j. colsurfa.2009.12.017.

[81] R.A. Gittens, L. Scheideler, F. Rupp, S.L. Hyzy, J. Geis-Gerstorfer, Z. Schwartz, B. D. Boyan, A review on the wettability of dental implant surfaces II: biological and clinical aspects, Acta Biomater. 10 (2014) 2907–2918, https://doi.org/10.1016/j. actbio.2014.03.032

## Appendix A. Supplementary data

Supplementary Table 3.1 - Rietveld indices obtained after the refining process for all Ti grade 2 groups.

| Group | $R_{wp}$ | $R_{exp}$ | $\chi^2$ |
|---|---|---|---|
| Control | 25.40 | 23.13 | 1.2059 |
| G1 | 17.79 | 13.74 | 1.6764 |
| G2 | 21.28 | 20.61 | 1.0661 |
| G3 | 22.93 | 21.01 | 1.1911 |
| G4 | 22.67 | 20.84 | 1.1833 |
| G5 | 21.37 | 19.53 | 1.1973 |
| G6 | 14.38 | 13.18 | 1.1904 |
| G7 | 19.11 | 13.61 | 1.9715 |
| G8 | 14.92 | 12.07 | 1.5280 |
| G9 | 15.18 | 13.81 | 1.2082 |

Supplementary Table 3.2 - Rietveld indices obtained after the refining process for all Ti grade 5 groups.

| Group | $R_{wp}$ | $R_{exp}$ | $\chi^2$ |
|---|---|---|---|
| Control | 23.77 | 22.60 | 1.1062 |
| G1 | 16.47 | 12.99 | 1.6076 |
| G2 | 21.28 | 19.91 | 1.1424 |
| G3 | 22.22 | 20.09 | 1.2233 |
| G4 | 21.90 | 19.47 | 1.2652 |
| G5 | 24.46 | 20,81 | 1.3816 |
| G6 | 17.68 | 12.51 | 2 |
| G7 | 23.68 | 14.25 | 2.7614 |
| G8 | 15.32 | 12.96 | 1.40 |
| G9 | 15.46 | 13.58 | 1.2960 |

Supplementary Table 3.3 - Roughness parameters measured on all Ti grade 2 groups (mean ± standard deviation (SD)).

| Group | Ra (nm) | Rq (nm) |
|---|---|---|
| Control | 132.93 ± 3.13 | 165.55 ± 10.65 |
| G1 | 226.7 ± 3.12 | 267.72 ± 12.62 |
| G2 | 18.81 ± 2.44 | 22.39 ± 3.09 |
| G3 | 11.05 ± 3.27 | 13.5 ± 3.99 |
| G4 | 45.52 ± 2.66 | 59.93± 7.3 |
| G5 | 22.5 ± 2.71 | 28.36 ± 4.56 |
| G6 | 23.49 ± 2.38 | 28.65 ± 2.63 |
| G7 | 20.77 ± 2.33 | 26.64 ± 4.38 |
| G8 | 42.78 ± 2.16 | 52.11 ± 7.32 |
| G9 | 35.09 ± 2.79 | 44.45 ± 4.39 |

Supplementary Table 3.4 - Roughness parameters measured on all Ti grade 5 groups (mean ± standard deviation (SD)).

| Group | Ra (nm) | Rq (nm) |
|---|---|---|
| Control | 10.89 ± 2.01 | 14.5 ± 1.97 |
| G1 | 20.42 ± 1.71 | 25.31 ± 3.35 |
| G2 | 10.24 ± 2.29 | 12.71 ± 2.76 |
| G3 | 10.52 ± 1.91 | 13.36 ± 2.21 |
| G4 | 57.58 ± 2.8 | 72.52 ± 9.83 |
| G5 | 45.96 ± 2.4 | 59.71 ± 7.04 |
| G6 | 18.87 ± 1.31 | 22.83 ± 2.13 |
| G7 | 15.65 ± 2.31 | 20.14 ± 3.58 |
| G8 | 34.49 ± 2.55 | 40.05 ± 3.42 |
| G9 | 33.22 ± 2.59 | 38.82 ± 3.02 |

.

# CHAPTER 4

## AUGMENTING THE OSTEOGENIC CAPACITY OF HUMAN MESENCHYMAL STEM CELLS THROUGH THE APPLICATION OF HUMAN FIBRONECTIN COATING IN XENO-FREE AND SERUM-FREE CULTURE ENVIRONMENTS

This chapter describes in vitro culture of human mesenchymal stem cells using conventional substrates and xeno-free and serum-free cell culture reagents.

F. Melo-Fonseca[a,b,c], H. S. Domingues[c,d,e], M. Gasik[g,h], F.S. Silva[a,b], G. Miranda[i], Inês Mendes Pinto[c,f]

[a]Center for MicroElectroMechanical Systems (CMEMS-UMinho), University of Minho, Campus de Azurém, 4800-058 Guimarães – Portugal

[b]LABBELS – Associate Laboratory, Braga, Guimarães, Portugal

[c]Internaltion Iberian Nanotechnology Laboratory (INL), 4715-330 Braga, Portugal

[d]Life and Health Sciences Research Institute (ICVS), School of Medicine, University of Minho, Braga, Portugal

[e]ICVS/3B's Associate Laboratory, PT Government Associated Laboratory, Braga/Guimarães, Portugal

[g]School of Chemical Engineering, Aalto University Foundation, FI-00076 Espoo, Finland

[h]Several Ltd., Helsinki, Finland

[i]CICECO, Aveiro Institute of Materials, Department of Materials and Ceramic Engineering, University of Aveiro, 3810-193 Aveiro, Portugal

[f]Institute for Research and Innovation in Health (i3S), Porto, Portugal

**Abstract**

Human mesenchymal stem cells (MSC) hold significant promise for cell-based therapies, particularly in the context of bone diseases, due to their ability to differentiate into osteoblasts. In contrast to the *in vitro* studies previously described in literature, this study aims to investigate the osteogenic differentiation potential of MSC using exclusively xeno-free and serum-free cell culture and by substrate bio-functionalization with human fibronectin. MSC were cultured for 21 days, and their osteogenic potential was evaluated by assessing cell morphological dynamics and the formation of a mineralized matrix. Although the use of fibronectin is not essential for culturing MSC on conventional substrates, it accelerates the start of osteogenic differentiation.

**Keywords:** Mesenchymal stem cells; Osteogenesis; Fibronectin; Cytoskeleton

## 4.1. Introduction

Mesenchymal stem cells (MSC) are versatile progenitor cells with the ability to differentiate into adipocytes, osteoblasts, and chondrocytes [1]. Their stem cell-like characteristics make them particularly valuable for therapeutic purposes, especially when sourced from young and healthy individuals, as seen in allogeneic cell therapies. Moreover, MSC exhibit self-renewal capabilities, high proliferative potential, and anti-inflammatory properties, further enhancing their potential for clinical applications [2].

Since their initial discovery in 1976, when first isolated from bone marrow, MSC have been found in various other tissue sources with distinct mechanical properties, including muscle, trabecular bone, adipose tissue, and blood [3,4] and are considered as an ideal candidate for cell-based therapies targeting bone diseases. Recent progress in bone tissue engineering includes the design of polymer-based scaffolds for reconstructive orthopaedics, such as repairing skeletal defects and accelerating bone healing [5]. Additionally, metallic biomaterials, such as plates and screws, or implants for joint arthroplasties, are implanted for more severe bone lesions, including the fracture of weight-bearing long bones [6]. Current therapies use acellular matrices that can be implanted into the injured site for proper host cell colonization or scaffolds combined with stem cells that will afterward differentiate towards osteogenic lineage. However, a deeper understanding of MSC mechanobiology both on 2D and 3D environments is required to optimize the surface and bulk properties of engineered materials to promote *in vivo* osteogenesis.

MSC are highly sensitive to their environment, and their integrins recognize and bind to different adhesion sites on proteins of the extracellular matrix (ECM) [7]. This recognition leads to

the formation of focal adhesions in the intracellular part of these cell adhesion receptors, which bind to actin and myosin filaments. Non-muscle myosin-II is incorporated within the actin fibers, creating a subcellular structure – the actomyosin cytoskeleton – key for mechanosensing [8,9], intracellular force generation and mechanotransduction in a dynamic interplay with the ECM [10,11]. MSC cultured on 2D stiffer substrates have shown increased osteogenic potential correlated with increased cellular tension [12] due to spatial confinement and adhesion [13,14,15,16].

MSC are highly permissive to mechanical stimuli and have a recognized role in regenerative medicine, such as in bone applications. The majority of cell studies that focus on the osteogenic differentiation of MSC cultured on 2D substrates use conventional cell culture media, supplemented with antibiotics and serum or other xenogeneic compounds. Foetal bovine serum (FBS) is the most common serum additive to support adhesion, growth and proliferation of mammalian cells. Despite its cost effectiveness and content in adhesion molecules, growth factors, micronutrients and hormones, it presents unclear quantitative composition, large lot to lot variation, risk of initiating xenogeneic immune responses and concerns about animal welfare [17,18]. In the present study, only xeno-free and serum- free media were used to better replicate the biochemical and physiological conditions. By “xeno-free” media it is understood that only human components and chemically defined substances are included and by “serum-free” that it does not comprise any serum, either from animals or humans. This approach aims to improve the accuracy of the results by avoiding the use of substances that could interfere with the behaviour of the cells. Furthermore, the influence of employing human fibronectin as substrate functionalization on the adhesiveness of MSC was studied to accelerate osteogenic differentiation. The use of xeno-free and serum-free components during all steps of cell culture is a promising approach that could lead to more reliable and clinically relevant results in MSC research, starting from conventional substrates.

## 4.2. Materials and Methods

### 4.2.1. Cell culture

One line of bone marrow-derived human mesenchymal stem cells (MSC) was purchased from ATCC (PCS-500-012™; LGC Standard, Spain) and cells were thawed and expanded in clinically compatible xeno-free and animal serum-free culture media, as described in Table 4.1.

Table 4.1 - Origin of human derived and recombinant proteins included in the cell culture media.

| **Product name** | **Cat. No.** | **Raw material** | **Component origin** |
|---|---|---|---|
| MSC NutriStem® XF Basal Medium | 05-200-1 | Transferrin | Human |
| | | HSA | Human |
| | | rh Insulin | Non-animal |
| NutriStem® MSC XF Supplement | 05-201-1 | HSA | Human |
| | | rh TGF-β3 | Non-animal |
| | | rh bFGF | Non-animal |
| | | rh PDGFbb | Non-animal |

rh: recombinant human; HSA: human serum albumin

MSC were cultured in a complete MSC medium, composed of NutriStem® MSC Basal Medium (05-200-1A; Sartorius AG, Spain), NutriStem® MSC Supplement Mix (05-201-1U; Sartorius AG, Spain) and PLTGold® Human Platelet Lysate (PLTGold27R; Sartorius AG, Spain) in a $CO_2$ incubator (95% of air and 5% $CO_2$ at 37 °C), and a complete medium change was performed every 2-3 days. The cell culture medium is a low-protein formulation containing L-glutamine, in which the human transferrin and human serum albumin (HSA) were collected from plasma units of human donors, whereas recombinant human (rh) insulin is a biosynthetic product produced by recombinant microbial expression in yeast (Saccharomyces cerevisiae). In addition, the growth factors present in the XF Supplement were expressed in E. coli and the Human Platelet Lysate was generated from large pools of platelets from multiple donors. MSC were passaged using an animal components-free recombinant trypsin solution (03-078-1; Sartorius AG, Spain) and 1X Soybean Trypsin Inhibitor (03-048-1C; Sartorius AG, Spain) solution diluted in DPBS (14040-133; Gibco, USA) to quench the trypsin. The recombinant trypsin solution is free from undesirable proteases such as carboxypeptidase A and chymotrypsin, preventing toxic effects, and is only composed of pure enzyme solutions optimized for an efficient dissociation of adherent sensitive cells. MSC from the 3rd to 7th passages were used to evaluate the osteogenic differentiation potential on plastic and glass coverslips and the remaining were cryopreserved in MSC Freezing Solution (05-712-1E; Sartorius AG, Spain). The latter is animal component-free (ACF), serum free, protein-free formulation containing Methylcellulose and 10% of Dimethyl Sulfoxide (DMSO) which does not contain any antibiotics, antimycotics, hormones and growth factors.

### 4.2.2. Substrate preparation and osteogenic differentiation

Cells were cultured at a cell density of $3x10^4$ cells/$cm^2$ either on plastic wells or glass coverslips and incubated in a $CO_2$ incubator. Two conditions were evaluated for both substrates: uncoated and pre-coated with human fibronectin. In the former, no pre-treatment was performed whereas, in the fibronectin-coated condition, a xeno-free solution containing human fibronectin (MSC attachment solution, 05-752-1; Sartorius AG, Spain) was used to assess whether it facilitates the attachment and spreading of MSC considering the serum-free cellular culture. After 24 hrs from cells seeding, cells reached 80% confluence and the medium was changed to osteogenic differentiation medium MSCgo™ Osteogenesis XF (05- 440-1; Sartorius AG, Spain), containing L-alanine-L-glutamine, dexamethasone (DEX) and ascorbic acid, aimed to facilitate osteogenic differentiation [19–21]. Cells were then incubated for up to 21 days and the medium was changed every 2-3 days. Up to six replicates of both conditions were acquired for plastic and glass coverslips substrates, at four timepoints: 0, 7, 14 and 21 days.

### 4.2.3. Evaluation of the osteogenic differentiation capacity

#### 4.2.3.1. Cell morphology and subcellular profiling

Cell morphology was analysed with the Nikon Eclipse TS100 inverted microscope (Nikon, Japan) and images were acquired by Nikon Digital Sight DS FI1 (Nikon, Japan) digital camera.

Uncoated and pre-coated glass coverslips were used for immunocytochemistry. Cells were fixed in 4% formaldehyde in PBS (1X), permeabilized with Triton X-100 in PBS (1X) for 10 min and blocked with 3% BSA in PBS for 1 h at room temperature. Cells were washed twice with PBS and incubated at 4 °C overnight with a rabbit anti-human antibody specific for the non-muscle myosin 2 B (NM2B) (Poly-19099; Biolegend, USA) (1:1000 dilution in blocking solution). On the following day, coverslips were washed three times with PBS and a second incubation was performed for 1 h at room temperature in dark. Cells were incubated with HCS CellMask™ Deep Red stain (H32721; Thermo Fisher Scientific, USA) (1:400 dilution), which labels the entire cell (cytoplasm and nucleus), with the Cy3-conjugated AffiniPure F(ab')2 Fragment Goat Anti-Rabbit IgG secondary antibody (111-166-047; Jackson ImmunoResearch Laboratories, Inc., UK) (1:200 dilution) to label NM2B and, finally, with Alexa Fluor 488 Phalloidin (1785486; Life Technologies, USA) (1:200 dilution) to visualize F-actin. Cells were again washed three times with PBS and nuclear stained with DAPI (1729803; Life Technologies, USA) for 10 min at room temperature in dark. After three washes in PBS, glass coverslips were mounted on microscope slides with Fluoroshield™ mounting

solution (F6182-20ML; Sigma-Aldrich, USA) and stored at 4 °C for at least 1 day before imaging. Samples were imaged in the confocal microscope LSM780 (Zeiss, Germany) available at the International Iberian Nanotechnology Laboratory (INL Nanophotonics & Bioimaging and Spectroscopy facility) and processed using the ImageJ software.

#### 4.2.3.2. Mineralization analysis

For assessing the osteogenic differentiation of MSC, Alizarin Red Solution (ARS) staining was used on cellular culture in plastic wells. Briefly, cells were cleaned with PBS and incubated for 30-60 minutes in cold ethanol 70% (v/v) at room temperature. After washing three times with double-distilled water (DDW), 2% ARS (TMS-008-C; Merck Life Science, Germany), calibrated at pH 4.1-4.3, was added and incubated at room temperature for 30-60 min. The excess dye was removed and washed at least four times with DDW. In this step, the calcium secreted from cells was washed out whereas the nodular structures remained with positive staining for calcium content. DDW was then added to each well to prevent cells from dying and to prepare the plate for visual inspection and image acquisition by Nikon Eclipse TS100 inverted microscope coupled with a Nikon Digital Sight DS FI1. Afterward, the ARS staining was quantified. Hexadecylpyridinium chloride monohydrate (CPC, C9002; Merck Life Science, Germany) was added to each well to elute the stain and incubated for 1 h at room temperature. Absorbance was read at 550 nm in the spectrometer Biotek Synergy H1 Microtiter Plate Reader (Agilent, USA).

In addition to ARS staining, mineralization was also evaluated using an ImageJ plugin created by Guzmán et al. [22]. The “ColonyArea” plugin was used to calculate two output parameters in duplicate: “colony area percentage”, i.e., the percentage of area covered by calcium deposits and “colony intensity percentage” which provides information about the intensity weighted deposit area percentage (calcium deposits intensity percentage). Wells where the thresholding was not successful using the standard method, were removed from analysis.

#### 4.2.3.3. Statistical analysis

In order to investigate the differences of the ARS staining and quantification, multiple unpaired t-test was performed. In addition, statistical differences of the area percent and intensity percent obtained by the “ColonyArea” plugin between uncoated and fibronectin-coated groups were assessed by the unpaired t-test. Statistical significance was defined for $p<0.05$ and GraphPad Prism v.9 (GraphPad Software, USA) was used for all statistical analysis.

## 4.3. Results and discussion

### 4.3.1. MSC morphological profile is similar in coated and uncoated substrates

Cellular adhesion and morphology during the incubation period in osteogenic differentiation medium were similar on both uncoated and fibronectin-coated plastic wells, as represented in Fig. 4.1. Similar morphologies were observed for both coating conditions on glass coverslips (images not shown).

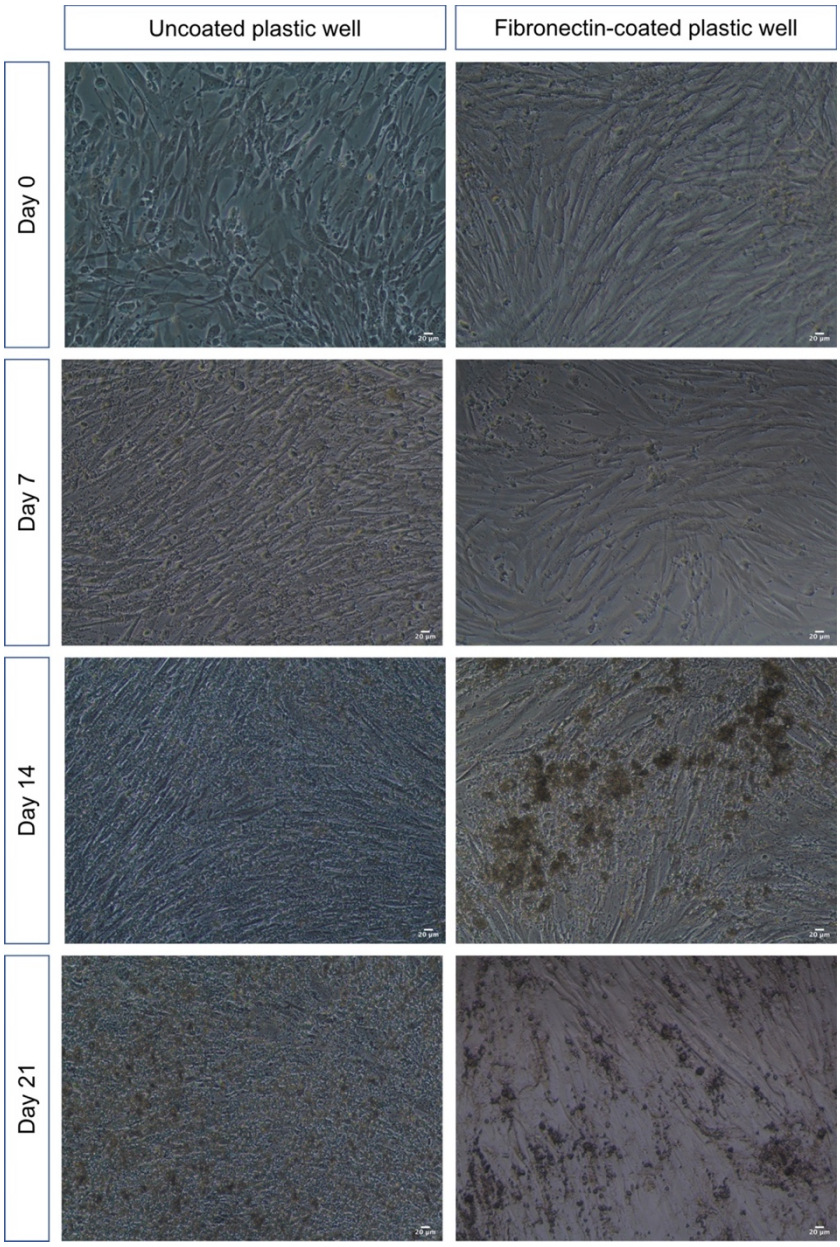



Figure 4.1 - Morphology of MSC cultured on uncoated (left) and fibronectin-coated (right) plastic wells during incubation for 21 days in osteogenic differentiation medium. All figures have a 20 μm scale bar.

During osteogenic differentiation, the fibroblast-like shape of MSC was changed to a fattened and polygonal shape of differentiated osteoblasts, as reported in other studies [23,24]. By visual

analysis, similar cell adhesion and morphology were observed either without or with a pre- coating of human fibronectin solution. The cell culture medium used for cell expansion contains proteins and cytokines that support MSC attachment and proliferation. Additionally, cell culture plastic plates are often treated so that its hydrophilic surface promotes the growth of adherent cells. Nevertheless, deposits are observed at 14 days for the fibronectin coating whereas only at 21 days for the uncoated condition, suggesting an anticipated differentiation of MSC into osteoblasts when fibronectin was used as coating.

Plastic plates are usually composed of a tissue culture polystyrene, a rigid polymer with a Young's Modulus between 2.28 and 3.38 GPa [25]. The glass coverslips, used for immunocytochemistry, are made of borosilicate glass with a Young's Modulus between 60 and 64 GPa [26] and, therefore, one order of magnitude higher than the Young's Modulus of the plastic plates. Experimental studies found that MSC differentiate towards different cell lineages in response to variations in extracellular mechanical force exerted on the cultured cells [27] and that osteogenesis is favoured when MSC are cultured on a more rigid [28] and highly adhesive substrates [29]. Despite the fact that the substrate rigidity has a direct effect on a particular cellular response and that the cortical bone stiffness is around 10-30 GPa [30,31], cell adhesion and morphology of MSC cultured either on plastic and glass coverslips were similar during the incubation period.

#### 4.3.2. Fibronectin coating promotes the osteogenic differentiation of MSC

ARS dye binds selectively to calcium salts, resulting in an ARS- calcium complex bright red stain. One mole of ARS binds to two moles of calcium and this staining is often used to evaluate the mineralization during osteogenic differentiation. MSC cultured on uncoated and fibronectin-coated plastic wells during 21 days in an osteogenic- induction medium were stained with ARS, as shown in Fig. 4.2.

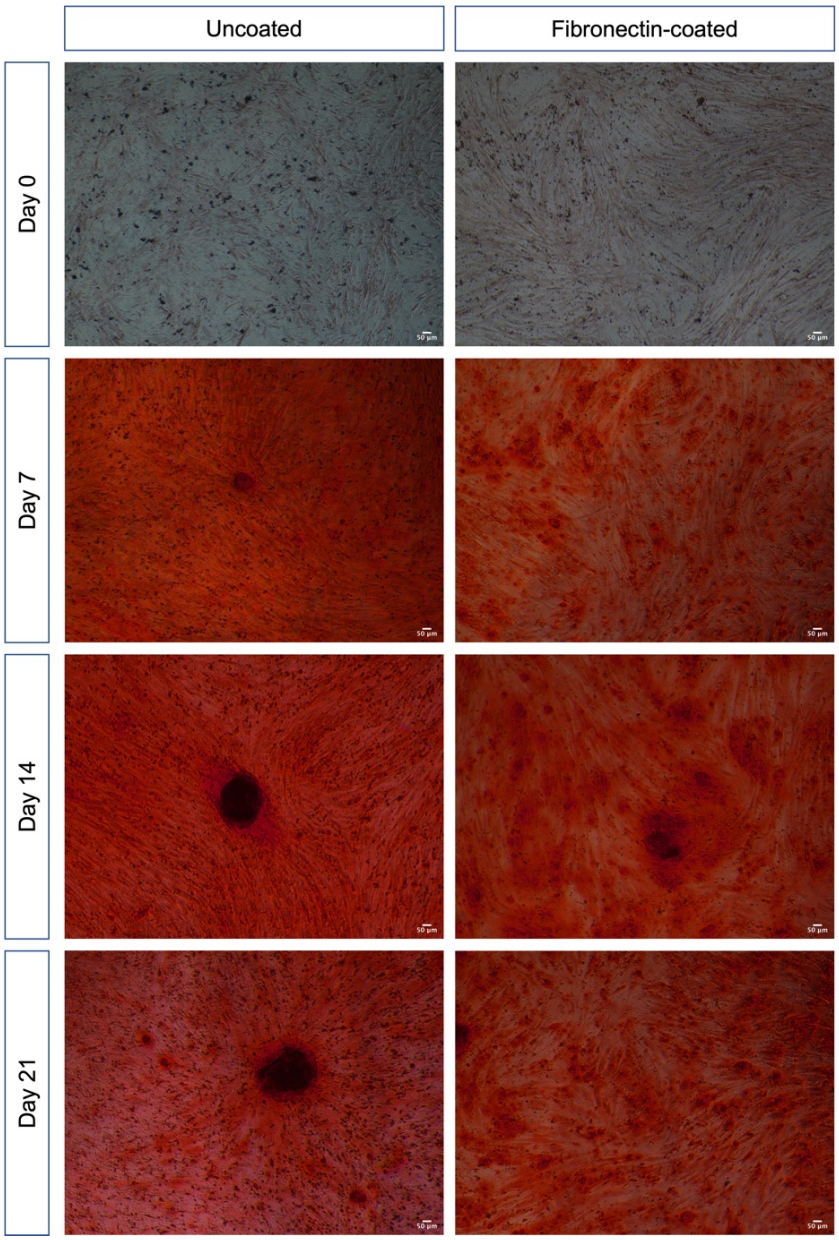



Figure 4.2 - Microscope images of MSC cultured on tissue culture plastic and stained with ARS to detect mineralization. All images include a 50 μm scale bar.

MSC were induced to osteogenic differentiation on day 0 and, by day 7, calcium deposits are positively stained by ARS, demonstrating that osteogenic differentiation has started during the first week in osteogenic differentiation medium. In addition to the visual inspection of the ARS staining, a semi-quantification of the mineralization was assessed and is graphically depicted in Fig. 4.3.

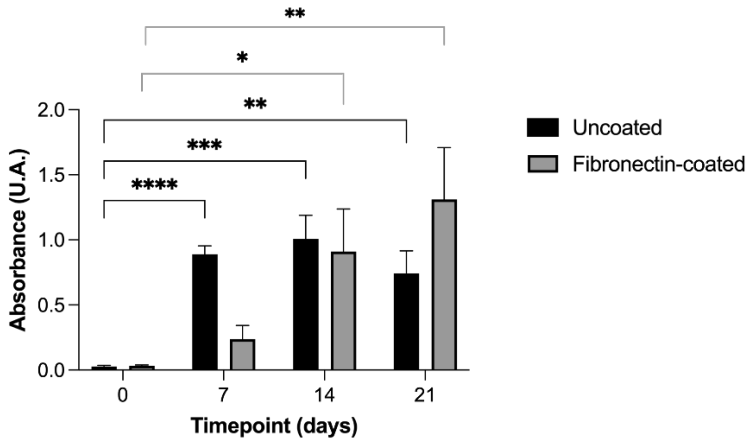



Figure 4.3 - Quantification by spectrophotometric analysis of mineralization in osteogenic- induced MSC cells cultured on uncoated and fibronectin-coated plastic wells up to 21 days. Data are shown in mean ± standard error of mean and statistically significant differences are denoted by * ($p<0.05$), ** ($p<0.01$), *** ($p<0.001$) and **** ($p<0.0001$).

Osteogenic differentiation results in the formation of mineralized culture with calcified nodules and calcium secretion. The longer incubation time in osteogenic medium, the more mineralized culture was obtained, as indicated by higher intensity of ARS staining. In the uncoated condition, the mineralization increased compared to the start of experiment and statistically significant differences were found at 7, 14 and 21 days. Differences for MSC cultured on fibronectin-coated wells were found at 14 and 21 days compared to the experiment. Culture of MSC on fibronectin-coated wells resulted in a regular increase during the incubation period whereas in the uncoated condition the mineralization increased until the 14th day and then decreased, suggesting that the level of calcium deposition saturated at 14 days. In fact, higher mineralization value was observed at day 7 for the uncoated conditions (*** $p<0.001$) however, at day 21 the highest mineralization was obtained for the fibronectin-coated group. MSC cultured either on uncoated or pre-coated plastic wells started to differentiate into osteoblasts during the first week in incubation, and the maximum staining of calcium deposits was observed at 14 and 21 days for the former and latter condition, respectively.

The “ColonyArea” ImageJ plugin [22] was used to quantify the percentage of stained area, i.e., covered by calcium deposits, and to provide information about the intensity weighted deposit area percentage, i.e., calcium deposits intensity percentage. The “ColonyArea” plugin automatically separates each well of the flatbed scanner acquired images by selecting a rectangular region of interest (ROI) and choosing the well-plate type, to then provide a stack of images. This ROI is converted to a grey scale (8-bit) and thresholded to detect the pixels containing the deposits and remove the background. Besides these images, which enable the identification of the deposits

on a white background, the computed thresholds applied to each well are displayed. The plugin then creates a new set of images, where the intensity is zero for pixels that do not contain deposits and a number between 1 and 255 for pixels that do contain, in a proportional manner. Flatbed scanner acquired images of both conditions at the four timepoints and the thresholded images for both uncoated and fibronectin-coated wells are shown in Figs. 4.4 and 4.5, respectively.

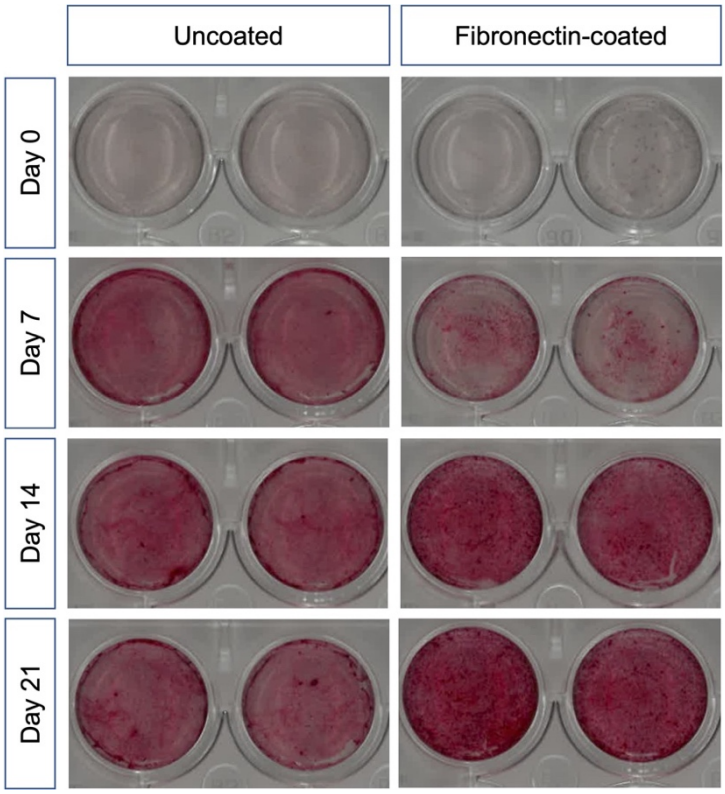



Figure 4.4 - Flatbed scanner acquired images of osteogenic-induced MSC stained with ARS, during incubation period of 21 days in osteogenic differentiation medium.

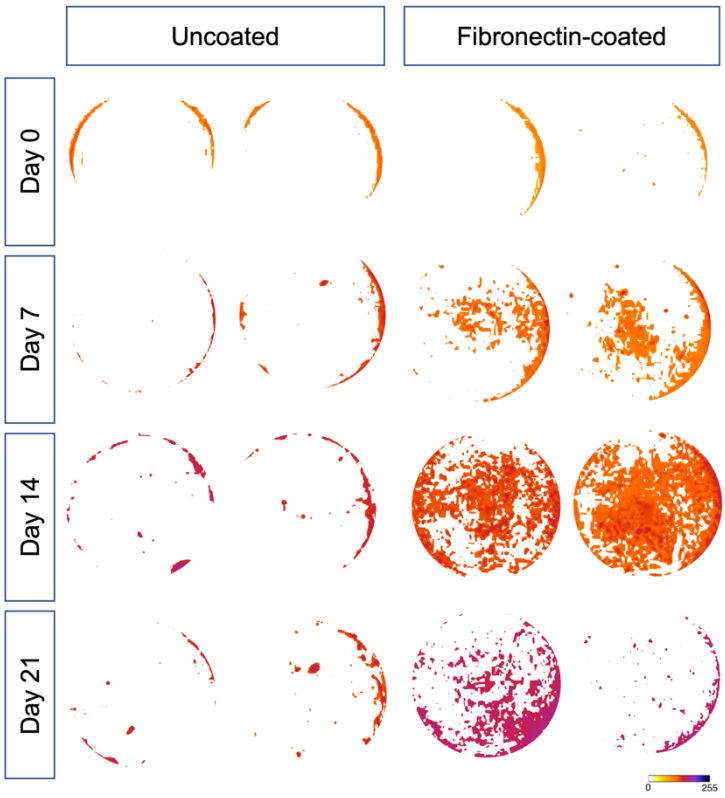



Figure 4.5 - For each timepoint, two 24 well-plate wells were cropped for both conditions and analysed by the "ColonyArea" ImageJ plugin. Colour bar represents the intensity scale displayed in the thresholded wells, where the zero intensity (white) corresponds to areas where no deposits were identified (background).

The "Colony measurer" tool was used to quantify the area percent and intensity percent of the new generated set of images. The latter parameter considers both the area covered by the deposits and their density (intensity of staining for each pixel), so higher intensity percentage reflect increasing density of deposits at any given pixel. The area percent and intensity percent values for both uncoated and fibronectin-coated conditions are graphically represented in Fig. 4.6.

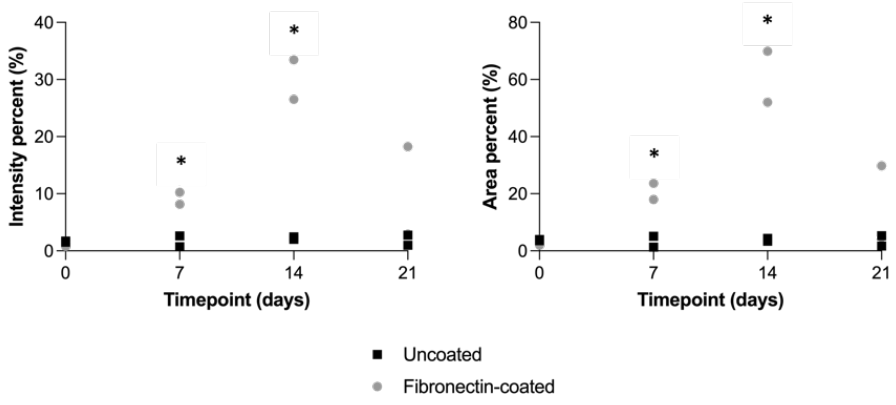



Figure 4.6 - Intensity percent and area percent plot for both uncoated and fibronectin-coated wells, during the incubation time. Data are presented as mean ± standard error of the mean and statistically significant differences are denoted by * ($p<0.05$).

Uncoated wells exhibited, approximately, the same area and intensity percentage during osteogenic differentiation. On the contrary, pre-coated wells showed an increase of the area and intensity percentages during the first three weeks of incubation and then a decrease at day 21. Therefore, for all timepoints, MSC cultured on fibronectin-coated culture plastic presented higher values of area percentage and intensity percentage of ARS staining compared to the uncoated plastic. However, this approach is presented only as an additional analysis and only limited wells were analysed. Nevertheless, considering the results obtained here, the area and intensity percentages were higher for the fibronectin-coated compared to the uncoated, presumably because of the attachment and spreading of MSC promoted by fibronectin [15,16]. ARS staining and quantification by spectrometry are commonly used to evaluate the mineralization resultant from the osteogenic differentiation. The "ColonyArea" plugin may be considered as an additional tool to evaluate the osteogenic potential as it evaluates the area and intensity of calcium mineral deposition. However, it is a computational tool and thus some factors may interfere with the results, such as some artifacts concerning background removal and can only be used in transparent substrates. On the other hand, semi-quantification is a more direct approach given that ARS is eluted and thus information of the extracellular matrix mineralization may be quantified.

### 4.3.3. Cytoskeleton architectural organization during osteogenic differentiation

Immunofluorescent images of MSC seeded on untreated and treated coverslips and subsequently induced to differentiate into bone cells were stained for DAPI, F-actin, NM2B and cell mask, as shown in Figs 4.7 and 4.8, respectively.

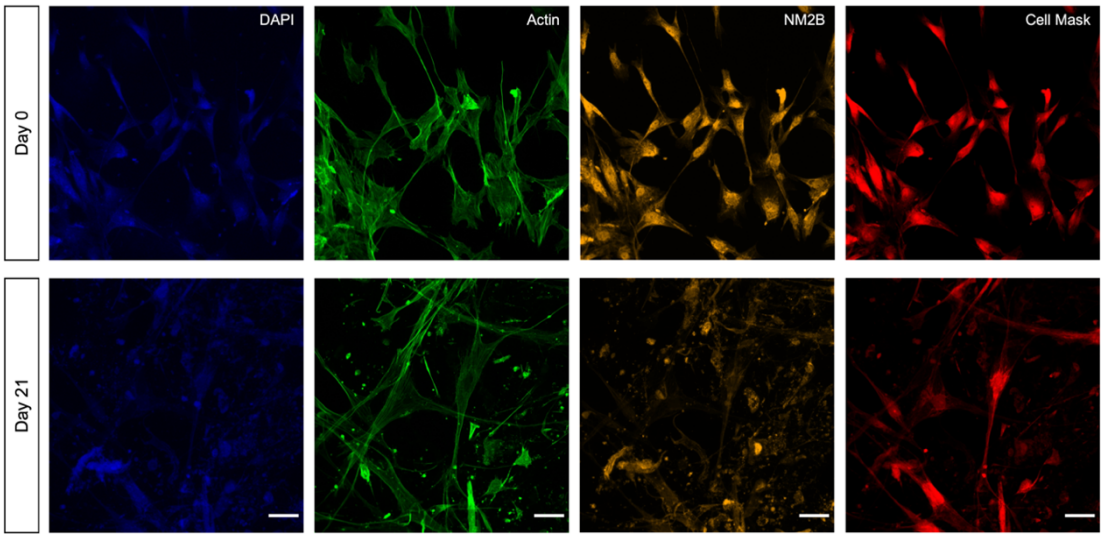



Figure 4.7 - Immunofluorescent images of induced MSC osteogenic differentiation cultured on uncoated glass coverslips. Cells are stained for nuclei (blue), F-actin (green), NM2B (orange) and cell mask (red). Images include a 50 μm scale bar.

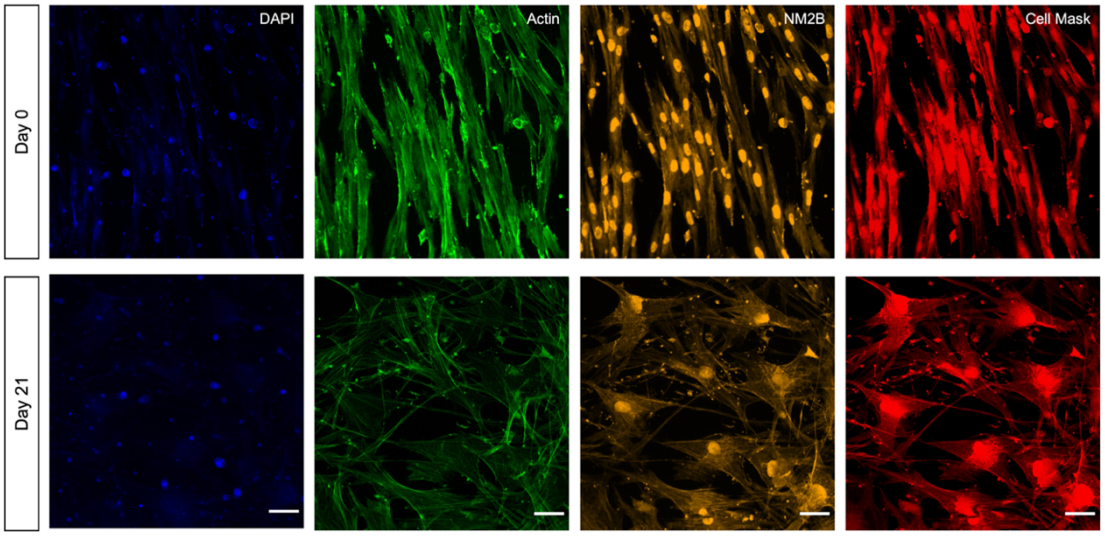



Figure 4.8 - Immunofluorescence images of induced MSC osteogenic differentiation cultured on human fibronectin-coated glass coverslips. Cells are stained for nuclei (blue), F-actin (green), NM2B (orange) and cell mask (red). Scale bar: 50 μm.

The actin cytoskeleton arrangement in stem cells differs from that of differentiated bone cells. The fibroblast-like shape of MSC is altered during the incubation period into a more cuboidal shape typical for mature osteoblasts [32]. Additionally, MSC demonstrated many thick actin fibers extending throughout the cytoplasm whereas, during osteogenic differentiation, thick stress fibers were replaced with a thinner actin cytoskeleton.

Despite the same cell confluence upon MSC seeding on glass coverslips, cells cultured on fibronectin-coated glass coverslips appear to be in higher number due to the increased adhesion promoted by fibronectin. On contrary to the plastic culture plates, glass coverslips were not treated, which could impact the adhesion and spreading of MSC. Nevertheless, changes on the cellular morphology were similar to that of plastic wells in which the osteogenic differentiation was confirmed by ARS staining. Mature osteoblasts appear to possess not only thinner actin fibers but also a lower density compared to undifferentiated MSC. Moreover, MSC display long and parallel stress fibers while, during osteogenesis, these fibers acquire a crisscross pattern, in accordance with what was reported in the literature [32–34]. Staining of F-actin and NM2B is shown in Fig. 4.9 for both conditions at days 0 and 21.

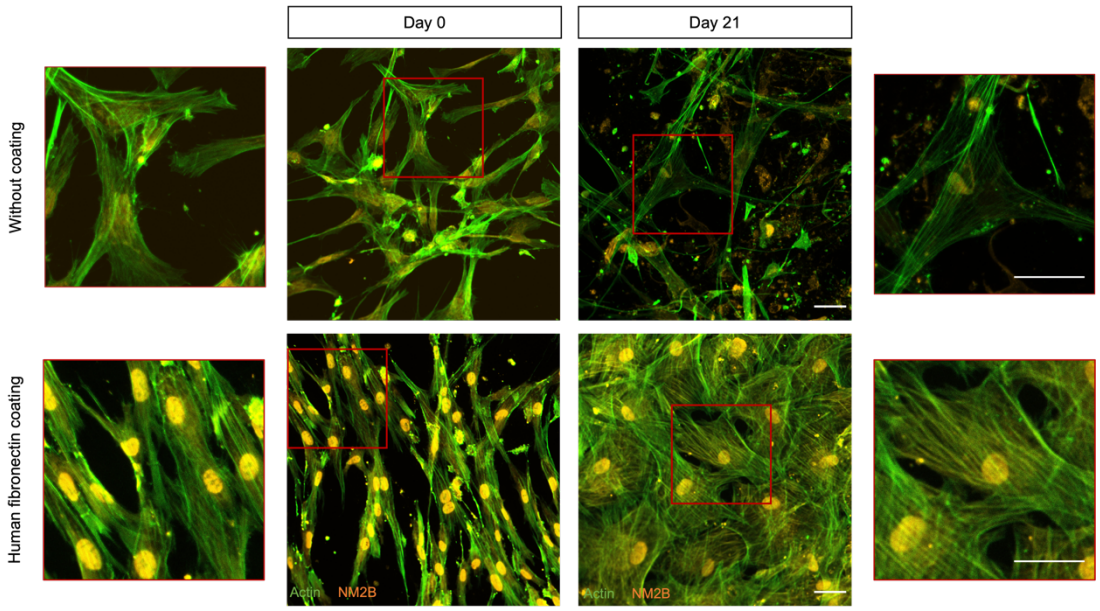



Figure 4.9 - Simultaneous staining of actin (green) and NM2B (orange) of MSC cultured on uncoated (top) and human fibronectin-coated (bottom) glass coverslips at 0 and at 21 days in osteogenic differentiation medium. Images have a scale bar of 50 μm.

By comparing the acquired images of both uncoated and fibronectin-coated coverslips, the actin cytoskeleton rearrangement during osteogenic differentiation is more notable in the human fibronectin coating condition. In the latter, disordered actin filaments at day 21 post- differentiation are notable, contrarily to the parallel and oriented actin filaments of MSC. These results suggest that the dynamic cytoskeleton reorganization regulates the osteogenic commitment of MSC, particularly when the adhesion and spreading of cells are promoted [32]. Besides actin filaments, myosin II is crucial in the molecular motor complex. Cell cytoskeleton motors are linked to focal adhesions and exert forces on actin, therefore, participating in the matrix-elasticity sensing and regulating specific lineage marker profiles [12,35]. Myosin II regulates actomyosin contractility in both muscle and non-muscle cells and three non-muscle isoforms known as non-muscle myosin IIA-C were identified in mammalian cells which expression was found in smooth, skeletal and cardiac muscles [36]. Myosin II has been described in the nucleus [37] and its staining is visible in both conditions, especially in the fibronectin-coated at 0 and 21 days. Kilian and Mrksich cultured MSC in a medium supplemented with blebbistatin, an inhibitor of non-muscle myosin, which was shown to compromise osteogenesis [38]. This suggests, therefore, that not only the actin cytoskeleton remodelling but also the dynamics of NM2B appear to regulate the fate of MSC. In the same study, after 10 days under standard growth conditions, osteogenesis was promoted on fibronectin-coated and high-affinity cyclic peptide ligands (cycRGD) substrates, on which cells proliferated and displayed a cuboidal phenotype. In addition, monolayers having a high-affinity

ligand promoted a more contractile cytoskeleton which induced osteogenic differentiation. In fact, monolayers presenting cycRGD displayed a higher degree of spreading, more stress fibers, and more focal adhesion structures and higher expression levels of NM2B when compared to cells on monolayers presenting linear peptide ligands (linRGD) [38]. Discher et al. concluded that MSC cultured on stiff matrices displayed an expression of NM2B up more than 2-fold relative to myosin level before differentiation [12], suggesting that osteogenesis may be particularly dependent on myosin II-based contractility. Ouyang et al. used human tendon stem/progenitor cells and observed a high-level expression of NM2B in oriented cells, reflecting strong actin-myosin contractions in response to a conformation to the mechanical environment [39]. Therefore, NM2B expression plays an important role in regulating the cytoskeleton and consequently on the osteogenic commitment of MSC.

## 4.4. Conclusions

MSC cultured on both plastic and glass substrates, either without or with human fibronectin coating, were performed using exclusively serum-free and xeno-free media. Alizarin red staining showed a higher mineralized culture with calcified nodules in the human fibronectin pre-coated plastic wells. Nevertheless, mineralization increased in both conditions compared to the beginning of experiment. During cell incubation in osteogenic differentiation medium, cell morphology was altered similarly in both plastic and glass materials, both substrates typically used in in vitro cell experiments. Cellular contractility and cytoskeleton tension are known to modulate the fate of MSC and, during osteogenic differentiation, major differences in the organization of actin stress fibers across the cell were perceived. Besides the important role of actin, NM2B appears to regulate the cellular commitment and fate.

## Acknowledgments

This work was supported by FCT (Fundação para a Ciência e a Tecnologia) through the grant SFRH/BD/141056/2018, and the projects POCI-01-0145-FEDER-030498 and UID/EEA/04436/2019.

## References

[1] P. Garg, M.M. Mazur, A.C. Buck, M.E. Wandtke, J. Liu, N.A. Ebraheim, Prospective Review of Mesenchymal Stem Cells Differentiation into Osteoblasts, Orthop. Surg. 9 (2017) 13–19. https://doi.org/10.1111/os.12304.

[2] A. Uccelli, L. Moretta, V. Pistoia, Mesenchymal stem cells in health and disease, Nat. Rev. Immunol. 8 (2008) 726–736. https://doi.org/10.1038/nri2395.

[3] A.J. Friedenstein, J.F. Gorskaja, N.N. Kulagina, Fibroblast precursors in normal and irradiated mouse hematopoietic organs, Exp. Hematol. 4 (1976) 267–274. http://europepmc.org/abstract/MED/976387.

[4] D.T. Chu, T.N.T. Phuong, N.L.B. Tien, D.K. Tran, V. Van Thanh, T.L. Quang, D.T. Truong, V.H. Pham, V.T.N. Ngoc, T. Chu-Dinh, K. Kushekhar, An update on the progress of isolation, culture, storage, and clinical application of human bone marrow mesenchymal stem/stromal cells, Int. J. Mol. Sci. 21 (2020). https://doi.org/10.3390/ijms21030708.

[5] L. Roseti, V. Parisi, M. Petretta, C. Cavallo, G. Desando, I. Bartolotti, B. Grigolo, Scaffolds for Bone Tissue Engineering: State of the art and new perspectives, Mater. Sci. Eng. C. 78 (2017) 1246–1262. https://doi.org/10.1016/j.msec.2017.05.017.

[6] R. Agarwal, A.J. García, Biomaterial strategies for engineering implants for enhanced osseointegration and bone repair, Adv. Drug Deliv. Rev. 94 (2015) 53–62. https://doi.org/10.1016/j.addr.2015.03.013.

[7] J.Z. Kechagia, J. Ivaska, P. Roca-Cusachs, Integrins as biomechanical sensors of the microenvironment, Nat. Rev. Mol. Cell Biol. 20 (2019) 457–473. https://doi.org/10.1038/s41580-019-0134-2.

[8] J. Klein-Nulend, R.G. Bacabac, A.D. Bakker, Mechanical loading and how it affects bone cells: The role of the osteocyte cytoskeleton in maintaining our skeleton, Eur. Cells Mater. 24 (2012) 278–291. https://doi.org/10.22203/eCM.v024a20.

[9] C. Wittkowske, G.C. Reilly, D. Lacroix, C.M. Perrault, In Vitro Bone Cell Models: Impact of Fluid Shear Stress on Bone Formation, Front. Bioeng. Biotechnol. 4 (2016) 1–22. https://doi.org/10.3389/fbioe.2016.00087.

[10] A.A. Wasik, H.B. Schiller, Functional proteomics of cellular mechanosensing mechanisms, Semin. Cell Dev. Biol. 71 (2017) 118–128. https://doi.org/10.1016/j.semcdb.2017.06.019.

[11] H.B. Schiller, R. Fässler, Mechanosensitivity and compositional dynamics of cell-matrix adhesions, EMBO Rep. 14 (2013) 509–519.https://doi.org/10.1038/embor.2013.49.

[12] A.J. Engler, S. Sen, H.L. Sweeney, D.E. Discher, Matrix Elasticity Directs Stem Cell Lineage Specification, Cell. 126 (2006) 677–689. https://doi.org/10.1016/j.cell.2006.06.044.

[13] K.A. Kilian, B. Bugarija, B.T. Lahn, M. Mrksich, Geometric cues for directing the differentiation of mesenchymal stem cells, Proc. Natl. Acad. Sci. 107 (2010) 4872– 4877. https://doi.org/10.1073/pnas.0903269107.

[14] M. Guo, A.F. Pegoraro, A. Mao, E.H. Zhou, P.R. Arany, Y. Han, D.T. Burnette, M.H. Jensen, K.E. Kasza, J.R. Moore, F.C. Mackintosh, J.J. Fredberg, D.J. Mooney, J. Lippincott-Schwartz, D.A. Weitz, Cell volume change through water efflux impacts cell stiffness and stem cell fate, Proc. Natl. Acad. Sci. U. S. A. 114 (2017) E8618– E8627. https://doi.org/10.1073/pnas.1705179114.

[15] L.A. Hidalgo-Bastida, S.H. Cartmell, Mesenchymal stem cells, osteoblasts and extracellular matrix proteins: Enhancing cell adhesion and differentiation for bone tissue engineering, Tissue Eng. - Part B Rev. 16 (2010) 405–412. https://doi.org/10.1089/ten.teb.2009.0714.

[16] N. Ogura, M. Kawada, W.J. Chang, Q. Zhang, S.Y. Lee, T. Kondoh, Y. Abiko, Differentiation of the human mesenchymal stem cells derived from bone marrow and enhancement of cell attachment by fibronectin, J. Oral Sci. 46 (2004) 207–213. https://doi.org/10.2334/josnusd.46.207.

[17] M. Guiotto, W. Raffoul, A.M. Hart, M.O. Riehle, P.G. Di Summa, Human platelet lysate to substitute fetal bovine serum in hMSC expansion for translational applications: A systematic review, J. Transl. Med. 18 (2020) 1–14. https://doi.org/10.1186/s12967-020-02489-4.

[18] H. Hemeda, B. Giebel, W. Wagner, Evaluation of human platelet lysate versus fetal bovine serum for culture of mesenchymal stromal cells, Cytotherapy. 16 (2014) 170– 180. https://doi.org/10.1016/j.jcyt.2013.11.004.

[19] M.B. Sordi, R.B. Curtarelli, I.T. da Silva, G. Fongaro, C.A.M. Benfatti, R. de Souza Magini, A.C. Cabral da Cruz, Effect of dexamethasone as osteogenic supplementation in in vitro osteogenic differentiation of stem cells from human exfoliated deciduous teeth, J. Mater. Sci. Mater. Med. 32 (2021) 1–9. https://doi.org/10.1007/s10856-020- 06475-6.

[20] R.D.C. Moretti, M.T. Duailibi, P.O. Martins, J.A. Dos Santos, S.E. Duailibi, Osteoinductive effects of preoperative dexamethasone in human dental pulp stem cells primary culture, Futur. Sci. OA. 3 (2017). https://doi.org/10.4155/fsoa-2016-0083.

[21] F. Langenbach, J. Handschel, Effects of dexamethasone, ascorbic acid and β-glycerophosphate on the osteogenic differentiation of stem cells in vitro, Stem Cell Res. Ther. 4 (2013). https://doi.org/10.1186/scrt328.

[22] C. Guzmán, M. Bagga, A. Kaur, J. Westermarck, D. Abankwa, ColonyArea: An ImageJ plugin to automatically quantify colony formation in clonogenic assays, PLoS One. 9 (2014) 14–17. https://doi.org/10.1371/journal.pone.0092444.

[23] H. Hanna, L.M. Mir, F.M. Andre, In vitro osteoblastic differentiation of mesenchymal stem cells generates cell layers with distinct properties, Stem Cell Res. Ther. 9 (2018) 1–11. https://doi.org/10.1186/s13287-018-0942-x.

[24] T. Bongiorno, J. Kazlow, R. Mezencev, S. Griffiths, R. Olivares-Navarrete, J.F. McDonald, Z. Schwartz, B.D. Boyan, T.C. McDevitt, T. Sulchek, Mechanical stiffness as an improved single-cell indicator of osteoblastic human mesenchymal stem cell differentiation, J. Biomech. 47 (2014) 2197–2204. https://doi.org/10.1016/j.jbiomech.2013.11.017.

[25] D.G. Callister Jr, W. D., & Rethwisch, Fundamentals of materials science and engineering: an integrated approach, John Wiley & Sons., 2012.

[26] M.M.P. Data, Borosilicate Glass, (n.d.). http://www.matweb.com/index.aspx (accessed February 3, 2020).

[27] A. Barui, F. Chowdhury, A. Pandit, P. Datta, Rerouting mesenchymal stem cell trajectory towards epithelial lineage by engineering cellular niche, Biomaterials. 156 (2018) 28–44. https://doi.org/10.1016/j.biomaterials.2017.11.036.

[28] J.S. Park, J.S. Chu, A.D. Tsou, R. Diop, Z. Tang, A. Wang, S. Li, The effect of matrix stiffness on the differentiation of mesenchymal stem cells in response to TGF-b, Biomaterials. 32 (2011) 3921–3930. https://doi.org/10.1016/j.biomaterials.2011.02.019.

[29] H. Lv, L. Li, M. Su, Y. Zhang, L. Chen, Y. Rong, Y. Li, Mechanism of regulation of stem cell differentiation by matrix stiffness, Stem Cell Res. Ther. 6 (2015) 1–11. https://doi.org/10.1186/s13287-015-0083-4.

[30] Q. Chen, G.A. Thouas, Metallic implant biomaterials, Mater. Sci. Eng. R Reports. 87 (2015) 1–57. https://doi.org/10.1016/j.mser.2014.10.001.

[31] D. Apostu, O. Lucaciu, C. Berce, D. Lucaciu, D. Cosma, Current methods of preventing aseptic loosening and improving osseointegration of titanium implants in cementless total hip arthroplasty: a review, J. Int. Med. Res. 46 (2018) 2104–2119. https://doi.org/10.1177/0300060517732697.

[32] I. Titushkin, M. Cho, Modulation of cellular mechanics during osteogenic differentiation of human Mesenchymal Stem Cells, Biophys. J. 93 (2007) 3693–3702. https://doi.org/10.1016/j.jbiomech.2011.07.024.

[33] G. Yourek, M.A. Hussain, J.J. Mao, Cytoskeletal changes of mesenchymal stem cells during differentiation, ASAIO J. 53 (2007) 219–228. https://doi.org/10.1097/MAT.0b013e31802deb2d.

[34] I.A. Titushkin, M.R. Cho, Controlling cellular biomechanics of human mesenchymal stem cells, in: Proc. 31st Annu. Int. Conf. IEEE Eng. Med. Biol. Soc. Eng. Futur. Biomed. EMBC 2009, 2009: pp. 2090–2093. https://doi.org/10.1109/IEMBS.2009.5333949.

[35] G.H. Koenderink, E.K. Paluch, Architecture shapes contractility in actomyosin networks, Curr. Opin. Cell Biol. 50 (2018) 79–85. https://doi.org/10.1016/j.ceb.2018.01.015.

[36] K. Clark, M. Langeslag, C.G. Figdor, F. N. van Leeuwen, Myosin II and mechanotransduction: a balancing act, Trends Cell Biol. 17 (2007) 178–186. https://doi.org/10.1016/j.tcb.2007.02.002.

[37] P. De Lanerolle, Nuclear actin and myosins at a glance, J. Cell Sci. 125 (2012) 4945–4949. https://doi.org/10.1242/jcs.099754.

[38] K.A. Kilian, M. Mrksich, Directing stem cell fate by controlling the affinity and density of ligand-receptor interactions at the biomaterials interface, Angew. Chemie -Int. Ed. 51 (2012) 4891–4895. https://doi.org/10.1002/anie.201108746.

[39] Z. Yin, X. Chen, J.L. Chen, W.L. Shen, T.M. Hieu Nguyen, L. Gao, H.W. Ouyang, The regulation of tendon stem cell differentiation by the alignment of nanofibers, Biomaterials. 31 (2010) 2163–2175. https://doi.org/10.1016/j.biomaterials.2009.11.083.

# CHAPTER 5

## ENGINEERING A HYBRID TI6AL4V-BASED SYSTEM FOR RESPONSIVE AND CONSISTENT OSTEOGENESIS

Submitted to an ISI index journal.

F. Melo-Fonseca[a,b,c,*], M. Gasik[d], A. Cruz[c], D. Moreira[e], F. S. Silva[a,b], G. Miranda[f], I. M. Pinto[e,*]

[a]Center for MicroElectroMechanical Systems (CMEMS-UMinho), University of Minho, Campus de Azurém, 4800-058 Guimarães – Portugal

[b]LABBELS – Associate Laboratory, Braga, Guimarães, Portugal

[c]Internaltion Iberian Nanotechnology Laboratory (INL), 4715-330 Braga, Portugal

[d]School of Chemical Engineering, Aalto University Foundation, FI-00076 Espoo, Finland

[e]Institute for Research and Innovation in Health (i3S), Porto, Portugal

[f]CICECO, Aveiro Institute of Materials, Department of Materials and Ceramic Engineering, University of Aveiro, 3810-193 Aveiro, Portugal

[*]Corresponding author

G. Miranda and I. M. Pinto share co-last authorship.

**Abstract**

As the aging population increases worldwide, the incidence of musculoskeletal diseases and the need for orthopaedic implants also arises. One of the most desirable goals in orthopaedic reconstructive therapies is de novo bone formation. Yet, reproducible, long-lasting and cost-effective strategies for implants that strongly induce osteogenesis are still in need.

Nanoengineered titanium substrates (and their alloys) are among the most used materials in orthopaedic implants. Although having high biocompatibility, titanium alloys hold a low bioactivity profile. The osteogenic capacity and osseointegration of Ti-based implantable systems is limited, as they critically depend on the body–substrate interactions defined by blood proteins adsorbed into implant surfaces that ultimately lead to the recruitment, proliferation, and differentiation of mesenchymal stem cells (MSC) to comply bone formation and regeneration.

In this work, a hybrid Ti6Al4V system combining micro and nanoscale modifications induced by hydrothermal treatment followed by a functionalization with a bioactive compound (fibronectin derived from human plasma) is proposed, aiming for bioactivity improvement. An evaluation of the biological activity and cellular responses in vitro with respect to bone regeneration indicated that the integration of morphological and chemical modification into Ti6Al4V surfaces induce the osteogenic differentiation of MSC to improve bone regeneration by an enhancement of the mineral matrix formation that accelerates the osseointegration process. Overall, this hybrid system has numerous competitive advantages over more complex treatments, including reproducibility, low production cost and potential for improved long-term maintenance of the implant.

**Keywords:** Orthopaedic implants; Titanium; Hydrothermal treatment; Fibronectin; Mesenchymal stem cells; Osteogenesis

## 5.1. Introduction

Osteoarthritis (OA) is a heterogenous disorder that, according to the Osteoarthritis Research Society International, “manifests first as a molecular derangement (abnormal joint tissue metabolism) followed by anatomic, and/or physiologic derangements (characterized by cartilage degradation, bone remodelling, osteophyte formation, joint inflammation and loss of normal joint function), that can culminate in illness” [1]. It is estimated to affect more than 240 million persons worldwide and more than 32 million only in the US [2]. Obesity, prior joint injuries, and genetics are the main risk factors for OA, whose dominant symptom is pain. Radiographs of patients with advanced osteoarthritis typically reveal osteophytes and narrowed joint spaces due to cartilage

loss. When physical rehabilitation and pharmacological treatments are not sufficient to relieve pain, joint replacement surgery is recommended [2]. Despite advancements in orthopaedic implant research and that total joint replacement is considered a clinically relevant and cost-effective treatment for end-stage OA, implant failures still occur. Up to 25% of patients report ongoing pain and disability one year following surgery [3] and, even when the results are satisfactory, the successful rate tends to decrease a decade after surgery, leading to revision surgeries and implant replacement [4].

Endosseous implants are made of commercially pure titanium (Ti) or titanium alloys, such as the Titanium 6-Aluminium 4-Vanadium (Ti6Al4V) alloy, whose implantation success and stability are multi-factorial dependent. The patient's bone quality, the selected surgical protocol, and the properties of the implant, such as its surface and geometry determined by the manufacturer, affect the clinical outcome. Considering the implant's environment, its stability is determined by the biomechanical properties of the bone-implant interface [5]. Nowadays, cementless implants are preferred and inserted in the bone cavity using the 'press-fit' technique, providing stability just after surgical insertion, i.e., primary stability. Afterwards, during the healing period, bone adapts its structure in response to the mechanical stress and starts to remodel. The properties of the newly formed bone tissue dictate the secondary stability which depends on the implant properties, such as its stiffness and surface topology [5].

Modifications on the surface of biomaterials may affect their physical and chemical properties which remarkably affect the cell behaviour. Therefore, in recent years, efforts have been made to provide an optimal microenvironment able to promote the adhesion and differentiation of mesenchymal stem cells (MSC) into bone cells and assure early and long-term biological stability of the implant [6,7]. Biocoatings confer bioactivity to Ti-based implants and improve their resistance to corrosion and wear stress. The recent developments in antimicrobial, protective and functional coatings of orthopaedic implants were reviewed by Kumar et al. [6]. Coatings with biomolecules, such as the extracellular matrix (ECM) proteins collagen [8–10] and fibronectin [11–14] enhance osteoinduction. Another alternative is the formation of a titanium dioxide layer whose wettability, roughness and crystallinity accelerate cellular regeneration [15,16]. This layer may be formed by different surface modification techniques, from complex, such as anodization [17,18], to simple and economic, such as hydrothermal treatment [19,20]. In a previous study, hydrothermally treated Ti6Al4V samples presented a moderate hydrophilic layer with both anatase and rutile crystalline phases [19]. In addition, the single step hydrothermal treatment on Ti-based substrates

confers antibacterial properties [21], promotes osteoblastic lineage [22] and enhances osteoconductivity *in vivo* [23].

Current orthopaedic implants lack the necessary biomechanical stimulus at the bone-implant interface, which compromises their long-term success. This study aims to investigate the effectiveness of three treatments in promoting adhesion and osteogenic differentiation of MSC, ultimately enhancing the adhesiveness and sustainability of the substrate-cell complex. The treatments considered are hydrothermal treatment to form a titanium dioxide (anatase and rutile) layer, biocoating with fibronectin (an osteogenic matrix protein), and a combination of both treatments. The goal of this study is to improve implant stability during the early healing phase and induce osteogenic differentiation, thus potentially prolonging the lifespan of orthopaedic implants.

## 5.2. Materials and methods

### 5.2.1. Preparation of Ti6Al4V samples

Ti6Al4V alloy (Ti grade 5) plates of dimensions 45 x 10 x 0.5 mm were acquired from Titanium Products Limited (United Kingdom) and cut into 2D substrates of 9 x 10 x 0.5 mm using a Nd:YV04 laser (XM-30D, XianMing Laser, China).

2D substrates were characterized in terms of roughness and wettability, as previously described [19]. As received samples presented an arithmetic average roughness value (Ra) of 10.89 ± 2.01 nm and water contact angle of 85 ± 3.5°, after autoclaving [19]. Samples were cleaned with ultrasonic rinsing with ethanol, dried in air and then divided into four groups: control (Ti-O), hydrothermal treatment (Ti-H), human fibronectin coating (Ti-OC) and hydrothermal treatment followed by human fibronectin coating (Ti-HC), as displayed in Fig. 5.1. Samples subjected to hydrothermal treatment were immersed in a polytetrafluoroethylene (PTFE, Teflon) beaker with 80 mL of distilled water and placed inside a proprietary designed reactor. Treatment was carried out at 180 °C for 180 min, and samples were removed and cooled at room temperature. Subsequently, all samples were sterilized by immersion in ethanol 70% (v/v) for 1 hour (each side) followed by irradiation by UVC light for 2 hrs (each side). Sterile Ti6Al4V samples were stored in 5 times concentrated phosphate buffered saline (5XPBS) for 24 hrs. The PBS solution was prepared from PBS tablets (A9201; PanReac AppliChem ITW Reagents, USA), which composition is 2.7 mM KCl, 140 mM NaCl and 10mM phosphate, at a pH of 7.4 (25 °C)

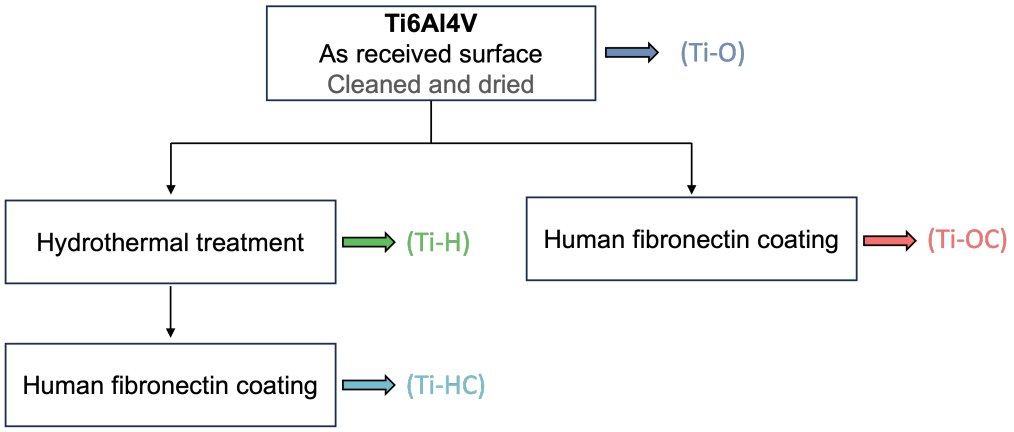



Figure 5.1 - Groups detailed description.

### 5.2.2. Cell culture and osteogenic differentiation of MSC

Bone marrow-derived human mesenchymal stem cells (MSC) were purchased from ATCC (PCS-500-012TM; LGC Standard, Spain). Cells were thawed and expanded in clinically compatible xeno-free, animal serum-free culture media, according to the Sartorius AG protocols. MSC were cultured in a complete MSC medium, composed of NutriStem® MSC Basal Medium (05-200-1A; Sartorius AG, Spain), NutriStem® MSC Supplement Mix (05-201-1U; Sartorius AG, Spain) and PLTGold® Human Platelet Lysate (PLTGold27R; Sartorius AG, Spain) in a $CO_2$ incubator (95% of air and 5%$CO_2$ at 37 °C), and a complete medium change was performed every 3 days. MSC were passaged using an animal components-free recombinant trypsin solution (03-078-1; Sartorius AG, Spain). MSC from the 3rd to 7th passages were used for osteogenic differentiation and the remaining were cryopreserved in MSC freezing solution (05-712-1E; Sartorius AG, Spain).

MSC were seeded on Ti6Al4V groups with no treatment (Ti-O), with hydrothermal treatment (Ti-H) and on both groups coated with human plasma-derived fibronectin (05-752-1, PRIME-XV Human Fibronectin; FUJIFILM Irvine Scientific, The Netherlands), correspondent to Ti-OC and Ti-HC, respectively. The plates correspondent to groups Ti-OC and Ti-HC were immersed in human fibronectin solution (5 µg/mL) and incubated overnight at 4 °C. MSC were seeded on all samples at a cellular density of $3x10^4/cm^2$. After 24 hrs of MSC seeding, the medium was changed to a calcium free osteogenic differentiation medium (05-440-1; Sartorius AG, Spain), containing dexamethasone (DEX) and ascorbic acid. Cells were incubated for up to 21 days and the medium was changed every 3 days.

### 5.2.3. Evaluation of the osteogenic capacity of MSC

#### 5.2.3.1. Measurement of calcium deposition

The osteogenic capacity of MSC in different Ti treated substrates and at different timepoints (0 to 21 days) was determined by Alizarin Red Solution (ARS). Briefly, the supernatant was removed, cells were washed with PBS and incubated with cold EtOH 70% for 30-60 minutes at room temperature. After washing three times with double-distilled water (DDW), fixed cells were stained with 2% ARS at pH 7.2 (TMS-008-C; Merck Life Science, Germany) and incubated at room temperature for 30-60 minutes. The excess dye was removed and washed at least four times with DDW. In this step, the calcium secreted from cells was washed out whereas the nodular structures remained with positive staining for calcium content. DDW was then added to each well to prevent cells from drying and to prepare the plates for visual inspection and image acquisition by Nikon Eclipse LV 100 ND (Nikon, Japan). Afterwards, a semi-quantitative assessment of the extracellular matrix mineralization was performed by ARS elution. 10% (w/v in DDW) of hexadecylpyridinium chloride monohydrate (CPC, C9002; Merck Life Science, Germany) was added to each well and incubated at room temperature for 1 h to de-stain cultures. The absorbance was then read at 550 nm using the spectrometer Biotek Synergy H1 Microtiter Plate Reader (Agilent, USA). The mineralization mean was determined by averaging five to six absorbance values and data are provided as mean ± standard error of the mean. The mineralization kinetics were estimated in intervals of 7 days by calculating the slope ($\Delta$absorbance/$\Delta$time).

#### 5.2.3.2. Analysis of Quantitative Real-Time Polymerase Chain Reaction (qRT-PCR)

The expression of osteogenic genes in MSC was examined by real-time quantitative reverse transcription-polymerase chain reaction (qRT-PCR). Total RNA was extracted from cultured cells at 0 and 21 days, in triplicate, using the NZY Total RNA Isolation kit (MB13402; nzytech, Portugal), according with manufacturer's instructions. RNA was treated with DNase I with the RNase Free DNase Set (79254; Qiagen GMBH, USA) and concentrated with the RNeasy MinElute Cleanup Kit (74204; Qiagen GMBH, USA). Purified RNA was transcribed into complementary DNA (cDNA) using the NZY First-Strand cDNA Synthesis kit (MB12501; nzytech, Portugal), according with the manufacturer's protocol, in a Veriti Thermal Cycler (Applied BiosystemsTM, Foster City, USA). Real-time PCR was performed using the NZY qPCR Green Master Mix (2x), ROX plus (MB21902; nzytech, Portugal), according with the manufacturer's instructions. Briefly, the PCR reaction volume included 5 µl of one-step NZY qPCR green master mix (2x), ROX, 0.4 µl of each primer (400 nM),

1 µl of cDNA template and 3.2 µl of RNA-free water, for a total of 5 µl per sample dispensed in each well.

All the experiments were performed in a StepOne PlusTMReal-Time PCR system (Applied BiosystemsTM, USA) with the StepOne™ Software v2.3. For the reaction conditions, initial activation was performed at 50 °C for 20 min and 95 °C for 10 min, followed by 40 cycles of thermal denaturation at 95 °C for 15 s, and annealing and elongation at 60 °C for 1 min. The melting curve stage was performed at 95 °C for 15 s, 60 °C for 1 min, 95 °C for 15 s and finally 60 °C for 15 s. A melting curve analysis was performed at the end of program to determine the validity of experimental results. All reactions were performed in triplicate.

Gene specific primers for human osteocalcin (OC), osteopontin (OPN), bone-morphogenetic protein 2 (BMP-2), alkaline phosphatase (ALP), runt-related transcription factor 2 (RUNX2) and glyceraldehyde-3-phosphate dehydrogenase (GAPDH) were designed by Eurofins Genomics (Austria), as shown in Table 5.1.

Table 5.1 - RT-PCR primers used for osteogenic gene expression.

| **Gene** | **Forward (5'-3')** | **Reverse (3'-5')** |
|---|---|---|
| OC | GAAGCCCAGCGGTGCA | CACTACCTCGCTGCCCTCC |
| OPN | CTCAGGCCAGTTGCAGCC | CAAAAGCAAATCACTGCAATTCTC |
| BMP2 | AACACTGTGCGCAGCTTCC | CTCCGGGTTGTTTTCCCAC |
| ALP | GACCCTTGACCCCCACAAT | GCTCGTACTGCATGTCCCCT |
| RUNX2 | TGTCATGGCGGGTAACGAT | AAGACGGTTATGGTCAAGGTGAA |
| GAPDH | TGGAGTCTACTGGCGTCTT | TGTCATATTTCTCGTGGTTCA |

Nucleobases: adenine (A), cytosine (C), guanine (G) and thymine (T)

The expression levels of the tested genes were determined by calculating cycle threshold (Ct) values on the StepOne™ Software version 2.3. Data were normalized based on the mRNA levels of the house-keeping gene GAPDH, and by using the $2^{-\Delta\Delta Ct}$ method, as described in [24]. Data are presented as mean ± standard error of the mean.

5.2.3.3. Statistical analysis

Statistical software GraphPad Prism v.9 (GraphPad Software, USA) was used for all analysis, and level of $p<0.05$ was considered as statistically significant considering normal distribution of

the data. Differences in mineralization at different timepoints and treatments were assessed by two-way ANOVA with post hoc Tukey's multiple comparison test and differences in gene expression between timepoints were assessed by multiple unpaired t-test.

Heatmaps were constructed in RStudio version 2023.6.0.421 [25]. For the mineralization data, outliers were detected and removed using the interquartile range (IQR) method within groups, where values exceeding 1.5 times the interquartile range (IQR) below the first quartile (Q1) or above the third quartile (Q3) were deemed as outliers. Then, the standard deviation of each group was used as a measure of the variability in mineralization for each treatment at different timepoints and plotted as a heatmap. Gene expression at day 21 was divided by that at day 0 for each experimental group and plotted as a heatmap.

## 5.3. Results and discussion

Total joint replacement is recommended for patients with advanced osteoarthritis. Despite it is considered the most effective intervention for severe, painful and disable osteoarthritis, orthopaedic failures are still observed due to an improper biomechanical compliance at the bone-implant interface. Therefore, the surface of endosseous implant must be improved to promote adhesiveness of MSC and subsequent programming to differentiate into bone cells. In this work, we report the development of a hybrid system aiming to promote bone regeneration and long-term stability of the implant, as illustrated in Fig. 5.2.

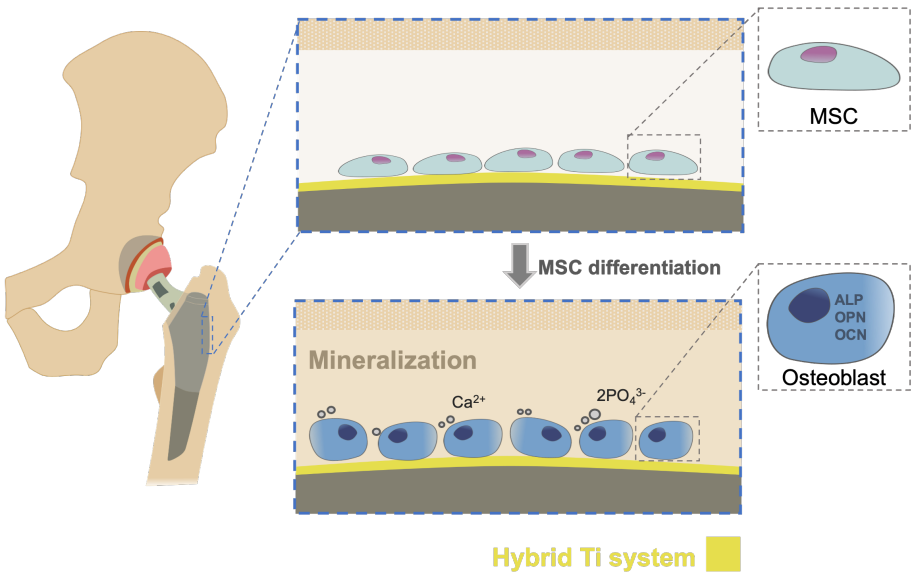



Figure 5.2 - Conventional implants result in bone resorption compromising their success implantation outcomes. On the other hand, implants with modified surface present unique features capable of improving the surface properties of the implant, resulting in the activation of cellular response and long-term maintenance. The programming and responsiveness of bone cells is expected

to increase the longevity of the implant, which would improve the patient's quality of life, and reduce healthcare cost burdens by minimizing the need for revision surgeries.

### 5.3.1. Human fibronectin-based functionalization of Ti6Al4V substrates

Alizarin red is the water-soluble sodium salt of alizarin sulfonate acid, which chelates with calcium salts in calcium carbonate or calcium phosphate to form an orange-red complex. Therefore, it is used to assess calcium rich deposits in cultured cells and the matrix mineralization is crucial to guarantee the bone tissue quality. Mineralization increased in all groups compared to the start of experiment (day 0) (Fig. 5.3), suggesting that MSC cultured in all Ti6Al4V surfaces successfully differentiated into bone cells. In addition to the extracellular mineralization observed in all groups, the stability of the cell-material complex was evaluated by the dispersion of mineralization values (Fig. 5.3a). Ti6Al4V groups with no fibronectin coating (Ti-O and Ti-H) presented a low dispersion at the beginning of experiment but it increased at 21 days of experiment. On the contrary, Ti6Al4V groups coated with fibronectin (Ti-OC and Ti-HC) had the opposite behaviour, presenting a low dispersion of mineralization values at 21 days under osteogenic differentiation. Therefore, fibronectin coating improves the adhesion of cells during the cell culture period, resulting in a higher stability of the cell-material complex over time. These differences in mineralization are not due to differences in cell number given that no statistically significant differences were observed during incubation (data not shown). The processes of cell proliferation and differentiation are inversely correlated [26–29], corroborating the finding that when MSC start to differentiate the proliferation slows down.

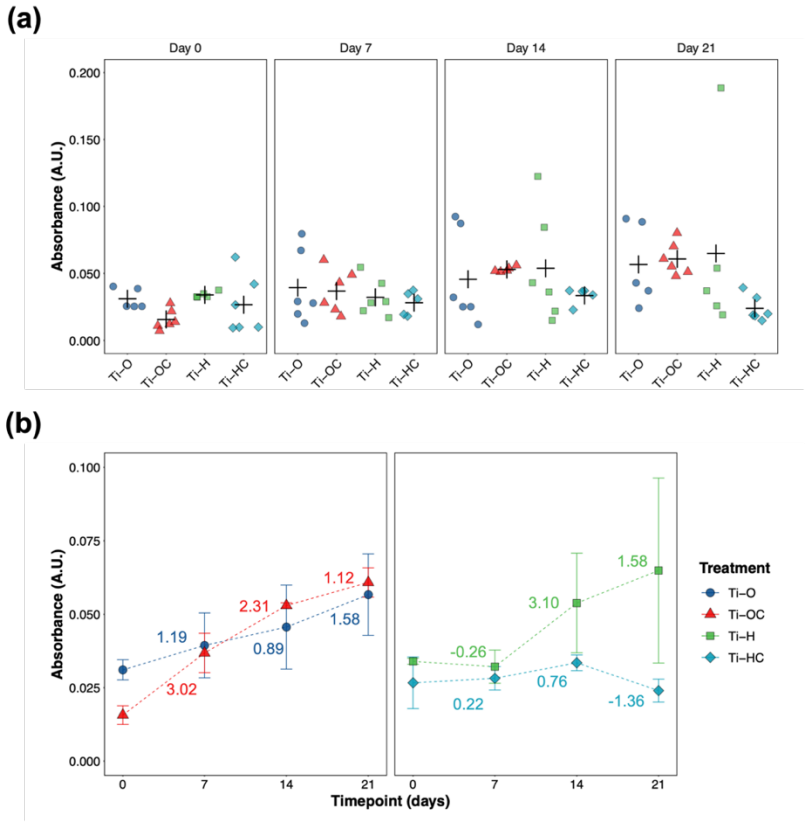



Figure 5.3 - (a) Mineralization values (absorbance read at 550 nm) from 0 to 21 days are shown in a scatter plot, in which the mean of each group is displayed by a cross. (b) Mineralization is displayed for both Ti-O and Ti-OC (left) and both Ti-H and Ti-HC (right) as mean ± standard error of the mean, and kinetics are displayed on top of each line (A.U./day, x$10^3$).

The bone extracellular matrix is composed of organic (collagen and non-collagenous proteins) and inorganic components (hydroxyapatite and other minerals) which act as the template for cellular activities, including attachment, proliferation and differentiation [30]. The communication between osteoblasts (bone-forming cells) and osteoclasts (bone-resorbing cells) occurs through membrane-bound ligands, secreted cytokines, growth factors deposited in the bone matrix and extracellular vesicles. Osteoblasts are known to release a subset of extracellular vesicles, so-called matrix vesicles, which are involved as initiators of matrix mineralization [31]. The release of these vesicles is first detected during maturation of osteoblasts and anchor to protein components of the surrounding extracellular matrix, particularly to the collagen matrix. These accumulate calcium and inorganic phosphate, which may be amorphous or crystalize into hydroxyapatite, eventually disrupting the vesicles' membrane. Their growth continues in the extracellular matrix space to form more stable crystals or propagate on the collagen fibrils, correspondent to the matrix mineralization [32]. Besides incorporating mineralization-specific components, such as calcium, these vesicles may function as carriers of osteogenic-related

proteins, such as BMPs, and non- collagenous matrix proteins [33]. The osteogenic culture medium used in this study is calcium free. Therefore, all calcium stained by ARS is a result of the extracellular mineralization occurred during osteogenic differentiation of MSC. Despite the increase in mineralization found in all groups compared to day 0, fibronectin coating was shown to promote the stability and sustainability of mineralization. Fibronectin is a glycoprotein that mediates many cellular interactions with the ECM [34]. It has been reported to facilitate cell adhesion and consequent spreading because it contains the arginine-glycine aspartic-acid (RGD) peptide which binds specifically to the receptors of integrins [7,13,35], promoting therefore an initial contact of MSC with the implant's surface. These results confirm other studies that the use of human fibronectin coating facilitates the attachment of MSC to the Ti6Al4V surface, improving the stability of the cell-substrate complex.

### 5.3.2. Hydrothermal treated Ti6Al4V interface promotes osteogenic programming

During fracture healing, several growth factors, including BMPs as well as platelet-derived growth factors (PDGFs) are secreted and rapidly stimulate MSC recruitment to the site of injury [36]. Afterward, bone formation by intramembranous ossification initiates with the formation of condensations by mesenchymal progenitor cells which grow and eventually mature, ultimately differentiating into osteoblasts [37]. Osteogenic differentiation is initiated with cell programming culminating in the extracellular mineralization. BMP-2, RUNX2, ALP, OPN and OC have been identified as key markers involved in osteogenesis [36,38,39]. The biomarkers expression profile during osteogenic differentiation and the functional readout as a result of mineralization are illustrated in Fig. 5.4a, and the gene expression of those osteogenic-related genes at 0 and 21 days is displayed in Fig. 5.4b.

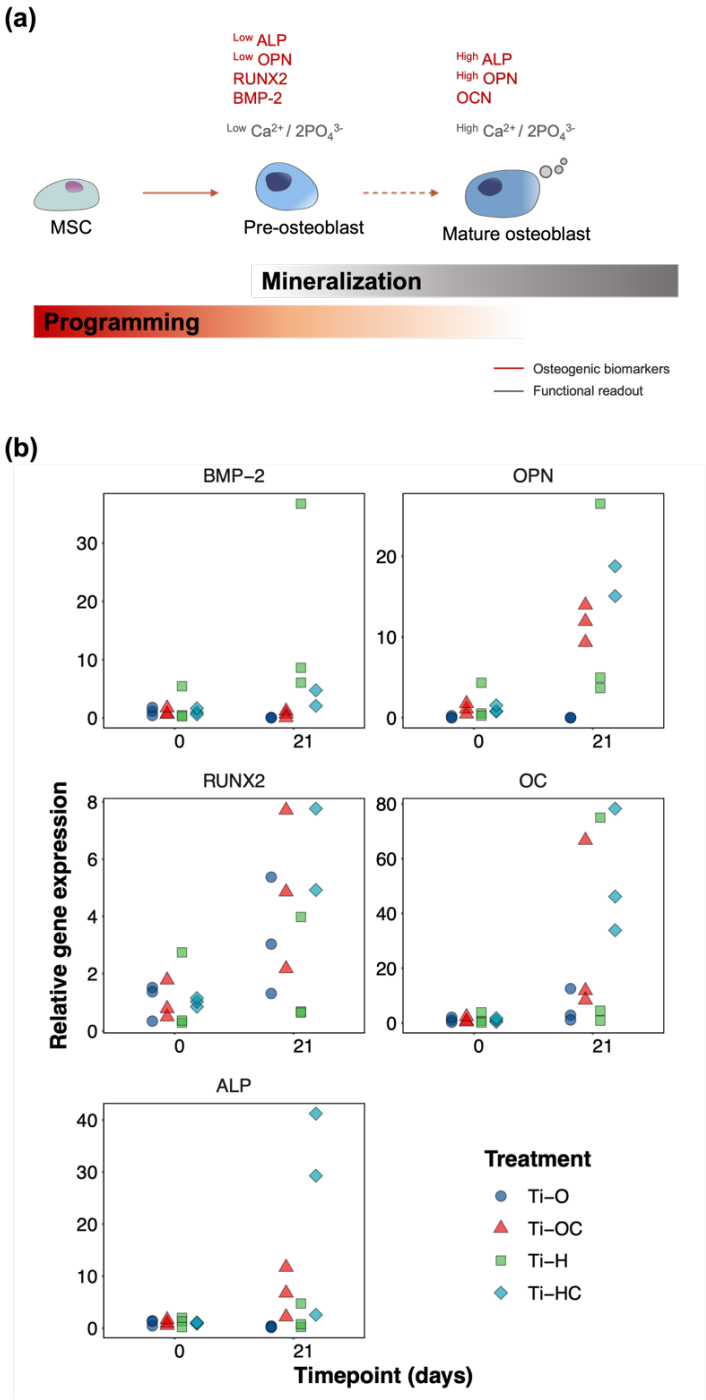



Figure 5.4 - (a) Biogenesis of osteoblasts. MSC are programmed to commit and differentiate into osteoblasts which express specific osteoblastic markers (highlighted in red), some of which are responsible for the extracellular matrix mineralization, consisting of collagen, calcium, and phosphorus. (b) Expression of osteogenic markers during osteogenic differentiation. Values are reported as mean ± standard error of the mean.

During the commitment of MSC, each biomarker presents a particular profile and function, as summarized in Supplementary Table 5.1. BMPs, including BMP-2, play a crucial role in bone remodelling and homeostasis. In the study conducted by Dragoo et al., human processed lipoaspirate cells treated with either exogenous recombinant BMP-2 (rh-BMP-2) or with adenovirus

containing the cDNA for BMP-2 (Ad-BMP-2), were shown to yield more osteogenic precursors than osteoblasts [40]. Gromolak et al. used ovine BM-MSCs and observed an increase of expression of BMP-2 at 14 days, RUNX2 and osterix at 14 days, and collagen type I, OC, and OPN at 21 days when αMEM was supplemented with both fibroblast growth factor 2 (FGF-2) and BMP-2 [41]. Ti6Al4V substrates that underwent hydrothermal treatment (Ti-H and Ti-HC) exhibited an increase of the relative expression of the gene encoding BMP-2, a powerful osteogenic factor responsible for promoting MSC differentiation into osteoblasts, despite not significant. RUNX2, a specific transcription factor, plays a crucial role in osteogenic differentiation by guiding the differentiation process towards pre-osteoblasts [36,42]. Its expression showed an overall increase in all groups, with a particularly significant rise in the Ti-HC group (* $p<0.05$). Additionally, RUNX2 is essential for the expression of non-collagenous proteins such as bone sialoprotein (BSP) and OC, further emphasizing its importance in early osteogenic differentiation [36]. ALP facilitates extracellular mineralization, and its overexpression was observed in all groups except the Ti-O group. Besides the overexpression of ALP, mature osteoblasts express OPN and OC. The gene encoding OPN was found to be upregulated in all groups except for the Ti-O and the highest overexpression was found for Ti-OC and Ti-HC (** $p<0.01$). This bone matrix glycoprotein has been reported to regulate collagen organization and mineralization [39]. Finally, osteocalcin is the most abundant non-collagenous protein in the bone ECM [39] and we found that its expression was upregulated in all four groups, particularly in Ti-HC (* $p<0.05$). OC has affinity for calcium and thus it has an important role during bone matrix mineralization [39].

The overexpression of these key osteogenic markers suggests MSC differentiation priming into mature bone cells. Non-treated Ti6Al4V substrate (Ti-O) and the hydrothermal treatment (Ti-H) had no significant effect on gene expression, whereas Ti-OC increased the expression of OPN and Ti-HC increased the expression of OPN, RUNX2 and OC. Therefore, among the four groups, Ti- HC exhibited increasing trends of expression of the transcription factors and osteoblast differentiation markers, after 21 days in xeno-free and serum-free osteogenic medium. Furthermore, the analysis of data at 21 days also suggests that fibronectin coating *per si* allows sustainability of the osteogenic capacity of MSC.

Surface features of Ti6Al4V biomaterials such as roughness and wettability are critical modulators of cell adhesion and activity. Meta-analyses were carried out to assess the effect and contribution of these and other factors in the osteointegration potential both in vitro and in vivo and concluded that an optimized titanium implant surface should have a Ra between 1.5 and 3.0 μm

and a surface treatment to form an anatase layer [43,44]. We have previously described an extensive surface characterization carried out on Ti6Al4V substrates either with no surface treatment or subjected to hydrothermal treatment, which correspond to Ti-O and Ti-H groups, respectively [19]. Compared to Ti-O, the hydrothermal treatment increased the roughness values from 10.89 ± 2.01 nm to 20.42 ± 1.71 nm, but no major differences were observed regarding wettability. Non-treated and treated substrates were moderate hydrophilic, as the water contact angles were 85 ± 3.5° and 83.5 ± 4.7° for Ti-O and Ti-H, respectively. However, the reported results were obtained for samples autoclaved at 125 °C for 15 min. On another hand, in the present study, samples were sterilized in alcohol followed by UV irradiation, which has been reported to increase surface wettability without changing the topography and roughness [45]. Besides altering the roughness of Ti6Al4V samples, the hydrothermal treatment was shown to effectively create a $TiO_2$ hydrophilic layer with both anatase and rutile crystalline phases [19]. Lorenzetti et al. investigated the effect of hydrothermally grown $TiO_2$-anatase coatings on Ti-substrates followed by photo-functionalization by UVB irradiation on the biological behaviour of human MSC and observed they became osteogenically active, presumably due to the 5 hrs UVB photo-induced hydrophilicity [29]. In addition to the creation of a $TiO_2$ layer, fibronectin coating on Ti6Al4V substrate facilitates the binding to osteogenic cell integrin receptors promoting cell adhesion. In fact, Lv et al. fabricated $TiO_2$ thin films of anatase and rutile phases by atomic layer deposition and post-deposition annealing on Si substrates and observed a more active conformation of the adsorbed fibronectin which resulted in better osteoblast compatibility in terms of adhesion, proliferation, differentiation, mineralization and osteogenesis-related gene expression [16]. Rapuano et al. found that fibronectin adsorbed on Ti6A4V did not accelerate osteoblast differentiation but instead increased ECM protein expression during the mineralization stage of osteogenic differentiation [11].

### 5.3.3. Summary of the results

The foundation for achieving clinical success with implants in bone, whether it is a dental implant or joint replacement system, lies in the stability of the implant. This stability is influenced by various factors such as surgical exposure, bone preparation, advancements in manufacturing, surface technology, and geometry. These elements contribute to primary stability and osseointegration during the healing process. Osseointegration refers to the direct connection between living bone and the implant, which enables load transfer, bone remodelling, and long-term fixation. Stimulating new bone formation on the implant surface can be achieved through material properties, surface topology, porosity, and chemistry. Enhancing the rate, quantity, and

quality of osseointegration has been a subject of research for many years. When selecting the optimal implant surface, considerations should include design, manufacturing, cleaning, sterilization, mechanical properties, biocompatibility, implantation, and in vivo response.

The treatment of the Ti6Al4V surface is a critical step in achieving sufficient osseointegration of the implant within the bone. Inadequate healing of the implant can lead to serious complications such as infection, inflammation, aseptic loosening, or the stress-shielding effect, which may require additional surgical procedures. In this work, Ti6Al4V surfaces were modified by different strategies aiming to improve its bioactivity and thus promote adhesion and consequent differentiation of MSC into bone cells. The osteogenic potential of each treatment is summarized Fig. 5.5.

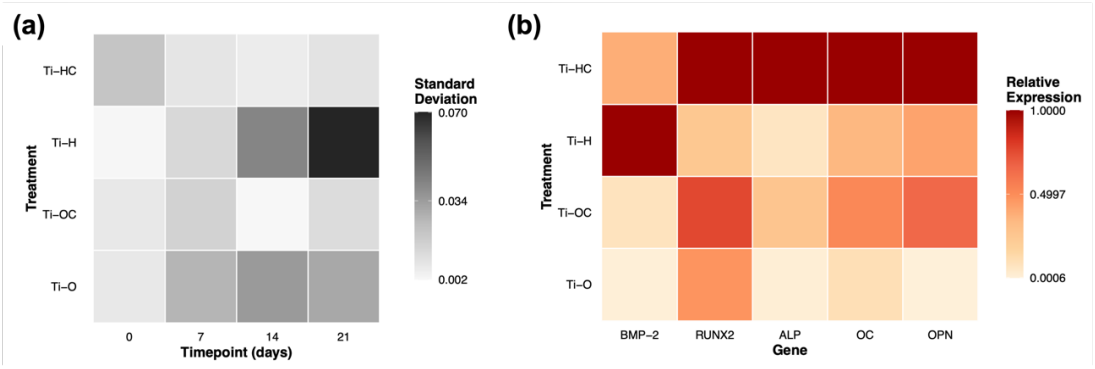



Figure 5.5 - Fibronectin coating reduces variability in mineralization and when combined with hydrothermal treatment upregulates the expression of gene associated with osteogenic differentiation. (a) Variability (standard deviation) in mineralization at different timepoints of bone marrow-derived human mesenchymal stem cells (MSC) seeded on Ti6Al4V subjected to different treatments. (b) Relative gene expression levels of hallmarks of osteogenic differentiation in MSC seeded on Ti6Al4V subjected to different treatments. Gene expression data are presented as fold- change at day 21 relative to expression level on day 0.

Among the many methodologies discussed in the literature, hydrothermal treatment is a simple approach able to produce oxide films which phase composition and wetting properties have been proved to be beneficial for cell behaviour. However, a variety of conditions were found, namely the choice of aqueous solution (such as sodium tripolyphosphate (STPP) and calcium hydroxide ($Ca(OH)_2$) [46,47], NaOH [21], calcium phosphate (Ca-P) solution [48], or simply distilled water [23]), temperature (up to 300 °C) [22] and duration (up to 72 hrs). Here, the hydrothermal treatment consisted simply of the immersion of samples in distilled water, at 180 °C for 180 min. The use of this method has numerous competitive advantages over more complex treatments, including ease of use, time reduction and cost-effectiveness. In addition, the benefits of a surface biocoating with fibronectin were evaluated either *per se* or combined with the hydrothermal treatment. Fibronectin mediates cell adhesion and spreading and is crucial during tissue repair and, in its soluble form, it is a major component of blood plasma [49]. In this study, only xeno-free

and serum-free reagents were used to closely replicate the human body chemical conditions, and the biocoating was performed using human derived fibronectin (carrier free), limiting immunogenicity risks.

MSC were cultured on Ti6Al4V substrates which underwent different surface treatments (Ti-O, Ti-H, Ti-OC and Ti-HC) and their osteogenic differentiation was evaluated based on the extracellular mineralization. Compared to the beginning of the experiment, extracellular mineralization increased, regardless of the surface treatment. Ti6Al4V surfaces coated with fibronectin (Ti-OC and Ti-HC) exhibited the lowest variability at day 21 (Fig. 5.5a). This finding aligns with previous observations regarding the positive impact of this glycoprotein in promoting the stability of the substrate-cell complex and enhancing the sustainability of osteogenic differentiation. Furthermore, in addition to its effect on mineralization, fibronectin coating also upregulated the expression of key osteogenic markers. The upregulation of pivotal genes associated with osteogenesis, including BMP-2, RUNX2, ALP, OC, and OPN, indicates successful cell programming. Among the four surface treatments evaluated in this study, Ti-HC demonstrated the highest upregulation of the majority of genes (Fig. 5.5b). In summary, our findings indicate that hydrothermal treatment does not impair cell viability and reactivity in Ti6Al4V substrates but rather it holds a positive effect. In fact, hydrothermal treatment followed by fibronectin coating offers a combination of minimal variability in extracellular mineralization rates and maximum upregulation of osteogenic genes. Thus, a simple hydrothermal treatment (preparation ease, cost, and duration effectiveness) combined fibronectin coating represents a simple and cost-effective surface treatment that enhances the adhesiveness of MSC to Ti6Al4V implant surfaces, while also activating their commitment and responsiveness to osteogenic differentiation.

## 5.4. Conclusions

Surface modification of Ti6Al4V implants is a critical step in achieving sufficient osseointegration of the implant within the bone. In the present study, the in vitro response of a titanium alloy implant coated with fibronectin was compared to that of a titanium implant using an established model. Both non-coated (Ti-O) and coated (Ti-C) demonstrated an osteoconductive surface that would potentially promote bone growth. However, the hydrothermally treated titanium with fibronectin coating exhibited a more robust bone-implant interface, which is particularly important for long-term implant stability.

It is important to note that the current study has limitations regarding the number of time points examined. Future studies with longer observation periods could provide valuable insights into different implant fixation strategies. Nonetheless, the strength of this study lies in its detailed reporting of implant substrates characterization, mechanical properties at the bone-implant interface. This level of detail allows for meaningful comparisons and contrasts, which can be challenging to achieve with clinical implantations. In conclusion, the Ti6Al4V subjected to hydrothermal treatment and coated with fibronectin demonstrated a stronger bone-implant interface, which is crucial for long-term implant stability and load transfer.

## Acknowledgments

This work was supported by FCT (Fundação para a Ciência e a Tecnologia) through the grants SFRH/BD/141056/2018, COVID/BD/152996/2022 and UMINHO/BID/2023/04, the project PTDC/EME-EME/1442/2020 and under the national support to R&D units grant, through the reference projects UIDB/04436/2020 and UIDP/04436/2020. In addition, this work was developed within the scope of the project CICECO-Aveiro Institute of Materials, UIDB/50011/2020, UIDP/50011/2020 & LA/P/0006/2020, financed by national funds through the FCT/MCTES (PIDDAC). The authors acknowledge Duarte Carvalho for fruitful discussions.

## References

[1] V. B. Kraus, F.J. Blanco, M. Englund, M.A. Karsdal, L.S. Lohmander, Call for standardized definitions of osteoarthritis and risk stratification for clinical trials and clinical use, Osteoarthr. Cartil. 23 (2015) 1233–1241. https://doi.org/10.1016/j.joca.2015.03.036.

[2] J. N. Katz, K.R. Arant, R.F. Loeser, Diagnosis and Treatment of Hip and Knee Osteoarthritis: A Review, JAMA - J. Am. Med. Assoc. 325 (2021) 568–578. https://doi.org/10.1001/jama.2020.22171.

[3] D.J. Hunter, S. Bierma-Zeinstra, Osteoarthritis, Lancet. 393 (2019) 1745–1759. https://doi.org/10.1016/S0140-6736(19)30417-9.

[4] D. Apostu, O. Lucaciu, C. Berce, D. Lucaciu, D. Cosma, Current methods of preventing aseptic loosening and improving osseointegration of titanium implants in cementless total hip arthroplasty: a review, J. Int. Med. Res. 46 (2018) 2104–2119. https://doi.org/10.1177/0300060517732697.

[5] X. Gao, M. Fraulob, G. Haïat, Biomechanical behaviours of the bone-implant interface: A review, J. R. Soc. Interface. 16 (2019). https://doi.org/10.1098/rsif.2019.0259.

[6] M. Kumar, R. Kumar, S. Kumar, Coatings on orthopedic implants to overcome present problems and challenges: A focused review, Mater. Today Proc. 45 (2021) 5269–5276. https://doi.org/10.1016/j.matpr.2021.01.831.

[7] R. Tejero, E. Anitua, G. Orive, Toward the biomimetic implant surface: Biopolymers on titanium-based implants for bone regeneration, Prog. Polym. Sci. 39 (2014) 1406–1447. https://doi.org/10.1016/j.progpolymsci.2014.01.001.

[8] S. Rammelt, E. Schulze, R. Bernhardt, U. Hanisch, D. Scharnweber, H. Worch, H. Zwipp, A. Biewener, Coating of titanium implants with type-I collagen, J. Orthop. Res. 22 (2004) 1025–1034. https://doi.org/10.1016/j.orthres.2004.02.011.

[9] U. Geißler, U. Hempel, C. Wolf, D. Scharnweber, H. Worch, K.W. Wenzel, Collagen type I-coating of Ti6A14V promotes adhesion of osteoblasts, J. Biomed. Mater. Res. 51 (2000) 752–760. https://doi.org/10.1002/1097-4636(20000915)51:4<752::AID- JBM25>3.0.CO;2-7.

[10] C. Somaiah, A. Kumar, D. Mawrie, A. Sharma, S.D. Patil, J. Bhattacharyya, R. Swaminathan, B.G. Jaganathan, Collagen promotes higher adhesion, survival and proliferation of mesenchymal stem cells, PLoS One. 10 (2015) 1–15. https://doi.org/10.1371/journal.pone.0145068.

[11] B.E. Rapuano, K.M. Hackshae, H.C. Schniepp, D.E. MacDonald, Effects of Coating a Titanium Alloy with Fibronectin on the Expression of Osteoblast Gene Markers in the MC3T3 Osteoprogenitor Cell Line, Int J Oral Maxillofac Implant. 27 (2012) 1081–1090. https://doi.org/10.1038/mp.2011.182.

[12] V. Vadillo-Rodríguez, M.A. Pacha-Olivenza, M.L. Gõnzalez-Martín, J.M. Bruque, A.M. Gallardo-Moreno, Adsorption behavior of human plasma fibronectin on hydrophobic and hydrophilic Ti6Al4V substrata and its influence on bacterial adhesion and detachment, J.

Biomed. Mater. Res. - Part A. 101 A (2013) 1397–1404. https://doi.org/10.1002/jbm.a.34447.

[13] N. Ogura, M. Kawada, W.J. Chang, Q. Zhang, S.Y. Lee, T. Kondoh, Y. Abiko, Differentiation of the human mesenchymal stem cells derived from bone marrow and enhancement of cell attachment by fibronectin, J. Oral Sci. 46 (2004) 207–213. https://doi.org/10.2334/josnusd.46.207.

[14] D.M. Rivera-Chacon, M. Alvarado-Velez, C.Y. Acevedo-Morantes, S.P. Singh, E. Gultepe, D. Nagesha, S. Sridhar, J.E. Ramirez-Vick, Fibronectin and vitronectin promote human fetal osteoblast cell attachment and proliferation on nanoporous titanium surfaces, J. Biomed. Nanotechnol. 9 (2013) 1092–1097. https://doi.org/10.1166/jbn.2013.1601.

[15] G. Wang, J. Li, K. Lv, W. Zhang, X. Ding, G. Yang, X. Liu, X. Jiang, Surface thermal oxidation on titanium implants to enhance osteogenic activity and in vivo osseointegration, Sci. Rep. 6 (2016) 1–13. https://doi.org/10.1038/srep31769.

[16] L. Lv, K. Li, Y. Xie, Y. Cao, X. Zheng, Enhanced osteogenic activity of anatase $TiO_2$ film: Surface hydroxyl groups induce conformational changes in fibronectin, Mater. Sci. Eng. C. 78 (2017) 96–104. https://doi.org/10.1016/j.msec.2017.04.056.

[17] T. Wang, L. Wang, Q. Lu, Z. Fan, Changes in the esthetic, physical, and biological properties of a titanium alloy abutment treated by anodic oxidation, J. Prosthet. Dent. 121 (2019) 156–165. https://doi.org/10.1016/j.prosdent.2018.03.024.

[18] B.Li,Y.Li,J.Li,X.Fu,C.Li,H.Wang,S.Liu,L.Guo,S.Xin,C.Liang,H.Li, Improvement of biological properties of titanium by anodic oxidation and ultraviolet irradiation, Appl. Surf. Sci. 307 (2014) 202–208. https://doi.org/10.1016/j.apsusc.2014.04.015.

[19] F. Melo-Fonseca, M. Gasik, S. Madeira, F.S. Silva, G. Miranda, Surface characterization of titanium-based substrates for orthopaedic applications, Mater. Charact. 177 (2021) 111161. https://doi.org/10.1016/j.matchar.2021.111161.

[20] M. Zuldesmi, A. Waki, K. Kuroda, M. Okido, High Osteoconductive Surface of Pure Titanium by Hydrothermal Treatment, J. Biomater. Nanobiotechnol. 04 (2013) 284–290. https://doi.org/10.4236/jbnb.2013.43036.

[21] J. Vishnu, V. K Manivasagam, V. Gopal, C. Bartomeu Garcia, P. Hameed, G. Manivasagam, T.J. Webster, Hydrothermal treatment of etched titanium: A potential surface nano-modification technique for enhanced biocompatibility, Nanomedicine Nanotechnology, Biol. Med. 20 (2019). https://doi.org/10.1016/j.nano.2019.102016.

[22] V.K. Manivasagam, K.C. Popat, Hydrothermally treated titanium surfaces for enhanced osteogenic differentiation of adipose derived stem cells, Mater. Sci. Eng. C. 128 (2021) 112315. https://doi.org/10.1016/j.msec.2021.112315.

[23] M. Zuldesmi, A. Waki, K. Kuroda, M. Okido, Hydrothermal treatment of titanium alloys for the enhancement of osteoconductivity, Mater. Sci. Eng. C. 49 (2015) 430–435. https://doi.org/10.1016/j.msec.2015.01.031.

[24] K. Okamura, Y . Inagaki, T .K. Matsui, M. Matsubayashi, T . Komeda, M. Ogawa, E. Mori, Y. Tanaka, RT-qPCR analyses on the osteogenic differentiation from human iPS cells: an investigation of reference genes, Sci. Rep. 10 (2020) 1–11. https://doi.org/10.1038/s41598- 020-68752-2.

[25] P. Team, RStudio: Integrated Development Environment for R. Posit Software, (2023). http://www.posit.co/.

[26] L. Zhu, A.I. Skoultchi, Coordinating cell proliferation and differentiation, Curr. Opin. Genet. Dev. 11 (2001) 91–97. https://doi.org/10.1016/S0959-437X(00)00162-3.

[27] G.S. Stein, J.B. Lian, Molecular mechanisms mediating proliferation/differentiation interrelationships during progressive development of the osteoblast phenotype, Endocr. Rev. 14 (1993) 424–442. https://doi.org/10.1210/edrv-14-4-424.

[28] T.A. Owen, M. Aronow, V. Shalhoub, L.M. Barone, L. Wilming, M.S. Tassinari, M.B. Kennedy, S. Pockwinse, J.B. Lian, G.S. Stein, Progressive Development of the Rat Osteoblast Phenotype In Vitro: Reciprocal Relationships in Expression of Genes Associated With Osteoblast Proliferation and Differentiation During Formation of the Bone Extracellular Matrix, J. Cell. Physiol. 143 (190AD) 420–439.

[29] M. Lorenzetti, O. Dakischew, K. Trinkaus, K. Susanne Lips, R. Schnettler, S. Kobe, S. Novak, Enhanced osteogenesis on titanium implants by UVB photofunctionalization of hydrothermally grown $TiO_2$ coatings, J. Biomater. Appl. 30 (2015) 71–84. https://doi.org/10.1177/0885328215569091.

[30] J. An, S. Leeuwenburgh, J. Wolke, J. Jansen, Mineralization Processes in Hard Tissue: Bone, in: Biominer. Biomater. Fundam. Appl., Woodhead Publishing Limited, 2016: pp. 129–146. https://doi.org/10.1016/B978-1-78242-338-6.00005-3.

[31] S. Ansari, B.W.M. de Wildt, M.A.M. Vis, C.E. de Korte, K. Ito, S. Hofmann, Y. Yuana, Matrix vesicles: Role in bone mineralization and potential use as therapeutics, Pharmaceuticals. 14 (2021) 1–27. https://doi.org/10.3390/ph14040289.

[32] Y. Wei, C. Tang, J. Zhang, Z. Li, X. Zhang, R.J. Miron, Y. Zhang, Extracellular vesicles derived from the mid-to-late stage of osteoblast differentiation markedly enhance osteogenesis in vitro and

in vivo, Biochem. Biophys. Res. Commun. 514 (2019) 252–258. https://doi.org/10.1016/j.bbrc.2019.04.029.

[33] N.N. Nahar, L.R. Missana, R. Garimella, S.E. Tague, H.C. Anderson, Matrix vesicles are carriers of bone morphogenetic proteins (BMPs), vascular endothelial growth factor (VEGF), and noncollagenous matrix proteins, J. Bone Miner. Metab. 26 (2008) 514–519. https://doi.org/10.1007/s00774-008-0859-z.

[34] R. Pankov, K.M. Yamada, Fibronectin at a glance, J. Cell Sci. 115 (2002) 3861–3863. https://doi.org/10.1242/jcs.00059.

[35] L.A. Hidalgo-Bastida, S.H. Cartmell, Mesenchymal stem cells, osteoblasts and extracellularmatrix proteins: Enhancing cell adhesion and differentiation for bone tissue engineering, Tissue Eng. - Part B Rev. 16 (2010) 405–412. https://doi.org/10.1089/ten.teb.2009.0714.

[36] R.J. Miron, Y.F. Zhang, Osteoinduction: A review of old concepts with new standards, J. Dent. Res. 91 (2012) 736–744. https://doi.org/10.1177/0022034511435260.

[37] H. Kaul, B.K. Hall, C. Newby, Y. Ventikos, Synergistic activity of polarised osteoblasts inside condensations cause their differentiation, Sci. Rep. 5 (2015) 1–19. https://doi.org/10.1038/srep11838.

[38] A. Rutkovskiy, K.-O. Stensløkken, I.J. Vaage, Osteoblast Differentiation at a Glance, Med. Sci. Monit. Basic Res. 22 (2016) 95–106. https://doi.org/10.12659/MSMBR.901142.

[39] M.S. Carvalho, A.A. Poundarik, J.M.S. Cabral, C.L. da Silva, D. Vashishth, Biomimetic matrices for rapidly forming mineralized bone tissue based on stem cell-mediated osteogenesis, Sci. Rep. 8 (2018) 1–16. https://doi.org/10.1038/s41598-018-32794-4.

[40] J.L. Dragoo, J.Y. Choi, J.R. Lieberman, J. Huang, P. A. Zuk, J. Zhang, M.H. Hedrick, P . Benhaim, Bone induction by BMP-2 transduced stem cells derived from human fat, J. Orthop. Res. 21 (2003) 622–629. https://doi.org/10.1016/S0736-0266(02)00238-3.

[41] S. Gromolak, A. Krawczenko, A. Antończyk, K. Buczak, Z. Kiełbowicz, A. Klimczak, Biological characteristics and osteogenic differentiation of ovine bone marrow derived mesenchymal stem cells stimulated with FGF-2 and BMP-2, Int. J. Mol. Sci. 21 (2020) 1– 22. https://doi.org/10.3390/ijms21249726.

[42] L. Huang, B. Cai, Y. Huang, J. Wang, C. Zhu, K. Shi, Y. Song, G. Feng, L. Liu, L. Zhang, Comparative Study on 3D Printed Ti6Al4V Scaffolds with Surface Modifications Using Hydrothermal Treatment and Microarc Oxidation to Enhance Osteogenic Activity, ACS Omega. 6 (2021) 1465–1476. https://doi.org/10.1021/acsomega.0c05191.

[43] M. Gasik, L. Van Mellaert, D. Pierron, A. Braem, D. Hofmans, E. De Waelheyns, J. Anń, M.F. Harmand, J. Vleugels, Reduction of biofilm infection risks and promotion of osteointegration for optimized surfaces of titanium implants, Adv. Healthc. Mater. 1 (2012) 117–127. https://doi.org/10.1002/adhm.201100006.

[44] M. Gasik, A. Braem, A. Chaudhari, J. Duyck, J. Vleugels, Titanium implants with modified surfaces: Meta-analysis of in vivo osteointegration, Mater. Sci. Eng. C. 49 (2015) 152–158. https://doi.org/10.1016/j.msec.2014.12.074.

[45] S. Li, J. Ni, X. Liu, X. Zhang, S. Yin, M. Rong, Z. Guo, L. Zhou, Surface characteristics and biocompatibility of sandblasted and acid-etched titanium surface modified by ultraviolet irradiation: An in vitro study, J. Biomed. Mater. Res. - Part B Appl. Biomater. 100 B (2012) 1587–1598. https://doi.org/10.1002/jbm.b.32727.

[46] P.K. Srivas, K. Kapat, B. Das, P. Pal, P.G. Ray, S. Dhara, Hierarchical surface morphology on Ti6Al4V via patterning and hydrothermal treatment towards improving cellular response, Appl. Surf. Sci. 478 (2019) 806–817. https://doi.org/10.1016/j.apsusc.2019.02.039.

[47] K. Kapat, P. P. Maity, A. P. Rameshbabu, P. K. Srivas, P . Majumdar, S. Dhara, Simultaneous hydrothermal bioactivation with nano-topographic modulation of porous titanium alloys towards enhanced osteogenic and antimicrobial responses, J. Mater. Chem. B. 6 (2018) 2877–2893. https://doi.org/10.1039/c8tb00382c.

[48] S. Yang, S. Lee, I. Bajpai, S. Kim, Hydrothermal treatment of Ti surface to enhance the formation of low crystalline hydroxyl carbonate apatite, Biomater. Res. 19 (2015) 1–6. https://doi.org/10.1186/s40824-014-0022-y.

[49] L. Parisi, A. Toffoli, B. Ghezzi, B. Mozzoni, S. Lumetti, G.M. Macaluso, A glance on the role of fibronectin in controlling cell response at biomaterial interface, Jpn. Dent. Sci. Rev. 56 (2020) 50–55. https://doi.org/10.1016/j.jdsr.2019.11.002.

[50] Y. Li, C. Ge, J.P. Long, D.L. Begun, J.A. Rodriguez, S.A. Goldstein, R.T. Franceschi, Biomechanical stimulation of osteoblast gene expression requires phosphorylation of the RUNX2

transcription factor, J. Bone Miner. Res. 27 (2012) 1263–1274. https://doi.org/10.1002/jbmr.1574.

[51] M. V. Bais, N. Wigner, M. Young, R. Toholka, D.T. Graves, E.F. Morgan, L.C. Gerstenfeld, T.A. Einhorn, BMP2 is essential for post natal osteogenesis but not for recruitment of osteogenic stem cells, Bone. 45 (2009) 254–266. https://doi.org/10.1016/j.bone.2009.04.239.

[52] Y. Takuwa, C. Ohse, E.A. Wang, J.M. Wozney, K. Yamashita, Bone morphogenetic protein-2 stimulates alkaline phosphatase activity and collagen synthesis in cultured osteoblastic cells, MC3T3-E1, Biochem. Biophys. Res. Commun. 174 (1991) 96–101. https://doi.org/10.1016/0006-291X(91)90490-X.

[53] C. Wennberg, L. Hessle, P. Lundberg, S. Mauro, L. Milla, Functional Characterization of Osteoblasts and Osteoclasts from Alkaline Phosphatase Knockout Mice, J. Bone Miner. Res. 15 (2000) 1879–1888. https://doi.org/https://doi.org/10.1359/jbmr.2000.15.10.1879.

[54] E.E. Golub, K. Boesze-Battaglia, The role of alkaline phosphatase in mineralization, Curr. Opin. Orthop. 18 (2007) 444–448. https://doi.org/10.1097/BCO.0b013e3282630851.

[55] T.E. Kruger, A.H. Miller, A.K. Godwin, J. Wang, Bone sialoprotein and osteopontin in bone metastasis of osteotropic cancers, Crit. Rev. Oncol. Hematol. 89 (2014) 330–341. https://doi.org/10.1016/j.critrevonc.2013.08.013.

[56] D.E. Rodriguez, T. Thula-Mata, E.J. Toro, Y.W. Yeh, C. Holt, L.S. Holliday, L.B. Gower, Multifunctional role of osteopontin in directing intrafibrillar mineralization of collagen and activation of osteoclasts, Acta Biomater. 10 (2014) 494–507. https://doi.org/10.1016/j.actbio.2013.10.010.

[57] P. Ducy, C. Desbois, B. Boyce, G. Pinero, B. Story, C. Dunstan, E. Smith, J. Bonadio, S. Goldstein, C. Gundberg, A. Bradley, G. Karsenty, Increased bone formation in osteocalcin- deficient mice, Nature. 382 (1996) 448–452. https://doi.org/10.1038/382448a0.

[58] S. Rammelt, M. Neumann, U. Hanisch, A. Reinstorf, W. Pompe, H. Zwipp, A. Biewener, Osteocalcin enhances bone remodeling around hydroxyapatite/collagen composites, J. Biomed. Mater. Res. - Part A. 73 (2005) 284–294. https://doi.org/10.1002/jbm.a.30263.

## Appendix A. Supplementary information

Supplementary Table 5.1 - Osteogenic markers and their impact on osteogenesis.

| Osteogenic marker | Impact on osteogenesis | Refs. |
|---|---|---|
| BMP-2 | Stimulate MSC recruitment to sites of injury;<br>Stimulates expression of other BMPs and stimulates osteoblast differentiation;<br>Upstream the transcription of RUNX2;<br>Stimulates alkaline phosphatase activity and collagen synthesis. | [36,50-52] |
| RUNX2 | Transcriptional factor which targets genes include OPN, BSP, OC and many others;<br>RUNX2 is required for the expression of non-collagenous proteins, including BSP and OC. | [36,50] |
| ALP | Participates in the initiation of mineralization;<br>It appears to act both to increase the local concentration of inorganic phosphate, a mineralization promoter, and to decrease the concentration of extracellular pyrophosphate, an inhibitor of mineral formation. | [39,53-56] |
| OPN | Regulates collagen organization and mineralization. | [39] |
| OC | It has affinity for calcium playing an important role in matrix mineralization;<br>By binding hydroxyapatite, it activates both osteoclasts and osteoblasts during early bone formation. | [57,58] |

# CHAPTER 6

## EXPERIMENTAL ANALYSIS AND PREDICTIVE MODELLING OF TI6AL4V LASER SURFACE TEXTURING FOR BIOMEDICAL APPLICATIONS

Published in Surfaces and Interfaces, 2022, 35, 102466

https://doi.org/10.1016/j.surfin.2022.102466

F. Melo-Fonseca[a, b, c, *], B. Guimarães[a,b], M. Gasik[c, d], F. S. Silva[a, b], G. Miranda[e, f]

[a]Center for MicroElectroMechanical Systems (CMEMS-UMinho), University of Minho, Campus de Azurém, 4800-058 Guimarães – Portugal

[b]LABBELS –Associate Laboratory, Braga, Guimarães, Portugal

[c]International Iberian Nanotechnology Laboratory (INL), 4715-330 Braga, Portugal

[d]School of Chemical Engineering, Aalto University Foundation, FI-00076 Espoo, Finland

[e]Several Ltd., Helsinki, Finland

[f]CICECO, Aveiro Institute of Materials, Department of Materials and Ceramic Engineering, University of Aveiro, 3810-193 Aveiro, Portugal

[*] Corresponding author

F. S. Silva and G. Miranda share co-last authorship.

**Abstract**

Laser surface texturing (LST) is a powerful technique for creating high quality micro-textured patterns with different shapes and sizes on metallic biomaterials. Textured surfaces may improve the interaction between bone and implant by increasing the surface contact area and thus promoting bone regeneration. The goal of this study was to explore Nd:YAG laser potential for texturing micro-scale pillars with pyramid geometry, with dimensions in a selected range, in a reproducible way. First, the design and texture of grooves were addressed, then proceeding to pillars. Two laser machining and marking strategies were investigated, and the consecutive laser processing strategy and continuous marking mode were selected due to the resultant smoother grooves. Then, a cross-hatched pattern was designed to texture a pillar pattern with targeted dimensions. Given the direct effect of the LST drawing and laser parameters on the texture dimensions, three mathematical models, one for each texture dimension (groove width, pillar width and pillar depth) were developed. These models are accurate tools for predicting the texture dimensions in the selected range and this LST approach was effective on creating well-defined, uniform and equally spaced surface textures on Ti6Al4V parts, in a reproducible way. A combination of drawing and laser parameters was selected for the target dimensions, also considering suitable wettability and roughness for biomedical applications.

**Keywords:** Laser surface texturing; Nd:YAG laser; Ti6Al4V; Predictive models; Surface roughness; Implants

## 6.1. Introduction

Metallic materials are widely used for dental and orthopaedic applications, especially titanium (Ti) and Ti-based materials, which are considered the number one choice due to a combination of corrosion resistance, fatigue strength, low Young's modulus amongst metals and alloys and biocompatibility [1–3]. Nevertheless, in order to improve the interaction between bone and implant, a broad set of surface treatments have been subject of great interest. These range from simple use of 2D materials, such as protective coatings, and the creation of porous structures to more complex processes, such as fabrication of textured surfaces [4,5]. More examples can be found in previous review studies on this matter [4,6,7]. Wang et al. added a protective coating on Ti alloys by anodization, which exhibited a lower contact angle, higher roughness and similar cell viability compared to untreated Ti alloy [8]. The hydrothermal treatment was proposed as capable of creating a potentially bioactive and hydrophilic layer on Ti able to enhance the bone-implant

interface [9]. Henningsen et al. investigated the potential of UV light and non-thermal plasma treatment of argon and oxygen on Ti surfaces and concluded that, after short-term functionalization, both techniques improved the surface properties and cellular response [10]. Another strategy is the fabrication of specific patterns on the implant's surface which, besides increasing the surface contact area, may improve some properties and performance, as wetting, tribological or biological behaviour [11–13]. In fact, cell-substrate adhesion is influenced by substrate topography and the impact of topographical features on cellular response and behaviour has been covered in the literature [14,15]. One of the most promising surface modification processes is the laser surface texturing (LST) due to its high beam quality, high efficiency, accuracy, flexibility, precision and environmental-friendliness [16]. Surface texturing obtained through the action of a laser consists in the incidence of a high-energy beam on the material surface, generating melting and vaporization of the material from the irradiated area [17]. Although this non-conventional machining process allows a good control of micro-textured patterns shape and size, Ding et al. had shown that the final surface topographies are strongly dependent on the laser parameters including the laser wavelength, pulse duration, frequency and laser power [18].

The Q-switched Nd:YAG laser technology has been used to produce a variety of textures such as microchannels [19], grooves [20], holes [21, 22] and pillars [23] on Ti-based materials. Topological features have been shown to influence the cellular response and therefore have a potential use for biomedical applications. Therefore, surface texturing has been investigated to enhance the antimicrobial properties and osseointegration to improve the long-term performance of metallic biomaterials [7,11]. Lawrence et al. used Nd:YAG laser to alter the surface properties of Ti6Al4V and concluded that by increasing the wettability as a result of an increased surface roughness, surface oxygen content and polar component of the surface energy, osteoblast cell activity was improved [24]. A groove pattern (20 and 60 μm width and 2 μm depth) was created on Ti6Al4V using a femtosecond laser and mesenchymal stem cells (MSC) aligned in the grooves direction and produced cytoplasmic extensions with focal contacts [25]. In another study, micro-grooves were fabricated using a combination of photolithography and inductively coupled plasma-based dry etching on Ti substrate with varying dimensions (groove width of 7 and 12 μm, ridge width of 3 and 10 μm and depth of 2 μm). These patterns enhanced the in vitro osteogenic differentiation of MC3T3-E1 preosteoblastic cells and the pattern with groove width of 7 μm and ridge of 3 μm presented the strongest contact guidance and could effectively stimulate the in vivo bone regeneration [26]. Tiainen et al. developed cross-hatched micropatterns on Ti6Al4V (varying

groove width of 40, 80 and 140 μm and groove spacing of 0, 20 and 100 μm) which wettability behaviour and structural stability were evaluated, the latter by friction tests against bone [27]. In a different study, laser-induced periodic surface structures (LIPSS) and nanopillars were produced by a femtosecond laser on Ti grade 2 and both laser patterns reduced the biofilm formation and bacterial adhesion, therefore reducing the risk of implant-associated infections [28]. Luo et al. used a femtosecond laser to produce nano-ripples on Ti6Al4V capable of preventing biofilm formation and bacterial adhesion, while promoting proliferation of rat MSC [29].

For the purpose of, for example, total joint replacements, surface texturing may be tailored not only to improve the biological interaction of the biomaterial but also the tribological performance, which can be improved by enhancing lubrication and wear resistance [30,31]. However, texture dimensions (groove width, pillar width and depth) depend on laser variables, such as laser power, scanning speed and number of passages, and drawing-based variables, as drawing pattern and dimensional features. Given these numerous variables, the selection of drawing features and laser parameters can be very demanding and time consuming. Therefore, research groups have dedicated effort towards optimization of surface textures, aiming different applications [32].

The goal of the present study was to explore the potential of the laser processing technique and analyse the influence of drawing and laser parameters to obtain a micro-scale pillars pattern which geometry and dimensions are suitable for the cellular ecosystem and, therefore, biomedical applications. In this context, this study explores the effect of laser and drawing parameters on the fabricated textures, by performing a design of experiments (DOE) and response surface method (RSM) to obtain a mathematical model for each texture dimension of interest. The final surfaces were evaluated regarding their geometry and dimensions, roughness, wettability, and reproducibility.

## 6.2. Materials and methods

### 6.2.1. Laser surface texturing

Ti6Al4V alloy plates (ASTM B265), with chemical composition present in Table 6.1, were purchased from Titanium Products (United Kingdom) and cut into plates with dimensions of 9.0 × 10.0 × 0.5 mm, using a Nd:YV04 laser (XM-30D, XianMing Laser, China) under an argon atmosphere.

Table 6.1 - Chemical composition of Ti6Al4V, according to manufacturer.

| **Material** | **Chemical composition (wt%, max)** | | | | | | | | |
|---|---|---|---|---|---|---|---|---|---|
| | N | C | H | Fe | O | Al | V | Ti | Other |
| Ti6Al4V | 0.050 | 0.100 | 0.015 | 0.400 | 0.200 | 5.500-6.750 | 3.500-4.500 | Matrix | 0.500 |

Surface texturing was performed using a Nd:YAG laser (OEM Plus, SISMA, Italy), which specifications are summarized in Table 6.2.

Table 6.2 - Laser Nd:YAG technical specifications.

| **Laser specifications** | |
|---|---|
| Average output power (W) | 6 |
| Peak power per pulse (kW) | 8.57 |
| Wavelength (nm) | 1064 |
| Spot size (μm) | 3 |
| Pulse width (ns) | 35 |
| Repetition rate (kHz) | 20 |
| Maximum pulse energy (mJ/pulse) | 0.3 |
| Beam quality factor, $M^2$ < | 1.8 |
| Cooling system | Forced-air cooling |

A schematically representation of the laser processing is depicted in Supplementary Fig. 6.1. Briefly, the laser power is controlled using a software interface and the laser beam is irradiated on the surface of the Ti6Al4V plate by a focusing unit containing fused quartz lens with a nominal focal length of 160 mm. The texture design (groups of vertical lines equally spaced and cross-hatched patterns for groove and pillars texturing, respectively) was defined in a computer-aided design software and then engraved on the metallic surfaces, according to specific laser parameters, through the laser connected Sisma Laser Controller (SLC) software. The texturing was assisted with a flow of air to remove sediments produced during laser processing. Afterwards, samples were cleaned in an ultrasonic bath with isopropyl alcohol (2-Propanol, Labsolve, Portugal) for 5 min and dried at room temperature.

The main goal of the present study was to explore micro-scale pillars texturing with pyramid elements with uniform size and spacing by laser surface texturing, with final dimensions in a

selected range. For that purpose, the main steps were identified, as schematically illustrated in Fig. 6.1.

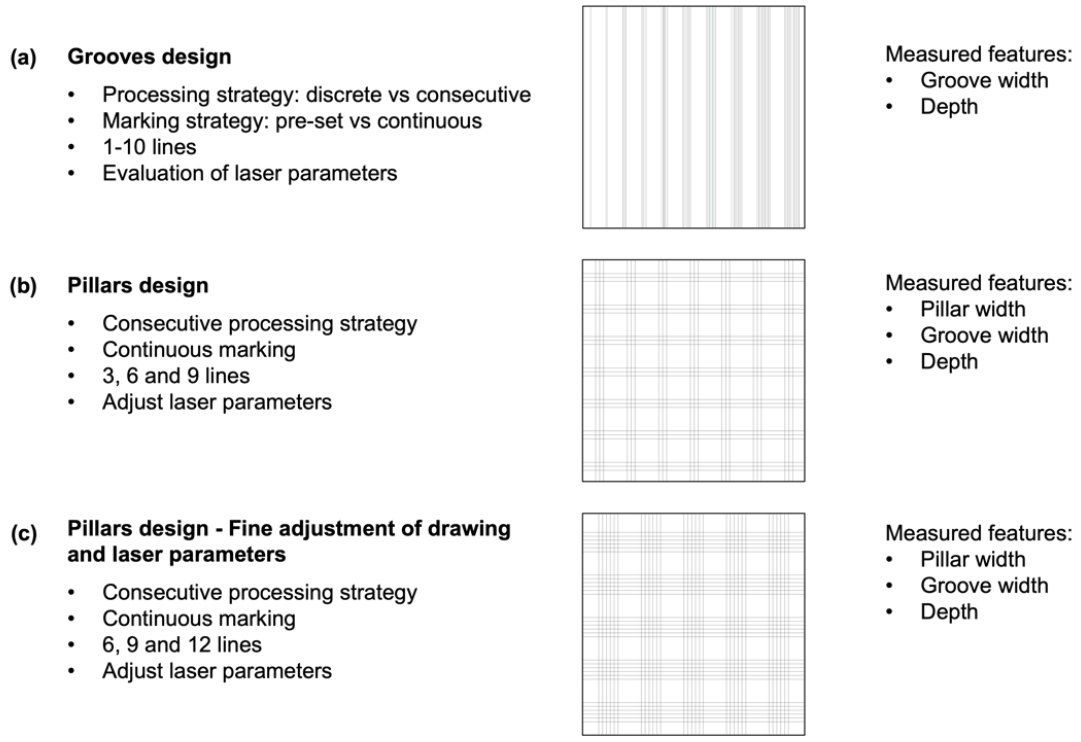



Figure 6.1 - The study of the micro-pillar surface laser texturing was divided into three main steps: (a) grooves design and texturing, followed by (b) pillars design and texturing and, finally, (c) a fine adjustment of the drawing and laser parameters to obtain a micro-scale pillars pattern with uniform size and dimensions in the selected range.

First, grooves were designed and textured to determine the groove width and depth. One to ten lines were engraved (Fig. 6.1a) by two different strategies: discrete laser processing and consecutive laser processing. In the former, the laser scans discrete zones at a time, creating one groove/laser ablation area and, afterwards the subsequent one, whereas in the second strategy the laser scans the total area of the sample consecutively (from left to right, and then returns to the beginning of the sample), as represented in Fig. 6.2.

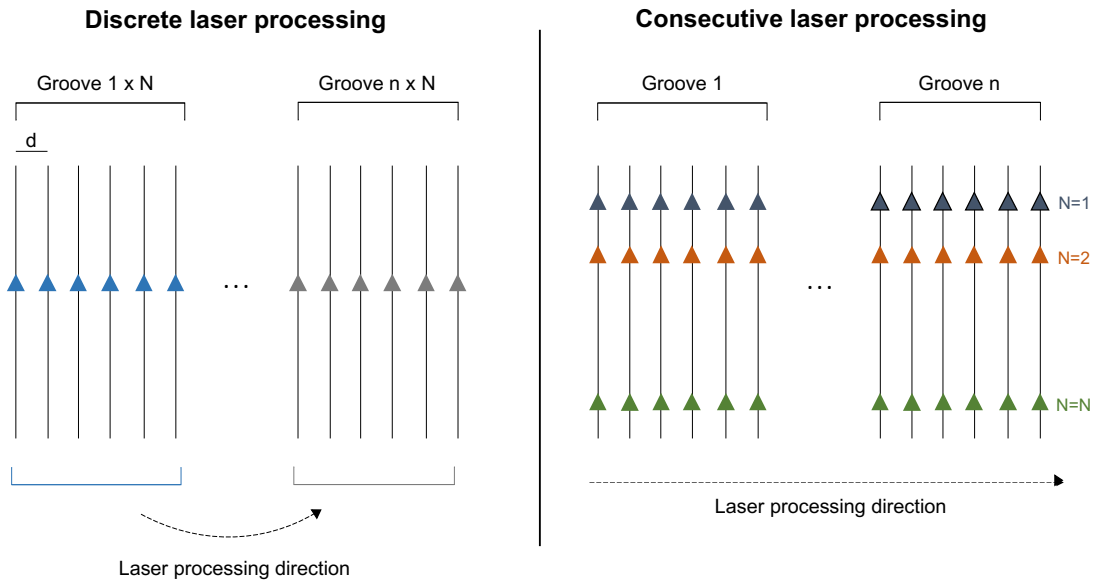



Figure 6.2 - Schematic representation of the grooves texturing processing, in which n is the number of grooves engraved by scanning vertical lines, spaced in between by d, in discrete and consecutive processing strategies. In the former, the laser engraves each groove (represented by one colour) at a time, whereas in the latter strategy each line is engraved consecutively from left to right, N number of passages (each passage is represented by one colour).

Three laser scanning parameters were adjusted to optimize the texturing process: laser power, scanning velocity and number of passages. Laser power (P) corresponds to the laser beam energy delivered per pulse (Watts); the scanning speed (v) is the leading edge of the beam front speed (mm/s), and the number of passages (N) corresponds to the number of scans carried out by the laser during the process. Another parameter defined in the laser software is the line spacing (d), correspondent to the distance between the scanned lines in mm. These parameters were used to calculate, for each condition, the laser energy density in J/mm$^2$, by using Eq. (6.1):

$$E = \frac{P \times N}{v \times d} \quad (6.1)$$

In the grooves design and texturing step (Fig. 6.1a), the laser power was set at 3 or 6 W, the number of passages at 20, 40 or 80, the scanning speed at 50, 100, 200 and 400 mm/s and the line spacing at 10 μm, so that the laser energy density was either 120 or 240 J/mm$^2$. For each condition, the two scanning strategies were investigated. After evaluating the quality of the grooves, the consecutive laser processing was selected. Subsequently, two different marking approaches were studied: pre-set marking and continuous marking. In the former, the laser scans each line in one direction, whereas the latter marking mode employs a fill calculation method which connects parallel lines in a way that the laser remains on as much as possible, as shown in Fig. 6.3.

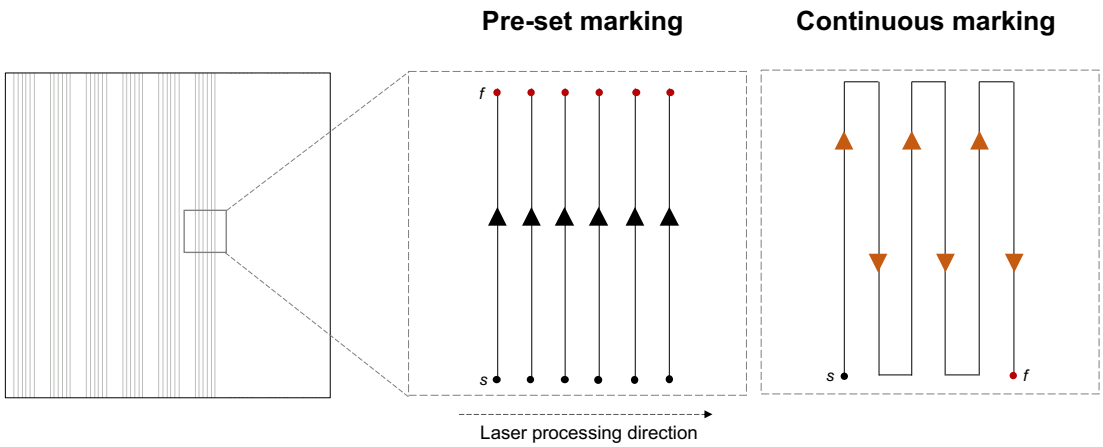



Figure 6.3 - The laser surface texturing begins at the point s (starting point) and finishes at f (finishing point), considering the laser scanning from left to right. In the set-marking approach the laser direction is from down to top repeatedly, whereas in the continuous marking parallel lines are connected so that the laser remains on as much as possible.

The continuous marking option presented a smoother surface compared to the one obtained by the pre-set marking and was, therefore, selected to investigate the combination of laser parameters and number of lines considering the targeted distance between pillars. For texturing the micro-scale pillars (Fig. 6.1b), the laser power was set at 3 W, the scanning speed at 100 mm/s, the number of passages varied between 65 and 125 and the line spacing at 10 μm. Based on the selected laser power and features, processing was performed at a laser fluence of 12.6 J/cm$^2$, according to ISO 11146–2 [33]. Despite what was initially predicted, considering the same number of lines, the groove width obtained for the pillars texturing, i.e., distance between pillars, did not correspond to the groove width obtained for grooves texturing. Consequently, the number of lines was again adjusted to obtain the targeted groove widths, and the laser parameter combinations were again evaluated. Finally, the drawings were fine-tuned to obtain the targeted dimensions (Fig. 6.1c): groove width of 60±5, 90±5 and 120±5 μm, pillar width of 20±5 μm and pillar depth of 50±5 μm.

In a preliminary texturing of pillars by consecutive processing strategy, the horizontal lines were first engraved (from up to down) followed by the vertical lines (from left to right), repeatedly by this order. It was observed that this strategy led to a variation of pillar depth along the sample. To counteract this effect and achieve a uniform pillar depth on the total sample area, the laser processing strategy was redefined, still following the consecutive processing strategy. The horizontal lines were engraved from up to down followed by the vertical lines engraved from left to right and then the laser processing was performed in the opposite directions, i.e., horizontal lines

were engraved from down to up and vertical lines from right to left. This laser processing order was repeated the selected number of passages.

### 6.2.2. Statistical analysis of the drawing and laser parameters

Response surface methodology (RSM) was used to analyse the relationship between explanatory variables (drawing and laser processing variables) and response variables (texture dimensions), which are depicted in Fig. 6.4.

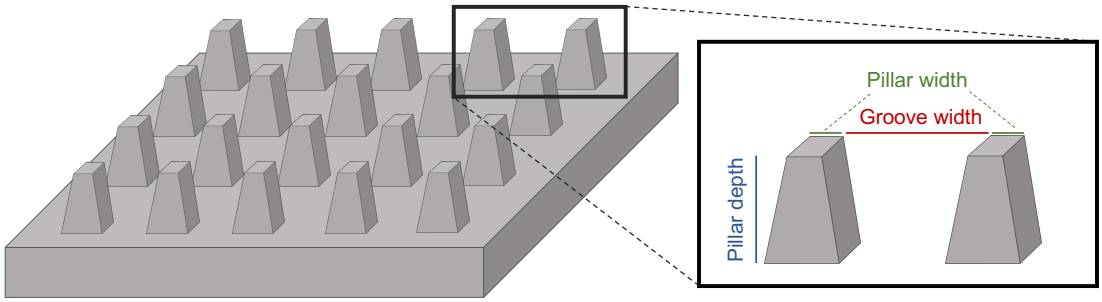



Figure 6.4 - Representation of the pillar laser texture dimensions: groove width, pillar width and pillar depth.

Three predictive models were obtained, one for each texture dimension: groove width, pillar width and pillar depth. Each output response, R, is obtained through the construction of a polynomial mathematical relationship, correspondent to Eq. (6.2),

$$R = a_0 + \sum_{i=1}^{k} a_i x_i + \sum_{i=1}^{k} a_{ii} x_i^2 + \sum_{i<j}^{k} a_{ij} x_i x_j + \varepsilon \quad (6.2)$$

where $a_0$ is a constant, $a_i$ is the linear coefficient, $a_{ii}$ is the quadratic coefficient, $a_{ij}$ is the interaction coefficient, $x_i$ and $x_j$ are the independent variables, $k$ is the number of factors and $\varepsilon$ is the associated error. These coefficients are predicted through regression analysis based on the measured responses.

The experimental matrix considering the levels of each parameter, summarized in Table 6.3, was constructed using Minitab software, which included a total of 81 combinations, as presented in Supplementary Table 6.1.

Table 6.3 - Multilevel factorial design of the experiment, including the input parameters and corresponding levels.

| **Input parameters** | | **Input levels** | | | | | | | | | |
|---|---|---|---|---|---|---|---|---|---|---|---|
| A_CAD | Groove width (µm) | 3-level | 50 | | | 80 | | | 110 | | |
| B_CAD | Pillar width (µm) | 3-level | 30 | | | 35 | | | 40 | | |
| N | Number of passages | 9-level | 65 | 70 | 75 | 80 | 85 | 110 | 115 | 120 | 125 |

The obtained texture dimensions were measured as described in Section 6.2.3.1. and the experimental data was inserted in the Minitab software. Using the RSM tool, the results were analysed, and the three mathematical models obtained. Afterwards, ANOVA was applied to each mathematical model with a 95% confidence interval to investigate the reliability, namely the contribution of each individual and combined parameters in the final response.

### 6.2.3. Surface characterization

#### 6.2.3.1. Surface topography

Textured samples were analysed by scanning electron microscopy (SEM) using JSM-6010 LV (JEOL, Japan). The surface of groove textured samples was assessed by SEM and texture dimensions were calculated using the ImageJ software. The groove width was measured by averaging five measures using a top view SEM image and the groove depth using a cross-section SEM image view.

The topography of pillar textured samples was assessed by a S neox 3D Optical Profiler (Sensofar, Spain) with a 10X objective and analysed with the Gwyddion software to assess the texture dimensions. The 2D profile was acquired in the horizontal direction and each texture dimension corresponded to the average of five measurements. For a better comprehension, texture dimensions were grouped according to the study timeline: first, the goal setting dimensions were selected, then the drawing dimensions were defined in a CAD file and finally, after processing, the dimensions were measured by profilometry. As opposed to the groove width and pillar width, which are strongly influenced by the 2D drawing dimensions (A_CAD and B_CAD), the desired pillar depth is primarily achieved by selecting the appropriate laser parameters, particularly the number of passages (N). The abbreviation of each dimension denomination is summarized in Table 6.4.

Table 6.4 - Texture dimension denomination along the study.

| | **Goal (G)** | **2D Drawing (CAD)** | **After processing (AP)** |
|---|---|---|---|
| **Groove width (A)** | A_G | A_CAD | A_AP |
| **Pillar width (B)** | B_G | B_CAD | B_AP |
| **Pillar depth (C)** | C_G | - | C_AP |

#### 6.2.3.2. Surface wettability

The wetting behaviour of post-processed samples was assessed using the contact angle system OCA 15 plus (Dataphysics, Germany). Samples were ultrasonically cleaned with isopropyl

alcohol for 5 min, stored at 60 °C overnight and stored in a desiccator. 180 days after surface laser texturing, a 4 μL droplet of distilled water was dispersed at a dosing rate of 1 μL/s at room temperature and the contact angles were determined using the DataPhysics SCA software.

6.2.3.3. Surface roughness and shape factor

Sample roughness can be obtained at a micro or macro scale. In the former, Ra and Rq were obtained by averaging ten measurements by selecting 2D profiles both in horizontal and vertical directions. At a macro-level, within a defined sample area, Sa, Sq and Sku of the 3D surface texture were obtained. The latter was used to evaluate the sharpness of the surface height distribution, which may be skewed above the mean plane (Sku<3), normal and thus sharp when indented portions co-exist (Sku=3) or spiked (Sku>3), as illustrated in Fig. 6.5 [34]. The roughness values were obtained for an area of interest defined in the Gwyddion software.

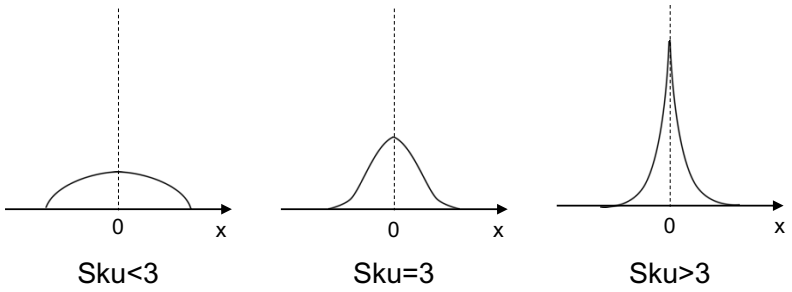



Figure 6.5 - Sku measures the sharpness of the roughness profile.

To quantitively evaluate the shape of the textured pillars, a formula to determine the geometry shape factor was defined in Eq. (6.3). The shape factor was calculated for the input variables combinations which texture dimensions, after processing (AP), were closer to the range of the targeted dimensions.

$$Shape\ factor = \frac{D}{d} \quad (6.3)$$

in which D is the groove width and d the distance correspondent to the horizontal plane of the groove, as represented in Fig. 6.6.




Figure 6.6 - The shape factor of a (a) rectangular geometry is equal to one, whereas a (b) pyramid geometry presents a shape factor higher than 1 (D>d).

## 6.3. Results and discussion

The main goal of the present study was to explore the capability for obtaining a micro-scale pyramid pillars pattern by laser surface texturing with groove width (A_G) of 60±5, 90±5 and 120±5 μm, pillar width (B_G) of 20±5 μm and pillar depth (C_G) of 50±5 μm. The study was focused, first, on the design and texture of grooves with the targeted widths and then on adjusting the laser and drawing parameters to design and texture pillars with uniform size and equally spaced with dimensions in the defined range.

### 6.3.1. Grooves design and texturing

#### 6.3.1.1. Discrete vs consecutive processing laser

In this study, two laser scanning strategies were evaluated: discrete and consecutive laser processing, which principle is shown in Fig. 6.2. Considering the same laser parameters, and thus the same laser energy density, the consecutive laser processing strategy resulted in smoother grooves, as presented in Fig. 6.7. When scanning the overall sample through consecutive laser processing, the generated temperature in the groove is lower compared to when creating discrete grooves, leading to a lower number of defects and thus smoother grooves [35].

#### 6.3.1.2. Pre-set vs continuous marking

Besides the machining strategy, two laser marking approaches were investigated: pre-set and continuous marking, as schematically represented in Fig. 6.3. The latter was selected due to the obtained smoother surface, as shown in Fig. 6.7.

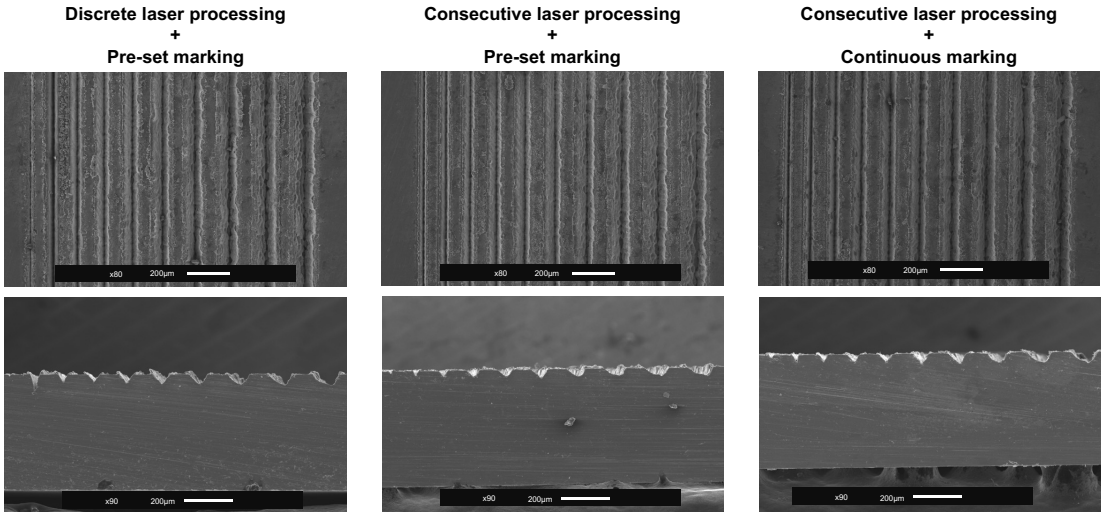



Figure 6.7 – Top and cross-section scanning images of discrete laser processing (left) and consecutive laser processing (middle) strategies by pre-set marking and consecutive laser processing and continuous marking (right). One to ten lines (from left to right) were engraved with 3 W laser power, scanning speed of 100 mm/s and 80 laser passages.

In the pre-set marking, the laser goes on/off on each line which may, therefore, present some power variations. On the contrary, in the continuous marking mode, the laser is as close as possible to be always on throughout the whole processing process, and thus, the laser power distribution is more uniform and constant. Nevertheless, the grooves-textured surfaces present some debris, which are typical for a LST process [36]. Different laser parameters were evaluated for both laser processing and marking strategies and the obtained groove width and depth of one to ten lines engravement are summarized in Supplementary Tables 6.2 and 6.3. The laser power was set at 3 or 6 W, the scanning speed at 50, 100, 200 and 400 mm/s and the number of passages at 20, 40 or 80 so that the laser energy density was either 120 or 240 J/mm$^2$.

The first main step included the design and texture of grooves to evaluate the effect of some drawing and laser parameters on the obtained groove width and depth. Discrete and consecutive laser processing strategies were investigated, and a smoother surface was achieved on the consecutive laser processing. Afterwards, the pre-set and continuous marking modes were compared, and the latter was selected for this study. A more uniform laser energy distribution for the continuous marking mode resulted in a surface with less debris and smoother ablated zones.

### 6.3.2. Pillars design and texturing

After selecting the consecutive laser processing as the machining strategy and the continuous marking mode, the obtained groove width and depth were evaluated to select the laser power, scanning speed and number of lines for pillars design and texturing. The laser power was

set at 3 W, the scanning speed at 100 mm/s and the CAD drawings of cross-hatched patterns were designed with groups of 3, 6 and 9 lines, as shown in Fig. 6.1b. However, the groove width obtained by processing grooves (groups of vertical lines) was higher than the groove width obtained for the cross-hatched pattern (groups of vertical and horizontal lines), considering the same number of lines and laser parameters. This is probably related to the fact that texturing grooves is faster, because only vertical lines are engraved (from left to right). Consequently, the temperature of the textured sample is higher when the laser returns to the beginning and the accumulated heat in the ablation area leads to a wider machined area [35,37]. For this reason, the number of lines was adjusted to 6, 9 and 12 lines to obtain the targeted groove widths (60, 90 and 120 μm, respectively), as schematically represented in Fig. 6.8a-c. Besides the number of lines, which is predicted to directly influence the groove width, another drawing parameter is the distance between the groups of lines, which was set as 30, 35 and 40 μm, as shown in Fig. 6.8d-f.

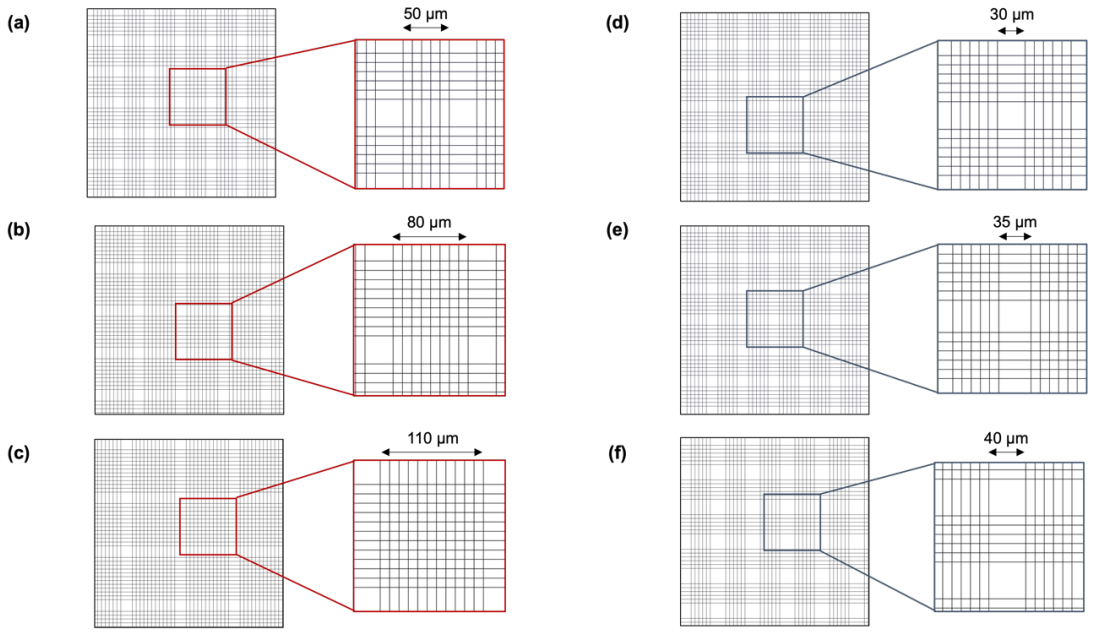



Figure 6.8 - CAD drawings of cross-hatched patterns with a groove width of (a) 50 μm, (b) 80 μm and (c) 110 μm and pillar width of (d) 30 μm, (e) 35 μm and (f) 40 μm, in this case exemplified for the design pattern with a groove width of 50 μm.

The laser parameters were fixed to a power of 3 W, the scanning speed to 100 mm/s and the number of passages was varied between 65 and 125, making a total of 81 combinations, as summarized in Supplementary Table 6.1.

When texturing the cross-hatched design pattern, the laser ablation is increased when the vertical and horizontal lines are intersected. In fact, on those areas, the number of passages is the double, creating high depth holes as demonstrated in Fig. 6.9.

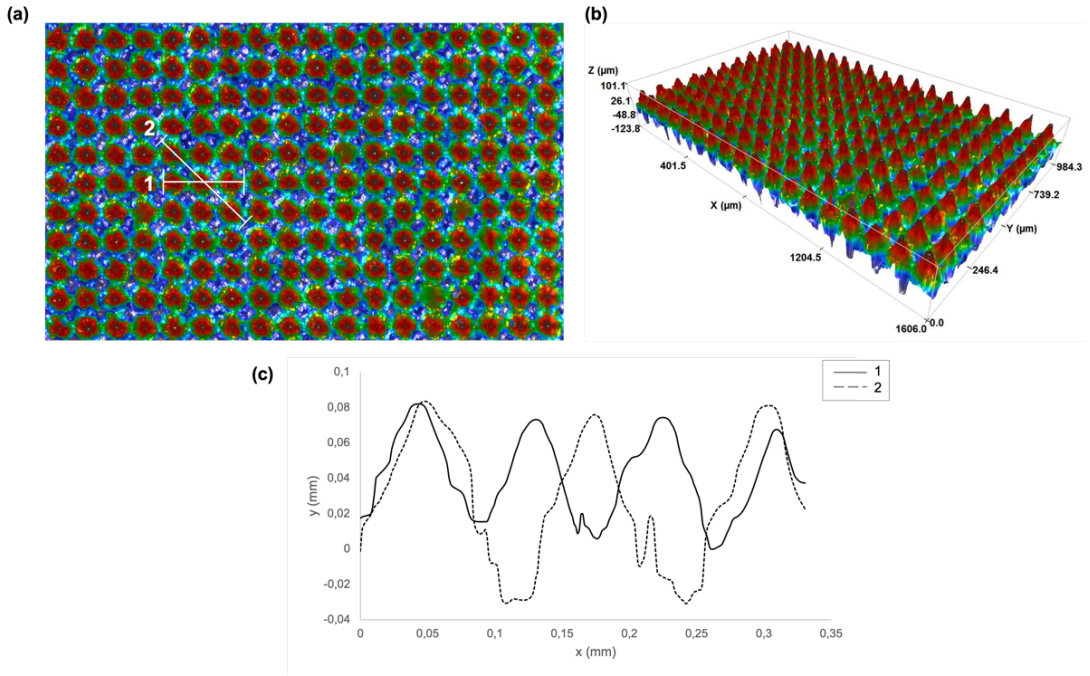



Figure 6.9 - (a) 2D and (b) 3D optical profilometry images of a textured sample and the corresponding (c) extracted profiles, in which the black corresponds to the horizontal line and the grey to the diagonal one. Pillar peaks are in red and deeper holes in blue. The displayed images were acquired for Exp. No. 35 (A_CAD=50 µm, B_CAD=40 µm and N=70).

### 6.3.3. Mathematical models

For each experiment the texture dimensions (A_AP, B_AP and C_AP) were measured and collected to perform a statistical analysis. A two-second order regression model was developed for each texture dimension and the effect of individual and combined variables were investigated using ANOVA. The coefficients reflect the main effects of the drawing and laser processing parameters and their interaction. The relationship between the responses and single input variables is statistically significant for all models ($p<0.001$). Furthermore, the interaction between variables has a significant effect, proving that LST is a complex process and that the texture dimensions are a result of the interaction of multiple variables. In this sense, mathematical models are a crucial tool to understand the effect of drawing and laser processing input variables, and to predict the texture dimensions for a particular set of input variables. All models are normally distributed and present heteroscedasticity, as shown by the plot of regular residuals and residuals versus fitted values in Supplementary Figs. 6.2–6.4.

One model for each texture dimension of interest (groove width, pillar width and depth) was proposed, as follows.

a) Groove width model

The mathematical model of the groove width, simplified with only significant terms, is described in Eq. (6.4).

$$Groove\ width\ (\mu m) = -13.1 + 1.475A + 1.16B - 0.501N - 0.002666A^2 - 0.01001BN \quad (6.4)$$

The suitability of the developed groove width model and the significance of linear and second order terms and the two-way interactions between terms are presented in Supplementary Table 6.4. The P-values of A, B and N are lower than 0.05, indicating that these factors are extremely significant for the groove width regression model. The interactions $A^2$ and BN are also significant terms (P-value<0.05). The groove width model describes the response given a low value of S (S = 1.91) and the regression is approximately 100 ($R^2$ = 99.40%), which indicates that 99.40% of the groove width variation can be explained by the regression model and thus the data fits the model. In addition, the high values of adjusted $R^2$ and predicted $R^2$ suggest that the model is adequate for the prediction of the groove width values within a confidence interval of 95%. In addition, the high F-value of the model (1311.78) indicates that the proposed model is significant.

b) Pillar width model

The pillar width mathematical model is described in Eq. (6.5), simplified with only significant coefficient, and the suitability of the model and significance of the terms are presented in Supplementary Table 6.5.

$$Pillar\ width\ (\mu m) = 17 - 0.284A - 1.03B + 0.540N + 0.001236A^2 - 0.00747BN \quad (6.5)$$

The P-values of A, B and N are extremely significant due to their P-value lower than 0.05. Regarding the interactions, $A^2$ and BN are the only significant interactions (P-value< 0.05). Although the S value is still considered low (S = 2.02), only 61.01% of the variation can be explained by the regression model. The adjusted $R^2$ and predicted $R^2$ values are close to 61%, suggesting that the model can only be used for a short acting range. In fact, the B_CAD was only varied between 30 and 40, which is suggested to be the main reason for a not high F-value (12.34). Nevertheless, the residual plots fall on a linear trend and the obtained model can be used for the pillar width range that was defined as target in this study.

c) Pillar depth model

The third mathematical model is the pillar depth model, which is plotted in Eq. (6.6), reduced to only significant coefficients. The suitability and the significance of linear and second-order terms are presented in Supplementary Table 6.6.

$$Pillar\ depth\ (\mu m) = -297.8 - 1.447A + 19.29B - 1.627N - 0.00492A^2 - 0.3243B^2 + 0.00685AN + 0.06558BN + 0.06480AB \quad (6.6)$$

All linear terms (A, B and N) and the interactions $A^2$, $B^2$, AN, BN and AB have a P-value lower than 0.05, which means they are significant terms for this model. Although the S of the depth model is higher than 2 (S=5.97), the model is still acceptable given the regression close to 100 ($R^2$ = 98.02%), as well as the high values of adjusted $R^2$ and predicted $R^2$, which suggest a proper fitting. Furthermore, the high F-value of the model (391.43) implies that the depth model is significant. In this sense, the proposed model for pillar depth is adequate for predicting depth values with a confidence interval of 95%.

6.3.3.1. Effect of the parameters on texture dimensions

The statistical analysis performed on the three mathematical models suggests that groove width (A_CAD), pillar width (B_CAD) and number of passages (N) have a significant effect on the texture dimensions (P-value<0.05). The main effects of each parameter on groove width (A_AP), pillar width (B_AP) and depth (C_AP) are plotted in Fig. 6.10.

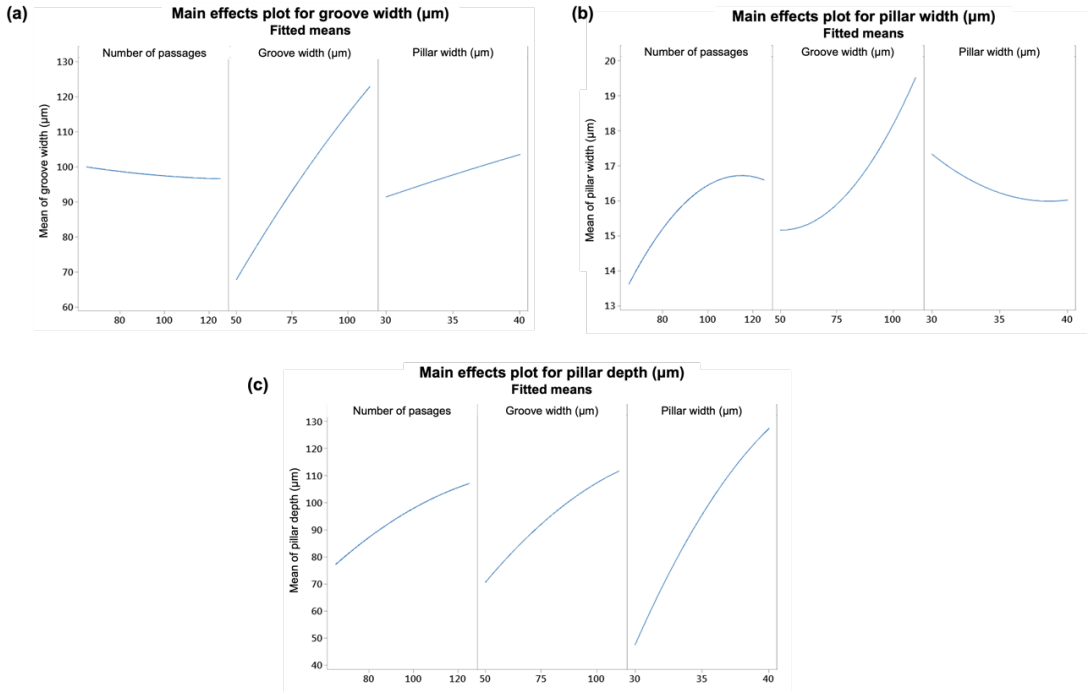



Figure 6.10 - Main effects of each parameter on (a) groove width, (b) pillar width and (c) pillar depth.

As initially predicted, the A_CAD has a proportional and evident effect on the groove width after processing. Although not so pronounced, a higher B_CAD increases the groove width, on contrary to the number of passages which does not have a linear effect (Fig. 6.10a). The pillar width increases, not linearly, with N and A_CAD and decreases with increasing B_CAD (Fig. 6.10b). Close to a linear tendency, the pillar depth increases with A_CAD, B_CAD and N.

Sen et al. studied the influence of laser processing parameters on micro-groove texturing of Ti6Al4V substrates using a fibre laser. The increment of the number of passages resulted in an increase of groove depth and width, the latter up to a certain number of passages because of the re-solidification of the molten material [38]. The correlation between picosecond laser processing parameters and the corresponding micro-groove dimensions were also assessed and the authors concluded that increased groove depth was obtained by increasing the number of passages or decreasing the scan speed [39]. According to Eq. (6.1), higher number of passages reflects a higher laser energy density, considering the same laser power, scanning speed and line spacing defined in the laser processing. In this sense, high laser energies result in higher pillar depths as a consequence of the greater ablation [40]. The same conclusion was claimed by Soveja et al., in which the analysis of developed mathematical models showed that the pulse energy was the most influential factor on the material removal rate [32].

Besides the significant contribution of each linear term, according to the analysis of variance present in Supplementary Tables 6.4–6.6, the combination of both pillar width (B_CAD) and number of passages (N) have a significant effect ($p<0.005$) on the groove width (A) and pillar width (B), whereas the combinations of the three variables have a significant effect ($p<0.005$) on the pillar depth (C). To better understand the effect of the second-order interactions in each texturing response, contour plots of the developed mathematical models are present in Fig. 6.11.

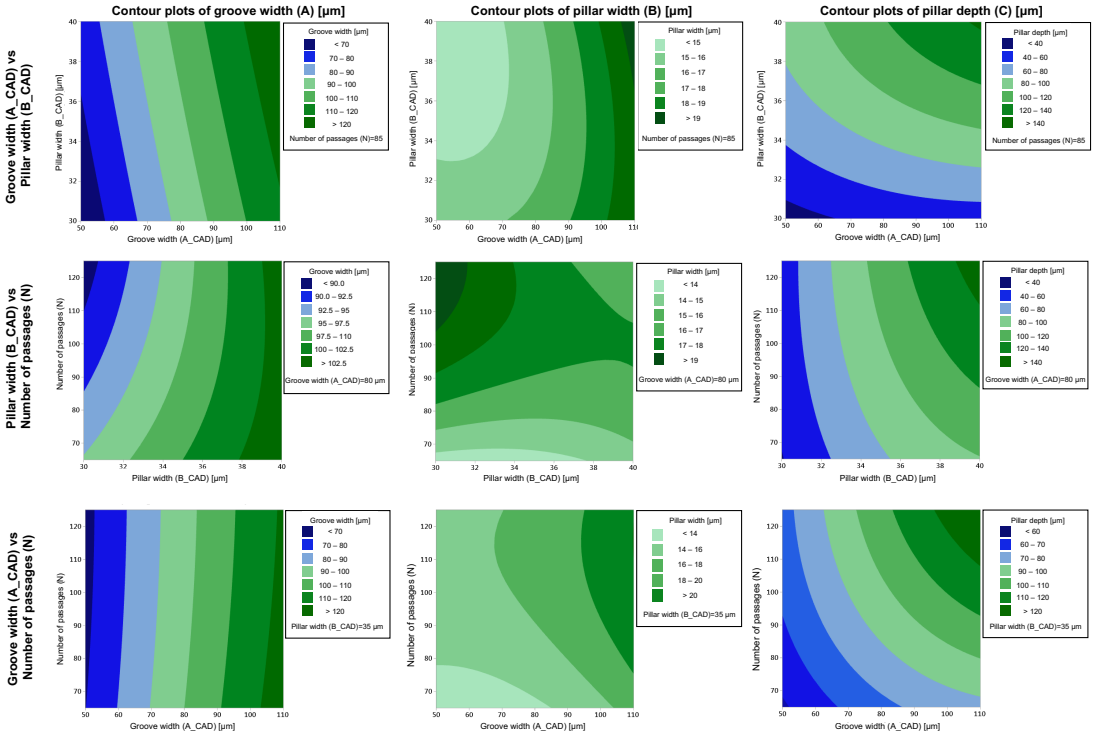



Figure 6.11 - Contour plots of groove width (A), pillar width (B) and pillar depth (C) in response of the combination of the input variables (A_CAD, B_CAD and N), by holding the third variable at the middle of its range.

The contour plots confirm that each texture dimension is well described by the developed mathematical models. The significant interactions of the input parameters on the three mathematical models are summarized in Table 6.5.

Table 6.5 - Significant effect of combined parameters in the final response for the obtained mathematical models.

| Model | Exp. No. | A_CAD (μm) | B_CAD (μm) | N | Output texture dimension (μm) | Significant interaction |
|---|---|---|---|---|---|---|
| Groove width model | 62 | 80 | 30 | 70 | A_AP=97.6 | B_CAD vs N |
| | 33 | | | 125 | A_AP=90.4 | |
| Pillar width model | 54 | 80 | 30 | 75 | B_AP=15.4 | B_CAD vs N |
| | 57 | | | 115 | B_AP=21.6 | |
| Pillar depth model | 49 | 80 | 30 | 85 | C_AP=37.5 | A_CAD vs B_CAD |
| | 63 | 110 | | | C_AP=59.5 | |
| | 57 | 80 | 30 | 115 | C_AP=47.2 | B_CAD vs N |
| | 52 | | 40 | | C_AP=144.1 | |
| | 60 | 50 | 35 | 65 | C_AP=54.2 | A_CAD vs N |
| | 42 | | | 120 | C_AP=73.9 | |

For the groove width model and focusing on the target groove widths (A_G = 60±5, 90±5 and 120±5 μm) the interactions A_CAD vs B_CAD and A_CAD vs N are not significant. On the other hand, the interaction between B_CAD and N has a significant effect on the groove width (e.g., comparison between Exp. No. 62 and 33). Considering the actuation range predicted by the pillar width model, the interaction between B_CAD and N has a significant effect (e.g., by comparing Exp. No. 54 and 57). On the contrary, for the target pillar width (B_G = 20±5 μm) the interactions A_CAD vs B_CAD and A_CAD vs N do not have a significant effect. The only mathematical model which is strongly dependent on all input variables combinations is the pillar depth model. By focusing on the target pillar depth (C_G = 50±5 μm), the following combinations have a significant effect: A_CAD vs B_CAD (e.g., comparison between Exp. No. 49 and 63), B_CAD vs N (e.g., comparison between Exp. No. 57 and 52) and finally A_CAD vs N (e.g., comparison between Exp. No. 60 and 42).

The proposed mathematical models are therefore suitable to predict the texture dimensions for a set of input drawing and laser processing variables, for the range of dimensions selected for this study.

### 6.3.4. Characterization of textured samples

Topology and morphology of metallic surfaces can be modified by laser processing and achieved by changing the laser parameters. In fact, micro-scale patterns with pyramid elements were successfully obtained, with different texture dimensions. Considering each target texture dimensions, three combinations of drawing and laser processing parameters were selected, as displayed in Table 6.6.

Table 6.6 - Combinations of drawing and laser parameters for the targeted dimensions (groove width (A_G) of 60±5, 90±5 and 120±5 μm, pillar width (B_G) of 20±5 μm and pillar depth (C_G) of 50±5 μm).

| Exp. No. | Input parameters | | | Output texture dimensions | | | |
|---|---|---|---|---|---|---|---|
| | A_CAD (μm) | B_CAD (μm) | N | Groove width | | Pillar width | Pillar depth |
| | | | | A_G (μm) | A_AP (μm) | B_AP (μm) | C_AP (μm) |
| 41 | | 40 | 75 | | 70.5 ± 2.7 | 16.2 ± 1.5 | 78.8 ± 4.0 |
| 37 | 50 | 30 | 125 | 60±5 | 60.2 ± 2.8 | 16.6 ± 3.4 | 33.9 ± 3.2 |
| 46 | | 30 | 80 | | 60.0 ± 3.8 | 18.3 ± 1.2 | 32.4 ± 6.5 |
| 71 | | 30 | 80 | | 91.4 ± 3.0 | 19.0 ± 2.8 | 44.1 ± 2.9 |
| 57 | 80 | 30 | 115 | 90±5 | 88.2 ± 4.0 | 21.6 ± 4.0 | 47.2 ± 3.9 |
| 33 | | 30 | 125 | | 90.4 ± 2.4 | 18.6 ± 2.6 | 47.9 ± 5.2 |
| 25 | | 30 | 70 | | 121.6 ± 4.4 | 15.4 ± 2.8 | 50.7 ± 4.1 |
| 63 | 110 | 30 | 85 | 120±5 | 120.8 ± 3.5 | 19.2 ± 2.8 | 59.5 ± 3.5 |
| 65 | | 30 | 125 | | 114.2 ± 1.6 | 20.8 ± 4.2 | 54.0 ± 2.6 |

As any machining process, laser texturing presents a tolerance due to, for example, laser positioning and inherent error of the technology. Nevertheless, there is flexibility to adjust the drawing and laser parameters to obtain a micro-scale pillar pattern with dimensions of interest.

#### 6.3.4.1. Wettability

The wetting behaviour of textures which dimensions are in the range of the target was assessed by sessile drop measurement with distilled water and is displayed in Fig. 6.12. Surfaces with water contact angles (WCA) under 90° are defined as hydrophilic and above 90° as hydrophobic [41].

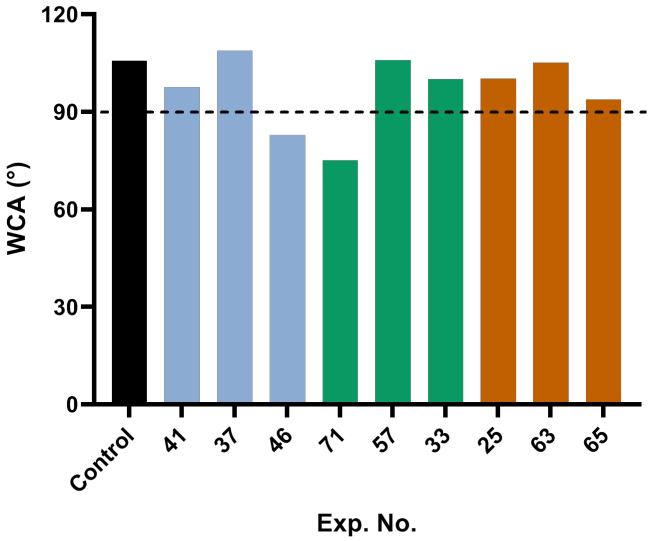



Figure 6.12 - Water contact angles of the experiment numbers which dimensions after processing are in the range of the target texture dimensions. The dark bar corresponds to the control group (non-textured), blue bars to textures with A_G = 60±5 μm, green bars to A_G = 90±5 μm and orange bars to A_G = 120±5 μm. The demarcation of hydrophilic and hydrophobic behaviour is represented by a dashed line at 90°.

When considering smooth surfaces, wetting is assessed by the Young model. However, two theories have been proposed to characterize the wetting behaviour on micro-structure surfaces: Wenzel and Cassie-Baxter solid-liquid wetting states. On the former, the water droplet penetrates the grooves, whereas on the latter the water droplet is suspended on the top of the texture features [42]. Given the heterogeneity associated to laser processing, textured samples are not smooth and thus air may be entrapped in surface irregularities, increasing the contact angle [43]. In addition, variations between the real and ideal surface contribute to contact angle hysteresis which influences the contact angle measurement [44]. Wettability of a solid surface is, therefore, determined by the surface morphology and topography, but also by its chemical composition [45]. Despite the fact it is a muti-variable dependent feature, some authors investigated the correlation between laser textured surfaces and wetting. Wang et al. performed pulsed laser ablation in liquid to engrave a grid pattern (spacing between adjacent scanning lines of 150 μm) on Ti6Al4V by nanosecond laser pulses [46]. The raw Ti6Al4V surface presented a contact angle of 77° and after texturization in air, deionized water and ethanol it increased to more than 150°. The transition to hydrophobic state was hypothesized to be related to the weak adhesion between textured surfaces and the droplet, impairing the complete immersion of the droplet (Cassie-Baxter state) and to the absorption of organic species during laser ablation which changed the surface polarization and thus the surface wettability [46]. In addition, storage conditions, in which are included the period

of time between texturing and the contact angle measurement, have been shown to influence wetting. Raimbault et al. fabricated grooves on Ti6Al4V by a femtosecond Yb-YAG laser (groove width of 25, 50 and 75 μm and depth of 1 or 5 μm) and concluded that contact angles increased in the days following the irradiation due to the passive hydrophobic hydrocarbon layer amplified by the surface topography [47]. Patel et al. observed that pillars textured samples presented a wetting behaviour up to 24 h after Nd:YAG laser irradiation but was altered to hydrophobic over time [23]. Similar behaviour was found by the study conducted by Yang et al., in which a nanosecond pulser laser was used to create line, grid and spot patterns on Ti grade 2. Immediately after laser treatment, surfaces were more hydrophilic while, after long-term exposure to air, the contact angles increased to more than 130° [45].

Compared to the non-textured group, textured surfaces displayed similar or lower contact angles. Laser treatments alter surface features, such as surface structure, roughness and chemical composition, and the combination of these dictate the surface wettability. Hydrophilic surfaces improve the interaction between the biomaterial and the in vivo environment and thus, adding textures to titanium samples by LST can increase their wettability, contributing to better osseointegration outcomes.

#### 6.3.4.2. Roughness, topography and morphology

The roughness of each texture may be acquired either by 2D profiles or by selecting a specific surface area. Amplitude parameters are considered the most important parameters to characterize the surface topography, as they are used to measure the vertical characteristics of surface deviations. Ra and Rq were calculated at the horizontal plane of grooves and Sa, Sq and Sku considering the surface of interest, as summarized in Table 6.7. Other parameters related to the surface roughness are shown in Supplementary Table 6.7.

A pyramid geometry was obtained through laser processing, as illustrated in Fig. 6.13, due to the Gaussian beam energy distribution. In order to quantitively assess the pillars geometry, a shape factor was calculated according to Eq. (3). The shape factor was calculated for the selected combinations through the 2D profilometry profile, as exemplified in Fig. 6.6. The rectangular shape was adopted as the comparing element and the calculated shape factors are summarized in Table 6.7.

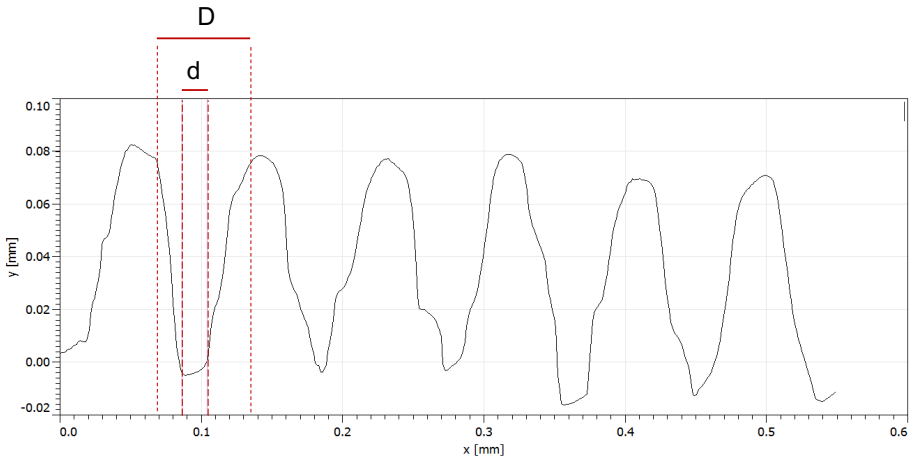



Figure 6.13 - The shape factor was calculated by randomly selecting lines in the 2D profile, as the acquired for Exp. No. 41 (A_CAD=50 μm, B_CAD=40 μm and N=75).

Table 6.7 - Groove and surface roughness values and shape factor of the experiment numbers which dimensions after processing met the target texture dimensions.

| Exp. No. | Ra (μm) | Rq (μm) | Sa (μm) | Sq (μm) | Sku | Shape factor |
|---|---|---|---|---|---|---|
| 41 | 2.73 ± 1.72 | 3.08 ± 1.93 | 32.21 | 39.91 | -0,32 | 3.94 ± 0.65 |
| 37 | 1.66 ± 0,83 | 2.12 ± 1.12 | 13.89 | 17.68 | 0,35 | 4.46 ± 0.92 |
| 46 | 1.68 ± 0.59 | 2.01 ± 0.76 | 13.74 | 17.99 | 0,85 | 4.83 ± 0.62 |
| 71 | 2.17 ± 1.10 | 2.68 ± 1.35 | 24.22 | 31.07 | 0,31 | 3.76 ± 0.83 |
| 57 | 2.23 ± 1.10 | 2.70 ± 1.28 | 25.18 | 32.02 | 0,25 | 5.02 ± 0.85 |
| 33 | 1.88 ± 0.63 | 2.26 ± 0.81 | 24.1 | 31.23 | 0,51 | 4.19 ± 0.52 |
| 25 | 2.36 ± 0.97 | 2.70 ± 1.09 | 31.22 | 38.75 | -0,29 | 2.32 ± 0.21 |
| 63 | 2.43 ± 1.23 | 3.04 ± 1.50 | 30.27 | 37.89 | -0,15 | 2.54 ± 0.37 |
| 65 | 1.96 ± 1.24 | 2.40±1.47 | 29.78 | 38.21 | 0.25 | 3.11 ± 0.44 |

When in direct contact with bone, the surface properties of metallic implants must elicit a cellular response that promotes bone regeneration and assures an implantation success. The mechanisms underlying the interaction between cells and biomaterials are complex and the optimal surface topography responsible for eliciting the target application remains a critical challenge. Surface treatment by a nanosecond laser is a promising technique to create specific topographies. In the current study, micro-pillar patterns with pyramid elements and different texture dimensions were textured on Ti6Al4V samples.

Chikarakara et al. performed a high-speed $CO_2$ laser melting of Ti6Al4V which resulted in a modified layer from 20 to 50 μm deep with improved microstructural properties [48]. Afterwards, the improved biocompatibility of these laser-treated surfaces (with average roughness values between 1.39 and 2.73 μm) was demonstrated by culturing fibroblast and osteoblast cell lines [49]. Topological features, such as micro-grooves, have been shown to regulate contact guidance which influences cell adhesion, shape and orientation and therefore the cellular response. Mukherjee et al. used a long-pulsed laser to create micro-ripple topographies on Ti6Al4V surfaces with different sizes (20, 40 and 100 μm width). Human MSC were prominently orientated on surfaces having 20 μm ripples (3D average roughness of 1.9 μm) and showed the highest differentiation potential towards osteoblastic lineage [50]. Voisey et al. textured groove arrays (40 μm width, 10 μm depth and ridge width of 20 μm) on commercially pure titanium using a Q-switched laser and the obtained surface with a Sa of 18±03 μm and groove Ra of 0.8±0.01 μm promoted a preferential alignment of human osteosarcoma cells with the groove length [51]. Zheng et al. machined micro-grooves on Ti6Al4V surface by a fibre laser marking machine (depth 10 μm, width 10, 20 and 30 μm and pitch 60, 105 and 150 μm) and higher roughness values (2.72±0.52 μm) improved MC3T3-E1 cell adhesion and biological activity [52]. Micro-texturing increases the surface area and rougher and hydrophilic or near hydrophilic surfaces promote adhesion, spreading and proliferation of cells and thus its potential application in bone tissue engineering. Laser texturing was performed in other materials which also promoted a positive cellular response. In vitro studies were conducted on squared ridges of ~$50 \times 50$ $\mu m^2$ (grooves with 100 μm width 80 μm depth) textured on a zirconia substrate using a Nd:YAG laser. The surface with Ra<3 μm, Sa of 17.1 μm and Sq of 21.4 μm promoted the attachment and proliferation of MC3T3-E1 cells [53].

The obtained surface roughness values are in line with the literature for laser texturing on metallic materials. Furthermore, surface roughness between 20 nm and 10 μm were reported to have a positive impact on the biocompatibility of metallic materials, as cells and biological molecules have an approximate length scale [54]. In the present study, the textured pillars have a pyramid shape (shape factor>1), and surface laser texturing may be used to create a micro-scale design with uniform size pillars that are evenly spaced. A set of drawing and laser parameters were selected for each targeted pattern dimensions as follows: A_CAD = 50, 80 μm and 110, B_CAD = 30 μm and N = 80 (for A_CAD = 50 and 80 μm) and N = 125 (for A_CAD = 110 μm), which correspond to a laser energy density of 240 and 375 $J/mm^2$ (for 80 and 125 laser passages,

respectively). The selected samples were hydrophilic or near hydrophilic and the roughness parameters and shape factors are similar for the three selected combinations. The micro-scale pillars texture of each selected sample was assessed by SEM, as represented in Fig. 6.14.

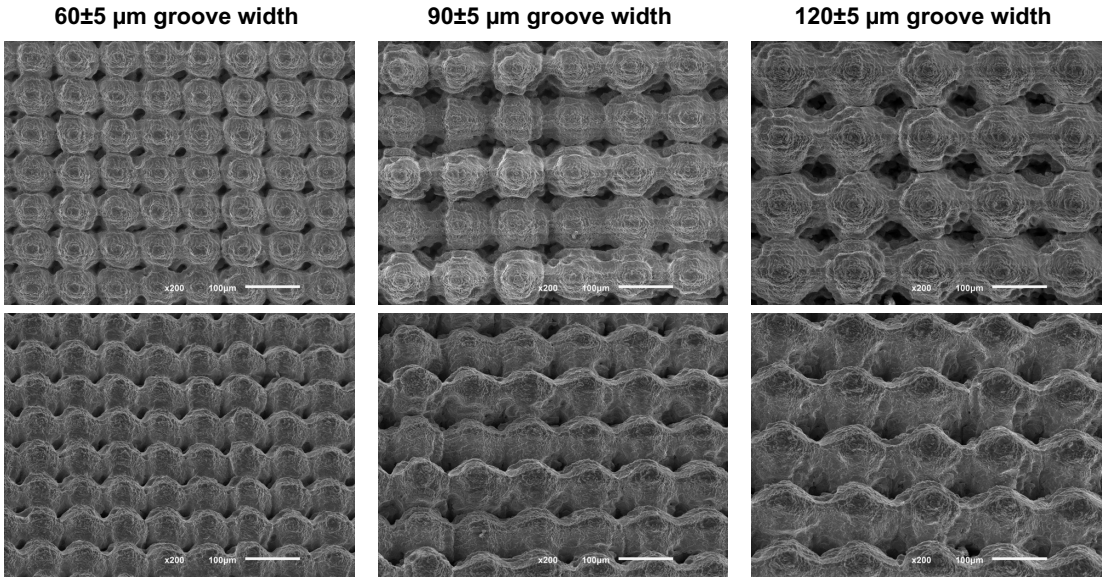



Figure 6.14 - SEM images of the selected patterns (top view and with tilting of 30°). The micro-scale pattern with pillar width of 20±5 µm, depth of 50±5 µm and groove width of 60±5, 90±5 and 120±5 µm correspond to the Exp. No. 46, 71 and 65, respectively.

## 6.4. Conclusions

The search for an improved surface micro-geometry on metallic implants, able to efficiently promote bone regeneration, remains a challenge. Laser surface texturing has been proposed as a promising tool to modify the surface of metallic biomaterials. However, several parameters including drawing and laser processing parameters, such as laser power, scanning velocity and number of passages, significantly influence the surface geometry and properties. The present study aimed to explore the capabilities of laser surface texturing on Ti6Al4V samples and, by assessing the influence of drawing and laser parameters, a set of input parameters was selected to obtain a micro-scale pattern with pyramid pillars with dimensions targeted for biomedical applications. On grooves texturing, two laser machining strategies and marking modes were investigated. The consecutive laser processing strategy and continuous marking mode were selected given the smoother grooves. Afterwards, a pillar pattern was designed and textured within a set of input drawing and laser parameters. Predictive models were developed for each texture dimension (groove width, pillar width and depth) and the main contributions of the input parameters were correlated with each dimension. This processing strategy was effective to obtain micro-scale

patterns and input combinations were selected based on the targeted dimensions, wetting behaviour, roughness values and shape factor, which are in accordance with reportedly adequate ranges for biomedical applications.

**Acknowledgments**

This work was supported by FCT (Fundação para a Ciência e a Tecnologia) through the grant SFRH/BD/141056/2018, the project PTDC/EME-EME/1442/2020 (Add2MechBio) and under the national support to R&D units grant, through the reference projects UIDB/04436/2020 and UIDP/04436/2020. In addition, this work was developed within the scope of the project CICECO-Aveiro Institute of Materials, UIDB/50011/2020, UIDP/50011/2020 & LA/P/0006/2020, financed by national funds through the FCT/MEC (PIDDAC).




**References**

[1] M. Kaur, K. Singh, Review on titanium and titanium based alloys as biomaterials for orthopaedic applications, Mater. Sci. Eng. C. 102 (2019) 844–862, https://doi.org/10.1016/j.msec.2019.04.064.

[2] Q. Chen, G.A. Thouas, Metallic implant biomaterials, Mater. Sci. Eng. R 87 (2015) 1–57, https://doi.org/10.1016/j.mser.2014.10.001.

[3] M. Marian, R. Shah, B. Gashi, S. Zhang, K. Bhavnani, S. Wartzack, A. Rosenkranz, Exploring the lubrication mechanisms of synovial fluids for joint longevity – a perspective, Colloids Surf. B 206 (2021), 111926, https://doi.org/10.1016/j. colsurfb.2021.111926.

[4] M. Marian, D. Berman, D. Nečas, N. Emami, A. Ruggiero, A. Rosenkranz, Roadmap for 2D materials in biotribological/biomedical applications – a review, Adv. Colloid Interface Sci. 307 (2022), https://doi.org/10.1016/j.cis.2022.102747.

[5] R. Shah, B. Gashi, S. Hoque, M. Marian, A. Rosenkranz, Enhancing mechanical and biomedical properties of protheses - surface and material design, Surf. Interfaces 27 (2021), 101498, https://doi.org/10.1016/j.surfin.2021.101498.

[6] B.R. Sunil, A.S. Kranthi Kiran, S. Ramakrishna, Surface functionalized titanium with enhanced bioactivity and antimicrobial properties through surface engineering strategies for bone implant

applications, Curr. Opin. Biomed. Eng. 23 (2022), 100398, https://doi.org/10.1016/j.cobme.2022.100398.

[7] N. Sirdeshmukh, G. Dongre, Laser micro & nano surface texturing for enhancing osseointegration and antimicrobial effect of biomaterials: a review, Mater. Today Proc. 44 (2021) 2348–2355, https://doi.org/10.1016/j.matpr.2020.12.433.

[8] T. Wang, L. Wang, Q. Lu, Z. Fan, Changes in the esthetic, physical, and biological properties of a titanium alloy abutment treated by anodic oxidation, J. Prosthet. Dent. 121 (2019) 156–165, https://doi.org/10.1016/j.prosdent.2018.03.024.

[9] F. Melo-Fonseca, M. Gasik, S. Madeira, F.S. Silva, G. Miranda, Surface characterization of titanium-based substrates for orthopaedic applications, Mater. Charact. 177 (2021), 111161, https://doi.org/10.1016/j.matchar.2021.111161.

[10] A. Henningsen, R. Smeets, P. Hartjen, O. Heinrich, R. Heuberger, M. Heiland, C. Precht, C. Cacaci, Photofunctionalization and non-thermal plasma activation of titanium surfaces, Clin. Oral Investig. 22 (2018) 1045–1054, https://doi.org/ 10.1007/s00784-017-2186-z.

[11] J.A. Wahab, M.J. Ghazali, W.M.W. Yusoff, Z. Sajuri, Enhancing material performance through laser surface texturing: a review, Trans. Inst. Met. Finish. 94 (2016) 193–198, https://doi.org/10.1080/00202967.2016.1191141.

[12] E. Martínez, E. Engel, J.A. Planell, J. Samitier, Effects of artificial micro- and nano- structured surfaces on cell behaviour, Ann. Anat. 191 (2009) 126–135, https://doi.org/10.1016/j.aanat.2008.05.006.

[13] A.O. Ijaola, E.A. Bamidele, C.J. Akisin, I.T. Bello, A.T. Oyatobo, A. Abdulkareem, P. K. Farayibi, E. Asmatulu, Wettability transition for laser textured surfaces: a comprehensive review, Surf. Interfaces 21 (2020), 100802, https://doi.org/ 10.1016/j.surfin.2020.100802.

[14] L.A. Turner, M.J. Dalby, Nanotopography-potential relevance in the stem cell niche, Biomater. Sci. 2 (2014) 1574–1594, https://doi.org/10.1039/c4bm00155a.

[15] F. Melo-Fonseca, G. Miranda, H.S. Domingues, I.M. Pinto, M. Gasik, F.S. Silva, Reengineering bone-implant interfaces for improved mechanotransduction and clinical outcomes, Stem Cell Rev. Rep. (2020), https://doi.org/10.1007/s12015- 020-10022-9.

[16] M. Vishnoi, P. Kumar, Q. Murtaza, Surface texturing techniques to enhance tribological performance: a review, Surfa. Interfaces 27 (2021), 101463, https:// doi.org/10.1016/j.surfin.2021.101463.

[17] I. Shivakoti, G. Kibria, R. Cep, B.B. Pradhan, A. Sharma, Laser surface texturing for biomedical applications: a review, Coatings 11 (2021) 1–15, https://doi.org/ 10.3390/coatings11020124.

[18] Q. Ding, L. Wang, L. Hu, Tribology optimization by laser surface texturing: from bulk materials to surface coatings, Laser Surf. Eng. Process. Appl. (2015) 405–422, https://doi.org/10.1016/B978-1-78242-074-3.00016-7.

[19] A. Singh, D. Patel, J. Ramkumar, K. Balani, Micro-channels fabrication through pulsed Nd:YAG laser on Ti6Al4V, Nanotechnol. Better Living (2016), https://doi. org/10.3850/978-981-09-7519-7nbl16-rps-120, 120–120.

[20] G. Kibria, A. Sen, H.M. Tariq Aziz, B. Doloi, B. Bhattacharyya, Pulsed Nd:YAG Laser Surface Texturing of Pure Titanium Material, Springer, Singapore, 2018, https:// doi.org/10.1007/978-981-10-8767-7_14.

[21] S. Chatterjee, S.S. Mahapatra, V. Bharadwaj, A. Choubey, B.N. Upadhyay, K. S. Bindra, Drilling of micro-holes on titanium alloy using pulsed Nd:YAG laser: parametric appraisal and prediction of performance characteristics, Proc. Inst. Mech. Eng. Part B 233 (2019) 1872–1889, https://doi.org/10.1177/ 0954405418805604.

[22] N. Mirhosseini, P. L. Crouse, M. J. J. Schmidth, L. Li, D. Garrod, Laser surface micro- texturing of Ti-6Al-4V substrates for improved cell integration, Appl. Surf. Sci. 253 (2007) 7738–7743, https://doi.org/10.1016/j.apsusc.2007.02.168.

[23] D. S. Patel, A. Singh, K. Balani, J. Ramkumar, Topographical effects of laser surface texturing on various time-dependent wetting regimes in Ti6Al4V, Surf. Coatings Technol. 349 (2018) 816–829, https://doi.org/10.1016/j.surfcoat.2018.05.032.

[24] J. Lawrence, L. Hao, H.R. Chew, On the correlation between Nd:YAG laser-induced wettability characteristics modification and osteoblast cell bioactivity on a titanium alloy, Surf. Coatings Technol. 200 (2006) 5581–5589, https://doi.org/ 10.1016/j.surfcoat.2005.07.107.

[25] V. Dumas, A. Rattner, L. Vico, E. Audouard, J.C. Dumas, P. Naisson, P. Bertrand, Multiscale grooved titanium processed with femtosecond laser influences mesenchymal stem cell

morphology, adhesion, and matrix organization, J. Biomed. Mater. Res. Part A. 100 A (2012) 3108–3116, https://doi.org/10.1002/jbm. a.34239.

[26] M. Zhu, H. Ye, J. Fang, C. Zhong, J. Yao, J. Park, X. Lu, F. Ren, Engineering high- resolution micropatterns directly onto titanium with optimized contact guidance to promote osteogenic differentiation and bone regeneration, ACS Appl. Mater. Interfaces. 11 (2019) 43888–43901, https://doi.org/10.1021/acsami.9b16050.

[27] L. Tiainen, P. Abreu, M. Buciumeanu, F. Silva, M. Gasik, R. Serna Guerrero, O. Carvalho, Novel laser surface texturing for improved primary stability of titanium implants, J. Mech. Behav. Biomed. Mater. 98 (2019) 26–39, https://doi.org/10.1016/j.jmbbm.2019.04.052.

[28] A. Cunha, A.M. Elie, L. Plawinski, A.P. Serro, A.M. Botelho Do Rego, A. Almeida, M.C. Urdaci, M.C. Durrieu, R. Vilar, Femtosecond laser surface texturing of titanium as a method to reduce the adhesion of Staphylococcus aureus and biofilm formation, Appl. Surf. Sci. 360 (2016) 485–493, https://doi.org/10.1016/j. apsusc.2015.10.102.

[29] X. Luo, S. Yao, H. Zhang, M. Cai, W. Liu, R. Pan, C. Chen, X. Wang, L. Wang, M. Zhong, Biocompatible nano-ripples structured surfaces induced by femtosecond laser to rebel bacterial colonization and biofilm formation, Opt. Laser Technol. 124 (2020), 105973, https://doi.org/10.1016/j.optlastec.2019.105973.

[30] B. Mao, A. Siddaiah, Y. Liao, P.L. Menezes, Laser surface texturing and related techniques for enhancing tribological performance of engineering materials: a review, J. Manuf. Process. 53 (2020) 153–173, https://doi.org/10.1016/j. jmapro.2020.02.009.

[31] M. Marian, A. Almqvist, A. Rosenkranz, M. Fillon, Numerical micro-texture optimization for lubricated contacts—a critical discussion, Friction (2022), https:// doi.org/10.1007/s40544-022-0609-6.

[32] A. Soveja, E. Cicală, D. Grevey, J.M. Jouvard, Optimisation of TA6V alloy surface laser texturing using an experimental design approach, Opt. Lasers Eng. 46 (2008) 671–678, https://doi.org/10.1016/j.optlaseng.2008.04.009.

[33] ISO 11146-1:2005(en) Lasers and Laser-Related Equipment — Test methods For Laser Beam Widths, Divergence Angles and Beam Propagation Ratios — Part 1: Stigmatic and Simple Astigmatic Beams, Geneva, Switzerland, n.d., 2005 https://www.iso.org/standard/33626.html.

[34] E. S. Gadelmawla, M. M. Koura, T. M. A. Maksoud, I. M. Elewa, H. H. Soliman, Roughness parameters, J. Mater. Process. Technol. 123 (2002) 133–145, https:// doi.org/10.1016/S0924-0136(02)00060-2.

[35] B. Guimarães, C. M. Fernandes, D. Figueiredo, O. Carvalho, F. S. Silva, G. Miranda, Effect of laser surface texturing on the wettability of WC-Co cutting tools, Int. J. Adv. Manuf. Technol. 111 (2020) 1991–1999, https://doi.org/10.1007/s00170- 020-06155-3.

[36] M. Bussoli, T. Desai, D. Batani, B. Gakovic, M. Trtica, Nd:YAG laser interaction with titanium implant surfaces for medical applications, Radiat. Eff. Defects Solids. 163 (2008) 349–356, https://doi.org/10.1080/10420150701777678.

[37] L. Convert, E. Bourillot, M. Françọis, N. Pocholle, F. Baras, O. Politano, S. Costil, Laser textured titanium surface characterization, Appl. Surf. Sci. 586 (2022), 152807, https://doi.org/10.1016/j.apsusc.2022.152807.

[38] A. Sen, B. Doloi, B. Bhattacharyya, Experimental studies on fibre laser micro- machining of Ti-6Al-4V, in: 5th Int. 26th All India Manuf. Technol. Des. Res. Conf. (AIMTDR 2014), 2014, pp. 1–7.

[39] Z. Yu, G. Yang, W. Zhang, J. Hu, Investigating the effect of picosecond laser texturing on microstructure and biofunctionalization of titanium alloy, J. Mater. Process. Technol. 255 (2018) 129–136, https://doi.org/10.1016/j. jmatprotec.2017.12.009.

[40] C. G. Moura, O. Carvalho, L. M. V. Gonçalves, M. F. Cerqueira, R. Nascimento, F. Silva, Laser surface texturing of Ti-6Al-4V by nanosecond laser: surface characterization, Ti-oxide layer analysis and its electrical insulation performance, Mater. Sci. Eng. C. 104 (2019), 109901, https://doi.org/10.1016/j. msec.2019.109901.

[41] K.-Y. Law, H. Zhao, Surface Wetting: Characterization, Contact Angle, and Fundamentals, Springer International Publishing, Basel, Switzerland, 2016, https://doi.org/10.1007/978-3-319-25214-8.

[42] X. Wang, C. Fu, C. Zhang, Z. Qiu, B. Wang, A comprehensive review of wetting transition mechanism on the surfaces of microstructures from theory and testing methods, Materials (Basel) 15 (2022) 1–21, https://doi.org/10.3390/ ma15144747.

[43] I. G. Simões, A. C. dos Reis, M. L. da Costa Valente, Analysis of the influence of surface treatment by high-power laser irradiation on the surface properties of titanium dental implants: a

systematic review, J. Prosthet. Dent. (2021) 1–8, https://doi.org/10.1016/j.prosdent.2021.07.026.

[44] F. Rupp, L. Scheideler, J. Geis-Gerstorfer, Effect of heterogenic surfaces on contact angle hysteresis: dynamic contact angle analysis in material sciences, Chem. Eng. Technol. 25 (2002) 877–882, https://doi.org/10.1002/1521-4125(20020910)25: 9<877::AID-CEAT877>3.0.CO;2-D.

[45] C. Juan Yang, X. song Mei, Y. ling Tian, D. Wei Zhang, Y. Li, X. Ping Liu, Modification of wettability property of titanium by laser texturing, Int. J. Adv. Manuf. Technol. 87 (2016) 1663–1670, https://doi.org/10.1007/s00170-016- 8601-9.

[46] Y. Wang, X. Zhao, C. Ke, J. Yu, R. Wang, Nanosecond laser fabrication of superhydrophobic Ti6Al4V surfaces assisted with different liquids, Colloids Interface Sci. Commun. 35 (2020), 100256, https://doi.org/10.1016/j. colcom.2020.100256.

[47] O. Raimbault, S. Benayoun, K. Anselme, C. Mauclair, T. Bourgade, A.M. Kietzig, P. L. Girard-Lauriault, S. Valette, C. Donnet, The effects of femtosecond laser-textured Ti-6Al-4V on wettability and cell response, Mater. Sci. Eng. C. 69 (2016) 311–320, https://doi.org/10.1016/j.msec.2016.06.072.

[48] E. Chikarakara, S. Naher, D. Brabazon, High speed laser surface modification of Ti- 6Al-4V, Surf. Coatings Technol. 206 (2012) 3223–3229, https://doi.org/10.1016/ j.surfcoat.2012.01.010.

[49] E. Chikarakara, P. Fitzpatrick, E. Moore, T. Levingstone, L. Grehan, C. Higginbotham, M. Vázquez, K. Bagga, S. Naher, D. Brabazon, In vitro fibroblast and pre-osteoblastic cellular responses on laser surface modified Ti-6Al-4V, Biomed. Mater. 10 (2015) 15007, https://doi.org/10.1088/1748-6041/10/1/ 015007.

[50] S. Mukherjee, S. Dhara, P. Saha, Enhanced corrosion, tribocorrosion resistance and controllable osteogenic potential of stem cells on micro-rippled Ti6Al4V surfaces produced by pulsed laser remelting, J. Manuf. Process. 65 (2021) 119–133, https://doi.org/10.1016/j.jmapro.2021.03.023.

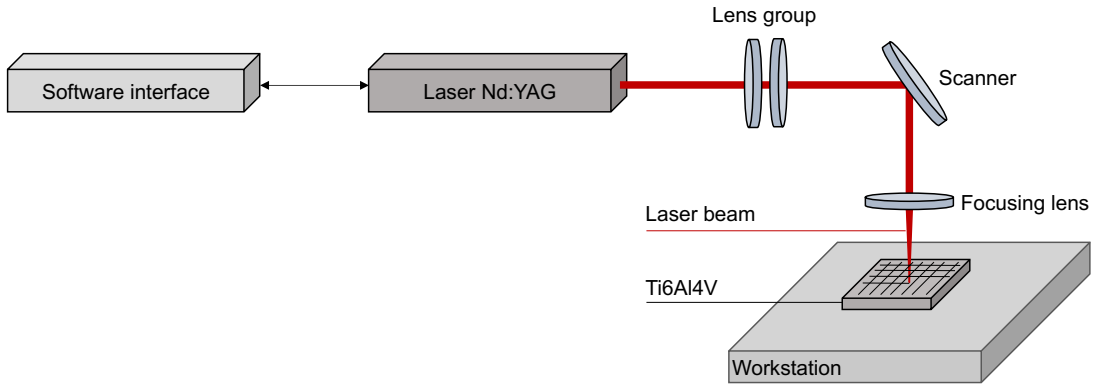
[51] K. T. Voisey, C. A. Scotchford, L. Martin, H. S. Gill, Effect of Q-switched laser surface texturing of titanium on osteoblast cell response, Phys. Procedia. 56 (2014) 1126–1135, https://doi.org/10.1016/j.phpro.2014.08.027.

[52] Q. Zheng, L. Mao, Y. Shi, W. Fu, Y. Hu, Biocompatibility of Ti-6Al-4V titanium alloy implants with laser microgrooved surfaces, Mater. Technol. 00 (2020) 1–10, https://doi.org/10.1080/10667857.2020.1816011.

[53] J. Mesquita-Guimarães, R. Detsch, A. C. Souza, B. Henriques, F. S. Silva, A. R. Boccaccini, O. Carvalho, Cell adhesion evaluation of laser-sintered HAp and 45S5 bioactive glass coatings on micro-textured zirconia surfaces using MC3T3-E1 osteoblast-like cells, Mater. Sci. Eng. C. 109 (2020), 110492, https://doi.org/ 10.1016/j.msec.2019.110492.

[54] K. Anselme, P. Davidson, A. M. Popa, M. Giazzon, M. Liley, L. Ploux,The interaction of cells and bacteria with surfaces structured at the nanometre scale, Acta Biomater 6 (2010) 3824–3846, https://doi.org/10.1016/j.actbio.2010.04.001.

## Appendix A. Supplementary data




Supplementary Figure 6.1 - Schematic representation of the Nd:YAG laser surface texturing performed on Ti6Al4V plates.

Supplementary Table 6.1 - Design of experiments for samples texturing.

| Exp. No. | Input parameters | | | Exp. No. | Input parameters | | |
|---|---|---|---|---|---|---|---|
| | A_CAD | B_CAD | N | | A_CAD | B_CAD | N |
| | Groove width (μm) | Pillar width (μm) | Number of passages | | Groove width (μm) | Pillar width (μm) | Number of passages |
| 1 | 50 | 40 | 120 | 42 | 50 | 35 | 120 |
| 2 | 80 | 35 | 70 | 43 | 50 | 40 | 115 |
| 3 | 50 | 35 | 125 | 44 | 80 | 40 | 75 |
| 4 | 80 | 35 | 75 | 45 | 110 | 35 | 85 |
| 5 | 110 | 35 | 75 | 46 | 50 | 30 | 80 |
| 6 | 50 | 30 | 120 | 47 | 80 | 40 | 120 |
| 7 | 50 | 40 | 125 | 48 | 110 | 35 | 115 |
| 8 | 110 | 30 | 80 | 49 | 80 | 30 | 85 |
| 9 | 50 | 40 | 80 | 50 | 110 | 30 | 65 |
| 10 | 110 | 40 | 80 | 51 | 50 | 40 | 65 |
| 11 | 80 | 35 | 65 | 52 | 80 | 40 | 115 |
| 12 | 80 | 40 | 80 | 53 | 50 | 30 | 115 |
| 13 | 80 | 40 | 110 | 54 | 80 | 30 | 75 |
| 14 | 50 | 35 | 70 | 55 | 80 | 40 | 125 |
| 15 | 80 | 35 | 125 | 56 | 50 | 35 | 80 |
| 16 | 110 | 35 | 110 | 57 | 80 | 30 | 115 |
| 17 | 110 | 40 | 115 | 58 | 110 | 40 | 65 |
| 18 | 110 | 30 | 75 | 59 | 110 | 30 | 120 |
| 19 | 80 | 30 | 65 | 60 | 50 | 35 | 65 |
| 20 | 110 | 40 | 125 | 61 | 50 | 30 | 85 |
| 21 | 110 | 40 | 85 | 62 | 80 | 30 | 70 |

| | | | | | | | |
|---|---|---|---|---|---|---|---|
| 22 | 50 | 35 | 85 | 63 | 110 | 30 | 85 |
| 23 | 50 | 35 | 75 | 64 | 110 | 35 | 65 |
| 24 | 80 | 35 | 80 | 65 | 110 | 30 | 125 |
| 25 | 110 | 30 | 70 | 66 | 80 | 30 | 110 |
| 26 | 50 | 40 | 85 | 67 | 80 | 40 | 85 |
| 27 | 110 | 40 | 75 | 68 | 50 | 30 | 110 |
| 28 | 50 | 35 | 115 | 69 | 110 | 40 | 110 |
| 29 | 80 | 35 | 115 | 70 | 80 | 35 | 120 |
| 30 | 110 | 40 | 70 | 71 | 80 | 30 | 80 |
| 31 | 110 | 35 | 120 | 72 | 50 | 30 | 70 |
| 32 | 80 | 40 | 70 | 73 | 50 | 30 | 65 |
| 33 | 80 | 30 | 125 | 74 | 80 | 35 | 85 |
| 34 | 110 | 35 | 125 | 75 | 110 | 35 | 70 |
| 35 | 80 | 40 | 65 | 76 | 110 | 30 | 110 |
| 36 | 80 | 35 | 110 | 77 | 110 | 30 | 115 |
| 37 | 50 | 30 | 125 | 78 | 50 | 40 | 70 |
| 38 | 80 | 30 | 120 | 79 | 50 | 35 | 110 |
| 39 | 110 | 35 | 80 | 80 | 110 | 40 | 120 |
| 40 | 50 | 40 | 110 | 81 | 50 | 30 | 75 |
| 41 | 50 | 40 | 75 | | | | |

Supplementary Table 6.2 - Discrete laser processing and pre-set marking of one to ten lines for different laser parameters. for a laser energy of 120 or 240 J/mm$^2$.

| Power (W) | Scanning speed (mm/s) | Number of passages | Number of lines | Groove width (µm) | Depth (µm) |
|---|---|---|---|---|---|
| 3 | 50 | 20 | 1 | 39.1 ± 1.4 | 17.41 |
| | | | 2 | 61.9 ± 0.9 | 70 |
| | | | 3 | 73.5 ± 3.2 | 82.22 |
| | | | 4 | 89.2 ± 8.7 | 97.04 |
| | | | 5 | 106.2 ± 2.0 | 102.22 |
| | | | 6 | 112.8 ± 4.2 | 138.89 |
| | | | 7 | 120.3 ± 10.4 | 153.33 |
| | | | 8 | 123.5 ± 10.3 | 168.89 |
| | | | 9 | 128.5 ± 10.9 | 186.67 |
| | | | 10 | 127.5 ± 5.2 | 190.37 |
| 3 | 100 | 40 | 1 | 35.0 ± 1.3 | 16.67 |
| | | | 2 | 65.6 ± 2.7 | 68.06 |
| | | | 3 | 59.1 ± 3.2 | 71.39 |
| | | | 4 | 71.1 ± 4.2 | 78.33 |
| | | | 5 | 77.2 ± 3.1 | 81.85 |
| | | | 6 | 86.3 ± 1.9 | 72.59 |
| | | | 7 | 94.6 ± 4.3 | 69.44 |
| | | | 8 | 109.7 ± 5.1 | 87.22 |
| | | | 9 | 116.3 ± 5.7 | 74.44 |
| | | | 10 | 123.5 ± 8.6 | 71.67 |
| 3 | 100 | 80 | 1 | 22.8 ± 3.5 | 7.5 |
| | | | 2 | 66.3 ± 3.7 | 70.83 |
| | | | 3 | 54.2 ± 6.3 | 43.89 |

| | | | | | |
|---|---|---|---|---|---|
| | | | 4 | 62.7 ± 8.4 | 35.19 |
| | | | 5 | 70.2 ± 3.6 | 42.96 |
| | | | 6 | 85.9 ± 4.6 | 49.44 |
| | | | 7 | 77.1 ± 5.1 | 48.33 |
| | | | 8 | 90.4 ± 8.4 | 45.56 |
| | | | 9 | 116.8 ± 9.0 | 48.15 |
| | | | 10 | 110.0 ± 5.2 | 51.67 |
| 6 | 200 | 80 | 1 | 60.9 ± 2.1 | 47.78 |
| | | | 2 | 69.0 ± 1.9 | 53.33 |
| | | | 3 | 84.7 ± 3.0 | 92.78 |
| | | | 4 | 100.5 ± 1.2 | 90.56 |
| | | | 5 | 101.4 ± 3.6 | 121.11 |
| | | | 6 | 104.0 ± 2.1 | 150 |
| | | | 7 | 117.2 ± 5.8 | 181.48 |
| | | | 8 | 118.6 ± 7.6 | 165.93 |
| | | | 9 | 123.1 ± 11.4 | 203.7 |
| | | | 10 | 121.5 ± 11.3 | 208.15 |
| 3 | 400 | 80 | 1 | 39.8 ± 4.6 | 9.72 |
| | | | 2 | 65.8 ± 4.2 | 58.61 |
| | | | 3 | 70.8 ± 3.3 | 73.33 |
| | | | 4 | 73.0 ± 3.1 | 46.67 |
| | | | 5 | 74.5 ± 1.7 | 50.56 |
| | | | 6 | 86.3 ± 3.6 | 44.07 |
| | | | 7 | 96.9 ± 4.6 | 50.37 |
| | | | 8 | 110.6 ± 4.0 | 46.67 |
| | | | 9 | 114.5 ± 5.7 | 50.37 |

| | | | | | |
|---|---|---|---|---|---|
| | | 10 | 121.8 ± 4.1 | 52.78 | |

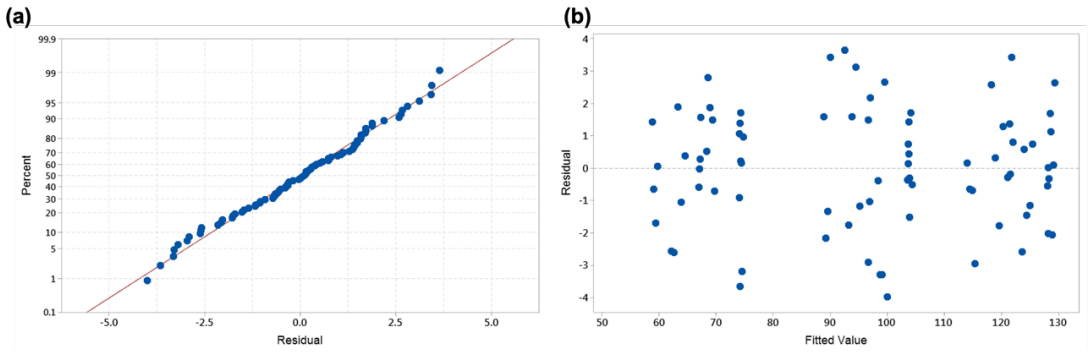
Supplementary Table 6.3 - Consecutive laser processing and pre-set marking vs continuous marking of one to ten lines for different laser parameters. for a laser energy of 120 or 240 J/mm².

| **Laser processing features** | | | | **Pre-set marking** | | **Continuous marking** | |
|---|---|---|---|---|---|---|---|
| **Power (W)** | **Scanning speed (mm/s)** | **Number of passages** | **Number of lines** | **Groove width (μm)** | **Depth (μm)** | **Groove width (μm)** | **Depth (μm)** |
| 3 | 50 | 20 | 1 | 59.2 ± 4.3 | 46.67 | 50.8 ± 2.2 | 18.03 |
| | | | 2 | 66.1 ± 2.6 | 75 | 61.6 ± 1.8 | 58.33 |
| | | | 3 | 73.7 ± 2.1 | 84.44 | 74.9 ± 4.6 | 68.94 |
| | | | 4 | 87.1 ± 3.8 | 92.78 | 79.7 ± 3.0 | 72.12 |
| | | | 5 | 89.7 ± 3.4 | 112.22 | 90.7 ± 4.8 | 116.66 |
| | | | 6 | 98.1 ± 3.6 | 128.89 | 102.4 ± 3.1 | 126.21 |
| | | | 7 | 116.2 ± 4.6 | 143.89 | 121.5 ± 6.9 | 118.78 |
| | | | 8 | 118.8 ± 7.2 | 155 | 134.1 ± 2.2 | 167.57 |
| | | | 9 | 120.5 ± 5.0 | 174.45 | 123.6 ± 6.9 | 196.43 |
| | | | 10 | 127.7 ± 9.9 | 195.56 | 130.8 ± 7.6 | 172.87 |
| 3 | 100 | 40 | 1 | 48.4 ± 3.1 | 14.85 | 37.7 ± 4.7 | 51.97 |

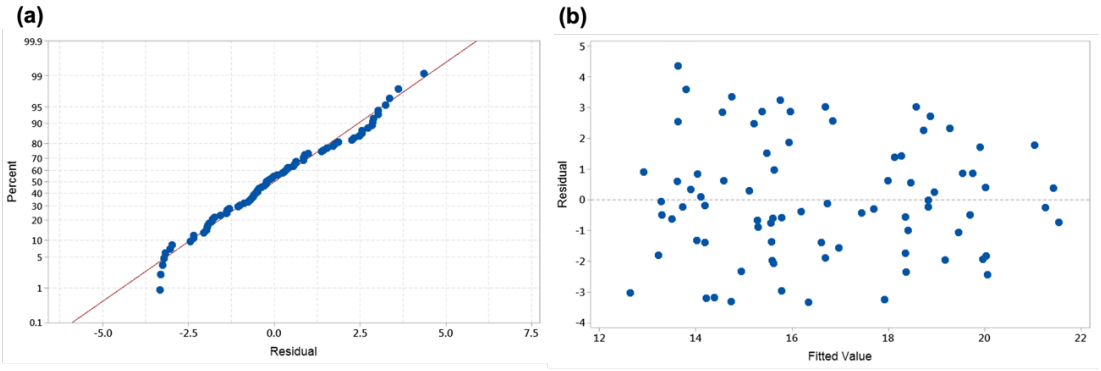
| | | | | | | | |
|---|---|---|---|---|---|---|---|
| | | | 2 | 60.4 ± 2.7 | 53.03 | 52.5 ± 2.9 | 57.27 |
| | | | 3 | 66.6 ± 3.0 | 41.36 | 60.4 ± 2.8 | 58.33 |
| | | | 4 | 69.0 ± 5.8 | 56.21 | 67.5 ± 6.3 | 77.42 |
| | | | 5 | 82.6 ± 3.7 | 58.33 | 73.5 ± 3.6 | 66.82 |
| | | | 6 | 85.9 ± 3.9 | 73.18 | 86.1 ± 5.9 | 70 |
| | | | 7 | 93.3 ± 8.8 | 61.51 | 94.3 ± 7.9 | 66.82 |
| | | | 8 | 97.8 ± 8.1 | 73.18 | 92.6 ± 3.6 | 72.12 |
| | | | 9 | 103.1 ± 5.2 | 84.85 | 100.9 ± 3.4 | 97.57 |
| | | | 10 | 113.1 ± 5.0 | 76.36 | 113.3 ± 4.3 | 94.39 |
| 3 | 100 | 80 | 1 | 49.5 ± 2.4 | 15.28 | 43.3 ± 1.7 | 16.48 |
| | | | 2 | 55.4 ± 2.4 | 23.61 | 47.8 ± 3.5 | 30.19 |
| | | | 3 | 62.5 ± 3.4 | 27.59 | 55.8 ± 2.0 | 32.59 |
| | | | 4 | 68.8 ± 2.6 | 31.67 | 63.8 ± 2.1 | 31.11 |
| | | | 5 | 79.0 ± 4 | 33.61 | 69.3 ± 4.2 | 33.33 |
| | | | 6 | 88.6 ± 2.5 | 38.89 | 82.6 ± 3.6 | 44.44 |

| | | | | | | | |
|---|---|---|---|---|---|---|---|
| | | | 7 | 90.8 ± 4.6 | 35.56 | 91.9 ± 2.8 | 47.04 |
| | | | 8 | 102.9 ± 3.5 | 32.78 | 99.5 ± 1.4 | 45.56 |
| | | | 9 | 106.8 ± 2.5 | 37.22 | 116.9 ± 4.3 | 46.11 |
| | | | 10 | 119.5 ± 3.5 | 41.11 | 118.8 ± 3.7 | 52.78 |
| 6 | 200 | 80 | 1 | 62.3 ± 1.2 | 82.72 | 52.3 ± 1.4 | 58.33 |
| | | | 2 | 69.7 ± 1.6 | 100.75 | 52.7 ± 3.5 | 68.94 |
| | | | 3 | 83.8 ± 4.4 | 112.42 | 63.7 ± 4.5 | 74.24 |
| | | | 4 | 93.3 ± 5.0 | 132.57 | 73.3 ± 6.3 | 97.57 |
| | | | 5 | 93.5 ± 8.4 | 148.48 | 77.8 ± 4.6 | 111.36 |
| | | | 6 | 109.1 ± 3.2 | 156.96 | 76.4 ± 8.8 | 117.72 |
| | | | 7 | 122.7 ± 5.0 | 58.02 | 89.5 ± 5.9 | 151.66 |
| | | | 8 | 121.7 ± 2.7 | 185.6 | 104.5 ± 7.0 | 149.54 |
| | | | 9 | 121.0 ± 5.6 | 174.99 | 103.3 ± 4.8 | 174.99 |
| | | | 10 | 125.8 ± 7.9 | 174.99 | 107.9 ± 4.2 | 185.6 |
| 3 | 400 | 80 | 1 | 43.2 ± 3.5 | 43.89 | 41.3 ± 1.6 | 50.91 |

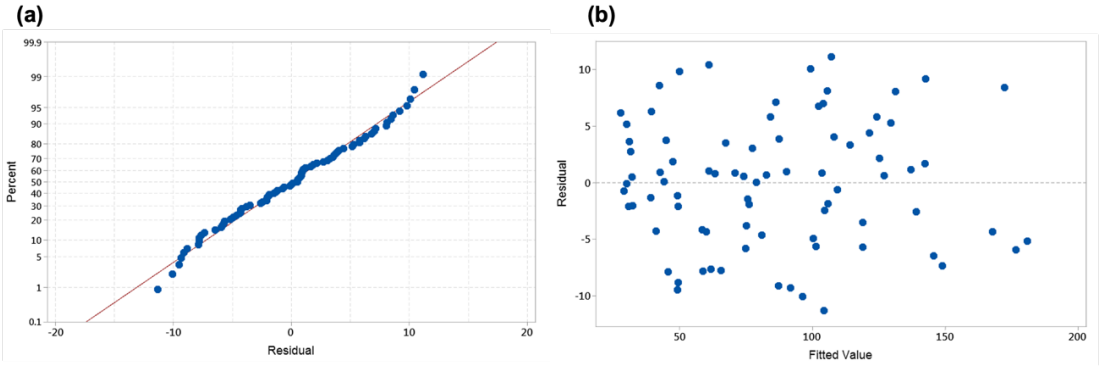
| | | | | | | | |
|---|---|---|---|---|---|---|---|
| | | | 2 | 55.8 ± 5.7 | 38.06 | 48.7 ± 3.5 | 50.91 |
| | | | 3 | 64.0 ± 3.6 | 30.83 | 55.8 ± 2.1 | 41.36 |
| | | | 4 | 71.4 ± 3.3 | 34.44 | 61.8 ± 5.4 | 55.15 |
| | | | 5 | 78.3 ± 2.9 | 41.48 | 68.5 ± 1.6 | 49.85 |
| | | | 6 | 84.7 ± 5.5 | 49.26 | 80.7 ± 1.2 | 49.85 |
| | | | 7 | 94.0 ± 6.2 | 45.56 | 90.9 ± 5.1 | 50.91 |
| | | | 8 | 96.9 ± 2.5 | 43.89 | 98.8 ± 5.1 | 49.85 |
| | | | 9 | 104.3 ± 2.9 | 37.22 | 108.8 ± 3.2 | 55.15 |
| | | | 10 | 123.9 ± 6.3 | 41.11 | 121.2 ± 2.3 | 62.57 |




Supplementary Figure 6.2 – (a) Normal distribution of residuals and (b) plot of residuals versus fitted values for groove width model data.




Supplementary Figure 6.3 - (a) Normal distribution of residuals and (b) plot of residuals versus fitted values for pillar width model data.




Supplementary Figure 6.4 - (a) Normal distribution of residuals and (b) plot of residuals versus fitted values for depth model data.

Supplementary Table 6. 4 - Analysis of variance of groove width model.

| Model terms | DF | Adj SS | Adj MS | F-value | P-value |
|---|---|---|---|---|---|
| Model | 9 | 43264.8 | 4807.2 | 1311.78 | <0.001 |
| A | 1 | 40875.4 | 40875.4 | 11154.03 | <0.001 |
| B | 1 | 1975.4 | 1975.4 | 539.05 | <0.001 |
| N | 1 | 125.2 | 125.2 | 34.17 | <0.001 |
| $A^2$ | 1 | 103.6 | 103.6 | 28.28 | <0.001 |
| $B^2$ | 1 | 1.1 | 1.1 | 0.29 | 0.590 |
| $N^2$ | 1 | 2.6 | 2.6 | 0.70 | 0.406 |
| AN | 1 | 3.1 | 3.1 | 0.85 | 0.360 |
| BN | 1 | 65.9 | 65.9 | 17.99 | <0.001 |
| AB | 1 | 6.1 | 6.1 | 1.67 | 0.201 |

| | | | | | |
|---|---|---|---|---|---|
| Error | 71 | 260.2 | 3.7 | | |
| Total | 80 | 43525.0 | | | |
| | | | | S: 1.91431 | |
| | | | | $R^2$: 99.40% | |
| | | | | Adjusted $R^2$: 99.33% | |
| | | | | Predicted $R^2$: 99.24% | |

DF, degrees of freedom; Adj SS, adjusted sum of squares; Adj MS, adjusted mean of squares

Supplementary Table 6.5 - Analysis of variance of pillar width model.

| **Model terms** | **DF** | **Adj SS** | **Adj MS** | **F-value** | **P-value** |
|---|---|---|---|---|---|
| Model | 9 | 454.132 | 50.459 | 12.34 | <0.001 |
| A | 1 | 253.798 | 253.798 | 62.09 | <0.001 |
| B | 1 | 23.070 | 23.070 | 5.64 | 0.020 |
| N | 1 | 96.489 | 96.489 | 23.60 | <0.001 |
| $A^2$ | 1 | 22.282 | 22.282 | 5.45 | 0.022 |
| $B^2$ | 1 | 3.669 | 3.669 | 0.90 | 0.347 |
| $N^2$ | 1 | 9.378 | 9.378 | 2.29 | 0.134 |
| AN | 1 | 0.137 | 0.137 | 0.03 | 0.855 |
| BN | 1 | 36.723 | 36.723 | 8.98 | 0.004 |
| AB | 1 | 15.080 | 15.080 | 3.69 | 0.059 |
| Error | 71 | 290.238 | 4.088 | | |
| Total | 80 | 744.370 | | | |
| | | | | S: 2.02185 | |
| | | | | $R^2$: 61.01% | |
| | | | | Adjusted $R^2$: 56.07% | |
| | | | | Predicted $R^2$: 50.07% | |

DF, degrees of freedom; Adj SS, adjusted sum of squares; Adj MS, adjusted mean of squares

Supplementary Table 6.6 - Analysis of variance of pillar depth model.

| Model terms | DF | Adj SS | Adj MS | F-value | P-value |
|---|---|---|---|---|---|
| Model | 9 | 125687 | 13965.3 | 391.43 | <0.001 |
| A | 1 | 22749 | 22748.7 | 637.62 | <0.001 |
| B | 1 | 86120 | 86120.1 | 2413.87 | <0.001 |
| N | 1 | 9726 | 9726.2 | 272.62 | <0.001 |
| $A^2$ | 1 | 353 | 353.1 | 9.90 | 0.002 |
| $B^2$ | 1 | 1183 | 1183.3 | 33.17 | <0.001 |
| $N^2$ | 1 | 87 | 87.2 | 2.45 | 0.122 |
| AN | 1 | 1113 | 1112.9 | 31.19 | <0.001 |
| BN | 1 | 2831 | 2830.9 | 79.35 | <0.001 |
| AB | 1 | 3401 | 3401.4 | 95.34 | <0.001 |
| Error | 71 | 2533 | 35.7 | | |
| Total | 80 | 128220 | | | |
| | | | | S: 5.97304 | |
| | | | | $R^2$: 98.02% | |
| | | | | Adjusted $R^2$: 97.77% | |
| | | | | Predicted $R^2$: 97.41% | |

DF, degrees of freedom; Adj SS, adjusted sum of squares; Adj MS, adjusted mean of squares

Supplementary Table 6.7 - Surface roughness values of the experiment numbers which dimensions after processing met the target texture dimensions, according to ISO 25178.

| Exp. No. | Sp (μm) | Sv (μm) | Sz (μm) | Ssk (μm) | Smean (μm) |
|---|---|---|---|---|---|
| 41 | 161.627 | 168.281 | 329.908 | 0.0580 | 2.074 |
| 37 | 66.962 | 76.146 | 143.107 | -0.272 | -1.340 |
| 46 | 78.184 | 89.872 | 168.055 | -0.397 | -0.278 |
| 71 | 106.616 | 130.766 | 237.382 | -0.329 | 0.195 |
| 57 | 117.678 | 145.543 | 263.221 | -0.319 | -1.185 |

| | | | | | |
|---|---|---|---|---|---|
| 33 | 133.758 | 131.477 | 265.235 | -0.306 | -0.112 |
| 25 | 94.153 | 123.513 | 217.666 | -0.138 | 2.723 |
| 63 | 98.518 | 127.255 | 225.773 | -0.050 | 4.030 |
| 65 | 117.139 | 168.681 | 285.821 | -0.494 | 4.896 |

# CHAPTER 7

## HYDROTHERMAL TREATMENT OF LASER MICRO-TEXTURED TI6AL4V SYSTEMS FOR OSSEOINTEGRATION OF ORTHOPAEDIC IMPLANTS

Submitted to an ISI index journal.

F. Melo-Fonseca[a,b,c,*], Michael Gasik[d], Paulo P. Freitas[c,e], Inês Mendes Pinto[c,f], Filipe S. Silva[a,b], Georgina Miranda[g]

[a]Center for MicroElectroMechanical Systems (CMEMS-UMinho), University of Minho, Campus de Azurém, 4800-058 Guimarães – Portugal

[b]LABBELS –Associate Laboratory, Braga, Guimarães, Portugal

[c]International Iberian Nanotechnology Laboratory (INL), 4715-330 Braga, Portugal

[d]School of Chemical Engineering, Aalto University Foundation, FI-00076 Espoo, Finland

[e]INESC Microsystems and Nanotechnologies, INESC-MN, and IN, 1000-029 Lisbon, Portugal

[f]Institute for Research and Innovation in Health (i3S), Porto, Portugal

[g]CICECO, Aveiro Institute of Materials, Department of Materials and Ceramic Engineering, University of Aveiro, 3810-193 Aveiro, Portugal

[*]Corresponding author

G. Miranda and I. M. Pinto share co-last authorship.

**Abstract**

New orthopaedic implant designs, coupled with tailored surface enhancements, strive to accelerate initial bone formation by enhancing the interface with the adjacent bone tissue. In this study, we report the conceptualization and *in vitro* testing of Titanium 6-Aluminium 4-Vanadium (Ti6Al4V) systems, focusing on the formation of a pyramid-inspired architectural structure integrating the precision of laser surface texturing with hydrothermal treatment. This configuration features micro-scaled pillars with uniform width and height, accompanied by grooves of diverse dimensions, providing spatial confinement for mesenchymal stem cells (MSC). Textured Ti6Al4V systems were profiled in terms of physicochemical characteristics (crystalline structure and wettability) and in vitro mineralization capacity in comparison with conventional Sand-blasted, Large-grit, Acid-etched (SLA). Notably, textured Ti6Al4V systems exhibited robust MSC adhesion, and their mineralization capacity was on par with, or even exceeded, that of the SLA Ti6Al4V surfaces. Together, the findings presented in this work indicate that engineering pillar micro-structures with controllable dimensional features is a promising strategy to modulate MSC activation for potential enhancement of osseointegration.

**Keywords:** Ti6Al4V; Laser texturing; Micro-scaled pillars; Ti6Al4V-cell interface; Osseointegration.

## 7.1. Introduction

Worldwide, millions of individuals are afflicted by orthopaedic disorders stemming from diverse causes, including aging, degenerative diseases, and traumatic injuries. Biomaterials, notably Titanium 6-Aluminium 4-Vanadium (Ti6Al4V), frequently emerge as potential substitutes for compromised bone structures due to their remarkable mechanical traits [1,2]. However, and despite ongoing efforts, persistent challenges remain in achieving durable biological fixation of orthopaedic implants.

Bone formation are governed by the cross talk between mesenchymal stem cells (MSC) [3] and the implanted biomaterial. When recruited for new bone formation, MSC initiate osteogenesis correlated with expression of specific biomarkers such as Runt-related transcription factor 2 (RUNX2) [4,5]. The success of biomaterial-bone tissue interactions heavily relies on the surface properties of the biomaterial, encompassing chemical composition, roughness, and topography. Surface modifications on biomaterials are aimed to enhance the interactions with human cells and thus improve the clinical outcome of orthopaedic interventions. Sandblasted and acid-etched (SLA) surfaces are considered the gold standard to achieve a regulated degree of surface roughness for

optimization of the bone-implant contact and accelerate the osseointegration [6–9]. Enhanced surface roughness amplifies the available surface area susceptible to protein adsorption, thereby fostering cell attachment, proliferation, and differentiation into bone cells. Nonetheless, the sandblasting technique, which involves directing a stream of abrasive particles onto the biomaterial's surface via compressed air, can lead to potential issues. This method may introduce surface contamination and trigger localized tissue inflammation due to abrasive alumina ($Al_2O_3$) particles within the bodily environment [10]. Furthermore, an improved osseointegration rate requires improvements on the biomaterials surface to extend the longevity of orthopaedic implants. Nevertheless, these implants often lack sufficient biomechanical stimulus at the interface with the bone tissue compromising their long-term success [11]. In an attempt to overcome this unmet need, in recent years, novel methodologies have been explored for their potential to engineer Ti surfaces at nanoscales in the context of bone regeneration. A standout among these is laser surface texturing (LST), a technique that employs precise laser ablation to generate diverse three-dimensional topographical features on Ti substrates conceptually improving the interlocking between the implant and the bone. In addition to these structural modifications, LST also confers bioactivity and hydrophilicity (through the formation of titanium oxides) [12–16] to inert and hydrophobic Ti substrates improving the interaction between the biomaterial and the biological microenvironment increasing their osteogenic activity and contributing to a better osseointegration potential. Previous studies have highlighted the potential of laser texturization of Ti6Al4V to regulate mesenchymal stem cells (MSC) osteogenic differentiation dynamics [17,18]. The introduction of nanostructures through femtosecond laser processing of Ti6Al4V samples has exhibited the capability to enhance cell adhesion and mineralization compared to conventionally mirror-polished surfaces and Ti6Al4V sandblasted structures, respectively [17,18]. However, the dimensionality of these nano-texturized Ti surfaces reveals limitations in *in vitro* studies in terms of the lifespan of cell-substrate interactions.

Recent work from our group and others, have shown that Ti6Al4V surfaces subject to hydrothermal treatment [19,20] combined with fibronectin coating [21] enhances the adhesiveness of MSC to Ti6Al4V implant surfaces, while also activating their commitment and responsiveness to osteogenic differentiation. Hydrothermal treatment was shown to promote the formation of a crystalline $TiO_2$ layer containing anatase and rutile [19,22–24]. Besides its bioactive properties, $TiO_2$ is known to improve the mechanical properties of Ti implants and stability, as it protects the nascent surface and prevents possible release of metallic wear particles [25–27].

In this framework, we hypothesised if the combination of texturized of Ti6Al4V surface at the micrometre scale combined with hydrothermal treatments could provide an opportunity to increase the surface contact area and function of cells for long-lasting osteointegration of textured Ti6Al4V systems. The aim of this study was to investigate how nanosecond laser texturing combined with hydrothermal treatment of Ti6Al4V surfaces affects physicochemical features and the osseointegration potential, by comparing to a clinically relevant SLA Ti6Al4V. Micro-pillars with pyramid-inspired geometry were designed with similar width and height, but different groove width: 60, 90 and 120 μm. As a result of previous findings, human fibronectin was further coated on hydrothermally textured samples to promote substrate-MSC complex stability [26,28]. The biological performance of Ti6Al4V either subjected to SLA and hydrothermally treated textured samples was evaluated by assessing human MSC adhesion and *in vitro* mineralization.

## 7.2. Materials and methods

### 7.2.1. Ti6Al4V systems production

Ti6Al4V alloy plates (ASTM B265) with dimensions 45 x 10 x 0.5 mm were purchased from Titanium Products (United Kingdom). Ti6Al4V plates were sandblasted for 30 s using spherical alumina ($Al_2O_3$) particles with a granulometric range between 106 and 150 μm to obtain a moderate roughness (Ra) of 2-4 μm. After samples were subjected to acid etching in a solution composed of 32% hydrochloric acid (HCl), 96% sulphuric acid ($H_2SO_4$) and $H_2O$ (2:1:1) at room temperature for 5 min. After rinsed in distilled water, samples were ultrasonically cleaned with isopropyl alcohol (Labsolve, Portugal) for 5 min and dried at room temperature. This group of samples corresponds to the control given the sand-blasted, large grit and acid-etched (SLA) is the most commonly used surface modification of dental and orthopaedic implants [6].

Laser surface texturing was performed on as-received Ti6Al4V plates using a Nd:YAG laser (OEM Plus, SISMA, Italy), which specifications are in Supplementary Table 7.1. The pillar-texture was created in an area of 9.0 × 10.0 mm. The texture design (cross-hatched pattern for pillars texturing) was defined in a computer-aided design software (CoredDRAW) and then marked on the metallic surfaces, according to specific laser parameters, through laser connected Sisma Laser Controller (SLC) software. The texturing was assisted with a flow of air to remove any debris produced during laser processing and after samples were cleaned in an ultrasonic bath with isopropyl alcohol for 5 min and dried at room temperature.

Consecutive laser processing strategy and continuous marking mode were selected based on a previous study [29] and three set of micro-pillar textures were engraved aiming the following dimensions: pillar width of 20 ± 5 μm, pillar height of 25 ± 5 μm and groove widths of 60 ± 5, 90 ± 5 and 120 ± 5 μm, corresponding to the groups GW60, GW90 and GW120, respectively. A cross-hatched pattern (groups of vertical and horizontal lines) was designed to obtain the defined micro-textured samples (Supplementary Fig. 7.1) and considering the laser parameters described in Table 7.1.

Table 7.1 - Set of laser parameters.

| **Set of laser parameters** | **Units** |
|---|---|
| Laser power | 1.5 W |
| Scanning speed | 100 mm/s |
| Line spacing | 10 μm |
| Number of passages: | |
| GW60 | 80 |
| GW90 | 80 |
| GW120 | 125 |
| Laser energy density (J/mm$^2$): | |
| GW60 | 120 |
| GW90 | 120 |
| GW120 | 187.5 |

Ti6Al4V plates of the control and textured groups were then cut with an area of 9.0 x 10.0 mm using a Nd:YV04 laser (XM-30D, XianMing Laser, China) under an argon atmosphere for the cellular studies. After laser processing, textured samples were subjected to hydrothermal treatment in distilled water within a reactor set to a temperature of 180 °C for a duration of 180 min. After, the samples were gradually cooled to room temperature and subjected to a 5-minute ultrasonic cleaning using isopropyl alcohol.

### 7.2.2. Ti6Al4V surface characterization

#### 7.2.2.1. Ti6Al4V surface topography

The surface roughness of the control group was assessed by using a contact profilometer (Surftest SJ 201from Mitutoyo, Tokyo, Japan), using a filter to eliminate the largest scale elements from the surface of 0.8 μm and a filter to eliminate the smallest scale elements from the surface maximum of 2.5 μm at 0.25 mm/s, according to ISO 21920-2:2021. The average roughness ($R_a$) was calculated by averaging six measurements. Textured samples were analysed by a S Neox 3D Optical Profiler (Sensofar, Spain) with a 10X objective and analysed with the Gwyddion software to assess the texture profile and dimensions. The 2D profile was acquired both in horizontal and vertical directions and five measurements were averaged to calculate each texture dimension.

#### 7.2.2.2. Crystallographic analysis

X-ray diffraction (XRD) analyses were performed using a Bruker AXS D8 Discover equipment, with a CuKα radiation at a grazing angle of 1° and 2Θ between 20 and 80°. Raw data was treated with Profex software (Nicola Döbelin, Switzerland), in which the Rietveld refinement was performed with the BGMN Rietveld program developed by Jörg Bergmann using, among the favourite phases, anatase and rutile. The average percentage of anatase and rutile phases for textured samples was calculated using the Origin software, by calculating the ratio between the area of the crystalline contribution and the total area.

#### 7.2.2.3. Surface wettability

The wettability of the control and textured samples was assessed using the contact angle system OCA 15 plus (Dataphysics, Germany). Processed samples were stored at 60 °C overnight and stored in a desiccator. The water contact angles were determined (one per condition) using the DataPhysics SCA software on samples after processing and immediately after the sterilization process, by dispersing a 4 μL droplet of distilled water at a dosing rate of 1 μL/s at room temperature.

### 7.2.3. Processing Ti6Al4V systems for *in vitro* studies

The control group and laser processed samples subjected to hydrothermal treatment were sterilized by immersion in 70% (v/v) ethanol for 1 h each side, followed by irradiation of Ultraviolet-C (UV) light (wavelength of 100-280 nm) for 2 hrs each side, inside a laminar flow cabinet Bio II Advance Plus (Telstar). Afterward, samples were stored in 5 times concentrated phosphate

buffered saline (5XPBS) for 24 hrs. The PBS solution was prepared from PBS tablets (A9201; PanReac AppliChem ITW Reagents, USA), which composition is 2.7 mM KCl, 140 mM NaCl and 10mM phosphate, at a pH of 7.4 (25 °C). Sterilized textured samples were further coated with a 5 μg/mL human plasma-derived fibronectin solution (05-752-1, PRIME-XV Human Fibronectin; FUJIFILM Irvine Scientific, The Netherlands), and incubated overnight at 4 °C prior cell culture.

#### 7.2.4. MSC culture and osteogenic programming within Ti6Al4V systems

Bone marrow-derived human mesenchymal stem cells (MSC) were purchased from ATCC (PCS-500-012™; LGC Standard, Barcelona, Spain). Cell thawing and expansion were performed using uniquely clinically compatible xeno-free and animal serum-free culture media, according to the protocols of Sartorius AG. MSC were cultured in a complete MSC medium composed of NutriStem® MSC Basal Medium (05-200-1A; Sartorius AG, Madrid, Spain), NutriStem® MSC Supplement Mix (05-201-1U; Sartorius AG, Madrid, Spain) and PLTGold® Human Platelet Lysate (PLTGold27R; Sartorius AG, Madrid, Spain) in a $CO_2$ incubator (95% of air and 5% $CO_2$ at 37 °C), and a complete medium change was performed every 3 days. When reached a confluence of 80%, MSC were passaged using an animal components-free recombinant trypsin solution (03-078-1; Sartorius AG, Madrid, Spain) and used for osteogenic differentiation (from passage 5 to 6), whereas the remaining were cryopreserved in MSC freezing solution (05-712-1E; Sartorius AG, Madrid, Spain).

Aiming the osteogenic differentiation, MSC were seeded on the control Ti6Al4V group (SLA) and on fibronectin coated-textured samples at a cellular density of $3x10^4/cm^2$. After 24 hrs from seeding, the MSC culture medium was changed to the osteogenic differentiation medium (05-440-1; Sartorius AG, Madrid, Spain). Cells were incubated for up to 21 days and the medium was changed every 3 days. At least three replicates of the four surface conditions were acquired for each osteogenic differentiation assay, at day 0 and 21.

##### 7.2.4.1. Intracellular and extracellular profile of RUNX2 within Ti6Al4V systems

Following 24 hrs in culture, cells were washed with PBS and fixed in 4% formaldehyde in PBS (1X) for 10 min. After washing twice with PBS (1X) for 5 min each, cells were permeabilized with 0.1% Triton X-100 in PBS (1X) and washed twice with PBS. Then, cells were blocked with 3% BSA in PBS for 1 hour at room temperature and incubated at 4 °C overnight with rat anti-human antibody specific for RUNX2 (232902; R&D Systems, USA). On the following day, samples were

washed three times with PBS for 5 min and a second incubation was performed for 1 h at room temperature in the dark. Cells were incubated with the secondary antibodies Alexa Fluor Plus 569-conjugated goat anti-rat (A11077; Thermo Fisher Scientific, USA) specific for RUNX2 and with Phalloidin Alexa Fluor 488 (1785486; Life Technologies, USA) to visualize F-actin. Cells were again washed three times with PBS and nuclear stained with DAPI (1729803; Life Technologies, USA), for 15 minutes at room temperature in the dark. After three washes in PBS for 5 min each, titanium-based plates were mounted on microscope slides with Fluoroshiel™ mounting solution (F6182-20ML; Sigma-Aldrich, USA) and stored at 4 °C for one day before imaging. Samples were imaged using a confocal microscope LSM780 (Zeiss, Germany).

The secretion of RUNX2 to the culture medium was assessed by Enzyme-Linked Immunosorbent Assay (ELISA) at 21 days. ELISA for human RUNX2 was performed according to the manufacturer's instructions (Wuhan Fine Biotech Co. Ltd. Wuhan, China). Briefly, standards (20 ng/mL – 0.312 ng/mL) and test samples were added to the pre-coated well plate and incubated for 90 min at 37 °C. Subsequently, the plate was washed twice with wash buffer and Biotin-labelled antibody was incubated for 60 min at 37 °C. After washing the plate three times. the HRP-Streptavidin Conjugate was added to each well and incubated at 37 °C for 30 min. Then the wells were washed five times and TMB Substrate was incubated in dark for 20 min, again at 37 °C. The reaction was stopped with Stop Solution and the absorbance was read immediately at 450 nm in the spectrometer Biotek Synergy H1 Microtiter Plate Reader (Agilent, USA). The experiments were performed in triplicate for each timepoint.

#### 7.2.4.2. Mineralization assessment

The osteogenic differentiation was evaluated by comparing the calcium deposits staining with Alizarin Red Solution (ARS) at 0 and 21 days. The supernatant was removed, cells were washed with PBS and incubated with cold EtOH 70% for 30-60 min at room temperature. After washing three times with double-distilled water (DDW), fixed cells were stained with 2% ARS at pH 7.2 (TMS-008-C; Merck Life Science, Germany) and incubated at room temperature for 30-60 min. The excess dye was removed and washed at least four times with DDW. Afterwards, DDW was added to each well to prevent cells from drying and Ti samples using the Nikon Eclipse LV 100 ND (Nikon, Japan). Semi-quantitative assessment of the extracellular matrix mineralization was performed by ARS elution. Briefly, 10% (w/v in DDW) of hexadecylpyridinium chloride monohydrate (CPC, C9002; Merck Life Science, Germany) was added to each well and incubated at room

temperature for 1 h to de-stain cultures. The absorbance was then read at 550 nm using the spectrometer Biotek Synergy H1 Microtiter Plate Reader (Agilent, USA). The mineralization change was calculated according to the following normalization:

$$Mineralization\ fold\ change = \frac{Absorption\ at\ 21\ days - Absorption\ at\ 0\ days}{Absorption\ at\ 0\ days}$$

7.2.4.3. Statistical analysis

Multiple unpaired t-test and GraphPad Prism v.9 from GraphPad Software (California, USA) were used for all the statistical analyses.

## 7.3. Results and discussion

### 7.3.1. Detailed characterization of the laser processed Ti6Al4V

Ti6Al4V plates were subjected to sandblasting, obtaining a roughness values (Ra) of 3.66 ± 0.52 μm and subsequently to acid-etching (SLA), leading to a $R_a$ of 2.97 ± 0.53 μm, consistent with what was expected and previously reported under the same conditions [9,30]. The topography of the micro-pillar textures and culture of MSC are represented in Fig. 7.1 and texture dimensions are summarized in Table 7.2.

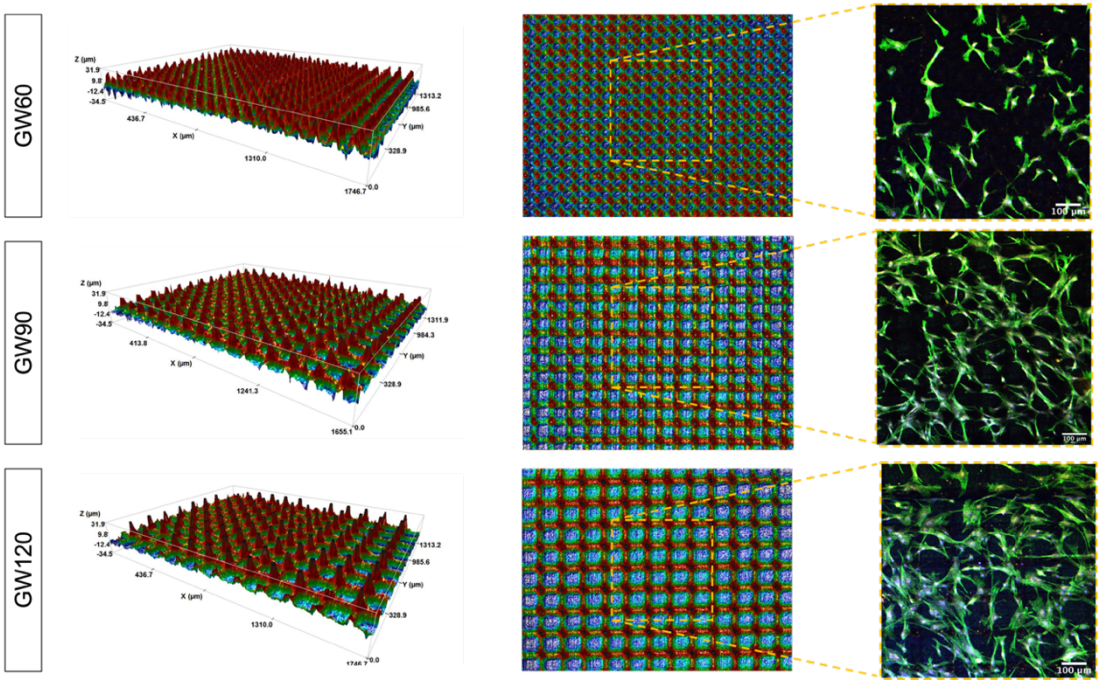



Figure 7.1 - 3D (left) and 2D (middle) optical profilometry images of the GW60, GW90 and GW120 micro-pillar textured samples and fluorescence images of MSC culture (right). Phalloidin staining was used to visualize the cytoskeleton of the cells (green fluorescence), the DAPI staining was used to demonstrate the nuclei of cells (blue fluorescence), the expression of RUNX2 was detected using brown fluorescence staining. All images include a 100 μm scale bar.

Table 7.2 - Texture dimensions of samples with micro-pillars produced by LST (mean ± standard deviation).

| Group | Groove width (µm) | Pillar width (µm) | Pillar height (µm) |
|---|---|---|---|
| GW60 | 64.2 ± 1.3 | 16.2 ± 2.7 | 21.8 ± 1.2 |
| GW90 | 93.2 ± 2.9 | 16.2 ± 1.0 | 18.8 ± 0.3 |
| GW120 | 125.8 ± 1.7 | 14.4 ± 1.4 | 26.1 ± 1.4 |

A micro-scale pattern with pyramid pillars was effectively obtained, which dimensions were in the expected range. Fluorescent images of MSC cultured on textured sample (Fig. 7.1) show a homogeneous distribution and interconnection between cells.

X-ray diffraction (XRD) analysis was performed for all groups and the Rietveld refinement was used to obtain the calculated diffraction profile, as displayed in Supplementary Fig. 7.2, and the crystalline phases were identified. The Rietveld refinements were successfully obtained, and the phase quantification of both anatase and rutile is shown in Fig. 7.2.

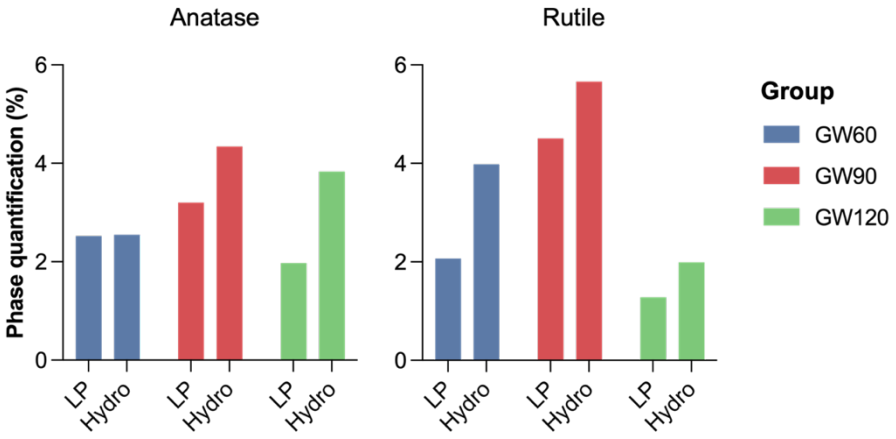



Figure 7.2 - Fraction of anatase and rutile in textured samples after laser processing (LP) and after hydrothermal treatment (Hydro).

As expected, the SLA group only presented Ti and TiVAl phases, among which the hexagonal closed packed (hcp) crystal structures are the major phases, in comparison to the body-centred cubic (bcc). Laser textured samples (GW60, GW90 and GW120), in addition to the Ti and TiVAl phases, present titanium oxide phases, including anatase and rutile (tetragonal crystal structure). Therefore, a titanium oxide layer is formed during LST, when the Ti6Al4V substrate interacts with oxygen from immediate ambient [31]. As expected, higher fractions of anatase and rutile were found after subjecting laser processing samples to hydrothermal treatment.

The wetting behaviour of the control group and textured surfaces after laser processing (LP), following hydrothermal treatment (Hydro) and subsequent UV irradiation is summarized in Fig. 7.3.

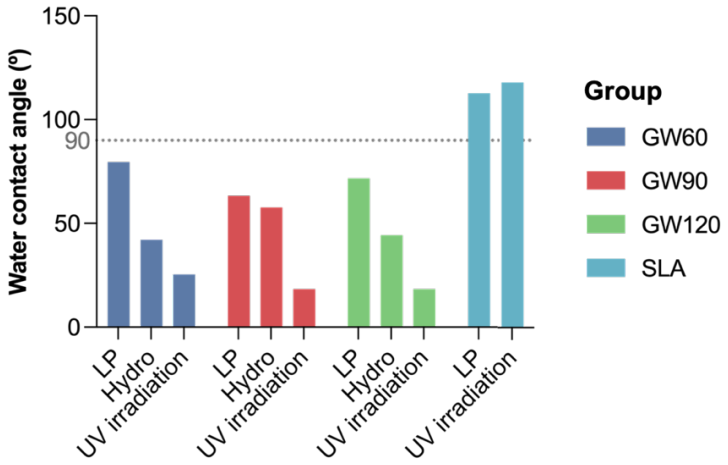



Figure 7.3 - Water contact angles of SLA, GW60, GW90 and GW120 after laser processing (LP), after hydrothermal treatment in the case of textured samples and after UV irradiation for 2 hrs.

Ti6Al4V subjected to SLA has a contact angle superior to 112.65o, before and after UV irradiation being, therefore hydrophobic. On the contrary, all textured samples have a contact angle inferior to 80° after laser processing. The wettability increased for all textured samples following the hydrothermal treatment, particularly for the GW60 in which the increase was close to 50%. Finally, the UV irradiation as sterilizing process further increased wettability, due to the formation of chemically reactive hydroxyl radical species with reduced surface negative charge [32]. The wettability of all textured samples increased by at least 40% after UV irradiation and the lowest contact angles were of 18.30o for both GW90 and GW120.

### 7.3.2. Textured Ti6Al4V samples promote differentiation of MSC

MSC seeded on treated and control Ti6Al4V were induced, in osteogenic culture media, to differentiate into osteoblasts for a total of 21 days. Osteoblasts produce and deposit calcium and this mineralization was assessed and correlated with ARS staining (Fig. 7.4).

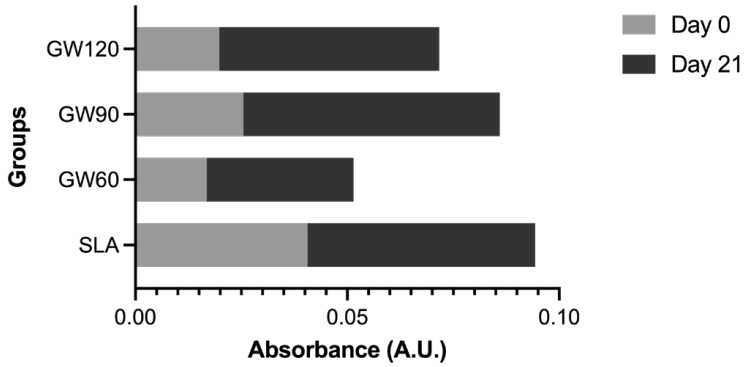



Figure 7.4 - Alizarin Red staining on MSCs cultured both on textured and control samples at 0 and 21 days.

During osteogenic differentiation, MSC's are subject to morphologic [33,34] and genetic program-changes [35,36] and specific osteoblastic markers such as RUNX2, ALP, osteopontin and osteocalcin are expressed to foster extracellular matrix mineralization [35]. The xeno-free and serum-free osteogenic medium used here contains dexamethasone (DEX) and ascorbic acid but is calcium free. Therefore, all calcium stained by ARS is a result of the osteogenic differentiation of MSC. An increase in mineralization was observed for all groups, indicating that all surfaces promoted mineralization. Among the textured samples, higher values at day 21 were found as follows: GW90 > GW120 > GW60. The relative change of mineralization between 0 and 21 days for the textured samples increased more than 100%, the highest of 161% observed for GW90, whereas the relative change of mineralization for the SLA was only of 32%. In addition to assessing mineralization through calcium deposit staining, the biomarker RUNX2 has been recognized for their pivotal involvement in osteogenesis [35–37]. In this study, a similar RUNX2 profiling was observed for SLA and textured Ti6Al4V systems at 21 days (Supplementary Fig. 7.3).

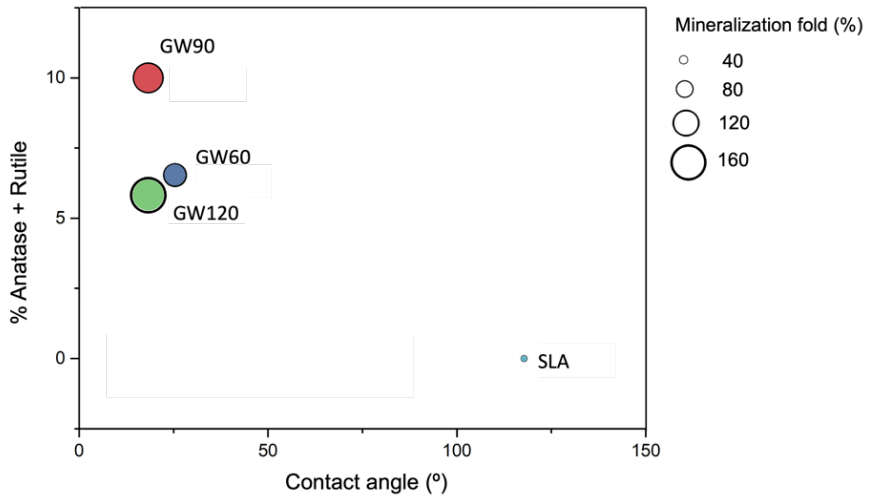



Figure 7.5 - Quantitative analysis assessing the impact of contact angle, anatase and rutile levels on the fold change of mineralization over a 21-day culture period.

Furthermore, the analysis of MSC cultured on textured Ti6Al4V samples (GW60, GW90 and GW120) after 21 days showed an increased mineralization fold when compared with SLA (Fig. 7.5). Among the different textured groups, higher mineralization fold was found for the GW90. The oxide film formed in all textured samples is based on anatase and rutile fractions known to promote bioactivity and osteogenesis [38].

## 7.4. Conclusions

Micro-scaled laser-texturing combined with hydrothermal treatment is a promising approach able to create highly reproducible topological surfaces and to potentially enhance bone-implant interactions due to increasing fraction of both anatase and rutile and wettability. In this framework, our results highlight an adequate mineralization performance potential of textured Ti6Al4V systems when compared to state-of-the-art Ti implants. It is however notable that despite promising outcomes, a more comprehensive investigation is required to quantify clinically relevant endpoints for LST deployment in implant manufacturing.

## Acknowledgments

This work was supported by FCT (Fundação para a Ciência e a Tecnologia) through the grants SFRH/BD/141056/2018, COVID/BD/152996/2022 and UMINHO/BID/2023/04, the project PTDC/EME-EME/1442/2020 and under the national support to R&D units grant, through the reference projects UIDB/04436/2020 and UIDP/04436/2020. In addition, this work was developed within the scope of the project CICECO-Aveiro Institute of Materials, UIDB/50011/2020,

UIDP/50011/2020 & LA/P/0006/2020, financed by national funds through the FCT/MCTES (PIDDAC).

## References

[1] M. Kaur, K. Singh, Review on titanium and titanium based alloys as biomaterials for orthopaedic applications, Mater. Sci. Eng. C. 102 (2019) 844–862. https://doi.org/10.1016/j.msec.2019.04.064.

[2] V. Goriainov, R. Cook, J.M. Latham, D.G. Dunlop, R.O.C. Oreffo, Bone and metal: An orthopaedic perspective on osseointegration of metals, Acta Biomater. 10 (2014) 4043– 4057. https://doi.org/10.1016/j.actbio.2014.06.004.

[3] E.M. Lotz, M.B. Berger, Z. Schwartz, B.D. Boyan, Regulation of Osteoclasts by Osteoblast Lineage Cells Depends on Titanium Implant Surface Properties, Acta Biomater. 68 (2018) 296–307. https://doi.org/10.1016/j.actbio.2017.12.039.

[4] P. Ducy, M. Starbuck, M. Priemel, J. Shen, G. Pinero, V. Geoffroy, M. Amling, G. Karsteny, A Cbfa1-dependent genetic pathway controls bone formation beyond embryonic development, Genes Dev. 13 (1999) 1898.

[5] P. Ducy, R. Zhang, V. Geoffroy, A.L. Ridall, G. Karsenty, Osf2/Cbfa1: A transcriptional activator of osteoblast differentiation, Cell. 89 (1997) 747–754. https://doi.org/10.1016/S0092-8674(00)80257-3.

[6] J.I. Rosales-Leal, M.A. Rodríguez-Valverde, G. Mazzaglia, P.J. Ramón-Torregrosa, L. Díaz-Rodríguez, O. García-Martínez, M. Vallecillo-Capilla, C. Ruiz, M.A. Cabrerizo-Vílchez, Effect of roughness, wettability and morphology of engineered titanium surfaces on osteoblast-like cell adhesion, Colloids Surfaces A: Physicochem. Eng. Asp. 365 (2010) 222–229. https://doi.org/10.1016/j.colsurfa.2009.12.017.

[7] P. Ming, S. Shao, J. Qiu, J. Yang, Y. Yu, J. Chen, W. Zhu, C. Tang, Superiority of calcium-containing nanowires modified titanium surface compared with SLA titanium surface in biological behavior of osteoblasts: A pilot study, Appl. Surf. Sci. 416 (2017) 790–797. https://doi.org/10.1016/j.apsusc.2017.04.152.

[8] J. Zhang, J. Liu, C. Wang, F. Chen, X. Wang, K. Lin, A comparative study of the osteogenic performance between the hierarchical micro/submicro-textured 3D-printed Ti6Al4V surface and

the SLA surface, Bioact. Mater. 5 (2020) 9–16. https://doi.org/10.1016/j.bioactmat.2019.12.008.

[9] A.I. Nicolas-Silvente, E. Velasco-Ortega, I. Ortiz-Garcia, L. Monsalve-Guil, J. Gil, A. Jimenez-Guerra, Influence of the titanium implant surface treatment on the surface roughness and chemical composition, Materials (Basel). 13 (2020) 1–13. https://doi.org/10.3390/ma13020314.

[10] X. Shen, P. Shukla, A Review of Titanium Based Orthopaedic Implants (Part-I): Physical Characteristics, Problems and the need for Surface Modification, Int. J. Peen. Sci. Technol. 1 (2020) 301–332.

[11] X. Gao, M. Fraulob, G. Haïat, Biomechanical behaviours of the bone-implant interface: A review, J. R. Soc. Interface. 16 (2019). https://doi.org/10.1098/rsif.2019.0259.

[12] A. Pérez Del Pino, P. Serra, J.L. Morenza, Coloring of titanium by pulsed laser processing in air, Thin Solid Films. 415 (2002) 201–205. https://doi.org/10.1016/S0040- 6090(02)00632-6.

[13] A. Pérez del Pino, J.M. Fernández-Pradas, P. Serra, J.L. Morenza, Coloring of titanium through laser oxidation: Comparative study with anodizing, Surf. Coatings Technol. 187 (2004) 106–112. https://doi.org/10.1016/j.surfcoat.2004.02.001.

[14] J. Lawrence, L. Hao, H.R. Chew, On the correlation between Nd:YAG laser-induced wettability characteristics modification and osteoblast cell bioactivity on a titanium alloy, Surf. Coatings Technol. 200 (2006) 5581–5589. https://doi.org/10.1016/j.surfcoat.2005.07.107.

[15] W. Pfleging, R. Kumari, H. Besser, T. Scharnweber, J.D. Majumdar, Laser surface textured titanium alloy (Ti-6Al-4V): Part 1 - Surface characterization, Appl. Surf. Sci. 355 (2015) 104–111. https://doi.org/10.1016/j.apsusc.2015.06.175.

[16] A. Cunha, A.P. Serro, V. Oliveira, A. Almeida, R. Vilar, M.C. Durrieu, Wetting behaviour of femtosecond laser textured Ti-6Al-4V surfaces, Appl. Surf. Sci. 265 (2013) 688–696. https://doi.org/10.1016/j.apsusc.2012.11.085.

[17] V. Dumas, A. Rattner, L. Vico, E. Audouard, J.C. Dumas, P. Naisson, P. Bertrand, Multiscale grooved titanium processed with femtosecond laser influences mesenchymal stem cell morphology, adhesion, and matrix organization, J. Biomed. Mater. Res. - Part A. 100 A (2012) 3108–3116. https://doi.org/10.1002/jbm.a.34239.

[18] W.A. Lackington, P. Schweizer, M. Khokhlova, C. Cancellieri, S. Guimond, A.L. Chopard-Lallier, J. Hofstetter, P. Schmutz, X. Maeder, M. Rottmar, Femtosecond Laser-Texturing the Surface of Ti-Based Implants to Improve Their Osseointegration Capacity, Adv. Mater. Interfaces. 9 (2022). https://doi.org/10.1002/admi.202201164.

[19] F. Melo-Fonseca, M. Gasik, S. Madeira, F.S. Silva, G. Miranda, Surface characterization of titanium-based substrates for orthopaedic applications, Mater. Charact. 177 (2021) 111161. https://doi.org/10.1016/j.matchar.2021.111161.

[20] M. Zuldesmi, A. Waki, K. Kuroda, M. Okido, High Osteoconductive Surface of Pure Titanium by Hydrothermal Treatment, J. Biomater. Nanobiotechnol. 04 (2013) 284–290. https://doi.org/10.4236/jbnb.2013.43036.

[21] D.M. Rivera-Chacon, M. Alvarado-Velez, C.Y. Acevedo-Morantes, S.P. Singh, E. Gultepe, D. Nagesha, S. Sridhar, J.E. Ramirez-Vick, Fibronectin and vitronectin promote human fetal osteoblast cell attachment and proliferation on nanoporous titanium surfaces, J. Biomed. Nanotechnol. 9 (2013) 1092–1097. https://doi.org/10.1166/jbn.2013.1601.

[22] J. Vishnu, V. K Manivasagam, V. Gopal, C. Bartomeu Garcia, P. Hameed, G. Manivasagam, T.J. Webster, Hydrothermal treatment of etched titanium: A potential surface nano-modification technique for enhanced biocompatibility, Nanomedicine Nanotechnology, Biol. Med. 20 (2019). https://doi.org/10.1016/j.nano.2019.102016.

[23] F. Liu, F. Wang, T. Shimizu, K. Igarashi, L. Zhao, Formation of hydroxyapatite on Ti-6Al- 4V alloy by microarc oxidation and hydrothermal treatment, Surf. Coatings Technol. 199 (2005) 220–224. https://doi.org/10.1016/j.surfcoat.2004.10.146.

[24] C. Xu, L. Y. Chen, C. Zheng, Z. Y. Zhang, R. Li, H. Y. Yang, J. Peng, L. Zhang, L.C. Zhang, Bioactive Performances of Surface Modification of Ti–6Al–4V Jointly Using Ultrasonic- Assisted Microarc Oxidation and Hydrothermal Treatment, Adv. Eng. Mater. 24 (2022) 1– 11. https://doi.org/10.1002/adem.202200674.

[25] Z. Fei Yin, L. Wu, H. Gui Yang, Y. Hua Su, Recent progress in biomedical applications of titanium dioxide, Phys. Chem. Chem. Phys. 15 (2013) 4844–4858. https://doi.org/10.1039/c3cp43938k.

[26] R. Tejero, E. Anitua, G. Orive, Toward the biomimetic implant surface: Biopolymers on titanium-based implants for bone regeneration, Prog. Polym. Sci. 39 (2014) 1406–1447. https://doi.org/10.1016/j.progpolymsci.2014.01.001.

[27] L. Petecchia, C. Usai, M. Vassalli, P. Gavazzo, Biophysical characterization of nanostructured $TiO_2$ as a good substrate for hBM-MSC adhesion, growth and differentiation, Exp. Cell Res. 358 (2017) 111–119. https://doi.org/10.1016/j.yexcr.2017.06.008.

[28] N. Ogura, M. Kawada, W.J. Chang, Q. Zhang, S.Y. Lee, T. Kondoh, Y. Abiko, Differentiation of the human mesenchymal stem cells derived from bone marrow and enhancement of cell attachment by fibronectin, J. Oral Sci. 46 (2004) 207–213. https://doi.org/10.2334/josnusd.46.207.

[29] F. Melo-Fonseca, B. Guimarães, M. Gasik, F.S. Silva, G. Miranda, Experimental analysis and predictive modelling of Ti6Al4V laser surface texturing for biomedical applications, Surfaces and Interfaces. 35 (2022) 102466. https://doi.org/10.1016/j.surfin.2022.102466.

[30] E. Velasco-Ortega, I. Ortiz-Garcia, A. Jiménez-Guerra, E. Núñez-Márquez, J. Moreno- Muñoz, J.L. Rondón-Romero, D. Cabanillas-Balsera, J. Gil, F. Muñoz-Guzón, L. Monsalve-Guil, Osseointegration of sandblasted and acid-etched implant surfaces. A histological and histomorphometric study in the rabbit, Int. J. Mol. Sci. 22 (2021). https://doi.org/10.3390/ijms22168507.

[31] V. Kashyap, P. Ramkumar, Improved oxygen diffusion and overall surface characteristics using combined laser surface texturing and heat treatment process of Ti6Al4V, Surf.Coatings Technol. 429 (2022) 127976. https://doi.org/10.1016/j.surfcoat.2021.127976.

[32] S.H. Choi, W.S. Jeong, J.Y. Cha, J.H. Lee, H.S. Yu, E.H. Choi, K.M. Kim, C.J. Hwang, Time-dependent effects of ultraviolet and nonthermal atmospheric pressure plasma on the biological activity of titanium, Sci. Rep. 6 (2016) 1–12. https://doi.org/10.1038/srep33421.

[33] I. Titushkin, M. Cho, Modulation of cellular mechanics during osteogenic differentiation of human mesenchymal stem cells, Biophys. J. 93 (2007) 3693–3702. https://doi.org/10.1529/biophysj.107.107797.

[34] J.P. Rodríguez, M. González, S. Ríos, V. Cambiazo, Cytoskeletal organization of human mesenchymal stem cells (MSC) changes during their osteogenic differentiation, J. Cell. Biochem. 93 (2004) 721–731. https://doi.org/10.1002/jcb.20234.

[35] A. Rutkovskiy, K.-O. Stensløkken, I.J. Vaage, Osteoblast Differentiation at a Glance, Med. Sci. Monit. Basic Res. 22 (2016) 95–106. https://doi.org/10.12659/MSMBR.901142.

[36] M.S. Carvalho, A.A. Poundarik, J.M.S. Cabral, C.L. da Silva, D. Vashishth, Biomimetic matrices for rapidly forming mineralized bone tissue based on stem cell-mediated osteogenesis, Sci. Rep. 8 (2018) 1–16. https://doi.org/10.1038/s41598-018-32794-4.

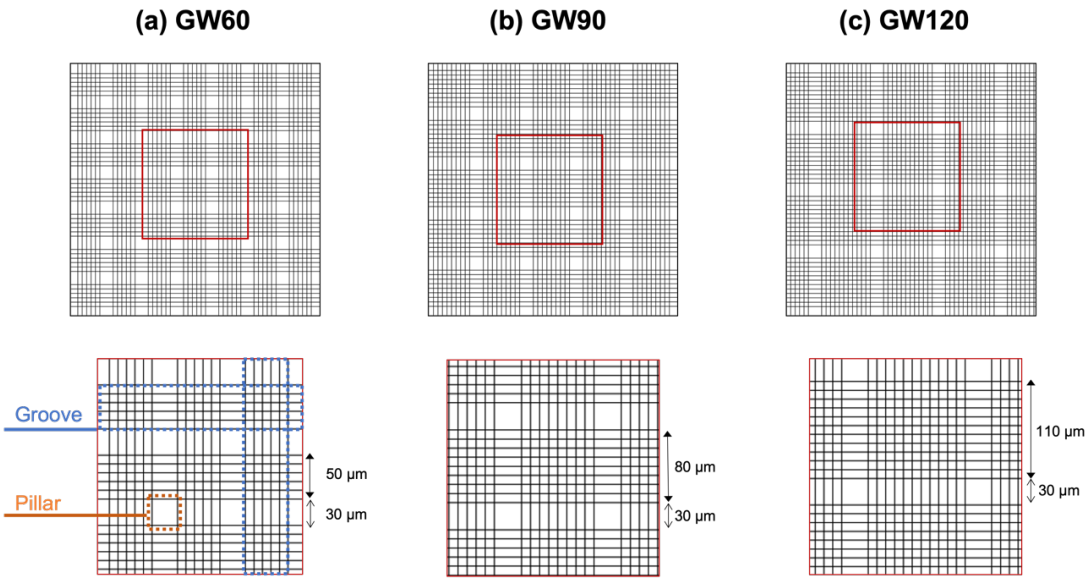
[37] R.J. Miron, Y.F. Zhang, Osteoinduction: A review of old concepts with new standards, J. Dent. Res. 91 (2012) 736–744. https://doi.org/10.1177/0022034511435260.

[38] Y. Y okoi, Osteoblast-like cell proliferation, alp activity and photocatalytic activity on sintered anatase and rutile titanium dioxide, Materials (Basel). 14 (2021). https://doi.org/10.3390/ma14164414.

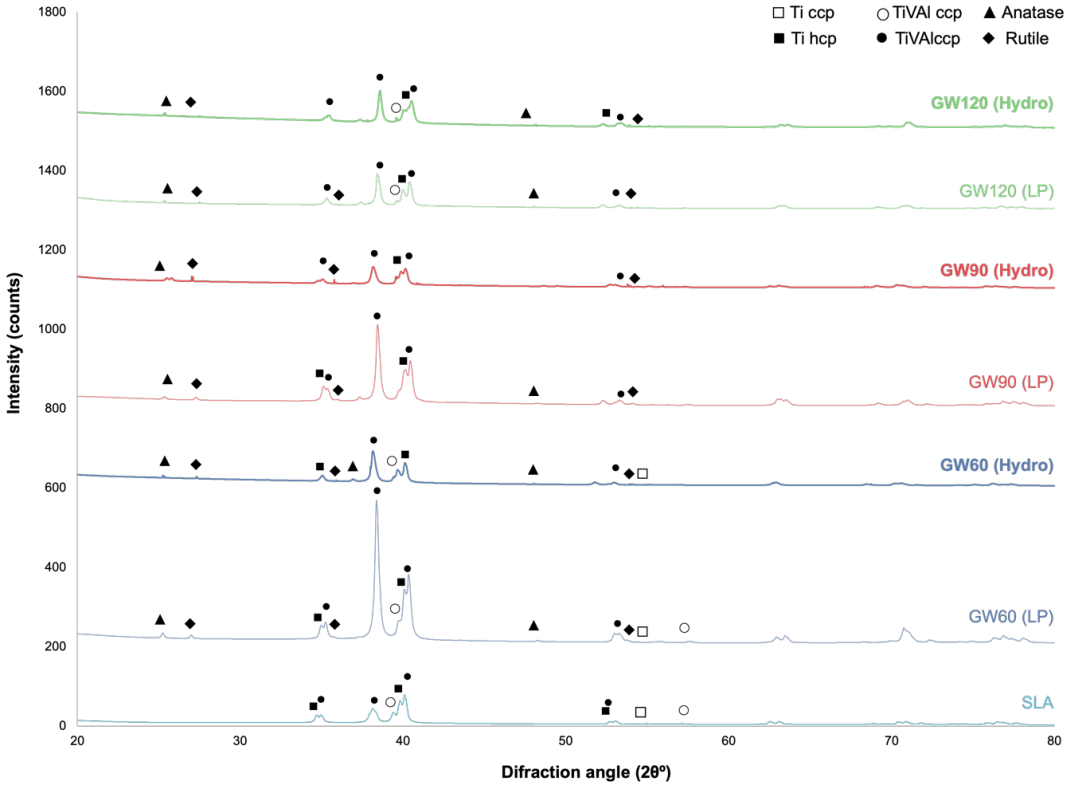
## Appendix A. Supplementary data

Supplementary Table 7.1 - Technical specifications of the Nd:YAG laser.

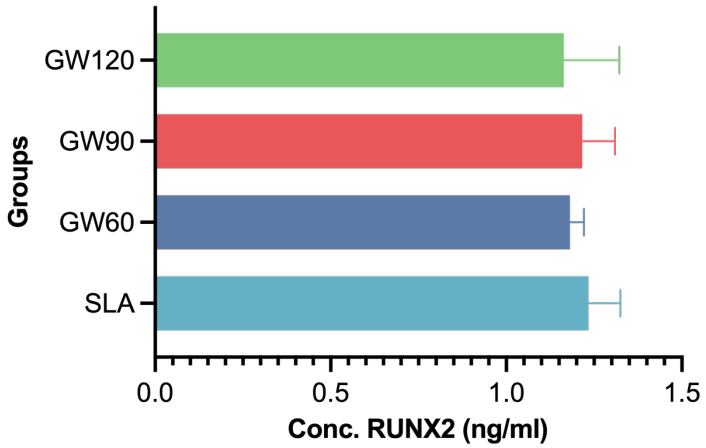
| **Laser specifications** | |
|---|---|
| Average output power (W) | 6 |
| Peak power per pulse (kW) | 8.57 |
| Wavelength (nm) | 1064 |
| Spot size (μm) | 3 |
| Pulse width (ns) | 35 |
| Repetition rate (kHz) | 20 |
| Maximum pulse energy (mJ/pulse) | 0.3 |
| Cooling system | Forced-air cooling |




Supplementary Figure 7.1 - CAD drawings of cross-hatched patterns with a drawing pillar width of 30 µm and groove width of (a) 50 µm, (b) 80 µm and (c) 110 µm of the textures GW60, GW90 and GW120, respectively.




Supplementary Figure 7.2 - X-ray diffraction patterns of the sandblasted and acid etched (SLA), and textured samples (GW60, GW90 and GW120) after laser processing (LP) and further hydrothermal treatment (Hydro). Identification of Bragg diffraction peaks characteristic of Ti ccp phase (# 04-016-5468), Ti hcp phase (# 04-001-8963), TiVAl ccp phase (04-0018-5433), TIVAl hcp phase (04-002-8708), anatase phase (# 04-007-0701) and rutile phase (# 04-003-0648).




Supplementary Figure 7.3 - Concentration of RUNX2 present in the culture medium at day 21 (mean ± standard deviation).

# CHAPTER 8

## MECHANICAL STIMULATION DEVICES FOR MECHANOBIOLOGY STUDIES: A MARKET, LITERATURE, AND PATENTS REVIEW

Published in Bio-Design and Manufacturing, 2023, 6, 340–371

http://doi.10.1007/s42242-023-00232-8

F. Melo-Fonseca[a, b, c], O. Carvalho[a, b], M. Gasik[d, e], G. Miranda[f], F. S. Silva[a, b]

[a]Center for MicroElectroMechanical Systems (CMEMS-UMinho), University of Minho, Campus de Azurém, 4800-058 Guimarães – Portugal

[b]LABBELS –Associate Laboratory, Braga, Guimarães, Portugal

[c]International Iberian Nanotechnology Laboratory (INL), 4715-330 Braga, Portugal

[d]School of Chemical Engineering, Aalto University Foundation, FI-00076 Espoo, Finland

[e]Seqvera Ltd., Helsinki, Finland

[f]CICECO, Aveiro Institute of Materials, University of Aveiro, 3810-193 Aveiro, Portugal

G. Miranda and F. S. Silva have contributed as co-last authors.

**Abstract**

Significant advancements in various research and technological fields have contributed to remarkable findings on the physiological dynamics of the human body. To more closely mimic the complex physiological environment, research has moved from two-dimensional (2D) culture systems to more sophisticated three-dimensional (3D) dynamic cultures. Unlike bioreactors or microfluidic-based culture models, cells are typically seeded on polymeric substrates or incorporated into 3D constructs which are mechanically stimulated to investigate cell response to mechanical stresses, such as tensile or compressive. This review focuses on the working principles of mechanical stimulation devices currently available on the market or custom-built by research groups or protected by patents and highlights the main features still open to improvement. These are the features which could be focused on to perform, in the future, more reliable and accurate mechanobiology studies.

**Keywords:** Biomaterials; Polymers; Actuators; Mechanical stress; Mechanotransduction

## 8.1. Contextualization

The adult human body is composed of approximately 37 trillion cells, all synchronized to maintain equilibrium [1]. Cells reside in a complex and dynamic microenvironment containing biological, chemical, physical, and mechanical cues which often regulate cell proliferation, migration, differentiation, and function, and ultimately, may be responsible for the development of disease [2]. To study and understand how cells respond to mechanical stimuli or how host cells will behave upon the implantation of biomaterials, researchers use mechanical stimulation devices. These devices subject biomaterials to a particular mechanical stress with the aim of stimulating cells through deformation of the biomaterials. Devices which are currently commercially available offer limited customization and restricted force measurement capabilities [3, 4]. As a consequence, a wide variety of apparatuses, with varying levels of sophistication, design, functionality, and precision, have been custom-built by research groups to meet particular needs, while others are protected by patents. This review focuses on the working principles, functionality, and main operational features of a number of mechanical stimulation devices developed over the past years, and highlights the main features still open to improvement.

## 8.2. The cellular microenvironment

All cells are in permanent interaction with the surrounding microenvironment, including the extracellular matrix (ECM) and neighbouring cells. That interaction is based on a combination of

multiple cues, including biological and physical cues able to influence cell behaviour [5, 6]. Cells are constantly and cyclically subjected to external forces whose type and magnitude are highly variable and dependent on location [7]. These forces are crucial from the beginning of cell life: throughout the development of embryos, and in everyday activities, in which cells experience shear stress during breathing and blood flow, or tensile and compressive stresses from skeletal muscle contraction, joint loading, and tendon/ligament stretching [8–11]. Their ability to sense externally imposed forces and mechanical properties of the surrounding ECM is denominated "cell mechanosensing" [12]. These signals are later converted into changes in intracellular biochemistry and gene expression, a process often referred to as "mechanotransduction" [13]. Mechanical stimuli include not only externally imposed forces (namely tensile, compressive, and shear forces), but also intrinsic cellular tensions generated by active cell contraction [7]. In fact, besides the intracellular response to dynamic modifications of the ECM, cells are also able to influence the environment, leading to a reciprocal interaction [7, 11]. Both outside-in and inside-out pathways exist in mechanotransduction processes, and are able to trigger signalling cascades [14, 15]. In this sense, the environment plays an important role in many cellular processes, such as cellular adhesion, migration, proliferation, differentiation, and apoptosis [15]. Given the importance of mechanical interactions in cellular behaviour, mechanobiology has emerged as a novel interdisciplinary field combining biology, mechanics, and engineering, which aims to understand how cells sense and behave in response to mechanical stimuli [7, 11, 16, 17]. Over the past few decades, researchers have developed systems to control the cellular microenvironment and, while some focus on improving cell culture conditions, others aim to study the effects of a particular mechanical stimulus on cells by using unique cells or biomaterial-based constructs.

## 8.3. Moving from 2 to 3D models

Biological systems are organized into several levels of structural organization, becoming more complex as the length scale increases. Beginning at the micrometre scale, cells assemble to form tissues, which are organized into organs, which together form the organism, the highest level of organization, on the metre scale. Biological model systems range from simplified two-dimensional (2D) cell cultures to more complex three-dimensional (3D) cell cultures, organoids, tissue explants, and model organisms, such as the mouse [2]. As the complexity rises, the associated cost and physiological relevance increase, while experimental accessibility decreases [2].

The 2D and 3D cell culture systems discussed below are illustrated in Fig. 8.1, in both static and dynamic modes. In conventional and static cell cultures, the nutrient supply is maintained by frequently changing the culture medium. Primary cells or established cell lines may be cultured as a 2D monolayer, in the case of an adherent culture, or as a cell suspension known as a "suspension culture". Although monolayer cultures are easily manipulated, used worldwide in life-science research, and still accepted as the gold standard, cells are highly anisotropic. This is why it has been experimentally observed that even within a particular cell line, cellular responses may differ for an identical mechanical input [18]. Moreover, it has been reported that cells may lose some differentiated characteristics [19] and that conventional 2D culture models, whether in Petri dishes or culture flasks, do not replicate the dynamic in vivo 3D microenvironment [2]. As a consequence, over the past decades, researchers have focused on more complex cell culture models which include cell seeding on prefabricated scaffolds or incorporate cells into 3D scaffolds (usually hydrogels made of synthetic polymers). These materials allow cellular spatial organization into functional cell-based constructs. In order to keep up with continuously more complex and demanding research, bioreactor systems were developed for numerous applications, for example, in the context of cell biology research and regenerative medicine therapies. While the absence of media mixing or circulation in a static aqueous environment leads to limited diffusion of fluids or gases and contributes to cell-waste accumulation and nutrition depletion [5, 20], 3D models with continuously mixed media in a dynamic culture allow homogeneous media and cell dispersion, better reproducing the in vivo spatial and biomechanical complexity [19]. Three-dimensional culture systems, particularly bioreactors, are not the scope of this review, but extensive works on this topic may be easily found in the literature [2, 20–23]. Briefly, fluid-flow-induced bioreactors are designed to enhance nutrient supply to cell cultures and replicate tissue-specific conditions [24]. They are often grouped into fed-batch [25], spinner-flask [26], rotating [24, 27], and perfusion bioreactors [21, 28]. Despite the continuous media agitation in bioreactors, an efficient supply of gases and nutrients is not always assured, and sample handling and maintenance of sterility are challenging. Because of the constraints related to bioreactor size, cost, and time consumption when running parallel multiple experiments, the reactor volumes in microfluidic systems can be reduced down to picolitres, while assuring a laminar-flow pattern [29, 30]. In addition to the decrease in reagent consumption, the culture environment is particularly controlled, because cell shape, dimensionality, and density are tightly regulated in 10–100 μm channels [31, 32]. In the category of micro-engineered devices, lab-on-a-chip-based devices are commonly used for point-of-care

diagnostics and are characterized by easy handling and high performance of body fluid analyses [33]. Organ-on-a-chip devices can be used for culturing cells, spheroids, organoids, and tissue biopsies and, among their final applications, can be used for drug screening and development, disease modelling, and the study of human physiology, due to their capability of closely replicating the dynamic microenvironment of living organs [30, 34]. However, the resultant fluid-flow-induced shear stresses may induce cell damage, and current devices lack automation and well-defined protocols [34]. In contrast to bioreactors, microfluidic-based culture models (or bioreactors on a chip) offer optimized culture conditions and precise control over the chemical and physical cellular environment through the integration of sensors [29].

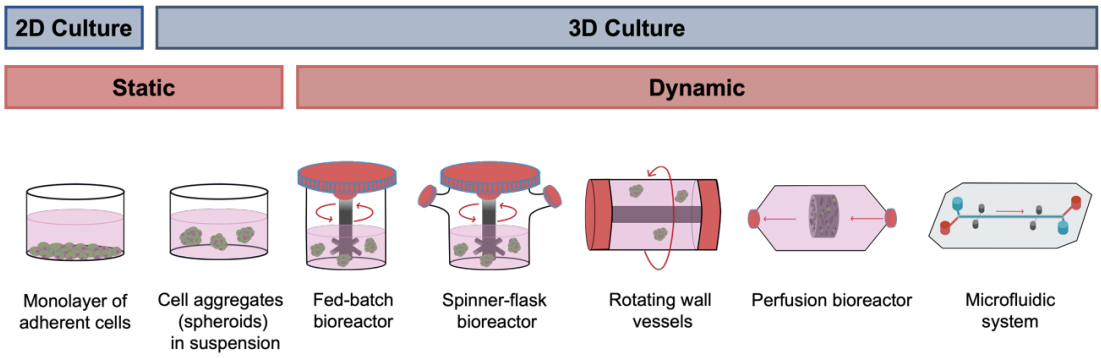



Figure 8.1 - Cell culture models may be in a static or dynamic mode. In 2D monolayer cultures, adherent cells are in contact with the culture vessel, neighbouring cells, and the culture medium. In non-adherent plates, 3D spheroids are grown in suspension, either without or with medium agitation (fed-batch bioreactor). In spinner-flask bioreactors, cell dispersion or cell-based constructs attached to a needle are in contact with a homogeneous medium due to agitation and medium perfusion. Rotating wall vessels enable cell culture mixing without an internal stirring mechanism by definition of a proper rotation speed. Perfusion bioreactors use continuous and fresh medium perfusion through cell-based constructs, provided by peristaltic pumps. Microfluidic systems are used for culturing and monitoring of both adherent and non-adherent cells. The fluid dynamics is represented by the red arrow.

Two-dimensional culture models are based on a cell monolayer in which cells are forced to adapt to an artificial, flat, and rigid surface [27], and thus do not provide meaningful information regarding the real dynamics that living cells and tissues experience. Therefore, 3D culture models have greatly increased in number and sophistication, and have the capability of more closely replicating the dynamic microenvironment. They are also more experimentally tractable than model organisms. Despite the fact that bioreactors and microfluidic-based platforms are attractive devices for transporting nutrients and thus improving overall cell culture conditions [2, 35], fluid-flow-induced shear stresses cannot be measured in this setting; thus, although this shear stress is considered an important contribution to cell metabolism, it cannot be considered as a mechanical input for mechanotransduction studies.

In the context of mechanobiology, external force can be applied through direct methods such as micropipette aspiration [36–38], atomic-force microscopy [38–41], and substrate deformation [32, 42–44]. Indirect methods can also be used, in which cells are, for example, subjected to optical or magnetic fields [45–47]. In direct methods, a generated and controlled force is applied directly on cells, leading, in some cases, to a large global cell strain. On the other hand, indirect methods allow researchers to monitor deformation in different regions of a cell, but not to precisely control or measure the applied stress [32, 47].

Mechanical stimulation devices have been developed to study cellular response to an externally applied mechanical stimulus or to mimic physiological dynamics to perform more reliable studies. For example, one can apply compressive or tensile forces on cells in a controlled way via biomaterials, as illustrated in Fig. 8.2. Typically, these devices consist of a culture medium vessel, a specific space for the cell-based construct/substrate, and clamping parts to apply tensile or compressive loading in a controlled computed way [21]. Furthermore, some devices allow real-time monitoring by the use of chambers composed of light-transparent materials and multi-chamber configurations for parallel experiments [21]. Individual components, such as biomaterials, ECM, and soluble and mechanical cues, may be integrated in these systems to closely mimic the in vivo environment and study physiology and screen therapeutics.

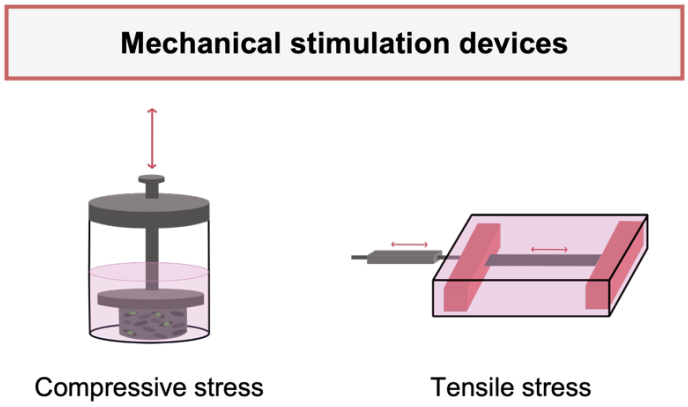



Figure 8.2 - Examples of mechanical stimulation devices used for mechanobiology studies. The commonly studied mechanical stresses are compressive and tensile stresses, either applied to cells incorporated inside 3D constructs (left) or cells seeded on a flexible substrate (right). The movement imposed on the biomaterials is represented by the red arrow.

## 8.4. Emerging mechanical stimulation devices

Mechanical stimulation devices have gained interest due to their potential for replicating mechanical cues observed in the in vivo microenvironment, controlling mechanical and physical properties with precision, and in some cases, allowing simultaneous analysis [48, 49]. Mechanical

strains in a given material obtained by applying either tensile or compressive stresses in any direction and at controlled loading features, such as strain magnitude and frequency, create a mechanical strain environment around the cultured cells. The strain profile obtained by such substrate deformation may occur in one of the three different modes illustrated in Fig. 8.3.

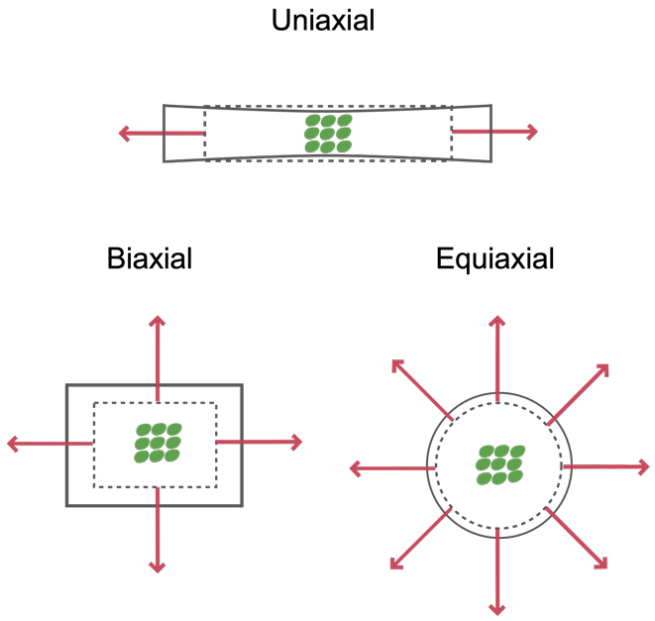



Figure 8.3 - The substrate on which cells (represented by green circles) are cultured may be subjected to different strain modes: uniaxial, biaxial, or equiaxial, as a consequence of substrate movement imposed by the load.

Novel and more complex devices have been developed to assure optimal cellular conditions during manipulation (e.g., application of a particular mechanical stimulus) and analyse the corresponding cellular behaviour in small-scale volumes. Some of the operational features of these mechanical stimulation devices are summarized in Table 8.1.

Table 8.1 - List of operational features of mechanical stimulation devices.

| **Device feature** | **Description** |
|---|---|
| Mechanical stimulus type | Selection depends on the study focus/application and may include at least one of the following: tensile, compressive, shear, or vibration stimulus |
| Definition of loading features | Strain mode (uniaxial, biaxial, or equiaxial), magnitude, frequency (static, cyclic, or intermittent), duration, and waveform (static, sinusoidal, ramp) |
| Aseptic conditions | The device parts in contact with the cell culture medium and/or cells must be sterile during sample handling and throughout the experiment |
| Incubation | - Short vs. long-term experiments<br>- The device either incorporates a means of changing the cell culture medium every few days, as well as controlling and maintaining the temperature at 37 °C, exchanging gases, and controlling humidity to perform long-term experiments (over more than 24 hrs), or has the correct geometry and dimensions to fit the incubator<br>- Static vs. dynamic culture (with or without continuous media mixing) |
| Multi-sample testing | Study more than one sample simultaneously (run in parallel more than one experiment) |
| Live imaging | Control and monitor cell behaviour in real time through glass or a transparent material, mostly by inverted confocal microscopy analysis |
| Automation | The drive mechanism may be automated |
| Maintenance | The device requires either low or high maintenance |

Depending on the goal of a particular study and consequently of the experimental design, cells may be seeded directly on the substrate or incorporated in functional constructs. Scaffolds or cell-based constructs are 3D structures often used to regulate the environment of cells, and in this sense, cells can be manipulated by controlling the mechanical properties of the scaffold, such as elasticity, rigidity, and strain. Natural scaffolds are made of naturally derived materials, namely collagen, fibrin, and components of decellularized tissues, whereas fully synthetic matrices are

often composed of poly(dimethylsiloxane) (PDMS) and poly(L-lactide-co-glycolide) (PLGA) [27]. One of the most common materials used in mechanobiology research is PDMS, because it is non-cytotoxic, autoclavable, and flexible. Furthermore, it has high optical transparency and low auto-fluorescence, which allows cell analysis by fluorescence and optical imaging techniques [7, 50]. Hydrogels are biocompatible and biomimetic 3D structures which, once again, facilitate imaging because the cellular behaviour in their interior can be monitored. Moreover, hydrogels are typically used to apply mechanical stimuli on cells because they allow a uniform distribution of stresses throughout the structure [21].

One of the most important concerns in mechanobiology studies is to ensure aseptic conditions during experiments. Therefore, all parts of the mechanical stimulation device are assembled inside a laminar-flow biosafety cabinet and then the complete and mounted device along with its electronic components is placed in a typical culture incubator, allowing maximally sterile conditions and, when required, a long-term experiment. As already mentioned, confocal imaging is often preferable to upright microscopy techniques, mainly to overcome issues related to device size constraints. Therefore, the design of some devices considers the overall device dimensions to ensure that it fits in the microscope chamber, and the incorporation of a glass coverslip or other materials with similar optical properties to allow high-magnification imaging of the cultured or encapsulated cells, for example, for performing live imaging studies [32, 42, 51, 52]. Other developments are intended to produce high-throughput capabilities, such as by increasing the number of wells/chambers which can be loaded simultaneously [51, 53–57].

## 8.5. Commercially available cell-stimulation devices

In vitro mechanical stimulation devices have been developed to apply specific mechanical stimuli to biomaterials and, in this way, stimulate cells, for example, as they would be stimulated by external cues typically observed in physiological conditions. Some tension and compression devices are available on the market, and the most well-known companies are FLEXCELL International Corporation, TA Instruments, CellScale, IonOptix, BISS, and Strex. Some features of their commercially available products, including the type of mechanical stimulus and the maximum strain and frequency that can be applied, are summarized in Table 8.2. Fig. 8.4 is a graphical representation of the maximum strain/displacement and frequency provided by the device models.

Table 8.2 - Summary of commercially available devices which apply tensile and/or compressive stresses.

| **Company** | **Product model** | **Stress type** | **Loading capacity** | **Maximum strain (%) or displacement (mm)** | **Maximum frequency (Hz)** |
|---|---|---|---|---|---|
| FLEXCELL International Corporation | FX-6000T Tension System | Uniaxial/biaxial tensile stress | | 33% | 5 |
| | FX-5000C Compression System | Uniaxial compressive stress | 62 N | | |
| TA Instruments | Biodynamic 5110* | Uniaxial tensile/compressive stress | 200 N | 6.5 mm | 20 |
| | Biodynamic 5170* | Uniaxial tensile stress | | | |
| | BioDynamic 5210* | Uniaxial tensile/compressive stress | | | 15 |
| | BioDynamic 5270* | Uniaxial tensile stress | | | |
| CellScale | MCB1 | Biaxial tensile stress | 10 N | 20% | 2 |
| | MCFX | Uniaxial tensile stress | 30 N | 12.5% | 0.5 |
| | MCT6 | | 200 N | >100% | 2 |
| | MCTR | Uniaxial compressive stress | 700 kPa | | 0.5 |
| | MCTX | | 100 N | 2 mm | 2 |
| | MCJ1 Bioreactor | Uniaxial tensile stress | 100 N | 25.4 mm | 2 |
| IonOptix | C-Stretch | Uniaxial tensile stress | | 20% | 10 |
| BISS | TE200 | | 200 N | 25 mm | 13 |

| | | | | | |
|---|---|---|---|---|---|
| | TE500 | Uniaxial tensile/compressive stress | 500 N | | |
| | TE40[a)] | | 40 N | 4.5 mm | |
| Strex | STB-1400 | Uniaxial tensile stress | | 20% | 1 |
| | STB-100 | | | | |
| | STB-150W | | | 30% | |
| | STB-190-XY | Biaxial tensile/compressive stress | | | |

[a)] The device also allows a pulsatile flow stimulation

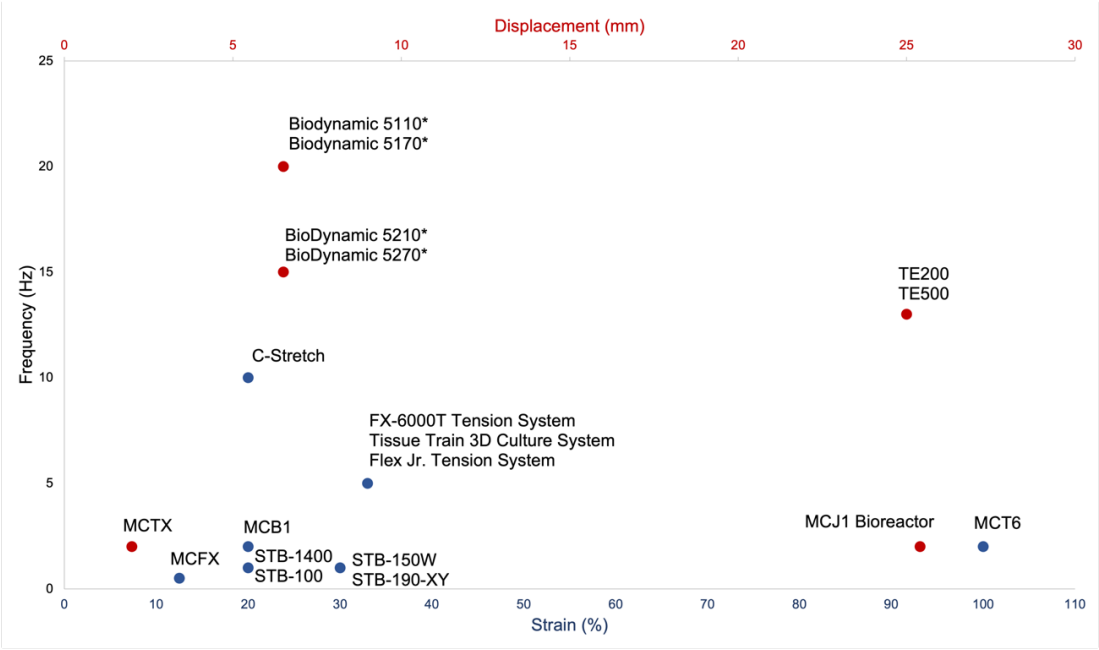



Figure 8.4 - Graphical arrangement of the commercially available mechanical stimulation devices according to their maximum strain/displacement and frequency.

Some of the commercialized devices may be used to evaluate a variety of specimens, including cells seeded in monolayers, 3D cell-seeded constructs (e.g., hydrogels), natural tissues, or bioartificial tissue samples. Stretching devices commercialized by FLEXCELL use regulated vacuum pressure and positive air pressure to deform flexible-bottomed culture plates. Depending on the type of culture plate, equibiaxial or uniaxial tension may be applied. Flexcell FX-2000 and FX-4000 created by FLEXCELL International Corporation, and recently upgraded to FX-6000 T, were used to promote tensile loading [58–61].

The Flexcell FX-2000 cell-strain unit is composed of a circular silicone rubber membrane at the bottom of each well of the culture plate, in which biaxial strain is regulated by applying vacuum, promoting a multi-radial uniform stretch. One group exposed flexor tendon cells to biaxial tensile strain of 0.0075% at 1 Hz and analysed the formation and organization of the actin stress-fibre network and cell–cell adherent junctions under loading [58]. In another study, the same Flexcell unit was used to apply an equibiaxial cyclic strain of 3% at 0.25 Hz (2 s on, 2 s off) to human mesenchymal stem cells (hMSCs) for 16 days, which decreased proliferation and stimulated matrix mineralization over unstrained cells (Figs. 8.5a–c) [59]. Human embryonic stem cells (hESCs) were cultured on BioFlex culture plates coated with Matrigel and exposed to a biaxial 10% membrane strain for 10 cycles/min using the FX-4000 device [61]. The mechanical strain inhibited hESC differentiation, but self-renewal was promoted compared to an unstrained control [61]. Porcine valve interstitial cells and bone-marrow-derived hMSCs (bm-hMSCs) were cultured on BioFlex culture plates and exposed to a biaxial (radial and circumferential) tensile strain of 7%, 10%, 14%, and 20% respectively at 0.6 Hz for 4 days [62]. The strain magnitudes, which were homogenously distributed throughout the membrane, had an impact on collagen production [62]. More recently, the FX-6000 T Tension System was used on vascular smooth muscle cells derived from human-induced pluripotent stem cells (hiPSCs-VSMCs) [63]. Uniaxial cyclic tensile strain of 2.5% at 2.75 Hz applied for a period of 48 hrs enhanced the expression of VSMC and ECM markers and also the formation of phalloidin, mostly in a perpendicular direction to the tensile loading direction [63]. A Flexcell FX-4000 strain unit was used by Sumanasinghe et al. to apply an uniaxial cyclic tensile strain to bm-hMSCs seeded on linear 3D type I collagen matrices [60]. Cyclic tensile strains of 10% and 12% at 1 Hz induced osteogenic differentiation compared to unstrained controls after 1 and 2 weeks, without osteogenic supplements [60].

Commercialized by IonOptix, C-Pace EM is a multi-mode electromechanical stimulator which can be coupled to the C- Stretch system. This stimulator was used to apply electrical, mechanical, and combined electromechanical stimulation to human-induced pluripotent stem-cell-derived cardiomyocytes (hiPSC-CMs) cultured on fibronectin-coated PDMS [64]. A uniaxial cyclic tensile strain of 5% was applied at 1 Hz for 3 or 7 days and, with regard to electromechanical stimulation, cells were also stimulated with an electrical field of 3 V/cm and 4 ms biphasic pulse duration at the end of the mechanical stimulus hold phase to mimic the isovolumetric contraction. All three stimulus modes resulted in stress-fibre formation and sarcomeric length shortening, but upon

electromechanical stimulus the transmembrane calcium current significantly decreased (Figs. 8.5d and 8.5e) [64].

A BioDynamicTM chamber mounted on an ELF3200 mechanical testing machine from the TA Instruments group was used in compressive loading studies [65, 66]. Five per cent global strain was applied by cyclic compressive loading (for 2 h on day 9 and then every 5 days up to and including day 19) to hMSCs cultured in 3D polyurethane (PU) scaffolds, and was found to promote osteogenic differentiation and mineralized matrix production [65]. MLO-A5 osteoblastic cells cultured on PU open-cell foam scaffolds were exposed to a compressive strain of 5% at 1 Hz (for 2 h per day on days 5, 10, and 15 of culture), which promoted the production of mineralized matrix (Figs. 8.5f–h) [66]. Endothelial progenitor cells (EPCs) isolated from rat bone-marrow were seeded in demineralized bone matrix (DBM) scaffolds under cyclic compressive loading. Cell-based constructs were placed in a BioDynamic ELF5110 device, and after being subjected to 5% strain at 1 Hz for 4 h/day for 7 days, proliferation of EPCs increased [67].

Cell tensile loading systems from Strex are reported in the literature for diverse purposes, including the evaluation of cell adhesion and mechanotransduction studies. Meniscal root and horn cells were cultured on rat tail COL1-coated polydimethylsiloxane and subjected to 2 hrs and 4 hrs treatment with 5% and 10% uniaxial cyclic tensile strain at 0.5 Hz, using a STB-140 system. The density of both root and horn cells was reduced after mechanical treatment, whereas expression of the chondrocyte-associated genes SOX9 and COL2A1 was significantly enhanced [68]. Using the same loading system, mouse primary chondrocytes were seeded into silicon stretch chambers coated with fibronectin, and after 48 hrs were subjected to cyclic tensile loading (0.5 Hz, 10% elongation) for 30 min in a $CO_2$ incubator. The excessive loading accelerated osteoarthritis development by inducing gremlin-1 (Figs. 8.5i and 8.5j) [69]. In a different study, Murali et al. seeded hMSCs onto silicone chambers coated with COL1 and subjected them to tensile loading at 1 Hz frequency and 8% strain for 6, 24, 48, and 72 hrs, using the ST-140 model. They suggested that when subjected to uniaxial loading, hMSCs underwent tenogenic differentiation through activation of epithelial sodium channels [70]. Takahashi et al. seeded normal human lung fibroblasts onto silicon chambers coated with COL1, and a uniaxial sinusoidal cyclic tensile loading of 30 cycles/min was applied for 10 min using the ST-140 model. The concentrations of ATP in the supernatant were significantly elevated by 20% strain, but not by 4% strain. The researchers also visualized ATP release during cell stretch in real time, using the NS-600 W model. Following a single uniaxial tensile strain of 22% for 1 s duration, the release of ATP continued and increased

in intensity [71] Besides application of tensile or compressive stresses, all models of TA Instruments presented in Table 8.2 include pulsatile stimulation. For example, the BioDynamic 5170 and BioDynamic 5270 test instruments permit a flow range of 17–1760 mL/min. These devices are computer-controlled, allowing a static, cyclic, or intermittent deformation in a range of frequencies, amplitudes, and waveforms. The substrates used for culture plates of commercialized mechanical stimulation devices are typically flexible and light-transparent materials that enable phase-contrast, fluorescence, or scanning confocal microscopy analysis. The design and material choices allow, in some cases, simultaneous and real-time visualization using inverted microscopes. While these are often preferred to upright microscopes because they do not limit the total height of the device, it is mandatory to ensure that the focal length is not compromised. Despite the notorious progress on the tensile and compressive loading devices available on the market, the main motivation for research groups to design and fabricate their own devices is related to these device-associated costs. The cost of these devices ranges from thousands to tens of thousands of dollars, and the total price may increase when considering maintenance and the need to purchase additional device-specific accessories (such as culture well plates) in order to maximize the number of samples that can be tested at the same time [3]. Moreover, the macroscopic dimensions of some devices limit their throughput, and it is usually difficult or impossible to adapt to particular experiments such as, for example, using other substrate materials than polymers, which restricts the utility of these devices in a research context [3, 51, 52, 72].

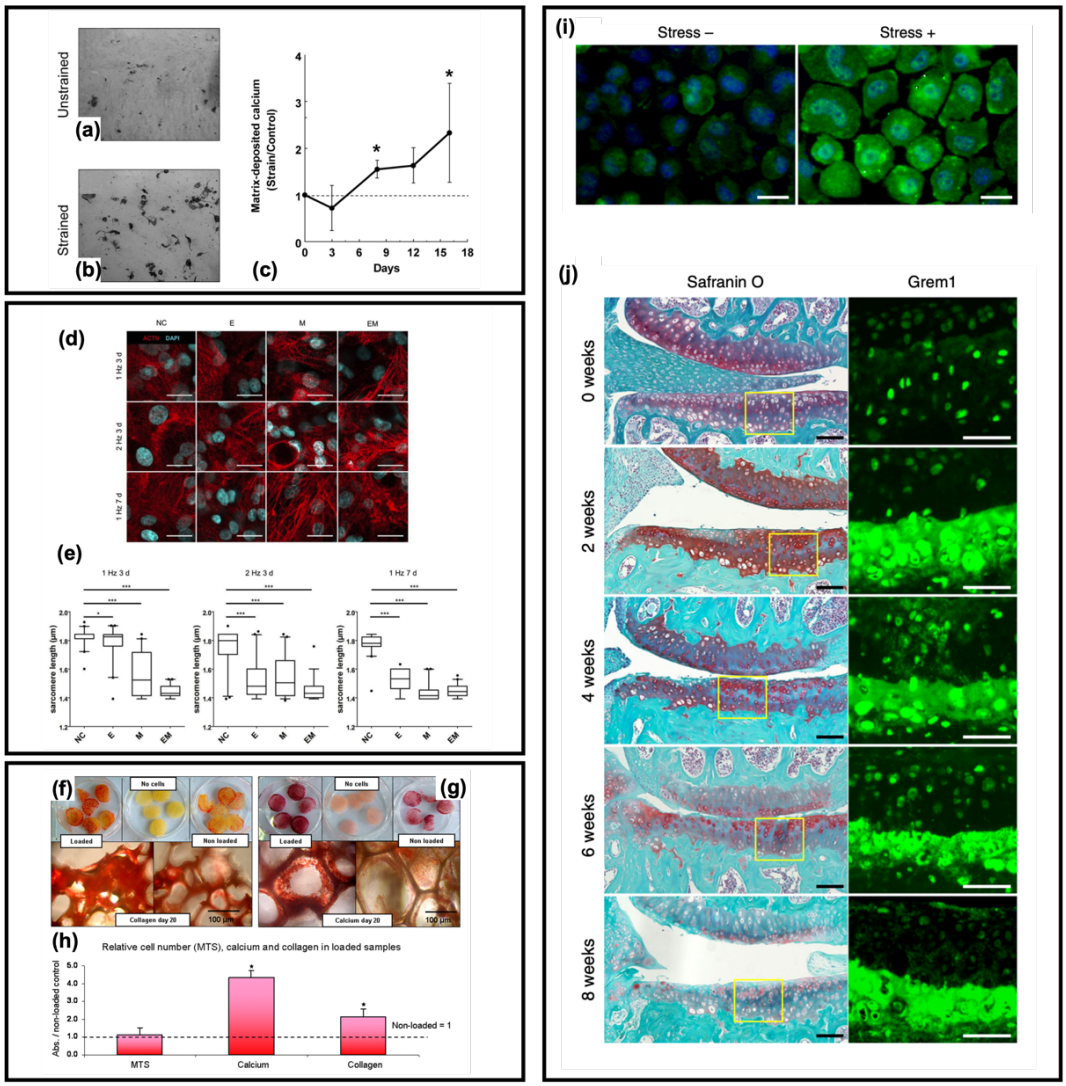



Figure 8.5 - Cellular results of studies which made use of commercially available devices. Von Kossa staining of cell layers after 16 days in culture showed that compared to the unstrained condition (a), hMSCs that underwent mechanical strain imposed by Flexcell FX-2000 had greater matrix mineralization (b), as corroborated by measurement of matrix-deposited calcium (c) (reproduced from [59], Copyright 2003, with permission from Elsevier). d Sarcomere length analysis by actin (ACTN, red) and nuclei (DAPI, cyan) staining of samples: non-conditioned (NC), electrically conditioned (E), mechanically conditioned by an IonOptix C-stretch (M), and electromechanically conditioned (EM) (scale bar: 25 mm). Results for different conditioning procedures (1Hz 3d, 2Hz 3d, and 1Hz 7d) are shown in a boxplot (e) (reproduced from [64], Copyright 2017, with permission from Elsevier). Empty and non-loaded scaffolds were loaded by a TA Instruments BioDynamic device coupled with an Electroforce testing machine, then cut into cross sections and stained with Sirius red (for collagen) (f) and alizarin red (for calcium) (g). Absorbance of MTS (for cell-viability assessment), alizarin red, and Sirius red per loaded scaffold at day 20 was normalized to a paired non-loaded scaffold (mean±SD) (h), and showed an increase of matrix mineralization after loading (reproduced from [66], Copyright 2009, with permission from Elsevier). (i) Expression of gremlin-1 (Grem1) protein (green) in mouse primary chondrocytes increased 24 hrs after tensile stress loading (stress+) was applied with the Strex STB-140 system, compared to the unloading condition (stress–) (scale bar: 50 μm). (j) An acceleration of mouse osteoarthritis development after surgical induction was observed through safranin O staining and gremlin-1 immunofluorescence. Scale bars: 100 μm and 50 μm, respectively (reproduced from [69] authored by Chang et al. under the Creative Commons license CC BY 4.0). hMSCs: human mesenchymal stem cells.

## 8.6. Custom-built cell-stimulation devices

Despite the focus on continuous innovation, mechanical stimulation systems available on the market present critical challenges. Consequently, numerous research groups have designed and developed custom-built devices to study the effects of tensile and compressive loading conditions on cellular behaviour.

### 8.6.1. Tensile loading devices

Several tensile loading devices with different designs and working principles have been developed in recent years. Table 8.3 lists uniaxial tensile loading studies in which devices were custom fabricated to meet research groups' needs. The tensile loading working principles were divided into four major groups: four-point bending apparatuses, linear sliding rake systems, clamped samples connected to a tensile device, and vacuum-actuated tensile devices, as represented in Fig. 8.6. The tensile loading devices designed by research groups are graphically arranged in Fig. 8.7, according to the maximum strain/displacement and frequency under study.

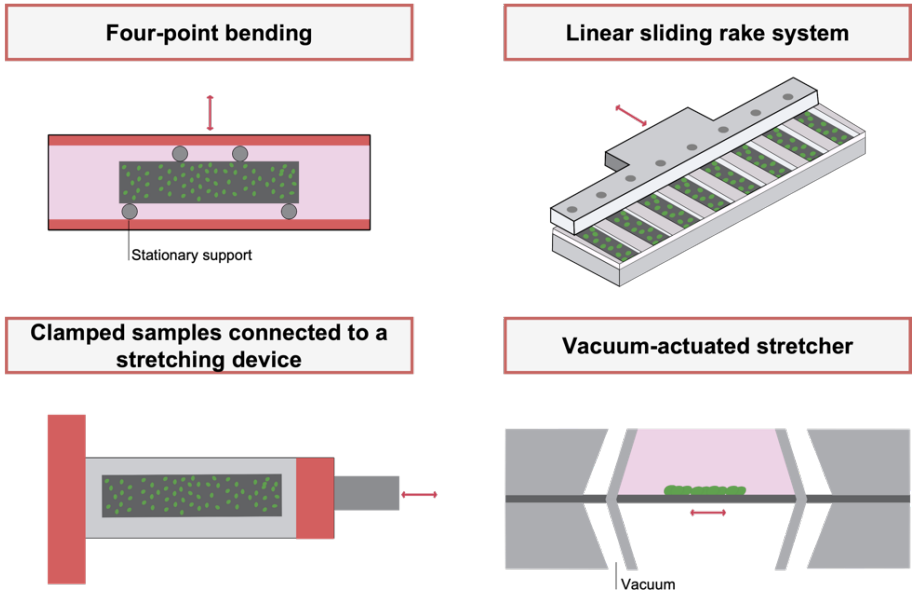



Figure 8.6 - Representation of four tensile working principles. In the four- point bending apparatus, the cell-based construct is supported by stationary supports and strain is distributed in the perpendicular plane to the applied load. However, the strain magnitude is not distributed uniformly between these horizontal planes because it increases from the central horizontal axis to the external medial and lateral faces (which are subjected to maximum tensile and compressive strains, respectively) [73]. Constructs can also be placed in cages and fixed at two opposite ends: one rigidly and the other to the rake attachment. The linear sliding rake is then controlled at the desired frequency and amplitude. Cell-based samples can also be clamped and connected to a tensile device (one end of the rectangular membrane is fixed while the other is connected to a computer-controlled movable frame). Finally, polymeric substrates may be exposed to uniaxial tensile loading with a vacuum-actuated tensile device. The movement imposed by the tensile loading device is represented by the red arrow.

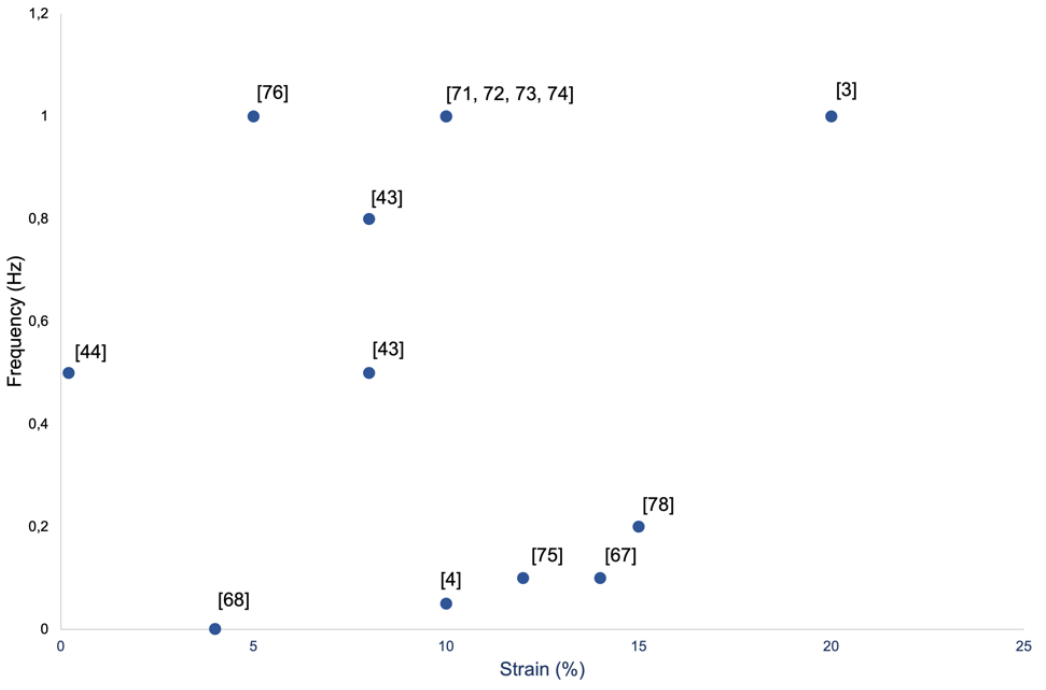



Figure 8.7 - Graphical arrangement of the devices designed and produced by research groups according to the maximum tensile strain/displacement studied at a particular frequency. Observation: despite the fact that Subramanian et al. [57] applied 2% uniaxial tensile strain to cells encapsulated in collagen constructs, the device used in this study may operate at a loading strain up to 12% at cyclic frequencies of 0.01–1 Hz.

The majority of tensile loading devices involve cell culture on a circular flexible membrane (fixed along its periphery) or rectangular flexible membrane (fixed at opposite ends) (Fig. 8.7). Some of the results obtained by the studies mentioned in Table 8.3 are summarized in Fig. 8.8.

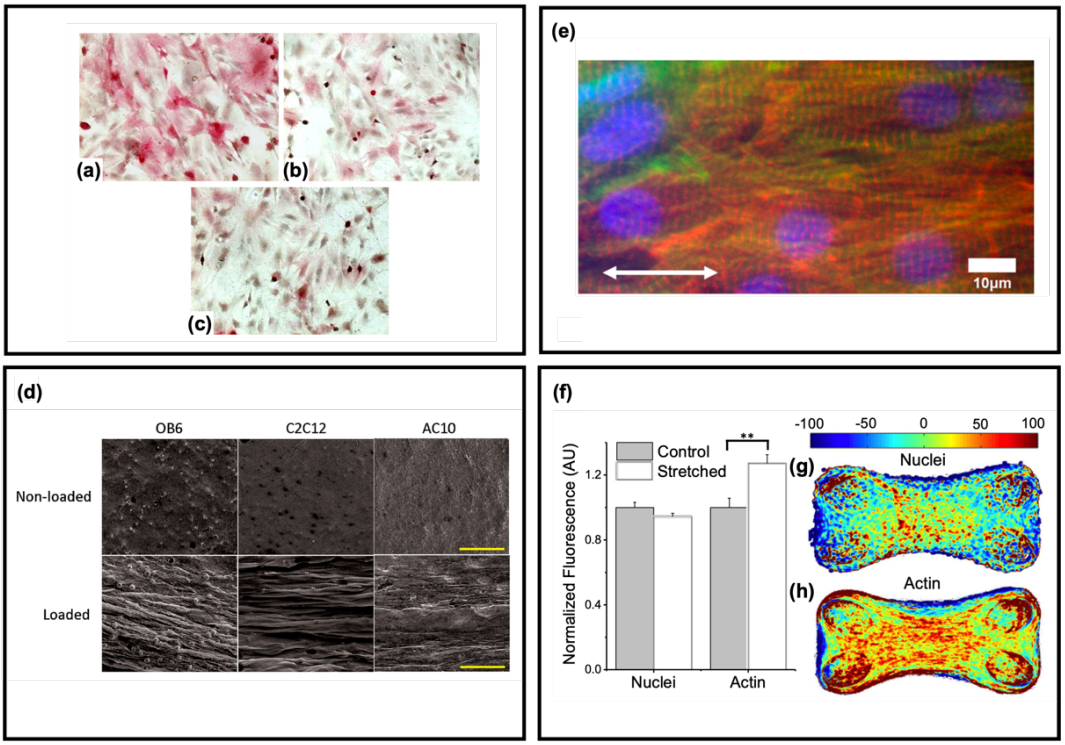



Figure 8.8 - Results of studies performed with customized tensile loading devices. ALP staining at 24 hrs was higher for cells subjected to mechanical loading by a four-point bending device (a) compared to unstretched cells (b) and control cells (c) (reproduced from [43], Copyright 2008, with permission from Elsevier). (d) Scanning electron micrographs of 3D collagen constructs encapsulated with OB6, C2C12, or AC10 cells at day 3 either loaded by a linear sliding rake system or non-loaded (scale bar: 100 μm) indicated that the fibre orientation of loaded cells was parallel to the axis of load application (reproduced from [57], Copyright 2017, with permission from Wiley). (e) Staining of actin (green), sarcomeric z-lines (red), and nuclei (blue) of cardiomyocytes cultured on clamped samples connected to a tensile device revealed that after being subjected to 6 hrs of cyclic uniaxial tensile loading, the cells aligned in the direction of loading (white arrow) (reproduced from [3], Copyright 2018, with permission from ASME). (f) No significant differences in the average normalized total fluorescence of nuclei were found between non-stretched (control) and stretched groups, but F-actin fluorescence significantly increased with loading performed with a vacuum-actuated tensile device. The spatial distribution of per cent change between stretched and control average nuclei (g) and F-actin fluorescence (h) showed that expression of F-actin increased after tensile loading (reproduced from [52], Copyright 2018, with permission from Springer Science Business Media, LLC, part of Springer Nature)

Table 8.3 – Loading features of the uniaxial tensile loading applied by the custom-built devices to the cell-based constructs, grouped by the device working principle.

| **Device working principle** | **Loading capacity** | **Maximum strain (%) or displacement (mm)** | **Frequency** | **Experiment duration** | **Cell-based construct** | **Ref** |
|---|---|---|---|---|---|---|
| Four-point bending apparatuses | 2 N | 0.2 mm | 5 mm/min | 250 cycles every 24 hrs for 16 days | Human bm-MSCs on DMB scaffolds | [74] |
| | | 0.2% | 0.5 Hz | 40 min at 0, 0.5, 1, 2, 6, 12, and 24 hrs | Rat bm-MSCs on flexible silicon-bottomed chambers | [43] |
| Linear sliding rake system | | 0%–10% | 1 Hz | 48 hrs and for 68 hrs | Bovine articular chondrocytes and MFC seeded on fibrin hydrogels | [53] |
| | | 10% | 1 Hz | Short (24 hrs) or extended (1–2 weeks) periods | Calf bm-SC-seeded fibrin hydrogels | [54] |
| | | 10% | 1 Hz | 3 hrs followed by 3 h without loading for 21 days | Human bm-SC encapsulated on PEG-based OPF hydrogel | [55] |
| | | 10% | 1 Hz | 10–120 min and for 10 min every 6 hrs for up to 6 days | Human bm-MSCs cultured in collagen-CG scaffold | [56] |
| | 1–3 N | 2% | 0.1 Hz | 1 h/day for 3 days | Human cardiomyocytes AC10, murine myoblasts C2C12, and murine osteoblasts OB6 encapsulated in collagen constructs | [57] |
| Clamped samples connected to a tensile device | | 5% | 1 Hz | 4 hrs for 2 days | Wistar rat MSCs cultured in porous CG scaffold | [75] |
| | 2.5 N | 4% grip-grip | 0.001 Hz | 30 min/day for 3 days | Mouse-derived MSCs seeded on PEUUR coated with fibronectin | [51] |

| | | | | | | |
|---|---|---|---|---|---|---|
| | | 2% and 8% | | Three times 2 hrs/day for 3 days | Human bm-MSCs on elastic silicone | [76] |
| | 9.81 N | 10% | 0.05 Hz | 720 cycles/day for 3 days | Murine MSC encapsulated in collagen type I sponges | [4] |
| | | 10% | 1 Hz | 18 hrs | Mouse bone-marrow-derived macrophages cultured on fibronectin-coated silicone | [3] |
| | | 20% | 1 Hz | From 0.5–1 h after seeding to 6.5–7 hrs after seeding | Neonatal rat ventricular myocytes cultured on fibronectin-coated silicone | |
| Vacuum-actuated tensile device | | 0%, 3%, 7% and 14% | 0.1 Hz | 2 days under loading, 2 days under static and then 2 days under loading | NIH3T3 cultured on PDMS | [52] |
| | | 1.5%, 3%, 8% | 0.5 Hz | 1, 2, and 7 min (respectively) | hi-PSC-CMs cultured on PDMS | [42] |
| | | 8% | 0.8 Hz | 2, 4, or 7 days | | |
| | | 5%–15% | 0.2 Hz | 5 hrs and 5 days (short and long-term, respectively). | Human alveolar epithelial cells and human pulmonary microvascular endothelial cells cultured on opposite sides of the PDMS membrane | [77] |

Substrate: demineralized bone (DMB); oligo(poly(ethylene glycol) fumarate) (OPF); poly(ethylene glycol) (PEG); collagen-glycosaminoglycan (CG); poly(ester urethane urea) (PEUUR). Cells: meniscal fibrochondrocytes (MFC); stromal cells (SC); human-induced pluripotent stem cells-derived cardiomyocytes (hiPSC)

Application of cyclic uniaxial (one direction) tensile strains sometimes leads to a heterogeneous biaxial strain profile, due to the Poisson effect. Therefore, custom-designed devices were developed to modulate equiaxial strains and generate a homogeneous strain environment [32, 44, 78, 79]. Other groups focused on reproducing a more complex physiological environment by applying biaxial strains [80, 81]. Tensile loading was also performed using piezoelectrically actuated pins of a Braille display [72]. Briefly, an elastomeric membrane of PDMS containing microwells was placed on top of an actuated pins array and deformed by the Braille pin movement. Each pin was independently computer-controlled and responsible for applying a cyclically radial strain (maximal 20%–25% radial and 12% tangential). Mouse myogenic C2C12 cells and human dermal microvascular endothelial cells (HDMECs) aligned to the loading direction at increasing frequencies of 0.2, 1, and 5 Hz, after 2, 4, and 12 hrs, in contrast to human lung adenocarcinoma epithelial A549 cells, which did not respond to tensile loading (Fig. 8.9) [72].

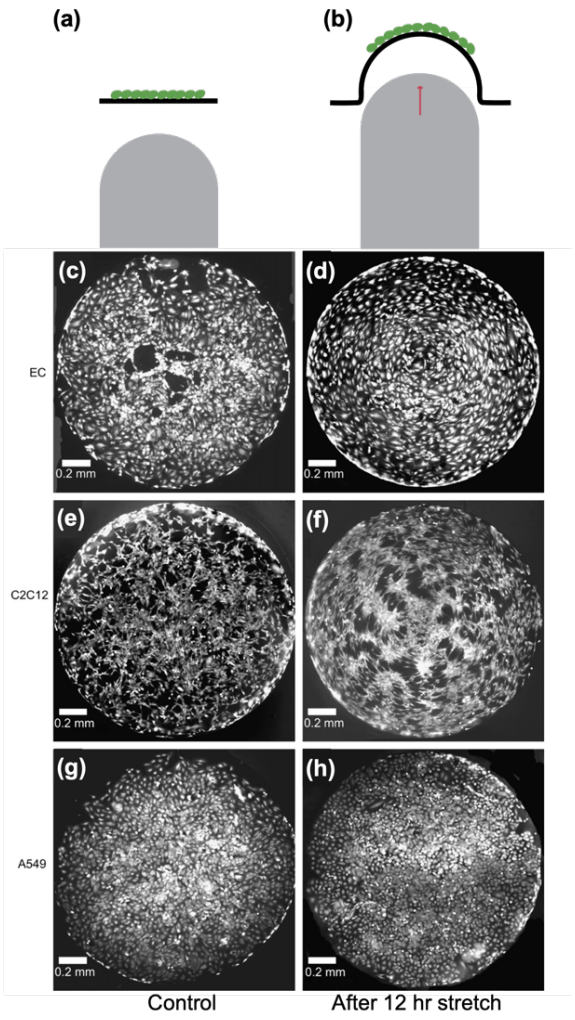



Figure 8.9 - Schematic representation of the cross section of cells (represented in green) cultured on flexible membranes (a) and the deformation of the latter as the pin moves upwards (b). The alignment of C2C12 and HDMECs in response to loading is

illustrated by fluorescent images of HDMECs (c, d), C2C12 myoblast cells (e, f), and A549 alveolar epithelial cells (g, h) stained with Calcein AM before loading (left column) and after being subjected to cyclical tensile loading (5 Hz for 12 hrs) (right column) (reproduced from [72], Copyright 2008, with permission from Elsevier). HDMECs: human dermal microvascular endothelial cells.

### 8.6.2. Compressive loading devices

Microfabricated devices have been developed to apply compressive strain to cell-encapsulated constructs. Typically, the compression is achieved by loading pistons actuated by a pneumatic system. This type of compressive device can generate three types of compression: unconfined, semi-confined, and confined, all of which are illustrated in Fig. 8.10.

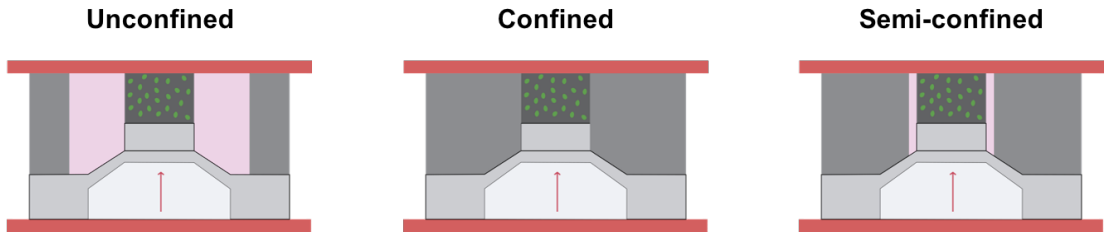



Figure 8.10 – Illustration of compression models: unconfined compression, confined compression, and semi-confined compression. The three-dimensional cell-based construct is compressed by the movement of a piston, in this case as a result of pressurized air (represented by the red arrow).

Unconfined compression was studied in the majority of compressive loading studies, as it represents the simplest microfabrication technique. One device was designed to study the influence of dynamic 10% compressive strain at 1 Hz for up to 3 weeks on chondrogenesis of goat bm-MSCs encapsulated in poly(ethylene glycol) diacrylate (PEGDA) hydrogels, as well as human embryonic body-derived (hEBd) cells encapsulated in tyrosine-glycine-aspartate-serine (YRGDS)-PEG-acrylate hydrogels [82]. The expression and synthesis of chondrocyte-specific matrix molecules were also studied, under the same loading conditions, with bovine bm-stromal cells encapsulated in agarose gels for 8 and 16 days [83]. Another group investigated the role of cyclical unconfined compression on osteogenesis by applying 10% and 20% compressive strains at 0.5 Hz for 4 hrs on rat pre-osteoblasts seeded into electrospun polycaprolactone (PCL) scaffolds [84]. Only the 10%-magnitude strain induced expression of osteogenic-related proteins and transcription factors, showing that elevated magnitudes may inhibit bone formation [84]. Ravichandran et al. designed a custom-fabricated device to apply a range of compressive strains to four independent chambers. hMSCs were seeded on polycaprolactone-$\beta$ tricalcium phosphate (PCL-TCP) scaffolds using fibrin gel and then exposed to 0.22%, 0.88%, and 1.1% compressive strain at 1 Hz, 4 hrs/day for 4 weeks [85]. Cyclic physiological compression of 0.22% resulted in higher ALP activity compared to supra-physiological strains; it also up-regulated osteogenic markers and generated high mineralization

levels [85]. C3H10T1/2 mouse MSCs were encapsulated in PEG hydrogels and exposed to 6%, 11%, 14%, and 26% compressive strains. Regardless of the strain magnitude, there was no significant difference in nuclear deformation, whereas cellular deformation only changed significantly at the highest strain levels [86]. The device proposed by Moraes et al. [86] consisted on an array of loading posts suspended over actuation cavities and was adopted and altered by Lee et al. to subject alginate-chondrocyte constructs to compressive strain [87]. These constructs were placed on PDMS balloons with different diameters and by varying only the cavity diameter (with the applied pressure remaining the same), it was possible to create a range of compressive strains. Because the balloons were inflated with pressurized air, compression on constructs was studied either in a static (14 kPa, 1 h) or dynamic (14 kPa, 1 Hz, 1 h) mode. Lee et al. found that the mean strain of chondrocytes was approximately 50% of the gel strain, with a permanent deformation of 9%–30% for static compression, and 0.5%–6% for dynamic compression. Finally, cell viability was found to be higher in dynamically loaded constructs, perhaps due to better nutrient transport [87]. Despite these findings, unconfined compression generates a heterogeneous strain distribution within the 3D construct. In contrast, confined compression generates a uniform strain, but challenges arise concerning its microfabrication. Semi-confined compression offers easier microfabrication, but uniform strains are only achieved in the central region of the biomaterial. These findings were obtained from the finite-element simulations (represented in Fig. 8.11), and the obtained strain fields for the three compression modes were compared [88].

The same group fabricated a semi-confined compression device, which was used to generate nominal strains of 20%, 30%, 40%, and 45% on PEG and collagen hydrogels. The authors concluded that this compression model enables the study of cellular responses to precisely applied strains on a range of polymerizable biomaterials, improving the applicability and versatility of the device [88]. Zhang et al. [89] used a custom-designed dynamic-compression loading system with a stepper motor to apply a 10% compressive strain on PCL scaffolds encapsulated with hMSCs. PCL-based constructs subjected to both mechanical and biochemical stimulation supported a chondroprotective effect [89].

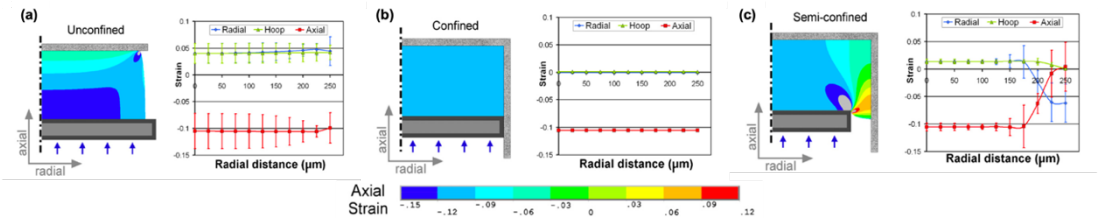



Figure 8.11 - Finite-element simulations of three compression modes all involved application of 10% compressive strain on PEG hydrogel (adapted from [88], Copyright 2011, with permission from IOP Publishing Ltd). Strain field within the hydrogel was generated for unconfined (a), confined (b), and semi-confined (c) compression modes and the radial, circumferential, and axial strains (mean and standard deviation) were plotted for the total axial thickness of the hydrogel.

## 8.7. Review of patents

Given the promising outcomes from engineered mechanical stimulation devices in mechanobiology studies like those described above, many patent applications have been filed in the past few decades. We looked at both granted patents and patent applications, and conducted our research through the Derwent Innovation Index [90] and Google Patents [91] databases, which include European, USA, and World Patents (WIPO—World Intellectual Property Organization). The keywords were related to mechanical cell stimulation and resulted in a total of 369 records. We excluded inventions whose descriptions could not be automatically translated to English, those with unclear abstracts, and those not within the scope of this review.

A total of 44 patents of devices able to create different stimuli (tensile, compressive, shear stresses, and vibration) were comprehensively studied and selected, taking into account their in vitro cellular purposes. Table 8.4 summarizes the selected inventions. They are organized first by frequency level (low to moderate vs. high frequency), then by actuator type, as schematically illustrated in Fig. 8.12, and finally by the imposed stress state. Inventions that obey non-conventional actuation principles are in a separate category.

Table 8.4 - Overview of inventions related to mechanical stimulation of cells.

| Frequency | Actuator type | | Stress state | Patent number | Publication year | Description | Observation | Ref |
|---|---|---|---|---|---|---|---|---|
| Low to high | Pneumatic | Pressure | Radial/equiaxial | WO 2,009,039,640 A9 | 2009 | A positive pressure is delivered to several actuation devices, generating tensile strains in the range of 0%–200%. | Each actuation device can also be connected to vacuum to apply compressive strains in the range of 0%–80%. | [92] |
| | | Vacuum | | US 4,839,280 | 1989 | Individual vacuum ports are affixed beneath each well base and the elongation of the membrane can be constant or cyclic, or may be irregular or applied in a pattern, as desired. | A flow means disposed between the plenum and vacuum source is a solenoid valve electrically connected to a computer. | [93] |
| | | | | US 10,246,676 B2 | 2019 | Vacuum pressure is applied to the cell-containment part, the bottom surface of which is made of flexible polymer material. | | [94] |
| | | | Equibiaxial, uniaxial, or | US 6,472,202 Bl | 2002 | A central opening defined in the planar member allows a vacuum to be drawn through and to pull a | | [95] |

| | | | | | | | |
|---|---|---|---|---|---|---|---|
| | | other stretching direction | | | portion of the flexible membrane downward. | | |
| | | Equiaxial | US 2013/0059324Al | 2013 | Below the flexible membrane is a pin plate (one pin per well) that applies compressive or tensile loading to the membrane bottom. | The mechanism to actuate the pins can include a mechanical linear actuator (e.g. a non-circular shaft coupled to a movable support) or electromagnetic system. | [96] |
| | | | US 2015/0050722Al | 2015 | The cell-culture plate is operatively coupled to a plenum device. | The device may also deliver electrical stimulation. | [97] |
| Hydraulic pressure | | Equiaxial | DE102009057698A1 | 2011 | A porous carrier membrane with an elastic breaking strain of 20%–100% separates two reactor part volumes (one filled with liquid cell culture and the other with gas atmosphere). | The support membrane is deformable through a pneumatic and/or hydraulic control device and volume, which is implemented as two magnet valves | [98] |

| | | | | | | |
|---|---|---|---|---|---|---|
| | | | | | and/or as a reciprocating piston.<br>Frequency in the range of 0.001 to 200 Hz. | |
| Hydrostatic pressure | | US 8980624 B2 | 2015 | A fluid pressure device supplies a pressurized fluid to the pressure chamber to deform the membrane and move the pressurizing member downward in each culture chamber, thereby exerting a mechanical compression force on cells. | | [99] |
| | | US 9,303,244 Bl | 2016 | A piston moving in and out of a cylinder generates pressures at high physiological levels up to at least 10 MPa. | The device may be configured to generate negative pressure or vacuum, wherein the chamber further includes a bleeding passageway for passing air or the gas. | [100] |
| | | US 2020/0339936 Al | 2020 | A magnetic component drives the moving component to shift between a | | [101] |

| | | | | | | |
|---|---|---|---|---|---|---|
| | | | | non-pressurizing and pressurizing position, and the moving component moves toward the bottom chamber surface and pressurizes the cell sample. | | |
| | | WO 2009/047045 A2 | 2009 | Actuating means comprise at least one first piston responsible for pressurization of the culture liquid contained in the sideways chamber, generating compression. | The device may also apply constant or cyclic direct compressive and shear stresses upon perfusion and simultaneous hydrostatic pressure and shear stress. | [102] |
| Motor-driven | Uniaxial | CN1834220A | 2006 | A stepper motor is connected to a leading screw and a pressure baffle plate which squeezes the test sample to within the 50-300 mN range. | | [103] |
| | | WO 2017/152080 Al | 2017 | The mechanical loading system comprises one fixed plate and at least one movable plate, each having several pins for holding at least a portion of the tensile loading chamber. The driving mechanism is | No gripping is required, so there is no risk of disintegration of mechanically fragile scaffolds | [104] |

| | | | | | | | |
|---|---|---|---|---|---|---|---|
| | | | | | configured for moving the movable plate in a uniaxial direction toward and away from the fixed plate. | during the fixation process. | |
| | | | WO 2013/090738 A9 | 2013 | A linear actuator bears against the specimen, which may be supported in a Petri dish, generating axial compression. | | [105] |
| | | | CN101372664A | 2009 | A motor driving bar is coupled to one extremity of the tissue to be cultivated and used to generate axial tensile and compressive stresses, and rotation. | | [106] |
| | | | CN102433258B | 2012 | The cell-culture material is fixed on a fixed support and a sliding support is connected to a stepper motor, generating tensile loading. | Also establishes electrical stimulation (constant voltage, pulsed voltage, or DC micro-electric stream). | [107] |
| | | | CN103966094A | 2014 | Elongation of the membrane is achieved with a cytoskeleton self-clamping module, in which one end is fixed and the other is moved. | | [108] |
| | | | US 2012/0100602 Al | 2012 | A sliding arm applies mechanical displacement in a predetermined | The sliding arm is connected to an | [109] |

| | | | | | | | |
|---|---|---|---|---|---|---|---|
| | | | | | direction, generating tensile, compressive, or a hybrid of both stresses. | actuator that can be powered by a high-precision stepper motor. | |
| | | | US 9617507 | 2017 | Several culture dishes are mounted to a fixed support and to a movable support by mounting posts, which are connected to a stepper motor coupled to tensile output (Frequency: 0.010–10 Hz; Stretch: 0%–50%). | The tensile output can drive one or more solenoids to provide a range of motion for the moving support. It also allows electrical stimulation (Frequency: 0.010–99 Hz; Pulse duration: 0.4–24 ms; Voltage: ±40 V and 240 mA). | [110] |
| | | | US 10,421,955 B2 | 2019 | | | [111] |
| | | | US20180164278A1 | 2018 | A three-dimensionally designed support structure admits the cell culture and is subjected to tensile or compression forces by actuators attached to the holding rack. | At least one of the actuators and/or counter-actuators is a piezo actuator, an electrothermal or electrically active | [112] |

| | | | | | | | |
|---|---|---|---|---|---|---|---|
| | | | | | | polymer actuator, or an electromechanical, electrochemical, magneto-strictive, hydraulic, pneumatic, bimetallic, or electromagnetic actuator. | |
| | | | WO 2011/013067 A2 | 2011 | Extension and relaxation of the substrate following translation of a rod controlled by a linear electric motor. The deformation and the force applied to the substrate can be controlled based on feedback control signals from the linear motor or from a load cell placed in the culture chamber. | It is possible to use an alternative motor or other driving system (these obtain an axial movement of the stem) or a hydraulic or pneumatic actuator (devices in which a piston is controlled by oil, compressed air, or another fluid). | [113] |
| | | | WO 2017/125159 Al | 2017 | A tensile strain of 5% to 10% is applied to the cell culture (frequency from 0.5 to 1.5 Hz). | Electrical pulses may be applied to cells having a | [114] |

| | | | | | | | |
|---|---|---|---|---|---|---|---|
| | | | | | Two magnets are placed outside the culture plates, one static, to fix one end of the silicone construct, and the other to pull the other end following a programmable pattern, thanks to a computer-controlled linear motor. | potential value from 10 mV/cm to 1000 mV/cm at a frequency between 0.5 and 1.5 Hz; | |
| | | | US 2012/0219981 Al | 2012 | Two engagement areas are located at opposite ends of the flexible substrate, and each is connected to a motor, such that either one end or both ends are stretched in opposite directions with respect to each other (up to 100% in its length from 0.5 to 10 Hz). | A voice-coil based motor may be used in the tensile system instead of a stepper motor to minimize heat generation during operation. | [115] |
| | | | CN101649291A | 2009 | Periodic or continuous dynamic tensile or compression loading can be applied to a plurality of cell-culture units simultaneously with a stepping motor. | | [116] |
| | | Biaxial | WO 2009/032174 Al | 2009 | Tuneable elastic gel substrates are disposed in multi-well plates and a ring-shaped punch indenter applies strain to the substrate, the characteristics of which are controlled by a motor assembly coupled to a control system. Lateral | The Z-drive motor can be a stepper motor or piezoelectric actuator; a lead screw connected to the bracket; or | [117] |

| | | | | | | |
|---|---|---|---|---|---|---|
| | | | | and longitudinal strains may be applied to the gel. | a linear or hydraulic piston. | |
| | Biaxial | US 5,348,879 | 1994 | A flexible membrane is secured and the displacement applicator (actuated by, for example, a cam) located below the membrane deforms the membrane. | | [118] |
| | | WO 2014/165056 Al | 2014 | A linear motor is operable to move the platen to cause one or more of the pistons to apply a mechanical force to the one or more wells with which the piston is aligned. | | [119] |
| | Radial | EP 1 679 366 A1 | 2006 | Substrate holding elements move away from the centre. | | [120] |
| | Uniaxial | US 2018/0216057 Al | 2018 | A cassette device to secure and expand the material with a linear actuator is connected by an arm to a first clip holder, and the scaffold response is measurable by the force measuring component. | A circuit board allows electrical stimulation. | [121] |
| | | US 2020/0199515 Al | 2020 | A flexible platform composed of three-dimensional walls made of PDMS coated with electrically conductive films of titanium and gold serves to stimulate cells that are | Allows simultaneous electrical stimulation. | [122] |

| | | | | | | |
|---|---|---|---|---|---|---|
| | | | | sitting on top of them, and their geometry and physical properties can be tailored to make them flexible (or rigid) enough to be bent by the range of forces applied by cells during contraction. One or two electrically controlled linear actuators provide reciprocating motion with a frequency of 0.5–5 Hz. | | |
| Magnetic actuation | Uniaxial | EP 1 428 869 A1 | 2004 | A magnetic body is attached to one end of the material and the material expands and contracts by electromagnetic force when the tensile stress is relieved. | Intermittent or gradual increase/decrease stress generation. | [123] |
| | | US 2008/0026419A | 2008 | An electromagnetic actuator transmits an upward directed force through a vertical piston to the culture dish, thereby providing controlled compression of a tissue sample. Loading frequency between 0.1 and 10 Hz. | Confined or unconfined compression. | [124] |
| | | US 2016/0032234Al | 2016 | Brackets attached to the flexible cell-culture pool accommodate a ferromagnetic element, extending the substrate. | Electrical stimulation can be applied either independently or simultaneously, by | [125] |

| | | | | | | | |
|---|---|---|---|---|---|---|---|
| | | | | | | placing a pair of electrodes at two opposing sides.<br>Several cell cultures may be stimulated by placing static magnets at the edge of each Petri dish and free magnets on the platform, which is movable by a mechanical arm coupled to a motor. | |
| | | | US 2021/0040427 Al | 2021 | Actuation platforms may use magnetism to induce minute movements between a fixed portion and actuated portion (both connected by a native ECM protein upon which cells can be cultured) thus imparting tensile strain. | The actuators may be a magnet or an electro-magnet, and may be made of a piezoelectric material or may be operably coupled to a hydraulic or pneumatic actuator. | [126] |

| | | | | | | | |
|---|---|---|---|---|---|---|---|
| | Fluid flow-induced shear stress | | CN103146574A | 2013 | A negative pressure generator provides flow-shear stress and mechanical tensile force to the cell culture. | | [127] |
| | | | US 8,852,923 B2 | 2014 | Fluid is passed through the passage at a Reynolds number lower than 2300 to achieve laminar flow through the passage, generating a shear stress of between 5.0 and 24 dynes/cm$^2$. | Movable and fixed anchors allow cyclic flexural and/or tensile stresses to be applied by an axial rod or axial rail, the movable one being connected to an actuator (a reciprocating motor, such as a linear motor). | [128] |
| Extremely high frequency | Piezoelectric actuator | | US 8,465,971 | 2013 | Longitudinal vibration (piezoelectric elements) is created with an external magnetic field.<br>Frequency of vibration is 100 MHz or lower. | | [129] |
| | | | WO2015167097A1 | 2014 | Ultrasonic elements create oscillation. | | [130] |
| | | | US 10,260,035 B2 | 2019 | | | [131] |

| | | | | | | | |
|---|---|---|---|---|---|---|---|
| Non-conventional principles of actuation | Laser (micro cavitation) | | US 2014/0100138A1 | 2014 | Generation of micro-cavitation bubbles using pulsed energy applies shear to cells. | | [132] |
| | Environmentally responsive | | US 2015/0093823Al | 2015 | Optically active micro-actuators allow one to fine-tune degrees and modes of tilting/bending, and local mechanical force is applied directly to cells. | | [133] |

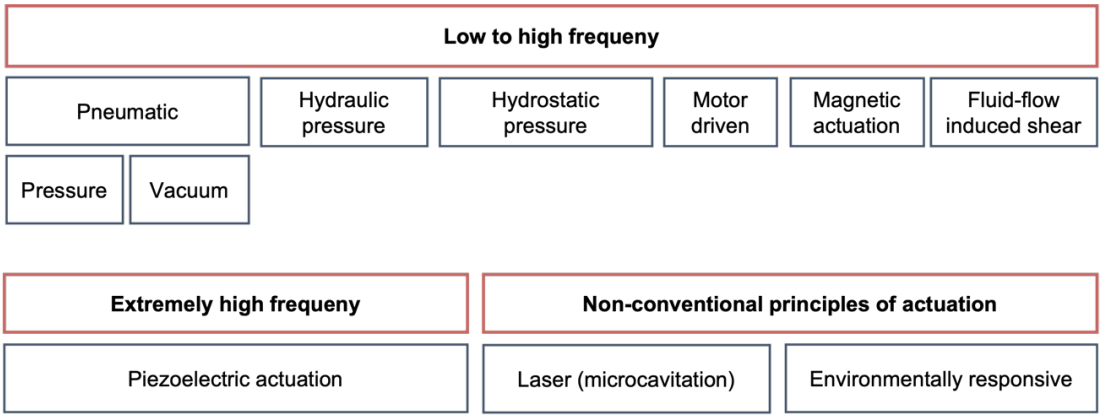



Figure 8.12 – Actuation principles of various mechanical cell-stimulation devices, divided by frequency level: low to high for values up to 200 Hz and extremely high frequency for values up to 100 MHz.

To better organize the resulting inventions, we grouped them according to their actuation principle. From low to high frequencies, the actuation may be pneumatic (either positive or negative pressure), motor-driven, or magnetic. However, some inventors disclosed more than one functionality principle. The invention of Sittampalam et al. [96] is a drug-screening device and system that attempts to impart strain to cells in a similar manner to physiological motion and rest. According to their description, different mechanical drive systems can be adopted to move the pins and thus exert mechanical strain on cells, including a linear actuator (Fig. 8.13a), an electromagnetic system, or a pneumatic system (Fig. 8.13b).

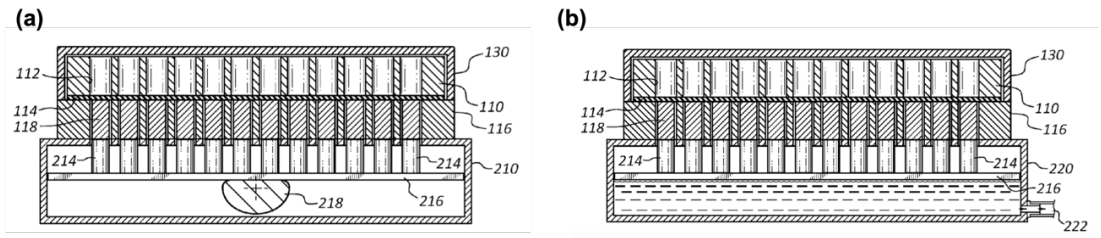



Figure 8.13 - The device of invention number US 2013/0059324 Al may be operated (a) by a mechanical drive mechanism, in which the rotation of a non-circular shaft (218) moves the movable support (216), thereby pushing the push members (214) in respect to the pins (118); or (b) by a pressurized mechanism (220), in which the change of fluid volume moves the support (216), imparting mechanical strain to the cells located in the wells (112). Illustrations from [96].

The device invented by Shapiro et al. [118], defined in Table 8.3 as belonging to the motor-driven category has, in fact, more than one approach to achieving membrane mechanical displacement (Fig. 8.14). The elastic membrane upon which the cell culture is placed is securely held in place and moved by a displacement applicator located, for example, on the bottom surface. Then, it is cyclically moved upward and downward by a force generator, deforming the membrane. This membrane deformation imparts biaxial forces (either tensile or compressive) to the cells

mounted thereon, and the strain profile may be either uniform or non-uniform. The electric motor drives an actuating apparatus, such as a cam (Fig. 8.14a), which revolves eccentrically about an axis, contacting the bottom surface of the rod and forcing the rod and displacement applicator to move upward to contact and deform the membrane. At the end of the upward stroke, the applicator moves to a lowered position out of contact with the membrane. The invention may also correspond to a mechanical actuated tensile apparatus which applies biaxial strain (Fig. 8.14b) or simultaneously applies tensile loading to several cell cultures (Fig. 8.14c). The removable and disposable wells are mounted above each available displacement applicator.

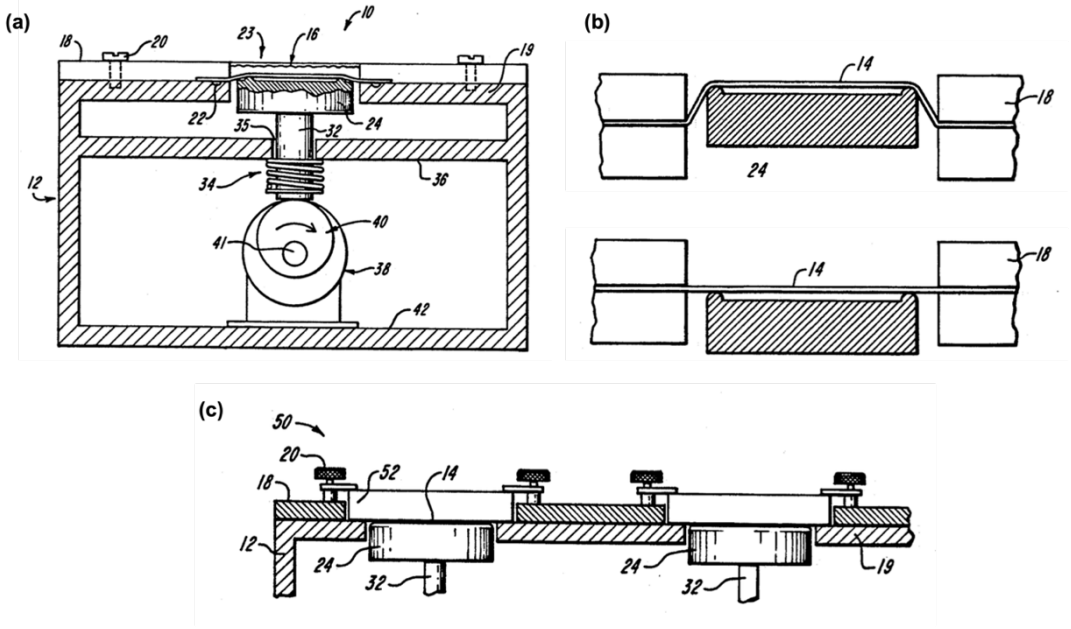



Figure 8.14 - Illustrations of invention number US 5,348,879 of Shapiro et al., with three different displacement applicators (represented in the drawing by 24). In (a), a cam deforms the membrane, in (b), the membrane is secured by plates and is deformed by the displacement applicator moving upward, and in (c), each well is mounted above the displacement applicator. Schematics from [118].

Substrate deformation through the pneumatic actuation principle may be achieved by pressure [92, 98] or vacuum [93–97], and by pulling a portion of the flexible membrane upward or downward, respectively. Despite the simple set-up, in both modes the stimulus frequency is low and may not even be capable of creating dynamic cycles. However, vacuum pumps are slower than pressure inlet. Other inventions aim to deform the membrane through pressurization of the fluid (e.g., culture medium) [99, 102], or by creating hydrostatic pressure using a piston [100]. If not carefully designed, moving the flexible membrane upward through a displacement applicator, by pressure or manually (e.g., with a piston), may cause friction between the membrane of interest and the loading post of the device, as represented in Fig. 8.15.

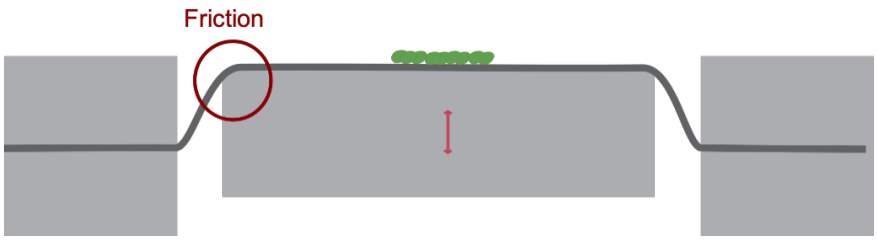



Figure 8.15 - The displacement applicator moves up and down, which may create friction between the flexible membrane and the loading post.

Hydraulic actuators are comprised of a hollow cylinder with a piston, and due to unbalanced pressure applied to the piston, a force is generated that deforms the membrane equiaxially. Although these actuators are often limited in terms of frequency, invention number DE102009057698A1 of Kiesow et al. [98] allows cyclic testing in a frequency range of 0.001 to 200 Hz.

Still, either in low- or high-frequency mode, the culture liquid in contact with the cells may be pressurized and the generated hydrostatic pressure then exerts a compressive mechanical force on cells.

The motor-driven mechanism involves the conversion of a rotary motion of an electric motor into linear displacement. The selected motor may be a stepper motor [103, 104, 106–111, 117], a linear DC motor [105, 113, 114, 119, 128], a servo motor [126], or a voice-coil motor [105, 115]. Stepper motors, which are composed of multiple toothed electromagnets, were preferred for some of these inventions. Despite the possibility of miniaturization, precise rotation (ranging from step angles through full 360° rotation), easy set-up and control, this type of motor is frequently slow due to a low transmission ratio (from rotational to linear movement). Moreover, it may cause small vibrations, which will act as an external disturbance to the system and thus should be considered separately from the substrate's deformation. Linear DC motors are two-wire continuous rotation motors with each pulse being so fast that the motor seems to be rotating constantly with no stuttering. Servo motors are also fast, with high torque, and can be precisely controlled because of their accurate rotation within a limited angle. This actuation principle is particularly suitable for uniaxial tensile loading and for larger engineered constructs. In addition, it allows multiple loading modes and precise control over the strain features, such as amplitude and frequency. On the other hand, some potential disadvantages are the risk of contamination and limitation of high-throughput capabilities [134].

The linear actuation principle may be preferable because it allows for automation, requires less maintenance, and offers a broader range of strain magnitudes, frequencies, and durations of mechanical stimulus. Invention number US10,421,955B2, assigned to IonOptix LLC in 2019 (Fig. 8.16), applies a tensile strain up to 50% (at 0.01–10 Hz) on a deformable rectangular culture dish made, for example, from silicone rubber [111]. A plurality of viewing ports is provided to enable cell culture observation by microscope and exchange of the culture medium, permitting long-term experiments to be performed.

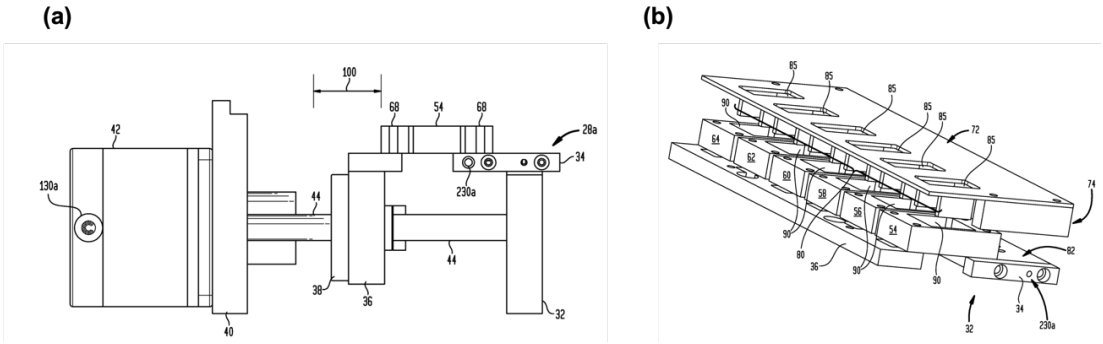



Figure 8.16 - Illustrations of invention number US10,421,955B2, assigned to IonOptix LLC. (a) is a side view of the electromechanical stage (28a) composed by a fixed support (32) and a moving support (36) connected to a stepper motor (42). (b) is a perspective view illustrating six culture dishes and supporting parts of the electromechanical stage. Figures from [111].

Muthiah et al. [115] developed a mechanical tensile device, invention number US 2012/0219981AI, with dimensions of 408 mm×150 mm (much larger than a 24-well plate). It is composed of two engagement areas located at opposite ends of a flexible substrate; each one connected to a movable element and a motor to promote opposite movements, as shown in Fig. 8.17. The device may include a temperature-control unit, such as a heating unit and/or a fan, to assure uniform distribution of heat and to maintain the temperature, a humidity reservoir unit, and a gas-control unit to control the gas parameters and supply. During or after tensile loading, the materials may also be imaged using a microscope base plate.

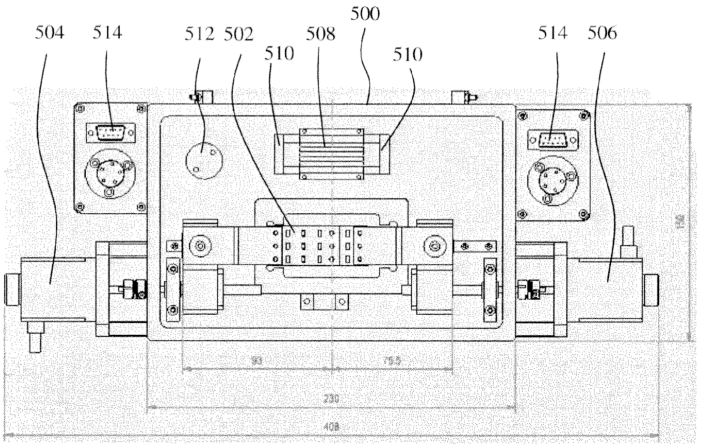



Figure 8.17 - SchematicsofinventionnumberUS2012/0219981Al, assigned to Muthiah and Lane [115], in which each motor (denoted by 504 and 506) is connected to an opposite end of the cell culture device (502). The embodiment includes a water reservoir (512), an electric heating unit (508) and cooling fans (510), and computer interface connections (514). Figures from [115].

The magnetic actuation principle is an indirect method used to apply mechanical stresses on the substrate of interest. The actuating part is never in contact with the moveable one, which decreases the risk of contamination, but it is hard to control the strain and velocity. In addition, there is a potential unwanted magnetic effect on cells.

Looking further at low- to high-frequency range, some inventions apply fluid-flow-induced shear stress to cells. Despite the fact that this stimulus cannot be considered a mechanical cue for mechanotransduction studies given that it cannot be measured, Jiang et al.'s invention number CN10314657A also provides, according to the inventors, tensile stresses on cells [127], and Boronyak et al.'s invention number US 8,852,923 B2 may be adapted to impose cyclic flexural and/or tensile stresses [128].

The aforementioned inventions apply tensile, compressive, or shear stresses to cells, and some allow simultaneous electric stimulation. When cells are stimulated by deformation of the substrate on which they are cultured, those forces generate uniaxial, biaxial, or equiaxial strains (previously described in Fig. 8.3). In-plane substrate distension through frictionless platen displacement (by vacuum, pressure, or another means) creates biaxial strain traction on a flexible culture membrane and produces a uniform strain field [119]. This strain-profile output may be required for more accurate and controlled mechanotransduction studies, given that all cells cultured on the substrate are subjected to the same strain.

Actuation using piezoelectric or ultrasound elements was used to create vibration/oscillation. The main advantage is easy set-up, but the deformation created exhibits low amplitude and high

frequency. In addition, the deformation of the piezo elements is not equal to the deformation of the substrate, and consequently of the cells, because losses are always present and, as the whole device vibrates, the vibrations can be even more attenuated.

## 8.8. Potential and future perspectives

Significant progress in research and technological fields has contributed to remarkable findings on the physiological dynamics of the human body. Basic life science research has moved from 2D culture systems to more complex 3D dynamic cultures, not only to improve cell culture conditions by promoting nutrient and oxygen flow to cells, but also to more closely mimic the complex physiological environment. Unlike bioreactors or microfluidic-based culture models, for the purpose of mechanobiology studies, cells are usually seeded on polymeric substrates or incorporated into 3D constructs and stimulated in mechanical force devices in order to investigate cell adaptation to different mechanical stresses, such as tensile or compressive stresses.

Regenerative medicine strategies involve the use of biomaterials whose mechanical properties and behaviour upon implantation may be studied in vitro by closely mimicking physiological conditions of, for example, bone [43, 74–76], heart muscle [42, 135], tendon [56], and lung [77]. By reproducing the physiological conditions to which the implants or biomaterials would be subjected, the need to perform in vivo animal testing would decrease. This would be in line with the European Directive 2010/63/EC which follows the "3Rs: reduction, refinement, and replacement" strategy to reinforce the importance of using alternative in vitro and in silico methods to obtain the maximal information from the intended product prior to clinical trials [136–138]. Despite more reliable studies conducted over the past years for multiple tissue-specific applications, there are still opportunities for further improvement. Mechanical stimulation devices should be designed (or integrated with other systems) to allow multiple and real-time assessment and evaluation of cell behaviour and responses at a microscale. One possibility is performing real-time imaging using non-invasive imaging techniques, fluorescence, or μCT. In order to assure optimal experimental conditions, mechanical stimulation devices could be coupled and assembled with sensors for monitor-based and cell-specific parameters, such as pH, temperature, oxygen, and secretion of small molecules and proteins.

## Acknowledgments

This work was supported by FCT (Fundação para a Ciência e a Tecnologia) through the grant SFRH/BD/141056/2018, the project PTDC/EME-EME/1442/2020 and under the national

support to R&D units grant, through the reference projects UIDB/04436/2020 and UIDP/04436/2020. In addition, this work was developed within the scope of the project CICECO-Aveiro Institute of Materials, UIDB/50011/2020, UIDP/50011/2020 & LA/P/0006/2020, financed by national funds through the FCT/MEC (PIDDAC).




## References

[1] A. L. Roy, R. S. Conroy, Toward mapping the human body at a cellular resolution, Mol. Biol. Cell. 29 (2018) 1779–1785. https://doi.org/10.1091/mbc.E18-04-0260.

[2] E. L. Jackson, H. Lu, Three-dimensional models for studying development and disease: moving on from organisms to organs-on-a-chip and organoids, Integr. Biol. 8 (2016) 672–683. https://doi.org/10.1039/c6ib00039h.

[3] H. Atcha, C.T. Davis, N. R. Sullivan, T. D. Smith, S. Anis, W. Z. Dahbour, Z.R. Robinson, A. Grosberg, W.F. Liu, A Low-Cost Mechanical Stretching Device for Uniaxial Strain of Cells: A Platform for Pedagogy in Mechanobiology, J. Biomech. Eng. 140 (2018) 1–9. https://doi.org/10.1115/1.4039949.

[4] A. R. Raveling, S. K. Theodossiou, N. R. Schiele, A 3D printed mechanical bioreactor for investigating mechanobiology and soft tissue mechanics, MethodsX. 5 (2018) 924–932. https://doi.org/10.1016/j.mex.2018.08.001.

[5] N. Yi, H. Cui, L.G. Zhang, H. Cheng, Integration of biological systems with electronic-mechanical assemblies, Acta Biomater. 95 (2019) 91–111. https://doi.org/10.1016/j.actbio.2019.04.032.

[6] F. Gattazzo, A. Urciuolo, P. Bonaldo, Extracellular matrix: A dynamic microenvironment for stem cell niche, Biochim. Biophys. Acta - Gen. Subj. 1840 (2014) 2506–2519. https://doi.org/10.1016/j.bbagen.2014.01.010.

[7] K. Uto, J.H. Tsui, C.A. Deforest, D. Kim, Dynamically tunable cell culture platforms for tissue engineering and mechanobiology, Prog. Polym. Sci. 65 (2017) 53–82. https://doi.org/10.1016/j.progpolymsci.2016.09.004.

[8] L. Li, J. Eyckmans, C.S. Chen, Designer biomaterials for mechanobiology, Nat. Mater. 16 (2017) 1164–1168. https://doi.org/10.1038/nmat5049.

[9] K. A. Jansen, D. M. Donato, H. E. Balcioglu, T. Schmidt, E. H. J. Danen, G. H. Koenderink, A guide to mechanobiology: Where biology and physics meet, Biochim. Biophys. Acta - Mol. Cell Res. 1853 (2015) 3043–3052. https://doi.org/10.1016/j.bbamcr.2015.05.007.

[10] A. W. Orr, B. P. Helmke, B. R. Blackman, M. A. Schwartz, Mechanisms of mechanotransduction, Dev. Cell. 10 (2006) 11–20. https://doi.org/10.1016/j.devcel.2005.12.006.

[11] K. H. Vining, D. J. Mooney, Mechanical forces direct stem cell behaviour in development and regeneration, Nat. Rev. Mol. Cell Biol. 18 (2017) 728–742. https://doi.org/10.1038/nrm.2017.108.

[12] Y. Chen, L. Ju, M. Rushdi, C. Ge, C. Zhu, Receptor-mediated cell mechanosensing, Mol. Biol. Cell. 28 (2017) 3134–3155. https://doi.org/10.1091/mbc.e17-04-0228.

[13] C. Wittkowske, G.C. Reilly, D. Lacroix, C.M. Perrault, In Vitro Bone Cell Models: Impact of Fluid Shear Stress on Bone Formation, Front. Bioeng. Biotechnol. 4 (2016) 1–22. https://doi.org/10.3389/fbioe.2016.00087.

[14] S. Ma, Z. Meng, R. Chen, K.-L. Guan, The Hippo Pathway: Biology and Pathophysiology, Annu. Rev. Biochem. 88 (2019) 577–604. https://doi.org/10.1146/annurev-biochem-013118-111829.

[15] C.C. DuFort, M.J. Paszek, V.M. Weaver, Balancing forces: architectural control of mechanotransduction, Nat. Rev. Mol. Cell Biol. 12 (2001) 308–319. https://doi.org/:10.1038/nrm3112.

[16] M. Gasik, Biomechanical characterization of engineered tissues and implants for tissue/organ replacement applications, in: Biomater. Organ Tissue Regen., Elsevier Ltd, 2020: pp. 599–627. https://doi.org/10.1016/b978-0-08-102906-0.00024-6.

[17] F. Melo-Fonseca, G. Miranda, H.S. Domingues, I.M. Pinto, M. Gasik, F.S. Silva, Reengineering Bone-Implant Interfaces for Improved Mechanotransduction and Clinical Outcomes, Stem Cell Rev. Reports. (2020). https://doi.org/10.1007/s12015-020-10022-9.

[18] D. Desmaële, M. Boukallel, S. Régnier, Actuation means for the mechanical stimulation of living cells via microelectromechanical systems: A critical review, J. Biomech. 44 (2011) 1433–1446. https://doi.org/10.1016/j.jbiomech.2011.02.085.

[19] S.N. Bhatia, D.E. Ingber, Microfluidic organs-on-chips, Nat. Biotechnol. 32 (2014) 760–772. https://doi.org/10.1038/nbt.2989.

[20] M.A. Asnaghi, T. Smith, I. Martin, D. Wendt, Bioreactors: Enabling Technologies for Research and Manufacturing, in: Tissue Eng., Second Ed, Elsevier Inc., 2015: pp. 347–392. https://doi.org/10.1016/B978-0-12-420145-3.00011-0.

[21] M. Brunelli, C. Perrault, D. Lacroix, A Review of Bioreactors and Mechanical Stimuli, in: Multiscale Mechanobiol. Tissue Eng., Springer, Singapore, 2019: pp. 1–22. https://doi.org/10.1007/978-981-10-8075-3_1.

[22] S. Eaker, E. Abraham, J. Allickson, T.A. Brieva, D. Baksh, T.R.J. Heathman, B. Mistry, N. Zhang, Bioreactors for cell therapies: Current status and future advances, Cytotherapy. 19 (2017) 9–18. https://doi.org/10.1016/j.jcyt.2016.09.011.

[23] C. Mckee, G. R. Chaudhry, Advances and challenges in stem cell culture, Colloids Surfaces B Biointerfaces. 159 (2017) 62–77. https://doi.org/10.1016/j.colsurfb.2017.07.051.

[24] A.B. Yeatts, J.P. Fisher, Bone tissue engineering bioreactors: Dynamic culture and the influence of shear stress, Bone. 48 (2011) 171–181. https://doi.org/10.1016/j.bone.2010.09.138.

[25] J. D. Berry, P. Godara, P. Liovic, D. N. Haylock, Predictions for optimal mitigation of paracrine inhibitory signalling in haemopoietic stem cell cultures, Stem Cell Res. Ther. 6 (2015) 1–16. https://doi.org/10.1186/s13287-015-0048-7.

[26] J.A. King, W.M. Miller, Bioreactor development for stem cell expansion and controlled differentiation, Curr. Opin. Chem. Biol. 11 (2007) 394–398. https://doi.org/10.1016/j.cbpa.2007.05.034.

[27] G. Mazzoleni, D. Di Lorenzo, N. Steimberg, Modelling tissues in 3D: The next future of pharmaco-toxicology and food research?, Genes Nutr. 4 (2009) 13–22. https://doi.org/10.1007/s12263-008-0107-0.

[28] I. Marijanovic, M. Antunovic, I. Matic, M. Panek, A. Ivkovic, Bioreactor-Based Bone Tissue Engineering, in: Adv. Tech. Bone Regen. 1., InTech, 2016: pp. 223–252. https://doi.org/http://dx.doi.org/10.5772/62546.

[29] D. van Noort, Bioreactors on a Chip, in: C.-F. Mandenius (Ed.), Bioreact. Des. Oper. Nov. Appl., First, Wiley-VCH Verlag GmbH & Co. KGaA, 2016: pp. 77–112. https://doi.org/10.1002/9783527683369.ch3.

[30] J.E. Sosa-Hernández, A.M. Villalba-Rodríguez, K.D. Romero-Castillo, M.A. Aguilar-Aguila-Isaías, I.E. García-Reyes, A. Hernández-Antonio, I. Ahmed, A. Sharma, R. Parra-Saldívar, H.M.N. Iqbal, Organs-on-a-chip module: A review from the development and applications perspective, Micromachines. 9 (2018) 536. https://doi.org/10.3390/mi9100536.

[31] G.M. Whitesides, The origins and the future of microfluidics, Nature. 442 (2006) 368–373. https://doi.org/10.1038/nature05058.

[32] J.M. Mann, R.H.W. Lam, S. Weng, Y. Sun, J. Fu, A silicone-based stretchable micropost array membrane for monitoring live-cell subcellular cytoskeletal response, Lab Chip. 12 (2012) 731–740. https://doi.org/10.1039/c2lc20896b.

[33] S. Haeberle, R. Zengerle, Microfluidic platforms for lab-on-a-chip applications, Lab Chip. 7 (2007) 1094–1110. https://doi.org/10.1039/b706364b.

[34] N. Azizipour, R. Avazpour, D.H. Rosenzweig, M. Sawan, A. Ajji, Evolution of biochip technology: A review from lab-on-a-chip to organ-on-a-chip, Micromachines. 11 (2020) 1–15. https://doi.org/10.3390/mi11060599.

[35] T.D. Brown, Techniques for mechanical stimulation of cells in vitro: A review, J. Biomech. 33 (2000) 3–14. https://doi.org/10.1016/S0021-9290(99)00177-3.

[36] G. Esteban-Manzanares, B. González-Bermúdez, J. Cruces, M. De la Fuente, Q. Li, G. V. Guinea, J. Pérez-Rigueiro, M. Elices, G.R. Plaza, Improved Measurement of Elastic Properties of Cells by Micropipette Aspiration and Its Application to Lymphocytes, Ann. Biomed. Eng. 45 (2017) 1375–1385. https://doi.org/10.1007/s10439-017-1795-7.

[37] B. González-Bermúdez, G. V. Guinea, G.R. Plaza, Advances in Micropipette Aspiration: Applications in Cell Biomechanics, Models, and Extended Studies, Biophys. J. 116 (2019) 587–594. https://doi.org/10.1016/j.bpj.2019.01.004.

[38] R. Daza, B. González-Bermúdez, J. Cruces, M. De la Fuente, G.R. Plaza, M. Arroyo-Hernández, M. Elices, J. Pérez-Rigueiro, G. V. Guinea, Comparison of cell mechanical measurements provided by Atomic Force Microscopy (AFM) and Micropipette Aspiration (MPA), J. Mech. Behav. Biomed. Mater. 95 (2019) 103–115. https://doi.org/10.1016/j.jmbbm.2019.03.031.

[39] Y.M. Efremov, W.H. Wang, S.D. Hardy, R.L. Geahlen, A. Raman, Measuring nanoscale viscoelastic parameters of cells directly from AFM force-displacement curves, Sci. Rep. 7 (2017) 1–14. https://doi.org/10.1038/s41598-017-01784-3.

[40] N. Schierbaum, J. Rheinlaender, T.E. Schäffer, Combined atomic force microscopy (AFM) and traction force microscopy (TFM) reveals a correlation between viscoelastic material properties and contractile prestress of living cells, Soft Matter. 15 (2019) 1721–1729. https://doi.org/10.1039/c8sm01585f.

[41] M. Krieg, G. Fläschner, D. Alsteens, B.M. Gaub, W.H. Roos, G.J.L. Wuite, H.E. Gaub, C. Gerber, Y.F. Dufrêne, D.J. Müller, Atomic force microscopy-based mechanobiology, Nat. Rev. Phys. 1 (2019) 41–57. https://doi.org/10.1038/s42254-018-0001-7.

[42] J. Kreutzer, M. Viehrig, R.P. Pölönen, F. Zhao, M. Ojala, K. Aalto-Setälä, P. Kallio, Pneumatic unidirectional cell stretching device for mechanobiological studies of cardiomyocytes, Biomech. Model. Mechanobiol. 19 (2020) 291–303. https://doi.org/10.1007/s10237-019-01211-8.

[43] M. -C. Qi, J. Hu, S.-J. Zou, H. -Q. Chen, H. -X. Zhou, L. -C. Han, Mechanical strain induces osteogenic differentiation: Cbfa1 and Ets-1 expression in stretched rat mesenchymal stem cells, Int. J. Oral Maxillofac. Surg. 37 (2008) 453–458. https://doi.org/10.1016/J.IJOM.2007.12.008.

[44] X. Trepat, L. Deng, S.S. An, D. Navajas, D.J. Tschumperlin, W.T. Gerthoffer, J.P. Butler, J.J. Fredberg, Universal physical responses to stretch in the living cell, Nature. 447 (2007) 592–595. https://doi.org/10.1038/nature05824.

[45] N.J. Sniadecki, A. Anguelouch, M.T. Yang, C.M. Lamb, Z. Liu, S.B. Kirschner, Y. Liu, D.H. Reich, C.S. Chen, Magnetic microposts as an approach to apply forces to living cells, Proc. Natl. Acad. Sci. U. S. A. 104 (2007) 14553–14558. https://doi.org/10.1073/pnas.0611613104.

[46] L. Izzo, M. Tunesi, L. Boeri, M. Laganà, C. Giordano, M.T. Raimondi, Influence of the static magnetic field on cell response in a miniaturized optically accessible bioreactor for 3D cell culture, Biomed. Microdevices. 21 (2019) 1–12. https://doi.org/10.1007/s10544-019-0387-8.

[47] S.R. Heidemann, D. Wirtz, Towards a regional approach to cell mechanics, Trends Cell Biol. 14 (2004) 160–166. https://doi.org/10.1016/j.tcb.2004.02.003.

[48] J. Barthes, H. Özçelik, M. Hindié, A. Ndreu-Halili, A. Hasan, N.E. Vrana, Cell Microenvironment Engineering and Monitoring for Tissue Engineering and Regenerative Medicine: The Recent Advances, Biomed Res. Int. 2014 (2014). https://doi.org/10.1155/2014/921905.

[49] S. Halldorsson, E. Lucumi, R. Gómez-Sjöberg, R. M. T. Fleming, Advantages and challenges of microfluidic cell culture in polydimethylsiloxane devices, Biosens. Bioelectron. 63 (2015) 218–231. https://doi.org/10.1016/j.bios.2014.07.029.

[50] L. Kim, Y. C. Toh, J. Voldman, H. Yu, A practical guide to microfluidic perfusion culture of adherent mammalian cells, Lab Chip. 7 (2007) 681–694. https://doi.org/10.1039/b704602b.

[51] J. A. Kluge, G. G. Leisk, R. D. Cardwell, A. P. Fernandes, M. House, A. Ward, A. L. Dorfmann, D.L. Kaplan, Bioreactor system using noninvasive imaging and mechanical stretch for biomaterial screening, Ann. Biomed. Eng. 39 (2011) 1390–1402. https://doi.org/10.1007/s10439-010-0243-8.

[52] M. Walker, M. Godin, A. E. Pelling, A vacuum-actuated microtissue stretcher for long-term exposure to oscillatory strain within a 3D matrix, Biomed. Microdevices. 20 (2018). https://doi.org/10.1007/s10544-018-0286-4.

[53] E. J. Vanderploeg, S. M. Imler, K. R. Brodkin, A. J. García, M. E. Levenston, Oscillatory tension differentially modulates matrix metabolism and cytoskeletal organization in chondrocytes and fibrochondrocytes, J. Biomech. 37 (2004) 1941–1952. https://doi.org/10.1016/j.jbiomech.2004.02.048.

[54] J. T. Connelly, E. J. Vanderploeg, J. K. Mouw, C. G. Wilson, M. E. Levenston, Tensile loading modulates bone marrow stromal cell differentiation and the development of engineered fibrocartilage constructs, Tissue Eng. - Part A. 16 (2010) 1913–1923. https://doi.org/10.1089/ten.tea.2009.0561.

[55] D. M. Doroski, M. E. Levenston, J. S. Temenoff, Cyclic tensile culture promotes fibroblastic differentiation of marrow stromal cells encapsulated in poly(ethylene glycol)-based hydrogels, Tissue Eng. - Part A. 16 (2010) 3457–3466. https://doi.org/10.1089/ten.tea.2010.0233.

[56] W. K. Grier, A. S. Moy, B. A. C. Harley, Cyclic tensile strain enhances human mesenchymal stem cell SMAD 2/3 activation and tenogenic differentiation in anisotropic collagen-glycosaminoglycan scaffolds, Eur. Cells Mater. 33 (2017) 227–239. https://doi.org/10.22203/eCM.v033a17.

[57] G. Subramanian, M. Elsaadany, C. Bialorucki, E. Yildirim-Ayan, Creating homogenous strain distribution within 3D cell-encapsulated constructs using a simple and cost-effective uniaxial tensile

bioreactor: Design and validation study, Biotechnol. Bioeng. 114 (2017) 1878–1887. https://doi.org/10.1002/bit.26304.

[58] J. R. Ralphs, A. D. Waggett, M. Benjamin, Actin stress fibres and cell-cell adhesion molecules in tendons: Organisation in vivo and response to mechanical loading of tendon cells in vitro, Matrix Biol. 21 (2002) 67–74. https://doi.org/10.1016/S0945-053X(01)00179-2.

[59] C. A. Simmons, S. Matlis, A. J. Thornton, S. Chen, Y. Wang, D.J. Mooney, Cyclic strain enhances matrix mineralization by adult human mesenchymal stem cells via the extracellular signal-regulated kinase ( ERK1 / 2 ) signaling pathway, J. Biomech. 36 (2003) 1087–1096. https://doi.org/10.1016/S0021-9290(03)00110-6.

[60] R. D. Sumanasinghe, S. H. Bernacki, E. G. Loboa, Osteogenic Differentiation of Human Mesenchymal Stem Cells in Collagen Matrices: Effect of Uniaxial Cyclic Tensile Strain on Bone Morphogenetic Protein (BMP-2) mRNA Expression, Tissue Eng. 12 (2006) 3459–3465. https://doi.org/10.1089/ten.2006.12.3459.

[61] S. Saha, L. Ji, J. J. De Pablo, S. P. Palecek, Inhibition of human embryonic stem cell differentiation by mechanical strain, J. Cell. Physiol. 206 (2006) 126–137. https://doi.org/10.1529/biophysj.107.119891.

[62] C. H. Ku, P. H. Johnson, P. Batten, P. Sarathchandra, R. C. Chambers, P.M. Taylor, M.H. Yacoub, A.H. Chester, Collagen synthesis by mesenchymal stem cells and aortic valve interstitial cells in response to mechanical stretch, Cardiovasc. Res. 71 (2006) 548–556. https://doi.org/10.1016/j.cardiores.2006.03.022.

[63] J. Luo, L. Qin, L. Zhao, A. Dardik, L.E. Niklason, Tissue-Engineered Vascular Grafts with Advanced Mechanical Strength from Human iPSCs Short Article Tissue-Engineered Vascular Grafts with Advanced Mechanical Strength from Human iPSCs, Stem Cell. (2020) 1–11. https://doi.org/10.1016/j.stem.2019.12.012.

[64] K. Kroll, M. Chabria, K. Wang, F. Häusermann, F. Schuler, L. Polonchuk, Electro-mechanical conditioning of human iPSC-derived cardiomyocytes for translational research, Prog. Biophys. Mol. Biol. 130 (2017) 212–222. https://doi.org/10.1016/j.pbiomolbio.2017.07.003.

[65] A. Sitticholechaiwut, J.H. Edwards, A.M. Scutt, G.C. Reilly, Short bouts of mechanical loading are as effective as dexamethasone at inducing matrix production by human bone marrow

mesenchymal stem cells, Eur. Cells Mater. 20 (2010) 45–57. https://doi.org/10.1111/j.1749-6632.1954.tb45891.x.

[66] A. Sittichockechaiwut, A.M. Scutt, A.J. Ryan, L.F. Bonewald, G.C. Reilly, Use of rapidly mineralising osteoblasts and short periods of mechanical loading to accelerate matrix maturation in 3D scaffolds, Bone. 44 (2009) 822–829. https://doi.org/10.1016/j.bone.2008.12.027.

[67] Z. Kong, J. Li, Q. Zhao, Z. Zhou, X. Yuan, D. Yang, X. Chen, Dynamic compression promotes proliferation and neovascular networks of endothelial progenitor cells in demineralized bone matrix scaffold seed, J. Appl. Physiol. 113 (2012) 619–626. https://doi.org/10.1152/japplphysiol.00378.2011.

[68] Y. Okazaki, T. Furumatsu, Y. Kamatsuki, K. Nishida, Y. Nasu, R. Nakahara, T. Saito, T. Ozaki, Differences between the root and horn cells of the human medial meniscus from the osteoarthritic knee in cellular characteristics and responses to mechanical stress, J. Orthop. Sci. 26 (2021) 230–236. https://doi.org/10.1016/j.jos.2020.02.015.

[69] S.H. Chang, D. Mori, H. Kobayashi, Y. Mori, H. Nakamoto, K. Okada, Y. Taniguchi, S. Sugita, F. Yano, U. il Chung, J. ri Kim-Kaneyama, M. Yanagita, A. Economides, E. Canalis, D. Chen, S. Tanaka, T. Saito, Excessive mechanical loading promotes osteoarthritis through the gremlin-1–NF-$\kappa$B pathway, Nat. Commun. 10 (2019) 1–5. https://doi.org/10.1038/s41467-019-09491-5.

[70] H.Y. Nam, M.R. Murali, R.E. Ahmad, B. Pingguan-Murphy, H.R.B. Raghavendran, T. Kamarul, Mechanical Strain-Mediated Tenogenic Differentiation of Mesenchymal Stromal Cells Is Regulated through Epithelial Sodium Channels, Stem Cells Int. 2020 (2020). https://doi.org/10.1155/2020/5385960.

[71] K. Takahashi, S. Ito, K. Furuya, S. Asano, M. Sokabe, Y. Hasegawa, Real-time imaging of mechanically and chemically induced ATP release in human lung fibroblasts, Respir. Physiol. Neurobiol. 242 (2017) 96–101. https://doi.org/10.1016/j.resp.2017.04.008.

[72] Y. Kamotani, T. Bersano-Begey, N. Kato, Y.C. Tung, D. Huh, J.W. Song, S. Takayama, Individually programmable cell stretching microwell arrays actuated by a Braille display, Biomaterials. 29 (2008) 2646–2655. https://doi.org/10.1016/j.biomaterials.2008.02.019.

[73] J. M. Gere, S. P. Timoshenko, Mechanics of Materials, 2nd ed., Brooks/Cole Engineering, 1984.

[74] J. R. Mauney, S. Sjostorm, J. Blumberg, R. Horan, J. P. O'Leary, G. Vunjak-Novakovic, V. Volloch, D. L. Kaplan, Mechanical Stimulation Promotes Osteogenic Differentiation of Human Bone Marrow Stromal Cells on 3-D Partially Demineralized Bone Scaffolds in Vitro, Calcif. Tissue Int. 74 (2004) 458–468. https://doi.org/10.1007/s00223-003-0104-7.

[75] E. M. Byrne, E. Farrell, L. A. McMahon, M. G. Haugh, F. J. O'Brien, V. A. Campbell, P. J. Prendergast, B. C. O'Connell, Gene expression by marrow stromal cells in a porous collagen-glycosaminoglycan scaffold is affected by pore size and mechanical stimulation, J. Mater. Sci. Mater. Med. 19 (2008) 3455–3463. https://doi.org/10.1007/s10856-008-3506-2.

[76] M. Jagodzinski, M. Drescher, J. Zeichen, S. Hankemeier, C. Krettek, U. Bosch, M. Van Griensven, I. Martin, C. Evans, Effects of cyclic longitudinal mechanical strain and dexamethasone on osteogenic differentiation of human bone marrow stromal cells, Eur. Cells Mater. 7 (2004) 35–41. https://doi.org/10.22203/eCM.v007a04.

[77] D. Huh, B.D. Matthews, A. Mammoto, M. Montoya-Zavala, H. Yuan Hsin, D.E. Ingber, Reconstituting organ-level lung functions on a chip, Science (80-. ). 328 (2010) 1662–1668. https://doi.org/10.1126/science.1188302.

[78] J. T. Butcher, B. C. Barrett, R. M. Nerem, Equibiaxial strain stimulates fibroblastic phenotype shift in smooth muscle cells in an engineered tissue model of the aortic wall, Biomaterials. 27 (2006) 5252–5258. https://doi.org/10.1016/j.biomaterials.2006.05.040.

[79] C. Moraes, J. H. Chen, Y. Sun, C. A. Simmons, Microfabricated arrays for high-throughput screening of cellular response to cyclic substrate deformation, Lab Chip. 10 (2010) 227–234. https://doi.org/10.1039/b914460a.

[80] W. Tan, D. Scott, D. Belchenko, H. J. Qi, L. Xiao, Development and evaluation of microdevices for studying anisotropic biaxial cyclic stretch on cells, Biomed. Microdevices. 10 (2008) 869–882. https://doi.org/10.1007/s10544-008-9201-8.

[81] R. A. Gould, K. Chin, T. P. Santisakultarm, A. Dropkin, J. M. Richards, C. B. Schaffer, J. T. Butcher, Cyclic strain anisotropy regulates valvular interstitial cell phenotype and tissue remodeling in three-dimensional culture, Acta Biomater. 8 (2012) 1710–1719. https://doi.org/10.1016/j.actbio.2012.01.006.

[82] V. Terraciano, J. Mizrahi, L. Moroni, H. Bin Park, N. Hwang, Z. Zhang, J. Elisseeff, D. Seliktar, Differential Response of Adult and Embryonic Mesenchymal Progenitor Cells to Mechanical

Compression in Hydrogels, Stem Cells. 25 (2007) 2730–2738. https://doi.org/10.1634/stemcells.2007-0228.

[83] J. K. Mouw, J. T. Connelly, C. G. Wilson, K. E. Michael, M. E. Levenston, Dynamic Compression Regulates the Expression and Synthesis of Chondrocyte-Specific Matrix Molecules in Bone Marrow Stromal Cells, Stem Cells. 25 (2006) 655–663. https://doi.org/10.1634/stemcells.2006-0435.

[84] B. Rath, J. Nam, T.J. Knobloch, J.J. Lannutti, S. Agarwal, Compressive forces induce osteogenic gene expression in calvarial osteoblasts, J. Biomech. 41 (2008) 1095–1103. https://doi.org/10.1016/j.jbiomech.2007.11.024.

[85] A. Ravichandran, J. Lim, M. S. K. Chong, F. Wen, Y. Liu, Y. T. Pillay, J. K. Y. Chan, S.H. Teoh, In vitro cyclic compressive loads potentiate early osteogenic events in engineered bone tissue, J. Biomed. Mater. Res. - Part B Appl. Biomater. 105 (2017) 2366–2375. https://doi.org/10.1002/jbm.b.33772.

[86] C. Moraes, G. H. Wang, Y. Sun, C. A. Simmons, A microfabricated platform for high-throughput unconfined compression of micropatterned biomaterial arrays, Biomaterials. 31 (2010) 577–584. https://doi.org/10.1016/j.biomaterials.2009.09.068.

[87] D. Lee, A. Erickson, T. You, A. T. Dudley, S. Ryu, Pneumatic microfluidic cell compression device for high-throughput study of chondrocyte mechanobiology, Lab Chip. 18 (2018) 2077–2086. https://doi.org/10.1039/c8lc00320c.

[88] C. Moraes, R. Zhao, M. Likhitpanichkul, C.A. Simmons, Y. Sun, Semi-confined compression of microfabricated polymerized biomaterial constructs, J. Micromechanics Microengineering. 21 (2011). https://doi.org/10.1088/0960-1317/21/5/054014.

[89] Z. Z. Zhang, Y. R. Chen, S. J. Wang, F. Zhao, X. G. Wang, F. Yang, J. J. Shi, Z. G. Ge, W. Y. Ding, Y. C. Yang, T. Q. Zou, J. Y. Zhang, J. K. Yu, D. Jiang, Orchestrated biomechanical, structural, and biochemical stimuli for engineering anisotropic meniscus, Sci. Transl. Med. 11 (2019). https://doi.org/10.1126/scitranslmed.aao0750.

[90] C. Analytics, Web of Knowledge—Derwent Innovation Index, (n.d.). http://www.webofknowledge.com.

[91] Google Patents, (n.d.). https://patents.google.com.

[92] C. Moraes, C. Simmons, Y. Sun, A system, apparatus and method for applying mechnical force to a material, WO2009039640A9, 2013. https://patents.google.com/patent/WO2009039640A1/en.

[93] A. J. Banes, Apparatus for applying stress to cell cultures, US4839280, 1989.

[94] L. Tae Yoon, H. Hee Tak, S. Jung Mok, S. Se Ra, K. Hyun Chui, Cell stimulation apparatus, US 10,246,676 B2, 2019.

[95] A. J. Banes, Loading station assembly and method for tissue engineering, US 6,472,202 Bl, 2002.

[96] G. S. Sittampalam, V. S. Nirmalanandhan, Systems and methods for mechanically strained cell culture, US 2013/0059324 Al, 2013.

[97] C. S. Simmons, B. L. Pruitt, J. Y. Sim, P. R. Bächtol, Cell culture strain array systems and methods for using the same, US2015/0050722Al, 2015.

[98] A. Kiesow, S. Schwan, B. Bartling, A. Simm, Bioreactor for multi-dimensional, mechanical stimulation of cells, cell complexes and/or cell tissue, comprises a first and a second reactor part volumes that are separated from each other through a carrier membrane, DE102009057698A1, 2011.

[99] W. Min-Hsien, L. Chun-Li, T. Shiao-Wen, L. Heng-Liang, L. Yen-Ting, Apparatus for high-throughput cell cultura with mechanical compression stimulation, US 8980624 B2, 2015.

[100] M. Kasra, Hydrostatic pressure generator device, US 9303244 Bl, 2016. http://www.google.ch/patents/US8668770.

[101] L. Dan-Jae, T. Ming-Tzu, H. Chao-Wei, C. Yi-Tao, Y. Chun-Hsu, Cell mechanical stimulating device, US 2020/0339936 Al, 2020.

[102] K. Lagana, M. T. Raimondi, G. Dubini, R. Santoro, Bioreactor for generation and complex mechanical stimulation of engineered biological tissue, WO 2009/047045 A2, 2009.

[103] B. C. Wang, L. Q, Zhu, J. Zhou et al Microstress applicator for in vitro cell, CN1834220A, 2006.

[104] G. Subramanian, M. Elsaadany, E. Yildirim-Ayan, Loading platform for three-dimensional tissue engineered scaffolds, WO 2017/152080 Al, 2017.

[105] C. Franck, E. Bar-kochba, Device and system for mechanical measurement of biomaterial, WO 2013/090738 A9, 2013.

[106] Y.B. Fan, J. C. Li, Y. W. Zou et al, Tissue engineering reactor having tissue cultures tension-compression and rotation functions, CN101372664A, 2008.

[107] Y. B. Fan, P. Li, M. L. Liu et al, Stretch-electricity combined stimulation three-dimensional cell culture device, CN102433258B, 2012.

[108] B. Zhang, Z. Q. Feng, G. F. Wang et al, Culture device applied to cell tensile stress and method, CN103966094A, 2014.

[109] H. H. Lu, M. Castillo, B. R. Dargis, Bioreactor system for mechanical stimulation of biological samples, US 2012/0100602 Al, 2012.

[110] P. G. W. Lee, D. L. Tillostson, R.T. Udale, K. L. Barber, Apparatus and method for culturing cells and tissue, US 9617507 B2, 2017.

[111] P. G. W. Lee, D. L. Tillostson, R. T. Udale, K. L. Barber, Apparatus and method for culturing cells and tissue, US 10,421,955 B2, 2019. https://doi.org/10.1111/2047-8852.12112.

[112] T. Meckel, E. Sapper, L.A. Schmitt, Testing arrangement for examining a cell culture under the effect of a dynamic force, US20180164278A1, 2018.

[113] L. Biagiotti, S. Cavalcanti, E. Giordano, F. Lotti, C. Muscari, C.M. Caldarera, M. Govobi, Bio reactor for stem cells stimulation, WO 2011/013067 A2, 2011.

[114] A. Bayés Genís, A. Llucià Valldeperas, C. Soler Botija, R. Bragós Bardia, F.X. Rosell Ferrer, Method for conditioning stem cells, WO 2017/125159 Al, 2017.

[115] M. Muthiah, E.B. Lane, Mechanical stretching device, US 2012/0219981 Al, 2012.

[116] H. Jing, Y. X. Qin, T. Hai et al, Extension and compression device of multi-unit cells, CN101649291A, 2009.

[117] R. Krishnan, C.Y. Park, D. Tschumperlin, F. Liu, J. Mih, J. Fredberg, Bio-Matrix Stretcher, WO 2009/032174 Al, 2008.

[118] A. R. Shapiro, M. L. Gray, L. A. Melendez, J. L. Schaffer, W. John D., J. G. Venegas, Cell stretching method, US 5,348,879, 1994.

[119] A. Baker, M. Wong, High-throughput mechanical strain generating system for cell cultures and applications thereof, WO 2014/165056 Al, 2014.

[120] T. Quinn, H. Majd, Device for cell culture on deformable surfaces, EP 1 679 366 A1, 2006.

[121] S. Campbell, J. Schwan, A. Kwaczala, T. Ryan, D. Jacoby, Y. Qyang, L. Sewanan, R. Ng, J.A. Clark, System and method for generating biological tissue, US 2018/0216057 Al, 2018.

[122] E.G. Roberts, Flexible device and its application for bio-cell in-vitro electrical and mechanical stimulation characterization, US 2020/0199515 Al, 2020.

[123] T. Takagi, S. Watanabe, Cell and structure incubator, EP 1 428 869 A1, 2004.

[124] M. Bottlang, M.B. Sommers, Method and systems for tissue culture, US2008/0026419A, 2008.

[125] F. X. Rosell Ferrer, B. Sánchez Terrones, R. Bragós Bardia, A. Bayés Genís, A. Llucià Valldeperas, Methods and devices for mechanical and electrical stimulation of stem cell monolayer and 3D cultures for tissue engineering applications, US2016/0032234Al, 2016. https://doi.org/10.1111/2047-8852.12112.

[126] H. Lee, H. Park, L. Solorio, A. Enriquez, S. Libring, High-throughput magnetic actuation platform for cancer treatment screening, US 2021/0040427 Al, 2021.

[127] X. Y. Jiang, W. F. Zheng, W. Zhang et al, High-flux microfluidic biomechanical long-term stimulation system and use thereof, CN103146574A, 2013.

[128] S. M. Boronyak, G. C. Engelmayr, S. Ramaswamy, M. S. Sacks, D. E. Schmidt, M. S. El-Kurdi, Flow-stretch-flexure bioreactor, US 8,852,923 B2, 2014.

[129] A. Kishida, T. Furunzono, K. Miyazaki, T. Masuzawa, Method for controlling biological function with mechanical vibration and device therefor, US 8.465,971 B2, 2013.

[130] H. S. Choi, W. J. Lee, J. T. Jung, Cell stimulating system, WO2015167097A1, 2015.

[131] H. S. Choi, W. J. Lee, J. T. Jung, Cell stimulating system, US 10,260,035 B2, 2019.

[132] E. L. Botvinick, V. Venugopalan, J. Compton, A. Hellman, Mechanical stress response analysis of cells and tissues, US 2014/0100138A1, 2014. https://patents.google.com/patent/US20140331942A1/en.

[133] A. A. Sutton, T. Shirman, J. Aizenberg, L. Zarzar, P. Kim, Environmentally responsive microstructured hybrid actuator assemblies for use in mechanical stimulation of cells, US 2015/0093823Al, 2015.

[134] W. Zhang, G. Huang, F. Xu, Engineering Biomaterials and Approaches for Mechanical Stretching of Cells in Three Dimensions, Front. Bioeng. Biotechnol. 8 (2020) 1–14. https://doi.org/10.3389/fbioe.2020.589590.

[135] R.K. Birla, Y.C. Huang, R.G. Dennis, Development of a novel bioreactor for the mechanical loading of tissue-engineered heart muscle, Tissue Eng. 13 (2007) 2239–2248. https://doi.org/10.1089/ten.2006.0359.

[136] M. Gasik, Understanding biomaterial-tissue interface quality: combined in vitro evaluation, Sci. Technol. Adv. Mater. 18 (2017) 550–562. https://doi.org/10.1080/14686996.2017.1348872.

[137] G. J. Patronek, A. Rauch, Systematic review of comparative studies examining alternatives to the harmful use of animals in biomedical education, J. Am. Vet. Med. Assoc. 230 (2007) 37–43. https://doi.org/10.2460/javma.230.1.37.

[138] J. Reifenrath, N. Angrisani, M. Lalk, S. Besdo, Replacement, refinement, and reduction: Necessity of standardization and computational models for long bone fracture repair in animals, J. Biomed. Mater. Res. - Part A. 102 (2014) 2884–2900. https://doi.org/10.1002/jbm.a.34920.

# CHAPTER 9

## DESIGN OF A DEVICE FOR CELL MECHANICAL STIMULATION AND REAL-TIME MONITORING

This chapter discloses a custom-made cell mechanical stimulation device and a preliminary *in vitro* study aiming for the device validation. A patent proposal of the device was submitted and is under analysis.

F. Melo-Fonseca[a, b, c], F. S. Silva[a, b], G. Miranda[d], Inês Mendes Pinto[c,e], M. Gasik[f], O. Carvalho[a, b]

[a]Center for MicroElectroMechanical Systems (CMEMS-UMinho), University of Minho, Campus de Azurém, 4800-058 Guimarães – Portugal

[b]LABBELS –Associate Laboratory, Braga, Guimarães, Portugal

[c]International Iberian Nanotechnology Laboratory (INL), 4715-330 Braga, Portugal

[d]CICECO, Aveiro Institute of Materials, University of Aveiro, 3810-193 Aveiro, Portugal

[e]Institute for Research and Innovation in Health (i3S), Porto, Portugal

[f]School of Chemical Engineering, Aalto University Foundation, FI-00076 Espoo, Finland

**Abstract**

Human cells are constantly subjected to mechanical stimuli, which exert a pivotal role on determining the cellular behaviour. In recent years, mechanobiology studies have gained increasing attention as researchers seek to elucidate the impact of these external signals on cellular processes by, for example, applying an external load on the culture substrate. However, a significant limitation in current *in vitro* studies is their limited focus to linear elastic 2D polymeric substrates, which fail to accurately replicate the complex mechanical environments found, for example, in load-bearing metallic composed implants, such as orthopaedic. To address this gap, we have developed a device tailored for mechanobiology studies, that subjects to a substrate, either polymeric or metallic, a bending loading which promotes in its upper surface tensile stress and allows simultaneous cell culture, application of the mechanical stimulation and real-time monitoring of cell behaviour. This advancement holds the potential to discover how cells dynamically sense and respond to mechanical loading and thus understand physiological and pathological events and evaluate the cellular response upon the implantation of biomaterials.

**Keywords:** Mechanical stimulation device; Tensile stress; Mechanobiology; Ti6Al4V; Mesenchymal stem cells

## 9.1. Introduction

Cells are constantly communicating with their environment via, among others, mechanical signalling. Mechanical stimuli play an important role on the cellular and subcellular level as it modulates cellular behaviour [1]. Over the past years, mechanobiology studies have gained attention to enlighten the effect of these external signals on regulating cellular signalling and gene expression. Having a comprehensive understanding of the microenvironment effect at the cellular level would allow to assess the dynamics underlying physiological and pathological events and evaluate the potential of therapies before proceeding to clinical trials.

Technological innovations for probing mechanobiological cues have garnered significant interest and many are still under development. Micropipette aspiration (MPA) [2,3], atomic force microscopy (AFM) [2,4–6], traction force microscopy (TFM) [7,8], optical and magnetic tweezers [9,10], substrate deformation and high-resolution microscopy imaging are some of the techniques used for studying how cells sense and respond to mechanical forces at the cellular and sub-cellular level. In the traditional MPA technique, a cell is immobilized at the tip of a pipette (with a smaller inner diameter than the cell diameter), and then drawn and deformed when a negative pressure is

applied [2]. Pressure is increased in time and the aspirated length of the cell is tracked using an optical microscope. The cell mechanical behaviour is assessed by measuring the cell geometry as a function of the pressure using mechanical models, which level of refinement has been increasing over the last years. Due to the limited temporal and spatial resolutions and extensive post processing, more complex variations MPA have been developed [3]. AFM consists of contacting the microscope cantilever with the cell surface to measure viscoelastic material properties from a force-displacement curve suing a mechanical model [2,4–6]. In TFM, cells are seeded on a deformable substrate coated with fluorescent beads. Using imaging techniques, the displacement of fluorescent beads is used to calculate the forces between cells and ECM (called traction forces) as cells spread or migrate [7,8]. If the first TFM technique is aimed to calculate the traction forces using 2D substrates, more recently, 3D TFM methods have arisen to quantify both tangential and normal forces using 3D images from confocal microscope. Besides the analysis on cellular traction forces, efforts have been made to analyse the cell-cell junctional or intracellular forces by applying the same principle of TFM. Intracellular force microscopy (IFM) and monolayer stress microscopy (MSM) are used to assess intracellular and intercellular forces of cells [7]. Forces quantified by IFM correspond to an average value in 1D and so 2D mapping is not possible, and by MSM, the mechanical properties of the intracellular components are assumed the same. Optical and magnetic tweezers consist of the entrapment of a single or intracellular cell structure between two beads [9,10]. One bead, often of polystyrene or silica, is fixed while the other is moving, either by an action of an optical or magnetic field, to stretch the cell or the cellular structure. Microscopical images are used to probe the cell movements and, combined with the time the cell takes to return to its initial shape, it is possible to estimate the stiffness. Typically, the force applied by optical tweezers is less than 1 μN to avoid cell damage. Another approach to apply mechanical loading on cells is by substrate deformation. Among those, external loads can be indirectly applied to cells by deforming the substrate of culture, such as by stretching or compressing it [1,11,12].

Human mesenchymal stem cells (MSC) possess a wide range of capabilities due to their multipotency, making them an important subject of extensive research. In the context of bone formation, studies have shown that tensile strain promotes the osteogenic differentiation of MSC. Sumanasinghe et al. applied a uniaxial strain using the commercially available FX-4000 device on MSC cultured on 3D collagen matrices (10% and 12% at 1 Hz for 4 h/day) and were the first to report that strain alone could induce osteogenic differentiation without the addition of osteogenic supplements [13]. Carroll et al. applied uniaxial tensile (10% strain at 0.5 Hz) to MSC encapsulated

in 3D fibrin hydrogels using a custom-made bioreactor, which enhanced the expression of osteogenic markers, while suppressing markers of adipogenesis [14]. In a different study, a 10% tensile strain applied for 14 days at 1 Hz (4 h/day) using FX-4000T device not only promoted osteogenesis of MSC from osteoporotic donors seeded in collagen gels, but also enhanced expression of angiogenic factors [15]. After subjecting the substrate to a particular mechanical stress, the assessment of cell behaviour may be performed using microscopy techniques. Recently, live cell imaging has emerged as a promising tool for observing the intrinsic and dynamic interactions of cells and therefore assessing and trying to understand the numerous and complex cellular processes. Using fluorescent dyes to label cellular compartments combined with video-enabled microscopy, it is possible to observe, interpret, and process cellular changes in real time. Nevertheless, care must be taken to prevent light exposure to cells given that the excitation of fluorescent probes (fluorescent proteins (FP) or dye molecules) results in oxygen-dependent reaction of free-radical species, causing phototoxicity in living cells [16]. In this sense, to enhance the resolution when performing live-cell imaging, the irradiation intensity should be minimized by optimizing the efficiency of light path, avoiding prolonged imaging times, detecting most of the fluorescence emission and using low concentrations of labelling probes to prevent introducing unwanted alterations to the biological processes under study [16,17].

Despite advances in the state of the art, devices for mechanical stimulation of cells are relatively limited in providing culture stimulation options for cell research and, as a result, in a limited understanding of cellular phenomena in general. In fact, current commercially available cell mechanical stimulation devices present limitations, such as the need for maintenance, and the demand to purchase additional device-specific accessories to conduct repeated experiments or meet specific requirements. This contributes therefore to the total cost of the device which, by itself, is available for dozens to hundreds of thousands of dollars. In addition, the mechanical stimulation devices available commercially or customised by research groups are only designed to study external mechanical loads on polymeric materials, limiting their practical relevance [18]. Studies focused on linear elastic 2D polymeric substrates under cyclic loading apply strains ranging from 2-12% [13,19], which range is much different from the physiological in bone (0.02-0.35%) [20,21]. Furthermore, these polymeric substrates strains are significantly higher than those achieved by metallic implants, such as the widely used Titanium 6-Aluminum 4-Vanadium (Ti6Al4V) alloy in orthopaedic implants and do not directly correlate with the physiological microscale loading experienced by cells [11]. Given this gap, we have designed a compact customized mechanical

cell stimulation device which can be used inverted depending on the substrate material and test. This device is aimed to subject a substrate, either polymeric or metallic, to a bending loading that promotes tensile stress on its upper surface and allows to simultaneously perform cell culture, mechanical stimulation, and live imaging. Up to this point and to the knowledge of the authors, this is the first designed and manufactured device for conducting *in vitro* mechanobiology studies using metallic substrates.

## 9.2. Materials and methods

### 9.2.1. Device requirements, design and fabrication

The cell mechanical stimulation device disclosed here was designed to be used in mechanobiological studies either using transparent and opaque substrates for cell culture. Considering the need to control numerous factors involved in the specimen environment, some requirements were considered, and the main features of the device and correspondent objectives are described in Table 9.1.

Table 9.1 - Features of the customized cell mechanical stimulation device and the correspondent aim and advantages.

| **Features** | **Aim** |
|---|---|
| Compact | • Fit the stage top incubator;<br>• Easier transportation and handling. |
| Possibility of inversion | • Device can be used in upright and inverted microscopes, the latter being a popular technique for live cell imaging;<br>• In the case of an opaque substrate, such as metallic, the device can be mounted as inverted to be used in an inverted fluorescence microscope;<br>• Cells can be visualized in real time when cultured either on transparent and opaque substrates. |
| 360° rotation of medium reservoir | • When the device is inverted, the medium reservoir is rotated by 180°, allowing the observation and image acquisition of live cells in real time;<br>• The continuous renovation of the cell culture medium is essential for long-term experiments;<br>• Reservoir is sealed by an O-ring to prevent leakages. |

| | |
|---|---|
| Divided into two parts | • The cell culture space is independent of the external container that connects the substrate to the actuation mechanism;<br>• Cell culture can be performed in a common cell incubator (37 °C, 5% $CO_2$) and, only when needed, connected to the actuation mechanism for mechanical stimulation;<br>• The apparatus is simplified and subject to fewer handling errors. |
| All parts are made of sterile materials | • All parts of the device, the coverslip glass and the PDMS are sterilized previous the beginning of experiment. |
| PDMS interface | • The separation between the sterile and non-sterile environments is made of a PDMS sealing and can be exchanged when needed. |

The cell mechanical stimulation device was designed to be used in a stage top incubator, such as the Universal Mounting Frame KM (PeCon GmbH, Germany), and thus the overall dimensions corresponded to 127.5 x 85.3 x 18 mm. The selected substrate for *in vitro* testing was a Ti6Al4V plate purchased from Titanium Products (United Kingdom) with dimensions 45 x 10 x 0.52 mm. One of the most crucial imaging limitations is the maximum focal length, in this case, equal to 0.28 mm. A borosilicate glass coverslip from VWR International (631-0178, USA) was selected because its thickness is the minimum available on the market (equal to 0.13 mm), resulting in a maximum distance between the objective (when touching the glass coverslip) and the Ti6Al4V surface of 0.11 mm. This glass coverslip was glued using an epoxy glue and left to dry during 24 hrs. After evaluating all limitations and the mechanical principles of inventions and devices available on the market [18], a cantilever beam deflection-based system was selected to subject the substrate to a bending loading and consequently impart tensile stress to the cultured cells, as illustrated in Fig. 9.1.

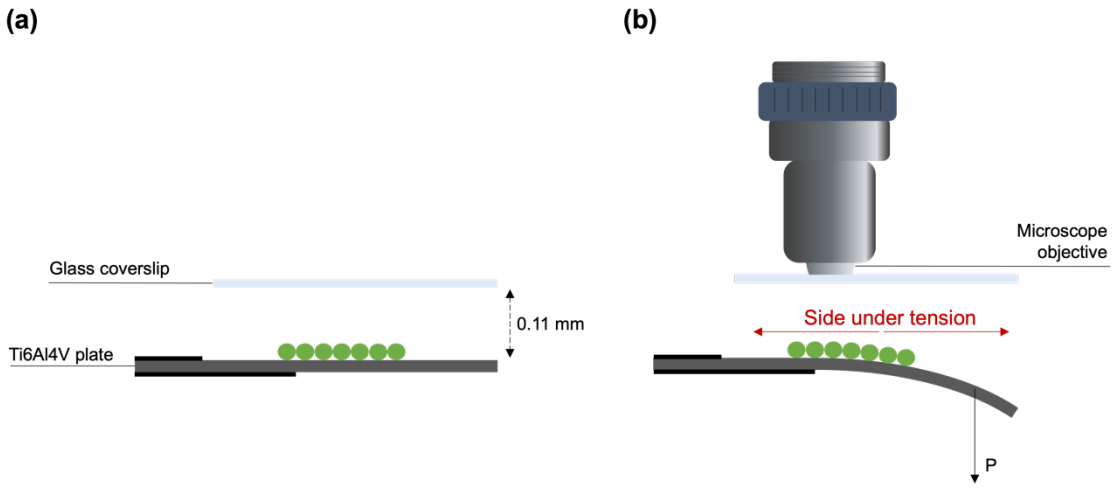



Figure 9.1 - Ti6Al4V plate at (a) neutral position and (b) under imposed force P. Cells (represented in green circles) cultured on the upper side of the substrate are subjected to tension and visualized through an inverted microscope. Note: image is not to scale.

After selecting the type and magnitude of the stress and the bending deformation-based system, some ideas were discussed on the actuation principle, as summarized in Appendix A. Then, after discussion of the pros and cons, a polydimethylsiloxane (PDMS) sealing placed on the bottom of the small container was selected to create the separation between the aseptic zone (culture medium) and the outside zone. In addition, an austenitic stainless-steel type 304 orthodontic wire (55.01.208; Morelli Ortodontia, Brazil) was selected to impose the mechanical loading on the substrate. For that purpose, on one end of the plate, a hole was performed at a distance of 2 mm using a Nd:YV04 laser (XM-30D, XianMing Laser, China) under an argon atmosphere. It therefore assures the aseptic conditions, and the mechanical loading is imposed externally by a micro-servo motor. In addition, the highest strains on the plate are observed in the region immediately after the support, corresponding therefore to the region of interest to be visualized through microscope imaging.

Depending on the design of experiments, from the time cells are cultured to the timepoint live imaging will occur, incubation may endure a few days or weeks. Therefore, during the incubation period living cells are grown in a cell culture incubator at 37 °C in an atmosphere of >95% humidity and 5% $CO_2$. The periodically exchange of culture medium is assured by the medium reservoir, which lid also provides consistent gas exchange while offering protection from the external environment. To create a versatile device, a medium reservoir was designed with the ability to rotate 360 degrees and sealed by an O-ring to prevent leakages. Therefore, the device may be used inverted allowing cellular imaging using opaque substrates, such as metallic.

The device was fabricated in stainless steel for sterilization purposes and all components were manufactured using laser technology. The PDMS sealing was prepared by mixing the PDMS curing agent with PDMS elastomer (1:10) using the SYLGARD™ 184 Silicone Elastomer Kit (DOW, Germany). After removing all bubbles in a vacuum desiccator, the PDMS was casted in place still in a liquid state already with the orthodontic wire. It was left to cure at 65 °C for 1 h and its sealing capacity was subsequently confirmed. Prior the beginning of each experiment, all parts of the device were autoclaved to prevent possible contaminations and their assembly was carefully performed inside a biological safety cabinet to assure aseptic conditions throughout the mounting process.

In order to apply mechanical loading, a servo motor was used due to its high velocity and torque and precise control over strain features, such as amplitude and frequency. A Micro Servo MG90S with metallic gear 1.8 kg (MOT03025; SAR - Soluções de Automação e Robótica, LDA, Portugal) was selected considering its low vibration and specifications described in Table 9.2.

Table 9.2 - Specifications of the Micro Servo MG90S with metallic gear.

| **Features** | |
|---|---|
| Operation voltage | 4.8 – 6 V (DC) |
| Rotational angle | 180 degrees |
| Velocity | 0.1 sec/60 degrees (at 4.8 V) |
| Torque | 1.8 kg cm (4.8 V) |
| Operating temperature | -30 °C ~ 60 °C |
| Dimensions | 22.8 x 12.2 x 28.5 mm |
| Weight | 13.4 g |

The motor wiring was connected to an Arduino (UNO R3) with an operating voltage of 5 V and the Arduino code, uploaded to the motor, is included in Appendix B.

### 9.2.2. Preliminary validation of the device

Based on the physiological bone conditions, the purpose of the present study is to apply a strain in the range of 800-1000 με at a 1 Hz rate [1]. Considering these loading conditions, the device was validated by numerical and experimental approaches. The first was performed using the COMSOL Multiphysics® v. 5.4. (COMSOL AB, Stockholm, Sweden) and the following restrictions

were defined: the Ti6Al4V plate is fixed on one extremity (supported by the bottom and top), in contact with one surface (bottom) in the next section, while the remaining extremity is free (with no support), as illustrated in Fig. 9.2.

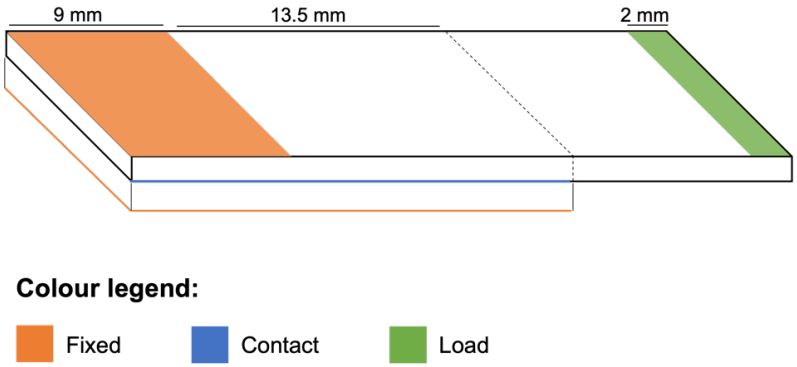



Figure 9.2 - Boundary restrictions imposed on the numerical simulation.

The numerical simulation was performed for Ti6Al4V (treated and aged condition) with the properties described in Table 9.3.

Table 9.3 - Properties of the Ti6Al4V selection used in the numerical simulation.

| **Property (unit)** | |
|---|---|
| Poisson's ratio (dimensionless) | 0.31 |
| Mass density (Kg/m$^3$) | 4428.784 |
| Tensile strength (N/mm$^2$) | 1050 |
| Yield strength (N/mm$^2$) | 827.37 |

Finally, the experimental approach consisted of applying a load on the Ti6Al4V substrate and assess the real strain using the Spider8 equipment. A strain gauge (Tokyo Sokki Kenkyujo Co., Ltd, Japan) which characteristics are displayed on Table 9.4, was bonded to the interest area of the Ti6Al4V plate using a rapid adhesive Z70 and connected to the Spider8 (HBM, Germany) data acquisition system, using the catman 3.1. software. The bridge was set as a quarter-half bridge with a measuring rate of 3 mV/V, the scaling method was defined as strain gage scaling (gage factor: 2 and bridge factor: 1) and the sample acquisition rate at 50 Hz.

Table 9.4 - Strain gauge characteristics.

| **Features** | |
|---|---|
| Type | FLA-3-11 |
| Gauge length | 3 mm |
| Gauge resistance | 120 ± 0.3 Ω |
| Gauge factor | 2.14 |
| Temperature compensation | 11 x $10^{-4}$/°C |
| Transverse sensitivity | 0% |

Additionally, the H100KS Hounsfield Universal Testing Instrument assembled with a 250 N load cell (Tinius Olsen) was used to apply a downward compressive load on the extremity of the Ti6Al4V plate (placed in the cell mechanical stimulation device). The maximum displacement was set at 10% and loading was applied at 240 mm/min.

### 9.2.3. Substrate preparation and topographical characterization

Ti6Al4V plates from Titanium Products (United Kingdom) were textured using a Nd:YAG laser (OEM Plus, SISMA, Italy) and laser parameters were selected as a result of a previous study [22]. Briefly, a pillar pattern was engraved by setting the laser power at 1.5 W, the scanning speed at 100 mm/s, the number of passages at 80 and the line spacing at 10 μm. Afterwards, samples were subjected to hydrothermal treatment, which consisted of placing the Ti6Al4V plates in a reactor and their immersion in distilled water for 180 min at 180 °C. Ti6Al4V substrates were then cooled till room temperature and ultrasonically cleaned with isopropyl alcohol for 5 min.

The topography of the modified surface was assessed using the S Neox 3D Optical Profiler (Sensofar, Spain) with a 10X objective and analysed with the Gwyddion software to assess the texture profile and dimensions. The 2D profile was acquired both in horizontal and vertical directions and five measurements were averaged to calculate each texture dimension.

### 9.2.4. Cell culture and stimulation conditions

Placental-derived amniotic membrane human mesenchymal stem cells from Evercyte (P-MSC/TERT308; Austria) were thawed and expanded using uniquely clinically compatible xeno-free and animal serum-free cell culture media, according to the protocols of Sartorius AG. Cells were cultured in T-flasks previously coated with NutriCoat™ Attachment Solution (05-760-1-15; Sartoris

AG, Spain) and incubated in a complete MSC medium composed of MSC NutriStem® XF Basal Medium (05-200-1; Sartorius AG, Spain), MSC NutriStem® XF Supplement Mix (05-201-1; Sartorius AG, Spain), PLTGold® Human Platelet Lysate (PLTGold27R; Sartorius AG, Spain) and G418 (ant-gn5; InvivoGen, France) in a $CO_2$ incubator (95% of air and 5% $CO_2$ at 37 °C). A complete medium change was performed every 3 days and when reached a confluence of 80%, MSC were washed with DPBS (D8537; Sigma- Aldrich, Germany) detached using CTSTM TrypLE™ Select Enzyme (A1285901; GibcoTM, USA) and used for osteogenic differentiation at passage 8.

Prior cell culture, Ti6Al4V substrates were sterilized, by immersion in 70% (v/v) ethanol for 1 h each side, followed by irradiation of UVC light (wavelength of 100-280 nm) for 2 hrs each side, inside a laminar flow cabinet Bio II Advance Plus (Telstar), and stored in the dark. MSC were seeded on the treated side of Ti6Al4V at a cellular density of $3x10^4/cm^2$ in a form of a droplet and incubated for 30-60 min. The complete MSC medium was then added and placed in a $CO_2$ incubator After 24 hrs, the MSC culture medium was changed to the osteogenic differentiation medium (05-440-1; Sartorius AG, Madrid, Spain). Cells were incubated for up to 4 days in static mode and then dynamic mechanical loading was applied for 15 min (900 με at 1 Hz). Before mechanical loading cells were incubated with CellMask™ Green Plasma Membrane stain (C37608, 1:1000; Invitrogen, USA) for 30 min in a $CO_2$ incubator. Immediately before and after mechanical stimulation, cells were live imaged in Leica DMI 6000 Timelapse (Leica Microsystems, Germany) with the camera Hamamatsu FLASH4.0 (Hamamatsu, Japan) and filter L5 (excitation: 460-500 and emission: 512-542) using a full environmental chamber with temperature and $CO_2$ control (37 °C, 5% $CO_2$). The LAS X software was used to acquire all images. For time-lapse imaging analyses one image was taken every 30 sec in a period of 3 min.

## 9.3. Results and discussion

### 9.3.1. Description of the cell mechanical stimulation device

The cell mechanical stimulation device was designed and projected to meet the requirements described in Table 9.1. This compact device aims to mechanically stimulate and monitor cells in real time using transparent or opaque culture substrates, such as metallic. The fact that it can be used inverted allows for the mechanical stimulation of cells and the simultaneous evaluation of cell behaviour in real time using an inverted fluorescence microscope. The device usage is divided into two stages: (a) cell culture in an isolated cell culture vessel comprising cell culture on the Ti6Al4V substrate, its immersion in the culture medium and incubation for the

desired period of time through periodic renewal of the culture medium and gas exchange through a reservoir; b) mechanical cell stimulation, which involves mounting the cell culture container in an external container by connecting the substrate to a lever and therefore to a motor that will apply cyclic loading to the substrate and therefore to the cells cultured on it. Given the opaqueness of the substrate, the device will be then inverted and positioned in an inverted florescence microscope, allowing cell monitoring in real time. The main parts of the device are displayed in Fig. 9.3 by order of assembly.

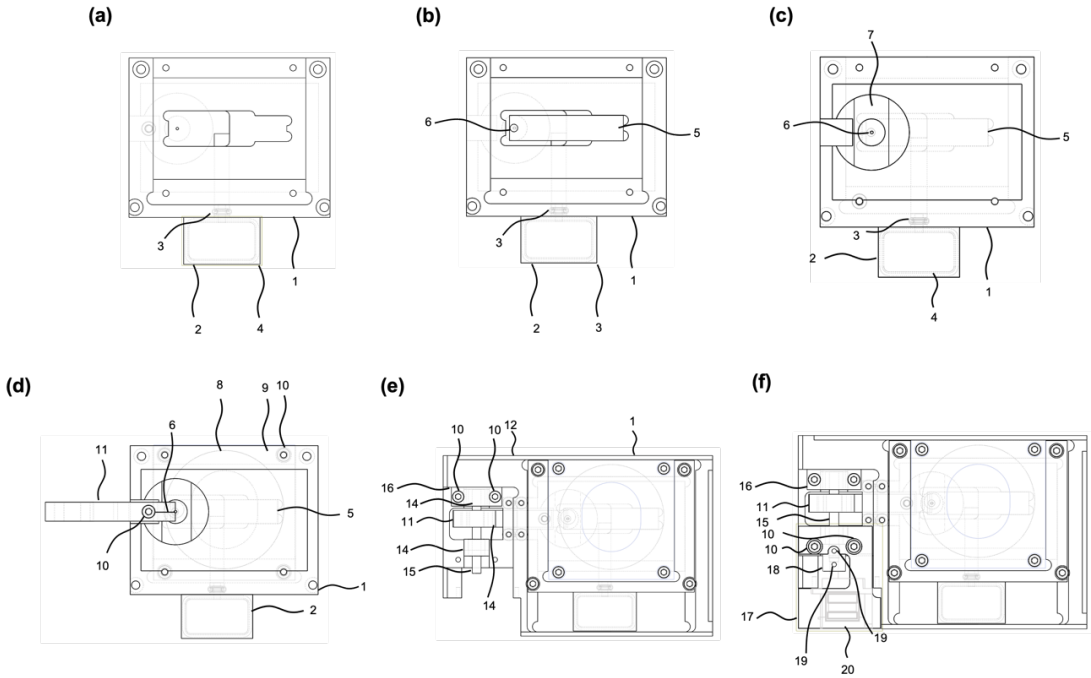



Figure 9.3 - Drawings of the mechanical stimulation device. The device is composed of two main parts: the cell culture container represented by 1 (a, b and c), and the mechanical cell stimulation involves the connection of a wire (6) fixed on one extremity of the Ti6Al4V substrate (5) (d), which involves mounting the cell culture container in an external container represented by 12 (e and f).

The cell culture container (1) includes a culture medium reservoir (2) whose arm is surrounded by an O-ring (3) and a reservoir lid (4) (Fig. 9.3a). The culture medium reservoir (2) is able to rotate 360° so that its lid is always facing upwards. Under sterile conditions, the substrate (5) is placed on a support so that one end is supported from below while the opposite end is free for stretching and a wire (6) is positioned trespassing the substrate. A membrane made of PDMS covers the circular base of the bottom of the cell culture container (1) and its thickness is defined by a plate (7) which is attached to the base so that the membrane is constrained between the base and the plate (7). Thus, the wire (6) passes through this membrane which, in turn, demarcates the sterile space from the non-sterile space (Fig. 9.3b). During the cell culture procedure, the cell

culture container (1) is handled while faced up and the cells are cultured on the upper side of the substrate, in this case, on the textured area. To ensure ideal incubation conditions, the cell culture container has a reservoir (2) and a lid (4) to allow media changes when necessary and appropriate gas exchanges. The cell culture container (1) is then closed with the lid of the cell culture container (9), to which a glass coverslip suitable for microscopy has previously been glued. An elliptical hole in the lid of the cell culture container (9) allows the entrance of the microscope objective (Fig. 9.3c). Until the begin of mechanical stimulation, the cell culture container (1) with the cells in culture is handled face up and in placed inside a $CO_2$ incubator. For the mechanical stimulation, the cell culture container (1) is placed inside an external container (12) and the wire (6) is connected to the lever (11) by positioning it around a screw (Fig. 9.3d). Three bearings (14) are placed, such as two are in the two concavities in the outer container (12) and the third inside the lever arm (11). An eccentric (15) is positioned inside the bearings which are secured by a support piece (16). A coupler (18) is used to connect the eccentric (15) to an electric motor (20). All support pieces (16 and 17) are secured by screws (10) (Figs. 9.3e and f). The actuation mechanism thus involves converting the rotary movement of the electric motor into linear movement via the lever.

### 9.3.2. Preliminary validation

#### 9.3.2.1 Numerical simulation

Considering the restrictions displayed in Fig. 9.2 and the bone physiological conditions, a strain of approximately 900 $\mu\varepsilon$ is obtained for a vertical load of 1.5 N applied to one extremity of the Ti6Al4V plate, generating a maximum deflection of 0.79 mm, as represented in Figs 9.4 and 9.5, respectively.

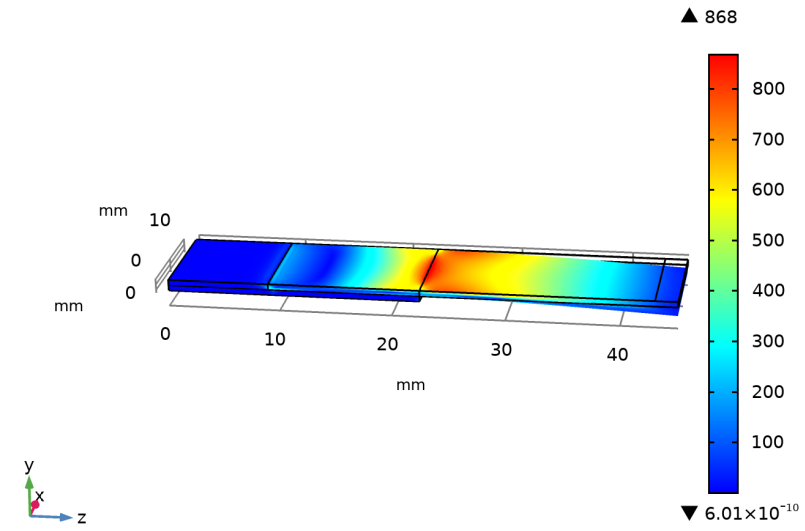



Figure 9.4 – First principal strain of the Ti6Al4V plate after applying a vertical load of 1.5 N at one extremity of the plate. The plate zone subjected to higher strain will be imaged through an inverted fluorescence microscope. Scale bar is in microstrain (strain x $10^6$, dimensionless).

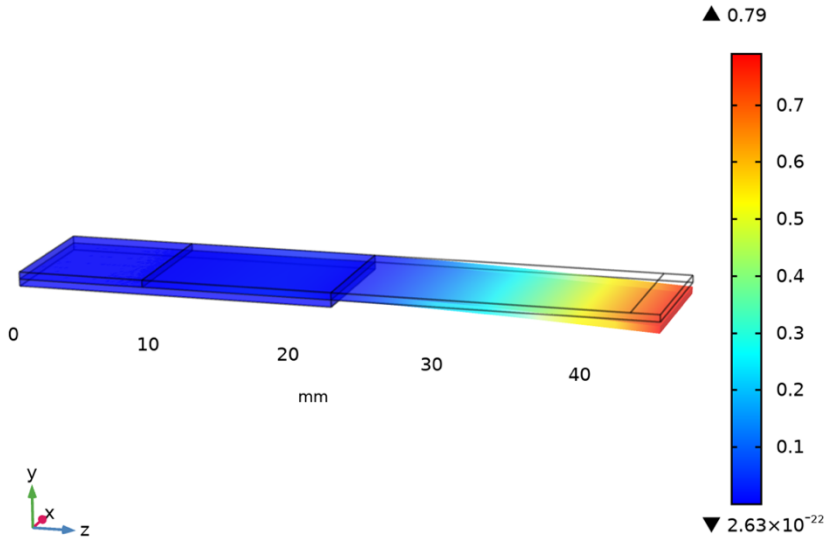



Figure 9.5 – Total displacement of the Ti6Al4V plate by applying a load of 1.5 N. Scale bar is in mm units.

As predicted, the region of the plate subjected to higher strains corresponds to that immediately after the contact with the bottom support, as corroborated in Fig. 9.4. The Ti6Al4V plate when at 0° is at the neutral position and during the bending deformation one extremity is pulled down, moving away from the glass coverslip, approximately at 0.79 mm, as observed in Fig. 9.5.

9.3.2.2 Experimental analysis

The real strain was assessed using the Spider8 equipment. The output of the transducer is expressed in either equivalent strain (x$10^{-6}$ strain) or voltage (mV/V) per excitation voltage, both being related as follows,

$$e = \frac{1}{4} Ks.E_v.\varepsilon \qquad \text{(eq. 9.1)}$$

where $e$ is the bridge output voltage, $Ks$ is the gage factor of strain gage, $E_v$ the excitation voltage and $\varepsilon$ the strain. The gage factor is 2 therefore,

$$2\frac{e}{E_v} = \varepsilon \qquad \text{(eq. 9.2)}$$

If $E_v$ = 1 (V), then

$$2e = \varepsilon \qquad \text{(eq. 9.3)}$$

The strain values acquired for a motor rotation angle of 180° are represented in Fig. 9.6.

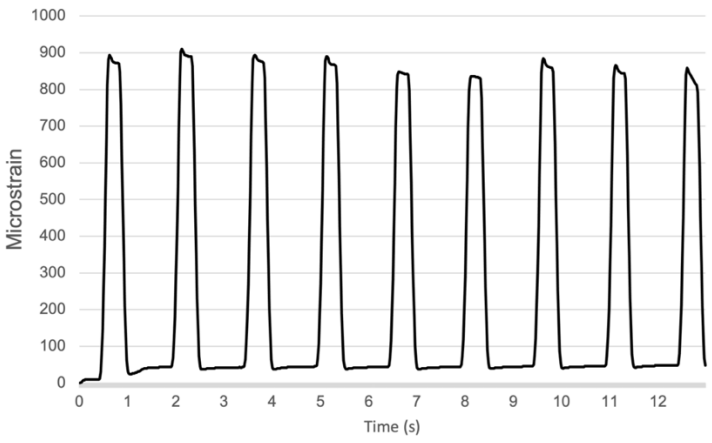



Figure 9.6 - Strain values of Ti6Al4V plate under tensile stress by setting a total rotation angle of 180°.

When the motor rotation angle is maximum (180°), the maximum strain is approximately 900 με. Therefore, considering the Ti6Al4V plate as the substrate to cultivate cells, a maximum strain of 900 με can be achieved using this mechanical stimulation device, using the selected motor. Additionally, for an applied load of 1.59 N, a maximum displacement of 0.79 mm was determined, which is in line with the numerical simulation.

9.3.3. *In vitro* testing of the device

Mesenchymal stem cells were cultured on hydrothermally treated Ti6Al4V substrates with a pyramid-inspired textured patterned, as shown in Fig. 9.7, with a groove width of 93.2 ± 2.3 μm,

pillar width of 15.0 ± 2.3 μm and pillar depth of 20.4 ± 1.3 μm. Immediately before and after being subjected to mechanical loading, cells were live imaged as displayed in Fig. 9.8.

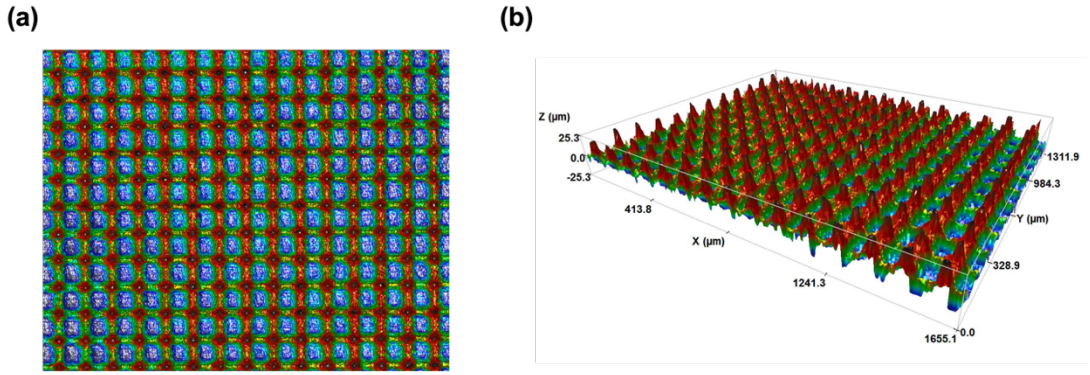



Figure 9.7 - (a) 2D and (b) 3D optical profilometry images of the textured sample. Pillar peaks are represented in red whereas deeper holes are in blue.

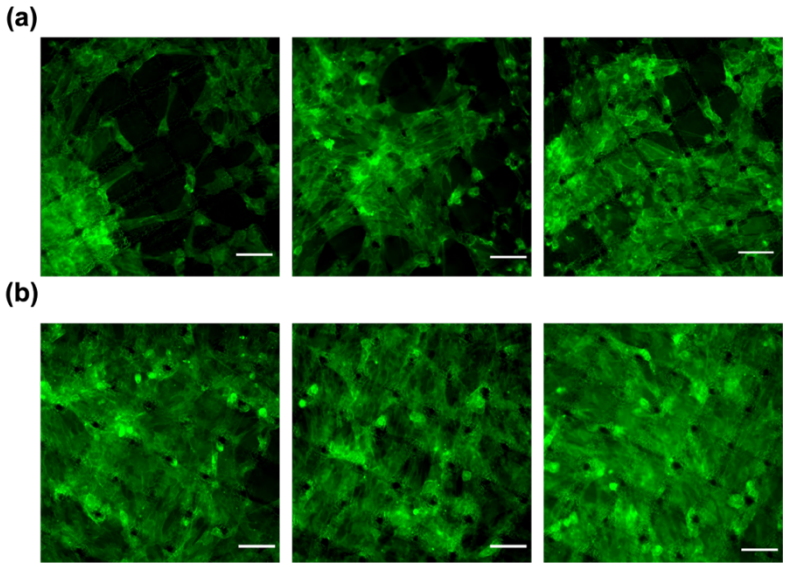



Figure 9.8 - Fluorescence microscopy was used to analyse MSC cultured in osteogenic differentiation medium for 4 days (a) before and (b) after mechanical loading. CellMask™ was used to visualize the plasma membrane (green fluorescence). All images include a 100 μm scale bar.

The present study comprised on stimulating MSC for solely 15 min which, as expected, did not have an impact on the cell morphology and potential osteogenic readout. This preliminary live cell dynamic study shows a uniform staining of the plasma membrane and a time-lapse of 30 sec shows no changes on the cellular morphology and behaviour (Fig. 9.9).

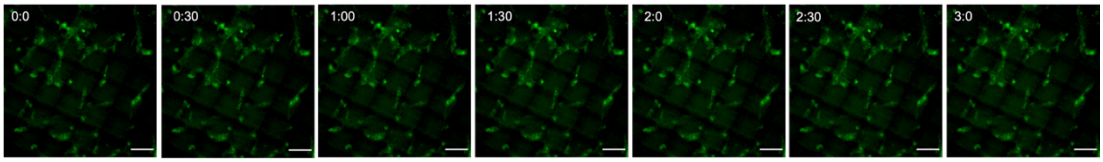



Figure 9.9 - Time-lapses live cell-imaging of MSC after performing the mechanical loading. Each image was taken every 30 sec, and all images include a 100 μm scale bar.

The purpose of this study was to validate a custom-designed device with regard to both its actuation mechanism and its biological compatibility, using MSC. When mechanical loading is applied to one end of the plate, it generates a strain gradient along its length. Consequently, cultured cells experience a gradient of strain rather than a single value. However, the available space for the microscope objective is currently limited, as the primary focus was to assess cellular behaviour under maximum amplitude loading conditions. This limitation is primarily due to the design of the upper lid of the device, specifically the space allocated for the microscope objective. To enhance the versatility of the experimentation, potential modifications to the device design could be considered. For instance, adjusting the microscope objective space would enable to study cellular behaviour under multiple mechanical conditions simultaneously by selecting specific areas of interest. Future studies will delve into the dynamics of MSCs and their response to mechanical loading, aiming to replicate physiological bone loading conditions by applying prolonged and repeated mechanical stimulation over days or weeks.

## 9.4. Conclusions

A novel mechanical cell stimulation device was designed and fabricated for mechanobiology studies, using polymeric or metallic substrates for cell culture. Its compactness and possibility to be used inverted, is used to subject the substrate to a bending load that promotes tensile stresses on its upper surface, and allows cell culture, mechanical stimulation and live imaging for mechanobiology studies to be carried out simultaneously. The device is capable of producing consistent and reliable strain profiles using a servomotor, which can be programmed to output various frequencies and stretch amplitudes by controlling the degree of rotation. A Ti6Al4V plate was used as the substrate for cell culture and a micro-pillar pattern was engraved by laser to augment the loading sensed by cells. The device was used to uniaxially strain mesenchymal stem cells in an osteogenic culture medium which were live imaged before and after mechanical loading. This preliminary validation confirms that the device can be used to subject cells to mechanical loading cultured on a metallic, and thus opaque substrate. This offers new possibilities for

mechanobiology studies as the physiological scenarios of orthopaedic implants may be closer reproduced.

## Acknowledgments

This work was supported by FCT (Fundação para a Ciência e a Tecnologia) through the grants SFRH/BD/141056/2018, COVID/BD/152996/2022 and UMINHO/BID/2023/04 and the projects PTDC/EME-EME/1442/2020, POCI-01-0145-FEDER-030498, UIDB/04436/2020 and UIDP/04436/2020. In addition, this work was developed within the scope of the project CICECO-Aveiro Institute of Materials, UIDB/50011/2020, UIDP/50011/2020 & LA/P/0006/2020, financed by national funds through the FCT/MCTES (PIDDAC). The authors would like to thank Senhor Araújo for assisting gluing the strain gauge to the Ti6Al4V and using of the Spider 8 equipment and to the Microscopy facility at I3S.

## References

[1] F. Melo-Fonseca, G. Miranda, H.S. Domingues, I.M. Pinto, M. Gasik, F.S. Silva, Reengineering Bone-Implant Interfaces for Improved Mechanotransduction and Clinical Outcomes, Stem Cell Rev. Reports. (2020). https://doi.org/10.1007/s12015- 020-10022-9.

[2] R. Daza, B. González-Bermúdez, J. Cruces, M. De la Fuente, G.R. Plaza, M. Arroyo-Hernández, M. Elices, J. Pérez-Rigueiro, G. V. Guinea, Comparison of cell mechanical measurements provided by Atomic Force Microscopy (AFM) and Micropipette Aspiration (MPA), J. Mech. Behav. Biomed. Mater. 95 (2019) 103–115. https://doi.org/10.1016/j.jmbbm.2019.03.031.

[3] M. Berardi, K. Bielawski, N. Rijnveld, G. Gruca, H. Aardema, L. van Tol, G. Wuite, B.I. Akca, Optical interferometry based micropipette aspiration provides real-time sub- nanometer spatial resolution, Commun. Biol. 4 (2021) 1–7. https://doi.org/10.1038/s42003-021-02121-1.

[4] Y.M. Efremov, W.H. Wang, S.D. Hardy, R.L. Geahlen, A. Raman, Measuring nanoscale viscoelastic parameters of cells directly from AFM force-displacement curves, Sci. Rep. 7 (2017) 1–14. https://doi.org/10.1038/s41598-017-01784-3.

[5] N. Schierbaum, J. Rheinlaender, T.E. Schäffer, Combined atomic force microscopy (AFM) and traction force microscopy (TFM) reveals a correlation between viscoelastic material properties and contractile prestress of living cells, Soft Matter. 15 (2019) 1721–1729. https://doi.org/10.1039/c8sm01585f.

[6] M. Krieg, G. Fläschner, D. Alsteens, B.M. Gaub, W.H. Roos, G.J.L. Wuite, H.E. Gaub, C. Gerber, Y.F. Dufrêne, D.J. Müller, Atomic force microscopy-based mechanobiology, Nat. Rev. Phys. 1 (2019) 41–57. https://doi.org/10.1038/s42254-018- 0001-7.

[7] S.S. Hur, J.H. Jeong, M.J. Ban, J.H. Park, J.K. Yoon, Y. Hwang, Traction force microscopy for understanding cellular mechanotransduction, BMB Rep. 53 (2020) 74– 81. https://doi.org/10.5483/BMBRep.2020.53.2.308.

[8] V. Marx, May mechanobiology work forcefully for you, Nat. Methods. 16 (2019) 1083–1086. https://doi.org/10.1038/s41592-019-0621-6.

[9] C. Arbore, L. Perego, M. Sergides, M. Capitanio, Probing force in living cells with optical tweezers: from single-molecule mechanics to cell mechanotransduction, Biophys. Rev. 11 (2019) 765–782. https://doi.org/10.1007/s12551-019-00599-y.

[10] S.R. Heidemann, D. Wirtz, Towards a regional approach to cell mechanics, Trends Cell Biol. 14 (2004) 160–166. https://doi.org/10.1016/j.tcb.2004.02.003

[11] K.H. Vining, D.J. Mooney, Mechanical forces direct stem cell behaviour in development and regeneration, Nat. Rev. Mol. Cell Biol. 18 (2017) 728–742. https://doi.org/10.1038/nrm.2017.108.

[12] K. Uto, J.H. Tsui, C.A. Deforest, D. Kim, Dynamically tunable cell culture platforms for tissue engineering and mechanobiology, Prog. Polym. Sci. 65 (2017) 53–82. https://doi.org/10.1016/j.progpolymsci.2016.09.004.

[13] R.D. Sumanasinghe, S.H. Bernacki, E.G. Loboa, Osteogenic Differentiation of Human Mesenchymal Stem Cells in Collagen Matrices: Effect of Uniaxial Cyclic Tensile Strain on Bone Morphogenetic Protein (BMP-2) mRNA Expression, Tissue Eng. 12 (2006) 3459–3465. https://doi.org/10.1089/ten.2006.12.3459.

[14] S.F. Carroll, C.T. Buckley, D.J. Kelly, Cyclic tensile strain can play a role in directing both intramembranous and endochondral ossification of mesenchymal stem cells, Front. Bioeng. Biotechnol. 5 (2017) 1–12. https://doi.org/10.3389/fbioe.2017.00073.

[15] A. Charoenpanich, M.E. Wall, C.J. Tucker, D.M.K. Andrews, D.S. Lalush, D.R. Dirschl, E.G. Loboa, Cyclic tensile strain enhances osteogenesis and angiogenesis in mesenchymal stem cells from osteoporotic donors, Tissue Eng. - Part A. 20 (2014) 67– 78. https://doi.org/10.1089/ten.tea.2013.0006.

[16] M.M. Frigault, J. Lacoste, J.L. Swift, C.M. Brown, Live-cell microscopy - Tips and tools, J. Cell Sci. 122 (2009) 753–767. https://doi.org/10.1242/jcs.033837.

[17] L. Schermelleh, A. Ferrand, T. Huser, C. Eggeling, M. Sauer, O. Biehlmaier, G.P.C. Drummen, Super-resolution microscopy demystified, Nat. Cell Biol. 21 (2019) 72–84. https://doi.org/10.1038/s41556-018-0251-8.

[18] F. Melo-Fonseca, O. Carvalho, M. Gasik, G. Miranda, F.S. Silva, Mechanical stimulation devices for mechanobiology studies: a market, literature, and patents review, Springer Nature Singapore, 2023. https://doi.org/10.1007/s42242-023-00232- 8.

[19] T. Kanno, T. Takahashi, W. Ariyoshi, T. Tsujisawa, M. Haga, T. Nishihara, Tensile mechanical strain up-regulates Runx2 and osteogenic factor expression in human periosteal cells: Implications for distraction osteogenesis, J. Oral Maxillofac. Surg. 63 (2005) 499–504. https://doi.org/10.1016/J.JOMS.2004.07.023.

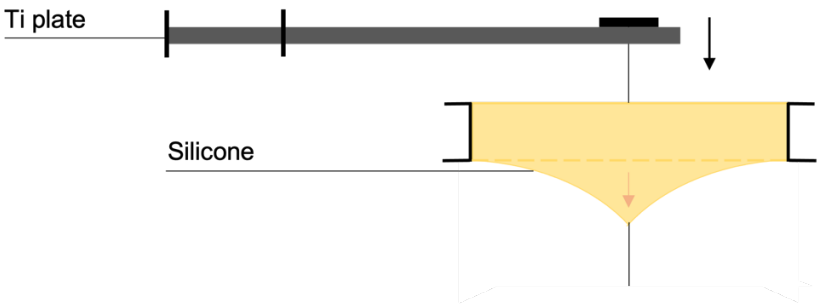
[20] C.T. Rubin, L.E. Lanyon, Osteoregulatory nature of mechanical stimuli: Function as a determinant for adaptive remodeling in bone, J. Orthop. Res. 5 (1987) 300–310. https://doi.org/10.1002/jor.1100050217.

[21] FROST, H. M., The Laws of Bone Structure. Springfield IL, Charles C. Thomas. (1964). https://ci.nii.ac.jp/naid/10006607916/ (accessed September 14, 2018).

[22] F. Melo-Fonseca, B. Guimarães, M. Gasik, F.S. Silva, G. Miranda, Experimental analysis and predictive modelling of Ti6Al4V laser surface texturing for biomedical applications, Surfaces and Interfaces. 35 (2022) 102466. https://doi.org/10.1016/j.surfin.2022.102466.

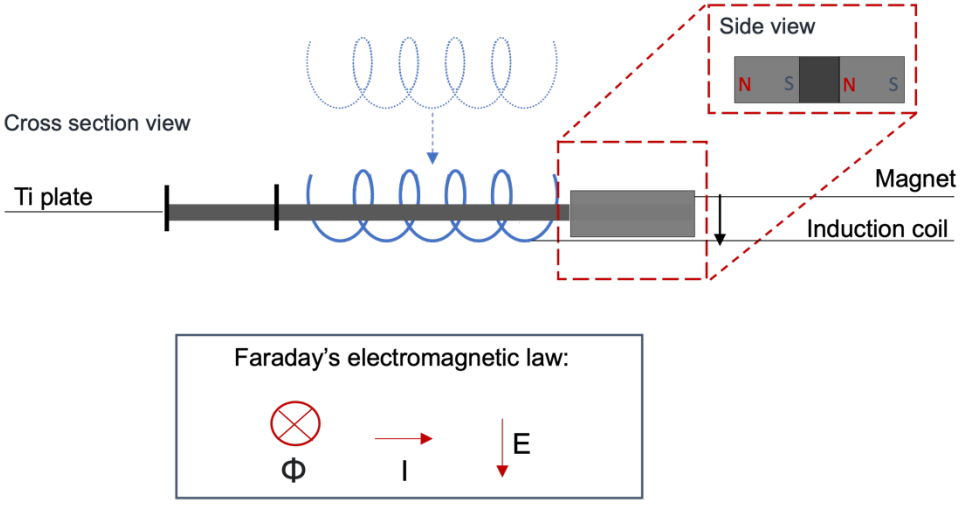
## Appendix A

After selecting the mechanical stress and the cantilever deformation-based system, some ideas were discussed regarding how to impose this movement on the substrate. One idea consisted of creating a hole on one extremity of the substrate and use a piece similar to a needle to trespassing it in order to pull the substrate down. The “needle”-like piece would impose the mechanical load on the free extremity of the substrate, through the action of a motor. This piece would penetrate a silicone membrane, so that the superior part of needle would never contact the air, preventing possible contaminations and sealing the region filled with liquid, as illustrated in Supplementary Fig. 9.1.




Supplementary Figure 9.1- A silicone membrane would be fixed and act as an impermeabilized material, in such a way that it would seal the region filled with liquid (sterile environment). The deformation of the silicone membrane while pulling down the plate would prevent contaminations.

Another approach included the magnetic actuation principle, in which two magnets would be tightly fixed on the plate, as represented in Supplementary Fig. 9.2. According to the Faraday's law of induction, an electric current (I) is induced when a magnetic field undergoes change. The magnitude of the electromotive force (E) generated in the circuit is proportional to the rate of change over time of the magnetic flux ($\Phi$) intersecting the circuit. Therefore, by the action of an induction coil the Ti-based substrate would be pulled down, but the deflection velocity could not be precisely controlled. In addition, the device material would correspond to austenitic stainless steel but, during the forming process, if the austenitic steel would suffer a mechanical stress, it could become partially magnetic due to a phase transformation compromising the actuation principle.




Supplementary Figure 9.2 - The magnetic principle would include the attachment of two magnets aside the titanium plate which, when desired, would deflect by the action of an induction coil.

## Appendix B

The appendix includes information regarding the designed device. The Arduino code, uploaded to the motor for the dynamic in vitro tests, is described as follows:

```
 #include <Servo.h>

#define SERVO 9 // Digital port 9 PWM

Servo myservo;

void setup()

{

  Myservo.attach(9);

}

void loop()

{

  myservo.writeMicroseconds(1000); // set servo to fully counter-clockwise

  delay(500);

  myservo.writeMicroseconds(2000); // set servo to fully clockwise

  delay(500);

}
```

# CHAPTER 10

## DISCUSSION AND CONCLUSIONS

This chapter presents the main conclusions of the work developed in this PhD thesis, some suggestions for future works and finally further contributions to this PhD thesis.

## 10.1. General discussion

This PhD was focused on the study of mechanotransduction modulation to enhance the osteointegration on the interface of orthopaedic implants, commonly composed of Titanium 6-Aluminum 4-Vanadium alloy (Ti6Al4V). Therefore, and having in mind that human mesenchymal stem cells (MSC) are mechanosensitive cells, this work focused on the improving biomaterial surface design to promote their commitment toward osteogenic lineage. Different surface modification techniques were evaluated including the hydrothermal treatment to create an oxide film and laser surface texturing to introduce a micro-pillar texture on Ti6Al4V substrates. The oxide layer and topographical features were characterized in terms of roughness, microstructure and wettability and the biological performance was assessed, in static mode. A custom-made cell mechanical stimulation device was designed and manufactured, and after validation, the cellular behaviour was assessed, in dynamic mode.

Despite the advancements in orthopaedic-related biomaterials, aseptic failures are still reported, often due to improper static and dynamic biomechanical compliance at the bone-implant interface. Therefore, in Chapter 2, a review was conducted on mechanobiological studies to evaluate the response of MSC to physical and mechanical cues in the context of bone research to ascertain the preferable signals for promoting physiological osteogenic differentiation, highlighting the impact of the design of orthopaedic implants.

Nanoengineered titanium substrates and their alloys, such as Ti6Al4V, are among the most commonly used materials in load-bearing applications. Although having high biocompatibility, Ti-based materials hold a low bioactivity profile. Therefore, in Chapter 3, different pre-treatments (alcohol and acidic) and modification treatments (anodic oxidation and hydrothermal treatment) were applied to commercially pure Ti and Ti6Al4V substrates. As a result of an extensive characterization of the oxide films, an alcohol pre- treatment followed by hydrothermal treatment was proposed as one strategy able to create a potentially bioactive and hydrophilic layer. Therefore, this surface treatment was selected for the cellular studies. Given the potential and advantages already covered in the literature [1,2], only Ti6Al4V was used for further studies.

Prior the cellular study on metallic substrates, a preliminary study was performed using MSC. The majority of cellular experiments use plastic well-plates and glass coverslips as substrates for cell culture and conventional cell culture media. On another hand, as described in Chapter 4, MSC were cultured using exclusively xeno-free and serum-free reagents, and higher values of

mineralization were observed when substrates were functionalized with a bioactive compound (fibronectin derived from human plasma). In addition, differences in the organization of actin stress fibers across the cell were observed during osteogenic differentiation, suggesting a correlation between cytoskeleton organization and cell commitment.

Subsequently, as stated in Chapter 5, MSC were cultured on different Ti6Al4V substrates. Due to the fact that the sterilization process disclaimed in Chapter 3 did not present a sufficiently low wettability for biomedical applications, a different sterilization approach was followed on Ti6Al4V, through UVC irradiation. Hydrothermal treatment followed by a functionalization with human fibronectin promoted osteogenic differentiation of MSC due to an increase in the mineral matrix formation and upregulation of osteogenic- related markers. This responsiveness to osteogenic differentiation is believed to be correlated with the oxide film characteristics produced by hydrothermal treatment, as well as the increase in cell adhesiveness as a result of functionalized human fibronectin, as demonstrated in Chapters 3 and 4, respectively.

Besides the oxide film aiming to confer bioactivity to the Ti6Al4V substrate, topography enhances the interface between host bone and implant. In fact, from the survey in Chapter 2, it was found that MSC are highly sensitive to the surface pattern as it has a profound impact on the cytoskeleton organization. Among the different patterns, pillars have been reported to have enhanced osteogenesis. Therefore, as in Chapter 6, pillars were produced by laser surface texturing on Ti6Al4V parts. Nd:YAG laser was used to texture micro-scale pillars with pyramid geometry with targeted groove width of 60±5, 90±5 and 120±5 μm, pillar width of 20±5 μm and pillar depth of 50±5 μm. The consecutive laser processing and continuous marking mode were selected based on the surface quality and accurate mathematical models were obtained for predicting features dimensions. Afterward, drawing and laser parameters were correlated with texture dimensions by ANOVA and the three target dimensions were achieved using a set of input parameters, with similar surface roughness, suitable for biomedical applications.

Based on the drawing and laser parameters evaluated in the study on Chapter 6, the osteogenic commitment of MSC cultured on pillar patterned Ti6Al4V was evaluated (Chapter 7). Due to variances in the laser processing, a fine adjustment on the laser parameters was required and patterns with groove widths of 60±5, 90±5 and 120±5 μm were obtained using the same laser. The laser surface texturing was combined with the hydrothermal treatment and fibronectin coating, based on the results from Chapters 3, 4 and 5 and the surface was characterized in terms

of topography, crystallography and wettability. Textured Ti6Al4V systems exhibited robust MSC adhesion and the in vitro mineralization capacity after 21 days in osteogenic differentiation medium was on par with, or even exceeded, that of conventional sand-blasted, large-grit, acid-etched (SLA) Ti6Al4V. Notably, the texture with groove width of 90 μm showed the highest mineralization capacity and potentially bioactivity.

All the *in vitro* studies described in the previous chapters were performed in static mode. However, one of the goals of this thesis was to address the cell behaviour in response to mechanical loading aiming to enhance the potential for osseointegration. Based on the promising results reviewed in Chapter 2, the working principle of existing mechanical stimulation devices were systematically evaluated in Chapter 8. The strategies of different mechanical stimulation devices were compared to not only enable an informed choice for a particular study but also highlight the main features still open to improvement to perform more reliable and accurate mechanobiology studies.

Despite the diversity of the devices covered in Chapter 8, their use is limited to apply and assess the cellular behaviour when cells are cultured on polymeric substrates or incorporated into three-dimensional constructs. However, orthopaedic implants are composed of metallic materials, such as Ti6Al4V. Therefore, a custom-made cell mechanical stimulation device was designed as described in Chapter 9. This device can be used to simultaneously culture cells, apply mechanical stimulation to the substrate, which can be polymeric or metallic, and perform live imaging, in inverted confocal microscopes. Given the cellular results of the Ti6Al4V systems disclosed in Chapter 7, micro-pillars with 90 μm groove width were engraved on Ti6Al4V and further subjected to hydrothermal treatment. MSC were cultured on this Ti6Al4V system for 4 days, and the device was validated by applying a tensile loading of 900 microstrain at 1 Hz for 15 min. Immediately before and after mechanical loading, cells were stained and monitored in real time using an inverted microscope.

The work discussed in this thesis combined engineering and biological-related concepts and techniques aiming to evaluate different strategies to improve the bioactivity of Ti6Al4V and promote osteogenic differentiation of MSC. Orthopaedic implants should be (1) osteoinductive to stimulate the differentiation of MSC into osteoblasts, (2) osteoconductive to enable the deposition of mineralized tissue on their surface, thereby binding to bone and, finally, promote (3) osteointegration to form a mechanically stable bond to the surrounding native bone [3]. Having

this purpose, the surface obtained by different strategies was characterized in-depth and evaluated through cellular assays. According to the last report on the Guidance on Good Cell Culture Practice produced by the European Commission's Joint Research Centre (JRC), minimum standards for cell and tissue cultures should be followed to maximize the reproducibility, reliability, credibility, acceptance and ensure the proper application of the obtained results [4]. Despite the myriad challenges inherent to scientific studies, a thoughtful compromise was forged to propose a promising strategy to modulate MSC activation towards improved osseointegration. Pillar micro-structures combined with hydrothermal treatment have shown a similar or even better performance compared to state-of-the-art implants surfaces in static mode, and the introduction of this topography augments the mechanical cues imposed on cells when in dynamic mode. The in-depth study of cellular behaviour when subjected to mechanical loading will pave the way to designing a novel osteogenic-stimulating implant.

## 10.2. Main conclusions

Based on the research conducted in this thesis, it can be inferred that:

- Human mesenchymal stem cells (MSC) are mechanosensitive and their differentiation into bone cells is promoted when conventional substrates are functionalized with human fibronectin, using exclusively xeno-free and serum-free reagents;
- The use of xeno-free and serum-free reagents should be widespread adopted in cell studies to enhance credibility and acceptance, particularly when translating the laboratory finding into clinical applications;
- Laser surface texturing of micro-pillars on Ti6Al4V combined with hydrothermal treatment and functionalization with human derived fibronectin promotes MSC activation and differentiation into bone cells;
- Mechanical loading modulates MSC behaviour, and the first device capable of simultaneously culturing cells, applying mechanical loading, and monitoring them in real time has been designed and tested.

## 10.3. Suggestions for future works

Based on the findings of this PhD work, some suggestions for future work can be enumerated:

- Test MSC from different donors due to genetic variability between donors;
- Deepen the osteogenic differentiation of MSC, in static mode;

- Test increased mechanical loading durations using the cell mechanical stimulation device;
- Study the osteogenic differentiation potential of MSC, both in static and dynamic modes, without osteogenic differentiation medium.

## 10.4. Further contributions to this thesis

In addition to the studies developed and described in this thesis chapters, the following conferences/workshops were attended during this PhD:

- F. Melo-Fonseca, Inês Mendes Pinto, M. Gasik, F. S. Silva, G. Miranda, *MSC morphofunctional programming for improved orthopaedic implantation outcomes.* CMBBE 2023: the 18th International Symposium on Computer Methods in Biomechanics and Biomedical Engineering, 3-5 May 2023, Arts Et Métiers - Institute of Technology, Institut De Biomécanique Humaine Georges Charpak, Paris, France. Oral presentation.
- F. Melo-Fonseca, M. Gasik, S. Madeira, F. S. Silva, G. Miranda, *Improving the interface between orthopaedic implants and bone – a comparison between different surface treatments*. Junior Euromat 2022. 19-22 July 2022, University of Coimbra, Coimbra, Portugal. Oral presentation.
- F. Melo-Fonseca, Inês Mendes Pinto, M. Gasik, F. S. Silva, G. Miranda, *Design of pro-active bone-stimulating implants*. VII International Conference IMFAHE, 3 May 2021 - online. Oral presentation.
- F. Melo-Fonseca, Inês Mendes Pinto, M. Gasik, F. S. Silva, G. Miranda, *Designing osteogenic-stimulating titanium-based implants*. 8th International Conference on Mechanics of Biomaterials and Tissues, 15-19 December de 2019, Waikoloa, Hawaii, United States of America. Oral presentation.
- F. Melo-Fonseca, Inês Mendes Pinto, M. Gasik, F. S. Silva, G. Miranda, *Improved implant-host bone interaction by stimulating physiological MSC - osteogenic differentiation*. Ciência 2019 - Science and Technology Summit in Portugal, 8 July 2019, Lisbon Congress Centre, Lisbon, Portugal. Poster presentation.
- F. Melo-Fonseca, Inês Mendes Pinto, M. Gasik, F. S. Silva, G. Miranda, *Understanding mechanobiology – Linking the mechanical stimulation to cellular response*. 8th National

Congress on Biomechanics, 15 and 16 February 2019, Unhais da Serra, Covilhã, Portugal. Poster presentation.

Furthermore, the present PhD provided opportunities for collaborations which have resulted in the publication of the following research articles in international journals:

- F. Melo-Fonseca, R. Lima, M. M. Costa, F. Bartolomeu, N. Alves, A. Miranda, M. Gasik, F.S. Silva, N.A. Silva, G. Miranda, *45S5 BAG-Ti6Al4V structures: The influence of the design on some of the physical and chemical interactions that drive cellular response*, Materials & Design, 160 (2018): 95-105. https://doi.org/10.1016/j.matdes.2018.08.056.
- M. M. Costa, R. Lima, F. Melo-Fonseca, F. Bartolomeu, N. Alves, A. Miranda, M. Gasik, F. S. Silva, N. A. Silva, G. Miranda, *Development of β-TCP-Ti6Al4V structures: Driving cellular response by modulating physical and chemical properties*, Materials Science and Engineering: C, 98 (2019): 705-716. https://doi.org/10.1016/j.msec.2019.01.016.

## References

[1] A.N. Aufa, M.Z. Hassan, Z. Ismail, Recent advances in Ti-6Al-4V additively manufactured by selective laser melting for biomedical implants: Prospect development, J. Alloys Compd. 896 (2022) 163072. https://doi.org/10.1016/j.jallcom.2021.163072.

[2] M. Kaur, K. Singh, Review on titanium and titanium based alloys as biomaterials for orthopaedic applications, Mater. Sci. Eng. C. 102 (2019) 844–862. https://doi.org/10.1016/j.msec.2019.04.064.

[3] G.L. Koons, M. Diba, A.G. Mikos, Materials design for bone-tissue engineering, Nat. Rev. Mater. 5 (2020) 584–603. https://doi.org/10.1038/s41578-020-0204-2.

[4] A. Bal-Price, S. Coecke, Guidance on Good Cell Culture Practice (GCCP), Cell Cult. Tech. (2011) 1–26. https://doi.org/10.1007/978-1-61779-077-5.